

**SILICON DEFECT PASSIVATION BY H<sub>2</sub>S REACTION AND PATTERNING  
PROCESS OF INTERDIGITATED BACK CONTACT SILICON  
HETEROJUNCTION (IBC-SHJ) SOLAR CELL**

by

Hsiang-Yu Liu

A dissertation submitted to the Faculty of the University of Delaware in partial fulfillment of the requirements for the degree of Doctor of Philosophy in Materials Science and Engineering

Spring 2018

© 2018 Hsiang-Yu Liu  
All Rights Reserved

**SILICON DEFECT PASSIVATION BY H<sub>2</sub>S REACTION AND PATTERNING  
PROCESS OF INTERDIGITATED BACK CONTACT SILICON  
HETEROJUNCTION (IBC-SHJ) SOLAR CELL**

by

Hsiang-Yu Liu

Approved:

\_\_\_\_\_  
Darrin J. Pochan, Ph.D.

Chair of the Department of Materials Science and Engineering

Approved:

\_\_\_\_\_  
Babatunde A. Ogunnaike, Ph.D.

Dean of the College of Engineering

Approved:

\_\_\_\_\_  
Ann L. Ardis, Ph.D.

Senior Vice Provost for Graduate and Professional Education

I certify that I have read this dissertation and that in my opinion it meets the academic and professional standard required by the University as a dissertation for the degree of Doctor of Philosophy.

Signed:

---

Robert W. Birkmire, Ph.D.  
Professor in charge of dissertation

I certify that I have read this dissertation and that in my opinion it meets the academic and professional standard required by the University as a dissertation for the degree of Doctor of Philosophy.

Signed:

---

Robert L. Opila, Ph.D.  
Member of dissertation committee

I certify that I have read this dissertation and that in my opinion it meets the academic and professional standard required by the University as a dissertation for the degree of Doctor of Philosophy.

Signed:

---

Chaoying Ni, Ph.D.  
Member of dissertation committee

I certify that I have read this dissertation and that in my opinion it meets the academic and professional standard required by the University as a dissertation for the degree of Doctor of Philosophy.

Signed:

---

Steven S. Hegedus, Ph.D.  
Member of dissertation committee

I certify that I have read this dissertation and that in my opinion it meets the academic and professional standard required by the University as a dissertation for the degree of Doctor of Philosophy.

Signed:

---

Ujjwal K. Das, Ph.D.  
Member of dissertation committee

I certify that I have read this dissertation and that in my opinion it meets the academic and professional standard required by the University as a dissertation for the degree of Doctor of Philosophy.

Signed:

---

Jose Luis Cruz-Campa, Ph.D.  
Member of dissertation committee



## **ACKNOWLEDGMENTS**

First and foremost I would like to express my sincere gratitude for my advisor Dr. Robert Birkmire, who has provided me the research opportunity, guided and supported me throughout my entire Ph.D. career with his knowledge, patience, and consideration, especially when I faced the challenge of finding a balance between my family and my research after Austin was born.

Another person I would like to thank particularly is Dr. Ujjwal Das, who has made a big impact on my Ph.D. research by guiding me throughout the day-to-day research, imparting his knowledge, creativity, and ideas in photovoltaic processing and analysis from material and device point of view. Additionally, I have learned tremendously about logic and organization in writing research articles from Dr. Ujjwal Das.

I would also like to thank my research committee members Dr. Steve Hegedus, Dr. Chaoying Ni, Dr. Robert Opila, and Dr. Jose Luis Cruz-Campa for their suggestions on my research, allowing my step-by-step accomplishment toward my research.

I will not be able to get as close as today to the end of my doctoral career without the help and assistance from the current and former students, as well as researchers at the Institute of Energy Conversion, especially Gowri Manasa Sriramagiri, Nuha Ahmed, Mike Lloyd, Dr. Sina Soltanmohammad, Dr. Robert Lovelett, Dr. Lei Chen, Dr. Thomas Mangan, Dr. Lulu Zhang, Dr. Zhen Shu, Brian McCandless, Shannon Field, John Elliot, and Wayne Buchanan. You have always

been very helpful and supportive to my research by sharing your knowledge and experiences about processing, characterization, and analysis.

I could never imagine how my life would be in graduate school with a baby until the day Austin was born. Even if it means staying awake for the entire night only to try soothe and calm a hungry and fussy baby down, making him sit on my lap in front of the computer when I was revising my paper to stop him from crying, or pausing my chemical reaction to rush to the daycare when I received a call from daycare, the process has brought Oliver and me so much joy and love. My achievement in graduate school cannot be carried out without my beloved husband, Oliver. Because to his understanding and consideration, I was able spend as much time as needed to focus on my research. He is not only a wonderful husband but also a super daddy. He means everything to me, to Austin, and to our family.

My parents in Taiwan deserve infinite appreciation for their unconditional support throughout the entire journey. They are my staunchest backing that has allowed me to realize my goal and on my way to attaining higher education by always providing any assistance they could without hesitation.

## TABLE OF CONTENTS

LIST OF TABLES .....	xi
LIST OF FIGURES .....	xiii
ABSTRACT .....	xx
GLOSSARY .....	xxiii

### Chapter

1	INTRODUCTION TO THE DISSERTATION .....	1
1.1	Research Motivation.....	1
1.2	Outline of Dissertation .....	3
2	BACKGROUND .....	6
2.1	Solar Energy and Crystalline Si Solar Cell .....	6
2.1.1	Si Heterojunction (SHJ) Solar Cell .....	8
2.1.2	Interdigitated Back Contact Si Heterojunction Solar Cell .....	14
2.2	Review of c-Si Surface Defect Passivation.....	17
2.2.1	Si Surface Recombination and Passivation Mechanisms .....	17
2.2.2	State of the art Surface Passivation Materials and Approaches ..	22
2.2.2.1	Silicon Dioxide (SiO <sub>2</sub> ).....	22
2.2.2.2	Hydrogenated Amorphous Silicon (a-Si:H) .....	24
2.2.2.3	Aluminum Oxide (Al <sub>2</sub> O <sub>3</sub> ).....	25
2.2.2.4	Hydrogenated Amorphous Silicon Nitride (a-SiN <sub>x</sub> :H) ..	28
2.3	Review of Multicrystalline Si Bulk Defect Passivation.....	29
2.3.1	Types of Bulk Defect.....	30
2.3.2	Traditional Bulk Defect Passivation Methods.....	31
3	EXPERIMENTAL TECHNIQUES .....	34
3.1	Fabrication.....	34

3.1.1	Wafer Cleaning Process .....	34
3.1.2	Wet Chemical Etching: HNA & TMAH .....	36
3.1.3	Plasma Enhanced Chemical Vapor Deposition System (PECVD) .....	38
3.1.4	Photolithography .....	42
3.1.5	Custom-Built Sulfurization / Selenization System .....	46
3.1.6	Electron Beam Metallization .....	50
3.2	Material Characterization .....	52
3.2.1	X-ray Photoelectron Spectroscopy .....	52
3.2.2	Fourier Transform Infrared Spectroscopy (FTIR) .....	59
3.2.3	Photoluminescence Image .....	64
3.3	Optical and Electrical Characterization .....	65
3.3.1	Variable Angle Spectroscopic Ellipsometry (VASE) .....	66
3.3.2	Effective Minority Carrier Lifetime Measurement .....	75
3.3.3	Current-Voltage Analysis .....	82
3.3.4	Quantum Efficiency Measurement .....	85
3.3.5	Laser Beam Induced Current Scanning .....	89
4	THE ROLE OF BACK CONTACT PATTERNING ON STABILITY AND PERFORMANCE OF SI IBC HETEROJUNCTION SOLAR CELLS .....	91
4.1	Summary .....	91
4.2	Introduction .....	92
4.3	Experimental Section .....	93
4.4	Results and Discussions .....	101
4.5	Conclusion .....	108
5	DIFFERENT FRONT STACK LAYER PASSIVATION FOR APPLICATION IN IBC-SHJ SOLAR CELLS .....	109
5.1	Summary .....	109
5.2	Introduction .....	110
5.3	Experimental .....	112
5.3.1	Wafer Cleaning and Preparation .....	112
5.3.2	Front Stack: i. a-Si:H / a-SiN <sub>x</sub> :H / a-SiC:H (control sample) ...	113
5.3.3	Front Stack: n <sup>+</sup> diffusion / i. a-Si:H (8nm) / a-SiN <sub>x</sub> :H / a-SiC:H .....	114
5.3.4	Front Stack: i. a-Si:H (8nm) / n. a-Si:H (20nm) / a-SiN <sub>x</sub> :H / a-SiC:H .....	115
5.3.5	Front Stack: n. a-Si:H (40nm) / a-SiN <sub>x</sub> :H / a-SiC:H .....	116

5.4	Results and Discussion.....	116
5.4.1	Stack Layer Passivation Level.....	116
5.4.2	J-V and QE Measurements and Analysis .....	117
5.5	Conclusion.....	124
6	SURFACE DEFECT PASSIVATION AND REACTION OF C-SI IN H <sub>2</sub> S. 126	
6.1	Summary .....	126
6.2	Introduction .....	127
6.3	Experimental .....	129
6.4	Results and Discussion.....	131
6.4.1	Effect of Reaction Temperature on $\tau_{\text{eff}}$ .....	131
6.4.2	Surface Bonding States.....	132
6.4.3	Origin of Oxygen.....	135
6.4.4	Reaction Pathways for Si Surface Passivation .....	137
6.4.5	Effect of Sulfur, Oxygen, and Hydrogen on Passivation Level .....	138
6.4.6	Degradation and Stability of Surface Passivation .....	143
6.5	Conclusion.....	148
7	A NOVEL DEFECT PASSIVATION FOR MULTICRYSTALLINE SI WAFFER BY H <sub>2</sub> S REACTION.....	149
7.1	Summary .....	149
7.2	Introduction .....	150
7.3	Experimental .....	151
7.4	Results and Discussion.....	152
7.4.1	Injection Level Dependent Minority Carrier Effective Lifetime.....	152
7.4.2	Passivation Stability and Reasons Causing Degradation .....	155
7.4.3	Wet Chemistry Process: Surface Removal and Repassivation..	158
7.4.4	Photoluminescence Images Demonstrate Improved mc-Si Bulk Quality .....	161
7.5	Conclusion.....	161
8	SUMMARY AND FUTURE PROSPECT .....	163
8.1	Summary .....	163
8.2	Future Prospects .....	166
	REFERENCES.....	169

## Appendix

A	SOLAR SPECTRAL IRRADIANCE: AM1.5 AND AM0.....	189
B	REPRINT PERMISSION LETTERS.....	191

## LIST OF TABLES

Table 2.1 Comparison of performance of homojunction solar cell and heterojunction solar cell .....	13
Table 2.2 The record cell comparison between front and back heterojunction solar cell. (The one Kaneka published in Nature Energy is 26.3%) .....	17
Table 3.1 The energy and line widths of available anode materials [128].....	55
Table 4.1 (a) Back surface patterning by PR: The sequence of all a-Si:H layers and its alloy deposition, and their each deposition conditions used for IBC-SHJ solar cells, including both front and back surfaces.....	97
Table 4.1 (b) Back surface patterning by a-SiN <sub>x</sub> :H: The sequence of all a-Si:H layers and its alloy deposition, and their each deposition conditions used for IBC-SHJ solar cells, including both front and back surfaces....	97
Table 4.2 Illuminated JV performance and model parameters for the cell processed with PR/LFC; Initial, degraded (180 days) and post-heat treatment. Area = 2.5 cm <sup>2</sup> .....	106
Table 5.1 The sequence of all a-Si:H layers and its alloy deposition, and their each deposition conditions used for IBC-SHJ solar cells with their front stack layers i. a-Si:H / a-SiN <sub>x</sub> :H / a-SiC:H .....	113
Table 5.2 The sequence of all a-Si:H layers and its alloy deposition, and their each deposition conditions used for IBC-SHJ solar cells with their front stack layers n <sup>+</sup> diffusion / i. a-Si:H / a-SiN <sub>x</sub> :H / a-SiC:H .....	114
Table 5.3 The sequence of all a-Si:H layers and its alloy deposition, and their each deposition conditions used for IBC-SHJ solar cells with their front stack layers i. a-Si:H / n. a-Si:H / a-SiN <sub>x</sub> :H / a-SiC:H.....	115
Table 5.4 The sequence of all a-Si:H layers and its alloy deposition, and their each deposition conditions used for IBC-SHJ solar cells with their front stack layers n. a-Si:H / a-SiN <sub>x</sub> :H / a-SiC:H .....	116

Table 5.5 $\tau_{\text{eff}}$ of stack layer passivation, comparing between different front stack layers. ....	117
Table 5.6: IBC-SHJ solar cell performances including parameters $V_{\text{OC}}$ , $J_{\text{SC}}$ , FF, and Efficiency ( $\eta$ ). Cell area 1.61 cm <sup>2</sup> .....	118
Table 6.1 XPS analysis of each component on Si surface and the passivation level after process indicates no passivation effect after O <sub>2</sub> /Ar annealing. ....	135
Table 6.2 Concentration of Si, S, and O on c-Si surface after H <sub>2</sub> S reactions, studies include different temperature, duration, and H <sub>2</sub> S concentration. ....	136
Table 6.3 Certificate of Analyses showed impurity level in H <sub>2</sub> S cylinder.....	137
Table 6.4 Bond association energies (kJ/mol) among elements Si, O, S, and H. ....	145



## LIST OF FIGURES

Figure 2.1 Solar PV global capacity and annual additions from 2006 to 2016 [7].	7
Figure 2.2 Drawing of traditional diffused-junction c-Si solar cell, including its band diagram. The wafer is p-type. Structure is not drawn to scale.	9
Figure 2.3 Drawing of a Si HJ solar cell as first developed by Sanyo, Japan, including its band diagram. The wafer used here is n-type.	11
Figure 2.4 Schematic of simple-designed front homojunction solar cell with full-area passivated back contact. Reprinted from Ref. [21], Copyright 2015 IEEE. (IEEE does not require individuals working on a thesis to obtain a formal reuse license.)	13
Figure 2.5 The schematic of IBC-SHJ solar cell with record efficiency of 26.3% released by Kaneka Corp in 2017. Reprinted from Ref. [3], Copyright 2017, with permission from Springer Nature.	16
Figure 2.6 Surface states on the c-Si surface can be terminated via oxygen or hydrogen by depositing or growing a passivation layer on top of c-Si surface, which is called chemical passivation.	20
Figure 2.7 Fixed charge in the passivation layer can repel one type of carriers and reduce its concentration and therefore the recombination rate can be improved. This is called field – effect passivation.	22
Figure 2.8 (a) and (b) are the density of electron (red line) and hole (blue line) at different depth from p-type c-Si surface affected by the fixed negative charge $Q_f = 2 \times 10^{12} \text{ cm}^{-2}$ in the $\text{Al}_2\text{O}_3$ film after the $\text{Al}_2\text{O}_3$ deposited on the c-Si surface. (c) is the c-Si band bending under influence of $Q_f$ . Data is obtained by simulation using PC1D for a $2 \Omega\text{cm}$ c-Si wafer under illumination. Reprinted from Ref. [74], Copyright 2012, with permission from AIP Publishing.	27
Figure 2.9 The percentage of annual production for thin film, mc-Si, and mono c-Si solar cell in photovoltaics field from 1980 to 2016 [8].	29

Figure 2.10 Neutron activation analysis data of total metal content in ingot-grown, ribbon, and sheet mc-Si materials, as determined from published data. Reprinted from Ref. [91], Copyright 2006, with permission from John Wiley and Sons.....	31
Figure 3.1 The schematic of the c-Si surface reactions during the cleaning processes in piranha oxidation and HF etch. X and R represent the impurities and organic residues on the c-Si surfaces. ....	36
Figure 3.2 Schematic of cross-section of the PECVD system at IEC. ....	40
Figure 3.3 Multi-chamber (MC) in-line PECVD system at IEC, in which the PECVD processes in this dissertation were conducted. ....	41
Figure 3.4 Karl Suss MJB standard 3 mask aligner used at IEC.....	44
Figure 3.5 General photolithography process flow. ....	46
Figure 3.6 The custom-built sulfurization / selenization system at IEC, with the heating jacket for heating up the reactor. ....	47
Figure 3.7 Schematic of the reactor with the major components labeled. ....	48
Figure 3.8 Schematic of electron beam evaporation system. ....	51
Figure 3.9 The internal geometry of the analytical components in Thermo Scientific K-Alpha [127]. ....	54
Figure 3.10 Schematic of the focusing X-ray monochromator used on Thermo Scientific XPS Instruments [127]. ....	56
Figure 3.11 The photoemission process involved for XPS surface analysis. The discs represent electrons and the bars represent energy levels within the material being analyzed. The equation governing the process is: $KE = h\nu - BE$ [129]. ....	57
Figure 3.12 The binding energy reference [129]. ....	58
Figure 3.13 The characteristic frequencies in IR match the molecule absorption energies and being absorbed with the molecule vibration, providing the resulting spectrum represents the molecule absorption and transmission, creating a molecule fingerprint of the sample. ....	60
Figure 3.14 A simple spectrometer layout provided by Thermo Nicolet Corporation [131]. ....	62

Figure 3.15 The configuration of variable angle spectroscopic ellipsometer [132].....	67
Figure 3.16 The linear polarized electromagnetic radiation emits and gets reflected by the sample, forming reflected elliptically polarized light, which includes the information (thickness, refractive index...etc.) of the characterized sample [133].....	67
Figure 3.17 General procedure used in optical measurement, which is also the standard procedure in ellipsometry measurements to determine the material properties from experimental data [133].....	70
Figure 3.18 The phase delay between the reflected beam and the beam traveling through the film can be caused by both the film thickness and the refractive index [133]. .....	72
Figure 3.19 The $\Psi$ curve for a series of SiO <sub>2</sub> films of different thicknesses [133]. .....	73
Figure 3.20 Variable angle spectroscopic ellipsometer (VASE) with AutoRetarder from J. A. Woollam [133]. .....	74
Figure 3.21 The completed system should look like this. The calibration wafer covers the sensor coil but cannot cover the small blue light sensor (standard solar cell). .....	76
Figure 3.22 The screen shot of QSSPC mode $\tau_{\text{eff}}$ measurement by Sinton Lifetime Tester WCT-100. The upper left plot: The decay overtime of illumination at reference cell and photoconductance signal. The upper right plot: Inverse lifetime after Auger correction at different carrier density (injection level). The lower left plot: Implied Voc calculated from lifetime measurement. The lower right plot: minority carrier lifetime without Auger correction at different carrier density (injection level). In this measurement, the $\tau_{\text{eff}}$ (highlighted in red box), saturate current density (highlighted in blue box), and implied Voc at 1-sun intensity (highlighted in green box) can be calculated from the photoconductance decay.....	79
Figure 3.23 A schematic of a c-Si wafer with its front and back surface recombination velocity, S1 and S2 respectively. ....	80
Figure 3.24 The schematic setup for current (density) – voltage measurement.....	82
Figure 3.25 Example of a J-V curve and the characteristic parameters calculated from it: V <sub>OC</sub> , J <sub>SC</sub> , FF, and efficiency $\eta$ . ....	83
Figure 3.26 Typical quantum efficiency curve of a c-Si solar cell [138]. .....	86

Figure 3.27 Configuration of quantum efficiency measurement [140].	88
Figure 3.28 The LBIC system setup [142].	90
Figure 4.1 (a) Back surface patterning by PR: Process flow of back surface of IBC-SHJ solar cell using PR as a patterning mask with 2 steps photolithography	96
Figure 4.1 (b) Back surface patterning by a-SiN <sub>x</sub> :H: Process flow of back surface of IBC-SHJ solar cell using a-SiN <sub>x</sub> :H as a patterning mask with 3 steps photolithography	96
Figure 4.2 Schematic structure of IBC-SHJ solar cell using (a) PR and (b) a-SiN <sub>x</sub> :H as masks for forming the interdigitated pattern. Note that two processes lead to different gap structures.	99
Figure 4.3 Cell efficiencies over time of 2.5 cm <sup>2</sup> IBC-SHJ solar cells fabricated with PR or SiN <sub>x</sub> as a mask. Note that two cells had an optional laser fired contact (LFC). The red arrows indicate days where the device was given 200 °C heat treatment and retested.	102
Figure 4.4 Relative cell parameter degradation for an IBC-SHJ solar cell fabricated with PR mask (PR / LFC).	103
Figure 4.5 The ratio of LBIC line scan at V <sub>mp</sub> to 0V biases of IBC-SHJ solar cells with three different patterning processes (PR/LFC/HT, SiN <sub>x</sub> /LFC and SiN <sub>x</sub> ).	105
Figure 4.6 Dark and light JV curves of 1.57 cm <sup>2</sup> IBC-SHJ solar cell showing a stable efficiency of ~17.9% fabricated by SiN <sub>x</sub> mask with no LFC.	107
Figure 5.1 Schematic drawing of the effect of the enhanced lateral current transport of the majority carriers via the front surface field (FSF). The lateral current transport through the FSF (b) can be seen as an additional transport path to the base lateral resistance (a). Reprinted from Ref. [155], Copyright 2008 IEEE. (IEEE does not require individuals working on a thesis to obtain a formal reuse license.)	111
Figure 5.2: IBC-SHJ solar cell performances by J-V curves of four different front structures. Cell area 1.61 cm <sup>2</sup>	118
Figure 5.3: QE of SHJ-IBC solar cells with different front structures	119

Figure 5.4 PC1D simulations [163] of the influence of the front surface recombination velocity on the efficiency of back-junction back-contact n type c-Si solar cells with and without the FSF. Device structure shown in Figure 5.6. Reprinted from Ref. [155], Copyright 2008 IEEE. (IEEE does not require individuals working on a thesis to obtain a formal reuse license.).....	121
Figure 5.5 Schematic cross-section of the n-type back-junction back-contact Si solar cell. Reprinted from Ref. [155], Copyright 2008 IEEE. (IEEE does not require individuals working on a thesis to obtain a formal reuse license) .....	122
Figure 5.6 Two-dimensional numerical simulations and measured values of the (a) FF & (b) series resistance on the back-junction back-contact Si solar cells as a function of the pitch size for two different base material c-Si wafer resistivities reveal the effect of FSF. (a) Reprinted from Ref. [155], Copyright 2008 IEEE. (b) Reprinted from Ref. [156], Copyright 2008 John Wiley and Sons. (IEEE does not require individuals working on a thesis to obtain a formal reuse license).....	123
Figure 6.1 Initial $\tau_{\text{eff}}$ at minority carrier density of $10^{15} \text{ cm}^{-3}$ on planar and textured Si (100) wafers right after reaction with 3.5% $\text{H}_2\text{S}$ diluted in Ar at different temperatures for 30 min.....	132
Figure 6.2 XPS measurements for three elements detected on the surface: Si, S, and O for three Si surfaces; (i) clean Si (top row), (ii) clean Si reacted in 100% Ar at 550°C for 30 min (middle row), and (iii) clean Si reacted in 3.5% $\text{H}_2\text{S}$ diluted in Ar at 550°C for 30 min (bottom row). Red, blue, and black lines represent measured XPS data, deconvoluted spectra and composite spectra respectively.....	133
Figure 6.3 The comparison of Si surface by XPS measurements on Si wafers reacted in 3.5% $\text{H}_2\text{S}/\text{Ar}$ and 4% $\text{O}_2/\text{Ar}$ at 550°C for 30 min. Red, blue, and black lines represent measured XPS data, deconvoluted spectra and composite spectra respectively. ....	135
Figure 6.4 S and O depth profiles determine from XPS characterization with sequential Ar sputtering for the samples reacted at 550°C for 30 min in different $\text{H}_2\text{S}$ concentration in Ar. Measured initial $\tau_{\text{eff}}$ and d values are listed in the legend.....	139
Figure 6.5 The variation of initial $\tau_{\text{eff}}$ with the surface S% (a) / O% (b) estimated from XPS. The S% / O% was varied by $\text{H}_2\text{S}$ reactions at different temperatures, times, and concentrations.....	142

Figure 6.6. FTIR observation of H <sub>2</sub> S-reacted Si sample, demonstrating no Si-H <sub>x</sub> on the reacted Si surface contributing to surface passivation. ....	143
Figure 6.7 The stability of surface passivation evaluated by change in $\tau_{\text{eff}}$ with storage time in air. ....	144
Figure 6.8. (a) Degradation of $\tau_{\text{eff}}$ of a S-passivated Si with time in air ( $\tau_{\text{eff}} \sim 2000$ $\mu\text{sec}$ degraded to $< 100$ $\mu\text{sec}$ in 70 min). (b) Change in $\tau_{\text{eff}}$ with time in air for a S-passivated Si coated with 80 nm a-SiN <sub>x</sub> :H deposited at 300 °C exhibits stable passivation level over time. A low ( $\tau_{\text{eff}} \sim 30$ $\mu\text{sec}$ ) but stable $\tau_{\text{eff}}$ is also observed for the Si passivated by only a-SiN <sub>x</sub> :H layer. ....	148
Figure 7.1 (a) $\tau_{\text{eff}}$ as a function of $\Delta n$ of monocrystalline Cz wafers comparing three different Si surface passivation methods; (b) $\tau_{\text{eff}}$ as a function of $\Delta n$ of mc-Si wafers with the same passivation methods as with Cz wafers demonstrating QHY/ME and a-Si:H can not passivate trap and recombination states in mc-Si effectively, while H <sub>2</sub> S reaction passivates both types of defects. ....	155
Figure 7.2 Comparison of the passivation stability after 100% H <sub>2</sub> S reaction: The Cz wafer $\tau_{\text{eff}}$ degraded from initial $\sim 2000$ $\mu\text{sec}$ to below 100 $\mu\text{sec}$ in $\sim 18$ days with storage in air; the mc-Si wafer was relatively stable over time. ....	156
Figure 7.3 XPS spectra of S 2p on a Cz Si surface after reaction with H <sub>2</sub> S at 650°C: comparison of the sulfur concentration before and after degradation where the initial $\tau_{\text{eff}}$ is $\sim 2000$ $\mu\text{sec}$ and the degraded $\tau_{\text{eff}}$ is below 100 $\mu\text{sec}$ . ....	157
Figure 7.4 (a) Graphic depiction of processing on mc-Si starting from HF-cleaned bare wafer, followed by H <sub>2</sub> S reaction for bulk and surface passivation. After H <sub>2</sub> S reaction, surface was removed by HNA and then repassivated by QHY/ME. Each step has $\tau_{\text{eff}}$ reported at $10^{15} \text{ cm}^{-3}$ . (b) Injection level dependent $\tau_{\text{eff}}$ after each step of processing, verifying the bulk passivation quality can be maintained with trap effect eliminated during surface removal and repassivation in wet chemistry. ....	160
Figure 7.5 PL images on clean bare mc-Si wafer (left) shows no luminescence and (right) 650°C H <sub>2</sub> S-passivated mc-Si wafer with a clear defined PL image. ....	161
Figure A.1 Spectral distribution of sunlight for the cases AM1.5 and AM0, with the ideal black body radiation at 5800 K for comparison [212]. ....	190

## ABSTRACT

The interdigitated back contact Si heterojunction (IBC-SHJ) solar cell has achieved record efficiency of 26.7% for Si based devices, because of excellent surface passivation provided by thin a-Si:H layers deposited at low temperature as the heterojunction partner and elimination of shading loss on the front surface of IBC structure, since both base and emitter contacts are at the rear surface.

The back contact patterning approach was evaluated to enhance the IBC-SHJ solar cell performance and improve its stability in this work. A single i. a-Si:H layer passivation at the gap between contacts and a potential contamination arising from presence of photoresist in PECVD a-Si:H growth lead to low and unstable cell efficiency, which was only 15% at the beginning and degraded to 14.3% within a day. Therefore, boosting the cell performance and stability with a robust back contact patterning method for a clean deposition process and sufficient gap passivation is the main goal of this work. The highest cell performance of 20.2% with a perfect stability over time was achieved with improved patterning approach.

To further improve the IBC-SHJ solar cell efficiency, front surface field (FSF) using more conductive doped layer for additional field-effect passivation and its effect on device series resistance was investigated. To evaluate the effect of FSF, four different structures of front surface stack layers were studied, including 1) i. a-Si:H / ARC (control sample); 2)  $n^+$  FSF / i. a-Si:H / ARC; 3) i. a-Si:H / n. a-Si:H / ARC; and 4) n. a-Si:H / ARC. The FSF can be provided by either  $n^+$  phosphorous diffusion or n. a-Si:H via PECVD. Slightly better surface passivation was observed using  $n^+$  FSF.

However, no improvement on device performance by FSF was found among these four different structures.

Since both the base and emitter contacts are at the back surface of IBC-SHJ solar cell, the optical and electrical properties can be optimized separately, and therefore high passivation level and minimum absorption loss are the two goals for the front surface of IBC-SHJ solar cell. Based on this idea, the i. a-Si:H with high absorption coefficient and bandgap of  $\sim 1.7$  eV mostly used for the front surface passivation can be replaced by alternative passivation layers with higher bandgap and reduced thickness to minimize the absorption loss and enhance its short circuit current ( $J_{SC}$ ). To realize this, we propose a new c-Si surface passivation scheme using  $H_2S$  reaction. X-ray photoelectron spectroscopy (XPS) identified the bonding state S-Si-S contributing to the passivation of c-Si surface defects. Monolayer thickness of sulfur forming on c-Si surface is capable of providing the same passivation level as  $\sim 8$  nm thick i. a-Si:H layer often used in IBC-SHJ solar cell. Compared to i. a-Si:H,  $SiS_2$  passivation layer possessing higher bandgap and reduced thickness shows a great potential for improving the  $J_{SC}$  of IBC-SHJ solar cell especially in shorter wavelength ( $< 700$  nm). Although the surface passivation by  $H_2S$  reaction is unstable in air due to hydrolysis and oxidation of  $SiS_2$ , the degradation of  $\tau_{eff}$  can be eliminated by a capping layer of a-SiN<sub>x</sub>:H deposited right after  $H_2S$  reaction, which also acts as an anti-reflection layer for IBC-SHJ solar cell.

It is found from XPS analysis that the sulfur not only terminated c-Si surface dangling bonds, but also can diffuse into Si bulk during  $H_2S$  reaction. This opened up another interesting concept of using  $H_2S$  reaction to passivate mc-Si wafer bulk defects. This work shows that the reduction of both trap and recombination states can be achieved by  $H_2S$  reaction of commercial mc-Si wafers, which is demonstrated from



the injection level dependent  $\tau_{\text{eff}}$  characterization. Further wet chemistry process confirmed both the surface and bulk of mc-Si wafer can be passivated in  $\text{H}_2\text{S}$  reaction, and the unstable  $\text{H}_2\text{S}$ -passivated surface can be removed and re-passivated by other materials without affecting the passivated bulk quality. The preservation of  $\text{H}_2\text{S}$  passivated bulk quality in multiple wet chemistry processes will allow fabrication of mc-Si / a-Si:H heterojunction solar cells.

## GLOSSARY

PV	photovoltaic(s)
c-Si	crystalline Si
mono c-Si	monocrystalline Si
mc-Si	multicrystalline Si
HJ	heterojunction
IBC-SHJ	interdigitated back contact Si heterojunction
HIT	heterojunction with intrinsic thin-layer
Fz wafer	Float zone wafer
Cz wafer	Czochralski wafer
PECVD	plasma-enhanced chemical vapor deposition
ARC	anti-reflection coating
FSF	front surface field
BSF	back surface field
LFC	laser fired contact
i. a-Si:H	intrinsic hydrogenated amorphous silicon
a-SiN <sub>x</sub> :H	hydrogenated amorphous silicon nitride
a-SiC:H	hydrogenated amorphous silicon carbide
SiO <sub>2</sub>	silicon dioxide
SiS <sub>2</sub>	silicon disulfide
Al <sub>2</sub> O <sub>3</sub>	aluminum oxide
TCO	transparent conductive oxide
H <sub>2</sub> S	hydrogen sulfide
HF	hydrofluoric acid
H <sub>2</sub> SO <sub>4</sub>	sulfuric acid
H <sub>2</sub> O <sub>2</sub>	hydrogen peroxide
TMAH	tetramethylammonium hydroxide
HNO <sub>3</sub>	nitric acid

QHY/ME	quinhydrone-methanol
KOH	potassium hydroxide
NaOH	sodium hydroxide
$Q_f$	fixed charge density
FWHM	full width at half maximum
$\Delta G_{\text{rxn}}$	Gibbs free energy of reaction
$\tau_{\text{eff}}$	minority carrier effective lifetime
PCD	photoconductance decay
QSSPC	Quasi-steady-state photoconductance
SRV	surface recombination velocity
J-V	current (density)-voltage
$V_{\text{OC}}$	open circuit voltage
$J_{\text{SC}}$	short circuit current density
FF	fill factor
$\eta$	cell efficiency
$R_s$	series resistance
$J_0$	saturation current density
QE	Quantum efficiency
XPS	x-ray photoelectron spectroscopy
KE	kinetic energy
BE	binding energy
FTIR	Fourier-transform infrared spectroscopy
VASE	variable angle spectroscopic ellipsometry
PL	photoluminescence
EL	electroluminescence
LBIC	Laser beam induced current
AFM	atomic force microscopy
ALD	atomic layer deposition

## **Chapter 1**

### **INTRODUCTION TO THE DISSERTATION**

#### **1.1 Research Motivation**

Solar energy shows great technical and theoretical potential among all other renewable energy sources and has becoming one of the promising renewable energy sources and been put in the place to replace conventional fuels [1]. PV technology converting sunlight directly into electricity was first developed in 1950s for space usage. Soon after that people found its potential in terrestrial application. PV can work as both off-grid power supply systems and grid-connected electricity generation system. However, high production cost is always a concern for solar energy. Solar energy is still not competitive without subsidies which hinder a true market breakthrough worldwide. To reduce the cost, enhancing the cell/module performance, simplifying the fabrication process, lower the material cost and consumption, or reducing the processing temperature are all possible efforts can be made to improve the solar market.

In this dissertation, the solar energy research focuses on c-Si wafer based solar cells. c-Si wafer based PV modules are still the mainstream of PV technology attributed to the abundance in material supply and high cell performance. The efficiency of 41.6% was achieved on a multi-junction concentrator solar cell [2]. In the c-Si wafer based solar cell, the highest efficiency cell structure is IBC-SHJ with record efficiency 26.7% reported by Kenaka in 2017 [3]. IBC-SHJ is also the main structure focused on in this dissertation, and two parts of work on IBC-SHJ have been discussed.

The first part is the modification of back surface patterning approach, to enhance the cell efficiency and improve the stability of cell performance overtime attributed to a more sufficient gap passivation and clean deposition without photoresist outgassing in PECVD chamber. The second part of IBC-SHJ work is the evaluation of front stack layers to form a FSF for better front surface passivation and lower device resistance. Another main project focused on is sulfurization of the Si surface in  $\text{H}_2\text{S}$  reaction for surface passivation on both mono c-Si wafers and bulk passivation on mc-Si wafers. Among all other state-of-the-art surface passivation technologies and materials,  $\text{H}_2\text{S}$  reaction provides a new scheme with minimized absorption loss due to its high bandgap and moderate reaction temperature, which is more compatible with downstream solar cell fabrication such as contact formation. During the mono c-Si surface passivation in  $\text{H}_2\text{S}$  reaction, it has been observed that sulfur not only terminated the surface dangling bonds, but also diffused into c-Si, which lead to the possibility of using  $\text{H}_2\text{S}$  reaction to passivate the bulk defects in mc-Si. Mc-Si solar cell has higher and higher production over years in solar industry due to its low material cost compared to mono c-Si solar cell. However, relatively lower efficiency compared to mono c-Si due to its poor bulk quality is always the main challenge in the production line. Most of traditional bulk passivation methods need a high processing temperature such as gettering at  $950^\circ\text{C}$  or higher [4], [5], or hydrogen drive-in by a-SiN<sub>x</sub>:H at about  $700^\circ\text{C}$  [6]. It is expected that improving the bulk quality by minimizing defects in mc-Si wafer at a moderate temperature and simpler processing will largely enhance its device performance and therefore reduce the cost.

## 1.2 Outline of Dissertation

The dissertation is presented in eight chapters.

Chapter 2 gave a brief introduction of solar energy and c-Si solar cell, primarily focusing on heterojunction and back contact structures. Defect passivation including surface defect on mono c-Si wafer and bulk defect in mc-Si wafer were also introduced in this chapter. For the passivation of surface defect on mono c-Si wafer, multiple state-of-the-art passivation materials and technologies have been described, including  $\text{SiO}_2$ , a-Si:H,  $\text{Al}_2\text{O}_3$ , and a-SiN<sub>x</sub>:H. Different types of bulk defect in mc-Si including metal impurities, dislocations, and grain boundaries and each of their passivation approaches needed were described.

Chapter 3 introduced the fabrication processes and the working mechanisms of characterization tools being used in this dissertation. The fabrication processes includes wafer cleaning, wet chemical etching on wafer surfaces, PECVD for the formation of intrinsic / doped a-Si:H, a-SiN<sub>x</sub>:H, and a-SiC:H, photolithography for patterning on IBC-SHJ solar cell, sulfurization for c-Si surface and bulk defect passivation, and electron beam metallization for contact formation on heterojunction solar cell. The characterization part includes optical, electrical, and material characterization.

Chapter 4 explored the modification of back surface patterning approach to improve device performance and stability. The original patterning method used photoresist as patterning mask which may cause the contamination to the interface and bulk of deposition layers, and also it formed insufficient gap passivation. The process contamination and insufficient gap passivation are two possible reasons causing low and unstable efficiency. The new patterning method, a-SiN<sub>x</sub>:H instead of photoresist was used as the patterning mask in the PECVD chamber, avoiding any photoresist

outgassing to contaminate the deposition layer and making a clean deposition process. Moreover, with the new patterning design, the gap can be passivated by multiple layers, allowing the sufficient gap passivation. With the new patterning method using a-SiN<sub>x</sub>:H as the patterning mask, the cell performance was largely enhanced from 15% to 20.2% and became stable overtime.

Chapter 5 focuses on the effect of FSF on IBC-SHJ solar cell where different combinations of stack layers including i. a-Si:H / ARC, n<sup>+</sup> / i. a-Si:H / ARC, i. a-Si:H / n. a-Si:H / ARC, and n. a-Si:H / ARC were evaluated. ARC is composed of a-SiN<sub>x</sub>:H and a-SiC:H. The effect of FSF was analyzed and compared via  $\tau_{\text{eff}}$ , device J-V, and QE measurements.

Chapter 6 investigated a new c-Si surface passivation scheme by reaction in H<sub>2</sub>S. The sulfurization process in H<sub>2</sub>S provides promising passivation quality comparable to state-of-the-art passivation technology in PV industry. The effect of reaction temperature, duration, and H<sub>2</sub>S gas concentration were all discussed in this project. XPS was used to explore the interaction between Si and reaction gas H<sub>2</sub>S and understand the passivation mechanism. The reason causing instability of passivation level and the solution to eliminate the degradation were both investigated in this chapter.

Chapter 7 is the only chapter about mc-Si. Having higher concentration of H<sub>2</sub>S react with mc-Si wafer makes sulfur diffuse into Si bulk deeper and passivate its bulk defects. The injection level dependent  $\tau_{\text{eff}}$  reveals the change of traps and recombination states before and after the reaction. The enhanced bulk quality in H<sub>2</sub>S reaction gives us more opportunity to develop different structures of mc-Si based solar cell.

Chapter 8 summarized the work from chapter 4 to chapter 7 and discussed all the ideas of future work to extend the research completed in this dissertation.



## **Chapter 2**

### **BACKGROUND**

#### **2.1 Solar Energy and Crystalline Si Solar Cell**

There is no doubt the importance of clean energy such as solar energy is increasing year by year due to its characteristic – renewable and environmental friendly. During 2016, at least 75 GW of solar PV capacity was added worldwide, which is equivalent to the installation of more than 31,000 solar panels every hour [7]. The solar PV global capacity and annual additions from 2006 to 2016 can be seen in Figure 2.1. Solar energy is expected to meet the major fraction of the world's need. Solar cell, also called photovoltaic device, is the indicative of the device that converts solar energy to electricity.



tremendous development of microelectronic industry, and therefore it is not surprising that c-Si PV has grown so fast. The last factor needs to be addressed is that Si is the second most abundant element among the earth's crust. All these factors mentioned above make c-Si modules the most economical choice for large-scale system.

However, the cost of stock and fabrication in c-Si PV is still high, especially when we consider the price per kWh. This makes the PV-electricity cost higher than electricity generated by other traditional materials such as coal, oil, and natural gas. There are two approaches to reduce the price per kWh for solar cells. The first one is to improve the cell efficiency, and the second one is to lower the cost from manufacturing and from the feed stock. These two ideas are the target for most of the PV scientists worldwide. The IBC-SHJ solar cell being discussed in this dissertation chapter 4 focuses on increasing the cell efficiency. The studies of different front stack layers in chapter 5 and different passivation approaches in chapter 6 and both provide the potential to improve the cell performance. Mc-Si solar cells are discussed in chapter 7.

### **2.1.1 Si Heterojunction (SHJ) Solar Cell**

The first Si solar cell was developed in 1941 by Russell Ohl with the conversion efficiency of 6%, achieved by high temperature ( $\sim 1000^{\circ}\text{C}$ ) process to form the pn junction. Si has become the major material in the PV field. However, the high temperature processing p-n junction, which is typically considered as a traditional solar homojunction cell, has limitation of cell efficiency mainly due to poor passivation between semiconductor and metal contact and to the high thermal budget and wafer thickness required for high temperature processing. The high temperature

processing makes thinner wafer fabrication more challenge since thinner wafers are prone to warping and cracking at high temperature. However, fabricating solar cells on thinner wafer is a important trend in the PV industry since this will dramatically reduce the cost [11].

As seen in Figure 2.2, the front surface passivation layer for diffused homojunction c-Si solar cell is a dielectric such as  $\text{SiO}_2$  and  $\text{SiN}_x$ , which are insulating, therefore metal contacts need to contact the emitter layer directly in a high temperature sintering process [12]. This results in a poor interface with high recombination states between the metal and the absorber c-Si surface. This is why the metal contact area is always a high recombination center for not only the front surface, but also the back surface. In summary, this diffused junction solar cell structure has direct contact between absorber and metal, causing high recombination and hence low  $V_{OC}$ .

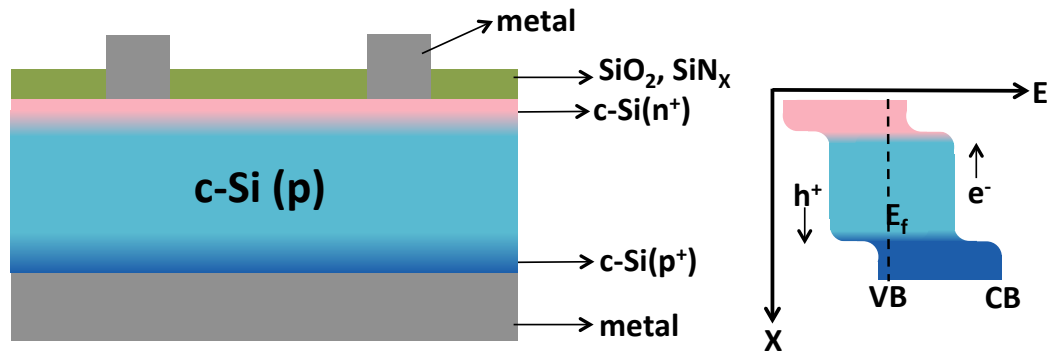


Figure 2.2 Drawing of traditional diffused-junction c-Si solar cell, including its band diagram. The wafer is p-type. Structure is not drawn to scale, and the texturing surfaces may apply.

To remove those limitations from traditional high temperature diffused junction c-Si solar cell, this work focuses on: 1) using low temperature processing to replace the high temperature processing, including emitter diffusion and metal sintering; 2) improving the passivation between the c-Si surface and metal contact, which can be achieved by inserting a relatively lower bandgap and ultra thin material for surface passivation between c-Si and metal, called “passivated contact” [13], [14]. Based on these two targets, Si HJ solar cell was first time developed by Sanyo (Panasonic today) in 2000 [15]. The key feature of heterojunction solar cell is the separation of highly recombination-active metal contacts from the c-Si surface by inserting a thin passivation layer with suitable bandgap, which needs to be slightly wider than c-Si of 1.12eV and hence i. a-Si:H becomes a very good candidate. A-Si:H can be considered as a conductive passivation material although it does not act as a electricity-generating layer in the device [16], and the anti-reflection coating (ARC) used for HJ cell is TCO instead of dielectric material such as a-SiN<sub>x</sub>:H [17]. HJ solar cell has a-Si:H for c-Si surface passivation and TCO for anti-reflection allowing the idea of “passivated contact” to be achieved without having metal directly contact the c-Si surface forming high recombination center. The improved surface passivation allows high open-circuit voltage ( $V_{OC}$ ) to be realized.

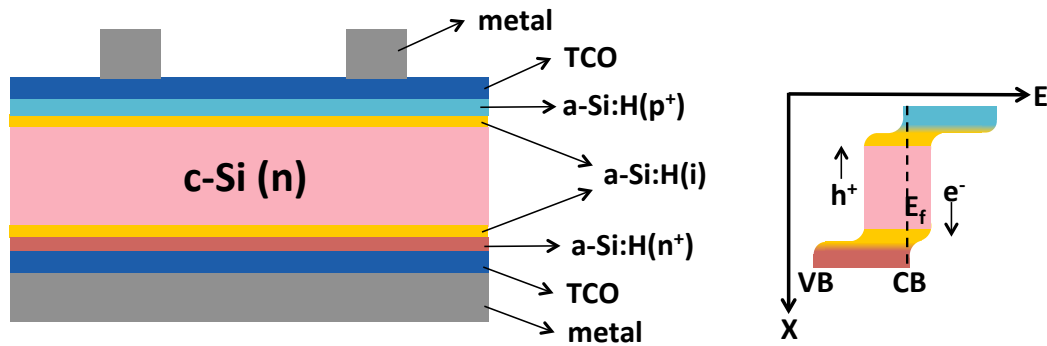


Figure 2.3 Drawing of a Si HJ solar cell as first developed by Sanyo, Japan, including its band diagram. The wafer used here is n-type, and the texturing surface may apply.

Figure 2.3 is the structure of a-Si:H / c-Si heterojunction solar cell and its band diagram developed by Sanyo with front and back surface both passivated by i. a-Si:H [15]. This Si Heterojunction with Intrinsic Thin-layer (HIT) solar cell confines charge carriers to a semiconductor active layer (here is c-Si) by sandwiching it between wider bandgap films (here is i. a-Si:H). From the processing perspective, there are three major advantages of the Si HJ processing technology [18]: 1) full exploitation of the excellent passivation properties of a-Si:H films, including both intrinsic and doped layers; 2) low-temperature (below 300°C) processing comparing to diffused junction requiring 800°C~1000°C, that enables the use of very thin wafers without causing substrate warping or breaking; 3) Simplified device fabrication process compared to high temperature diffused homojunction solar cell processing. Overall, compared to high-temperature diffused junction c-Si solar cell, higher efficiency and more reasonable production cost can be expected with Si HIT solar cell due to the improved

surface passivation especially at contact region leading to higher  $V_{oc}$ , and lower temperature processing [19].

A more precise definition of the cell structure in Figure 2.3 is Si front HJ solar cell with both front and back surface passivated by i. a-Si:H, which has a record efficiency 25.1% of large area ( $151.9 \text{ cm}^2$ ) published by KANEKA Corporation in 2015 [20]. To study the improved surface passivation and efficiency of Si HJ solar cell, we compare the Si HJ solar cell to a special designed homojunction solar cell shown in Figure 2.4, which was published in 2015 by Fraunhofer Institute for Solar Energy Systems, National Renewable Energy Laboratory, and Georgia Institute of Technology, where they reported a n-type c-Si front homojunction solar cell with full-area passivated back contact [21]. The difference between this cell structure and traditional homojunction solar cell is the back surface passivation. In traditional p-type homojunction solar cell as in Figure 2.2, the back surface typically has only a  $p^+$  BSF layer formed from the sintering of back metal contact Al. In this studied structure in Figure 2.4, the front surface had emitter by boron diffusion, and then passivated with a stack of  $\text{Al}_2\text{O}_3$  and  $\text{SiN}_x$ . This front structure design has the same concept of homojunction solar cell in Figure 2.2 [12]. The full-area passivated back contact by ultra-thin layer of  $\text{SiO}_x$  via low pressure chemical vapor deposition (LPCVD) is the main selling point discussed in this publication. This structure can still be considered as a homojunction solar cell. Table 2.1 shows the comparison of the cell performance between homojunction structure (Figure 2.4) and heterojunction structure (Figure 2.3).

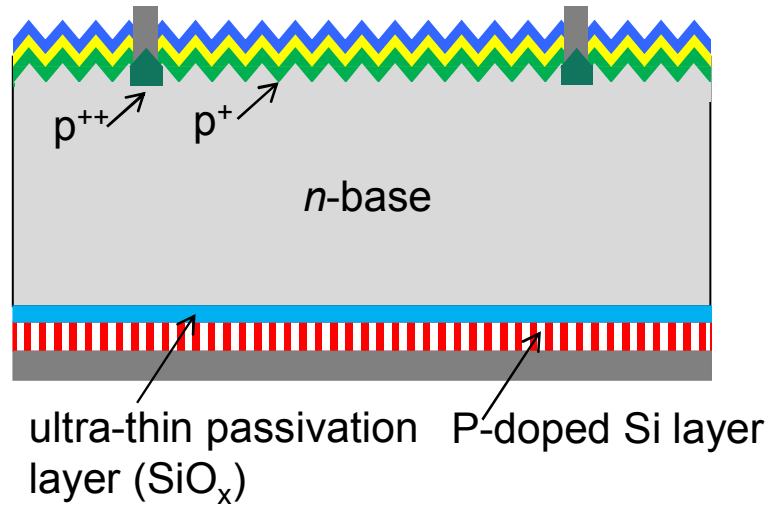


Figure 2.4 Schematic of simple-designed front homojunction solar cell with full-area passivated back contact. Reprinted from Ref. [21], with Copyright 2015 IEEE. (Please refer to Appendix B: Reprint Permission. IEEE does not require individuals working on a thesis to obtain a formal reuse license.)

Table 2.1 Comparison of performance of homojunction solar cell and heterojunction solar cell

Cell type	$V_{OC}$ (V)	$J_{SC}$ (mA/cm <sup>2</sup> )	FF (%)	Efficiency (%)	Area (cm <sup>2</sup> )	Article ref.
Heterojunction	0.738	40.8	83.5	25.1	151.9	[20]
Heterojunction	0.750	39.5	83.2	24.7	101.8	[22]
Homojunction	0.718	41.5	83.4	24.9	4.0	[21]

From Table 2.1, two high-efficiency HJ solar cell achievements were reported, with the gradually increase of cell performance attributed by multiple optimizations. Comparing heterojunction to homojunction, the higher  $V_{OC}$  in heterojunction is



contributed by excellent front and back surface passivation by a-Si:H. The front metal contact grid in homojunction solar cell is a non-passivated region, causing high carrier recombination, which is the main passivation and  $V_{OC}$  loss. However, heterojunction solar cell usually has relatively lower current than homojunction solar cell. This is due to the light absorption loss caused by passivation layer i. a-Si:H, front ITO, and the emitter layer doped a-Si:H [23], [24]. The thinner a-Si:H layer reduces absorption loss, however it will become more challenging to meet the same passivation level. In the homojunction solar cell, the front surface is passivated by dielectric materials such as  $SiO_2$ ,  $SiN_x$ , or  $Al_2O_3$ , making no absorption loss. (More details of those passivation materials will be discussed in section 2.2.3).

### **2.1.2 Interdigitated Back Contact Si Heterojunction Solar Cell**

As mentioned in the previous section, the trade-off between parasitic absorption and excellent surface passivation / optimized optical properties has given a motivation to design a back junction back contact solar cell structure. With both the emitter and base metal contacts moved to the back surface, both types of carriers are collected at the back side and the front surface can be optimized for only passivation and optical properties, without considering any electrical properties. For example, the front surface no longer needs conductive ARC such as ITO and therefore the absorption loss from ITO can be removed, or firing through dielectric ARC layers which always generate high recombination centers at the front surfaces and hence reducing  $V_{OC}$ . Also, with both metal contacts moved to the back surface, there is no metal grid shadowing loss to reduce  $J_{SC}$  on the front surface, which is unavoidable in front junction solar cell, including both homo- and hetero- junction devices. Moreover,

the restriction of contact geometry can be avoided when both the contacts are moved to the back surface, and therefore the contact coverage can be increased on the back surface and therefore reduce the device resistance [25], [26]. As the result, the trade-off between reflection loss and series resistance loss in the front contact structure will be eliminated, and FF will be increased due to the reduction of series resistance. From the perspective of module, the IBC design will simplify the cell interconnection and therefore reduce the material cost in the module packaging process [27].

The idea of IBC solar cell was first time proposed by Lammert in 1977 [28]. SunPower Corp. has been at the forefront of developing IBC diffused junction Si solar cell and already reached their record efficiency of 25% in 2016 [29]. IBC-SHJ solar cell combines the ideas of IBC structure and heterojunction. The device  $J_{SC}$  will be enhanced due to minimized optical loss from optimization of front stack layers and removal of metal grid, and  $V_{OC}$  will be enhanced due to the excellent surface passivation and passivated contact by low temperature deposition of i. a-Si:H. Moreover the FF will be increased due to decreasing series resistance attributed to larger metal contact coverage on the back surface. The record IBC-SHJ solar cell had the efficiency of 26.7% reported by Kaneka Corp in 2017 [3]. The schematic of cell structure is shown in Figure 2.5.

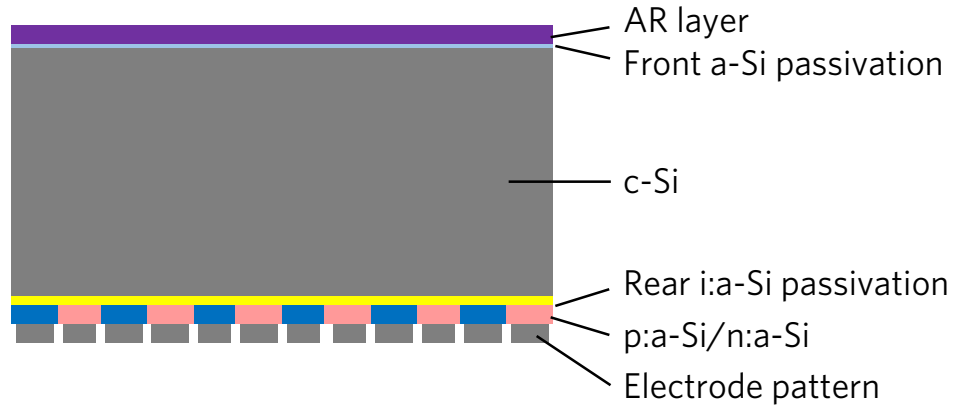


Figure 2.5 The schematic of IBC-SHJ solar cell with record efficiency of 26.3% released by Kaneka Corp in 2017. Reprinted from Ref. [3]. Please refer to Appendix B: Reprint Permission for Copyright 2017, with permission from Springer Nature.

Based on the heterojunction structure, the record cell performance of front HJ and IBC-SHJ can be compared in Table 2.2. The improvement of  $J_{SC}$  is as expected attributed to the reduction of absorption loss and illumination of metal shading loss on the front surface. The enhanced metal coverage on the back surface made slight improvement on the FF. Not surprisingly IBC-SHJ solar cell is the record cell structure due to those advantages mentioned above.

Table 2.2 The record cell comparison between front and back heterojunction solar cell.  
(The one Kaneka published in Nature Energy is 26.3%)

Cell type	V <sub>OC</sub> (V)	J <sub>SC</sub> (mA/cm <sup>2</sup> )	FF (%)	Efficiency (%)	Area (cm <sup>2</sup> )	Article ref.
Front HJ	0.738	40.8	83.5	25.1	151.9	[20]
IBC-SHJ	0.744	42.3	83.8	26.3	180.4	[3]

## 2.2 Review of c-Si Surface Defect Passivation

The quality of c-Si surface defect passivation is a prerequisite for high efficiency c-Si solar cells and has become even more critical with the industry trend towards thinner wafer for cost reduction, due to increasing surface – to – volume ratio [22], [30], [31]. c-Si is an indirect semiconductor material, hence the recombination loss is largely from defect levels within its bandgap, located both in the bulk and on the surface. However, normally high quality of float-zone (Fz) wafer and Czochralski (Cz) are used in PV industry, making the bulk defect density to a negligible level compared to surface defect density, and making the surface defects such as dangling bonds dominate the carrier recombination in the wafer. Two fundamental strategies are mainly applied to minimize the surface recombination loss, chemical passivation and field – effect – passivation. In this section, the mechanisms of these two passivation strategies will be thoroughly discussed, and some well-developed passivation materials based on these two approaches will be introduced as well.

### 2.2.1 Si Surface Recombination and Passivation Mechanisms

c-Si surface recombination is mainly caused by surface defects such as dangling bonds, which are due to the interruption of the periodic crystal lattice. Those

dangling bonds are unsaturated, and behave as highly recombination center, also called “surface states”. These surface states can be divided into intrinsic and extrinsic defects. Most of the cases are extrinsic defects, which are typically processing-related, due to dislocations or chemical residues and metallic depositions on the surface [32]. Therefore, “surface passivation” indicates the reduction of carrier recombination on the surface to keep the surface recombination losses at c-Si surfaces at a tolerable level. With a decent surface passivation, the recombination rate is decreased, and therefore enhancing the effective lifetime ( $\tau_{\text{eff}}$ ) and reducing the surface recombination velocity (SRV). The definitions of  $\tau_{\text{eff}}$  and SRV will be discussed in more details in chapter 3.

There are two passivation mechanisms for c-Si surface: 1) chemical passivation by reduction of the surface states; and 2) electrical passivation by reduction of the electron or hole concentrations on the surface. Before looking into more details about passivation mechanism, it would be better to understand some fundamentals of the surface recombination first. For the surface recombination, an electron from the conduction band recombines with a hole in the valence band through a defect level within the bandgap. The “defect level” here represents a surface state. The recombination caused by defects is called Shockley-Read-Hall (SRH) recombination [33]-[35]. For a single-level surface defect at an energy  $E_t$ , the recombination rate  $U_s$  can be expressed in Equation 2.1 [34], [36].

$$U_s = \frac{n_s p_s - n_i^2}{\frac{n_s + n_1}{S_{p0}} + \frac{p_s + p_1}{S_{n0}}} \quad (2.1)$$

$$\text{where } n_i \equiv n_i \exp\left(\frac{E_t - E_i}{kT}\right), p_i = \frac{n_i^2}{n_i}, S_{n0} \equiv \sigma_n v_{th} N_{st}, S_{p0} \equiv \sigma_p v_{th} N_{st}$$

$S_{n0}$  and  $S_{p0}$  are the SRV parameters of electron and hole,  $n_s$  and  $p_s$  are the concentrations of electron and hole,  $\sigma_n$  and  $\sigma_p$  are the capture cross sections of electron and hole,  $N_{st}$  is the number of surface states per unit area,  $E_i$  is the intrinsic Fermi energy,  $v_{th}$  is the thermal velocity of the charge carriers,  $k$  is the Boltzmann's constant,  $T$  is the temperature, and  $n_i$  is the intrinsic carrier density of the semiconductor. The relationship given by SRH theory between the recombination rate  $U_s$  and the properties of the surface states shown in Equation 2.1 shows that there are two fundamentally different technological possibilities to reduce the recombination rate at the semiconductor surface, which are 1) the reduction of the density of surface states and 2) the reduction of the concentration of either free electrons or holes at the surface.

Worth noting is that SRH recombination can occur either as a result of surface states, either through the bulk defects or impurities. In monocrystalline Si wafers, Cz and Fz wafers, the defects in the bulk is negligible and hence the SRH recombination causes by the surface states, which are typically dangling bonds. However if the wafer is mc-Si, then not only the surface, defects also exist in the bulk, including metal impurities, crystallographic defects such as dislocations, and the dangling bonds along the grain boundaries. The defects in mc-Si will be discussed in section 2.3.

### **Reduction of the density of surface states:**

The surface recombination rate is proportional to the defect density at the surface, which can be verified from Equation 2.1. The density of surface states  $N_{st}$  will

be drastically reduced by depositing or growing a passivation layer on top of the semiconductor surface. Oxygen and hydrogen are the two commonly used elements to reduce the density of surface states, as seen in Figure 2.6. Oxygen can be provided via  $\text{SiO}_2$  and hydrogen can be provided via a-Si:H. These two are most commonly applied and discussed in solar cell fabrication. More details will be discussed in section 2.2.2.

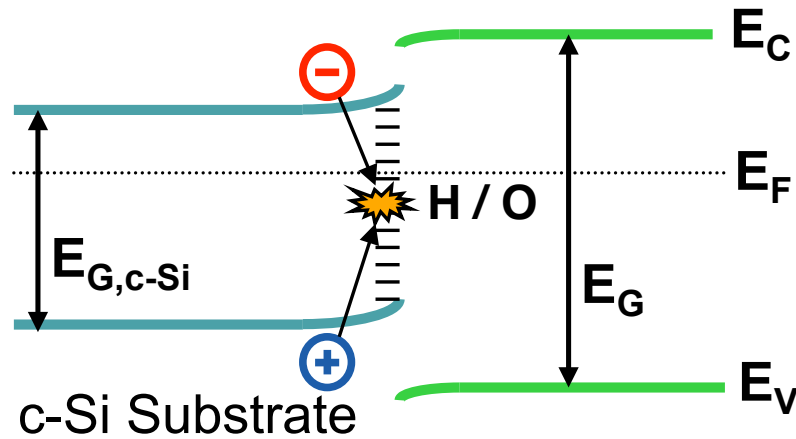


Figure 2.6 Surface states on the c-Si surface can be terminated via oxygen or hydrogen by depositing or growing a passivation layer on top of c-Si surface, which is called chemical passivation.

### Reduction of the surface concentrations of electron or hole

One electron and one hole need to be involved in a SRH recombination process, therefore the highest recombination rate can be reached when the surface concentrations of electron and hole are approximately equal [37]. Hence, if the concentration of one of the carriers, either electron or hole can be reduced, the

recombination rate can be strongly reduced. The reduction of either of the carrier concentration at the surface can be realized by the formation of an internal electrical field below the semiconductor surface, since electron and hole both carry electrical charge. Two independent techniques are commonly used to form this electric field to repel one type of carriers, and hence reduce the recombination rate: 1) Implementation of a doping profile below the Si surface, such as phosphorous for forming  $n^+$  layer below n-type c-Si surface, or boron for forming  $p^+$  layer below p-type c-Si surface. In a device structure, we typically call it front surface field (FSF) or back surface field (BSF). FSF or BSF consists of a higher doping region and makes a electric field form between this high-low junction ( $p$ - $p^+$  or  $n$ - $n^+$ ), introducing a barrier to minority carriers and keeping them away from the c-Si surface. The application of FSF on IBC-SHJ will be discussed in chapter 5. 2) Field – effect passivation, such as positive fixed charge in  $\text{SiN}_x$  or negative fixed charge in  $\text{AlO}_x$  [38]. These two materials are most commonly used for field effect passivation in the solar cell fabrication today. The positive fixed charge can be deposited on top of n layer to repel holes away and to attract electrons to the surface assisting the carrier collection. Similar idea, the negative fixed charge can be deposited on top of p layer to repel electrons away and to attract holes to the surface improving the carrier collection. Figure 2.7 is the schematic of field – effect passivation through fixed charge in the passivation layer. More details about field - effect passivation will be discussed in section 2.2.2.



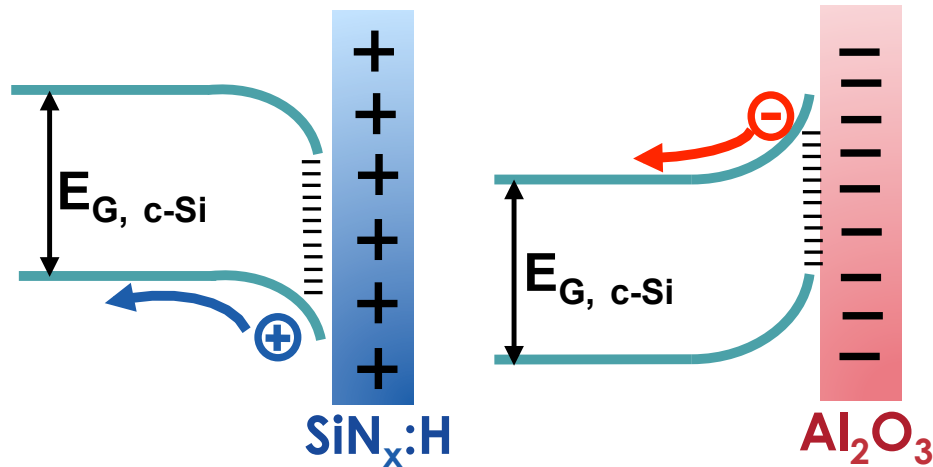


Figure 2.7 Fixed charge in the passivation layer can repel one type of carriers and reduce its concentration and therefore the recombination rate can be improved. This is called field – effect passivation.

## 2.2.2 State of the art Surface Passivation Materials and Approaches

Several materials and methods for c-Si surface passivation will be introduced in this section, including  $\text{SiO}_2$ , a-Si:H, a-SiN<sub>x</sub>:H, and  $\text{Al}_2\text{O}_3$ . Using stack layers to improve surface passivation quality has been broadly investigated by researchers, however in this section we will only focus on the function of each individual material.

### 2.2.2.1 Silicon Dioxide ( $\text{SiO}_2$ )

The most important benefit of thermally grown  $\text{SiO}_2$  is the high level of chemical passivation that can be achieved on both n-type and p-type c-Si surfaces over a wide range of relevant doping level. The field-effect passivation in  $\text{SiO}_2$  is not prominent due to comparatively low values of fixed charge density ( $Q_f$ ) in the range of

$10^{10} - 10^{11} \text{ cm}^{-2}$  [39]. The passivation level reached by thermally grown  $\text{SiO}_2$  is the SRV of 2 cm/sec for 1.5  $\Omega\text{cm}$  n-type wafer and 12 cm/sec for 1  $\Omega\text{cm}$  p-type wafer. The high resistivity 90  $\Omega\text{cm}$  n-type wafer demonstrates SRV of 0.5 cm/sec after  $\text{SiO}_2$  passivation, and 10  $\Omega\text{cm}$  p-type wafer shows SRV of 1.4 cm/sec [40]. All these data verified the flexibility of using  $\text{SiO}_2$  to passivation c-Si surface, among different dopant and a wide doping range. The excellent surface passivation by thermally grown  $\text{SiO}_2$  on the c-Si surface requires the thermal process at a high temperature of about 850°C by wet oxidation and about 1050°C by dry oxidation. With this high temperature range, thermal oxidation on high-resistivity Si wafer is capable of providing extremely low density of surface state of  $\sim 10^9 / \text{cm}^2 \text{ eV}^{-1}$  [41].

This high processing temperature requirement makes only the c-Si wafer with very low impurity level can be used without causing any degradation of the bulk lifetime. Another concern is the stability of passivation level by thermally grown  $\text{SiO}_2$ , that the interface defect density at  $\text{SiO}_2/\text{c-Si}$  was observed strongly increase under the ultraviolet light exposure [42]. The instability under light exposure can be terminated by capping layer such as a- $\text{SiN}_x\text{:H}$ , which can also act as a antireflection layer in the device [43], [44]. To avoid high temperature processing, using low temperature process to grow or deposit  $\text{SiO}_x$  to reach the same passivation level has brought people's attention. The processing approaches have been discussed such as low temperature [45] PECVD and chemical oxidation synthesis by  $\text{HNO}_3$  [46], [47]. However these two low temperature methods can only produce  $\text{SiO}_x$  with a few nanometers thick, which is obviously insufficient for c-Si surface passivation.  $\text{SiO}_x$  cannot provide a good surface passivation level with an extremely low density of surface states comparable to  $\text{SiO}_2$  formed by high temperature thermal oxidation.

#### 2.2.2.2 Hydrogenated Amorphous Silicon (a-Si:H)

The most critical benefit by a-Si:H is its low temperature processing via PECVD below 300°C. Besides PECVD, there are other methods such as hot wire CVD [48], photo-assisted CVD [49], and reactive sputtering [50]. The structural, electronic, and optical properties of a-Si:H also have been investigated broadly [51]. Independent of the sample preparation and deposition technique, a-Si:H film has been found to contain hydrogen in a range of 1% ~ 40%, and hence it is commonly denoted as a-Si:H [52]-[54]. Incorporation of hydrogen will reduce the density of defect in the a-Si:H film [55], [56]. This is because Si-Si bonds have distribution of bond angles, leading to strained bonds and some of them may break due to the accumulation of structural stress, generating dangling bonds. Hence, when the hydrogen is incorporated into the film, this will help reduce the density of broken Si-Si bonds in the amorphous structure by the formation of Si-H bonds by relieving the strain caused by the bond angle variations.

Several literatures have been investigated the optimization of a-Si:H for best passivation quality [57]-[59]. The parameters such as deposition temperature, chamber pressure, gas ratio have all been evaluated regarding their effect on  $\tau_{\text{eff}}$  and device performance. It is found the  $\tau_{\text{eff}}$  for a-Si:H film is a function of the total H<sub>2</sub> content present in the amorphous network [60], [61]. Most importantly, the best passivation quality resulting by a-Si:H has a high Si-H bond concentration and a low Si-H<sub>2</sub> concentration, which can be verified through Fourier-transform infrared spectroscopy (FTIR) and Raman spectroscopy [62]. Typically the optimized deposition temperature is between 225°C and 250°C. If the temperature is too low, the concentration of Si-H<sub>2</sub>

bond will increase, thus causing an insufficient passivation quality although the overall  $H_2$  content is increasing.

A-Si:H is mainly designed for c-Si surface passivation in HJ solar cell. Researchers have dedicated their creative efforts to a-Si:H material exploration, process engineering, and device physics to realize high efficiency a-Si/c-Si HJ solar cell [63]. Currently the extensively studied HJ solar cell has surface passivation by i. a-Si:H, therefore there is another term of this cell structure, HIT solar cell. The record HJ solar cell is IBC structure, with efficiency 26.7% had both front and back surfaces excellent passivated by low temperature i. a-Si:H and the SRV of passivated sample is below 1 cm/sec, which is believed to be one of the reasons pushing the cell efficiency close to the theoretical efficiency limit 29.1% [3]. The high surface passivation level by i. a-Si:H is primarily contributed by the excellent electrical quality of i. a-Si:H/c-Si interface with reduction of interface state density [64], [65], and may also slightly attributed to field-effect from a weak electric field introducing by band alignment to repel one type of carriers [66], [67]. There are two drawbacks with a-Si:H passivation: 1) the degradation induced by illumination, termed as Staebler-Wronski effect [68]-[70]; and 2) the parasitic light absorption loss [24], which has been discussed in section 2.1.

#### **2.2.2.3 Aluminum Oxide ( $Al_2O_3$ )**

Besides a-SiN<sub>x</sub>:H, another well-developed field – effect passivation material is  $Al_2O_3$ , which is also a dielectric layer and typically applied on diffused-junction solar cell [71]-[74]. The most widely used processing approach for  $Al_2O_3$  is atomic layer deposition (ALD) at a low temperature range, typically below 350°C [75], [76]. The

process ALD has the advantages of precise and uniform thickness control, and conformal deposition over large area surfaces.  $\text{Al}_2\text{O}_3$  has very high density of negative  $Q_f$ , which is about  $10^{12} \sim 10^{13} / \text{cm}^2$ , making it more suitable for p-type c-Si surface passivation [77]. The passivation level of  $\text{Al}_2\text{O}_3$  on lowly doped  $p^+$  emitter Si was demonstrated by Hoex et al., which was at least as good as by thermally grown  $\text{SiO}_2$  [71], [78]. Being passivated by the negative fixed charge in the  $\text{Al}_2\text{O}_3$  film, the extremely low SRV of 2 cm/sec was reported on 2  $\Omega\text{cm}$  n-type c-Si wafer and 6 cm/sec on p-type c-Si wafer, accomplished by low temperature ALD at 200°C [79]. One of the biggest advantages of  $\text{Al}_2\text{O}_3$  is its stability under light exposure. In other word, the defect density at the interface  $\text{Al}_2\text{O}_3 / \text{c-Si}$  was observed not to be affected by light exposure. The  $\text{Al}_2\text{O}_3$  layer for p-type Si surface passivation is expected to passivate the rear surface of conventional screen-printed p-type Si solar cells by replacing the Al-BSF. To date, the application of  $\text{Al}_2\text{O}_3$  on  $p^+$  emitter and on the p-type c-Si has improved the solar cell performances up to 23.9% [80]. The only concern for  $\text{Al}_2\text{O}_3$  is the low deposition rate of ALD, which may need about 5000 seconds to deposit the 30 nm thick film needed for the device. This low throughput limits the application of  $\text{Al}_2\text{O}_3$  by ALD for the commercial scale PV manufacturing.

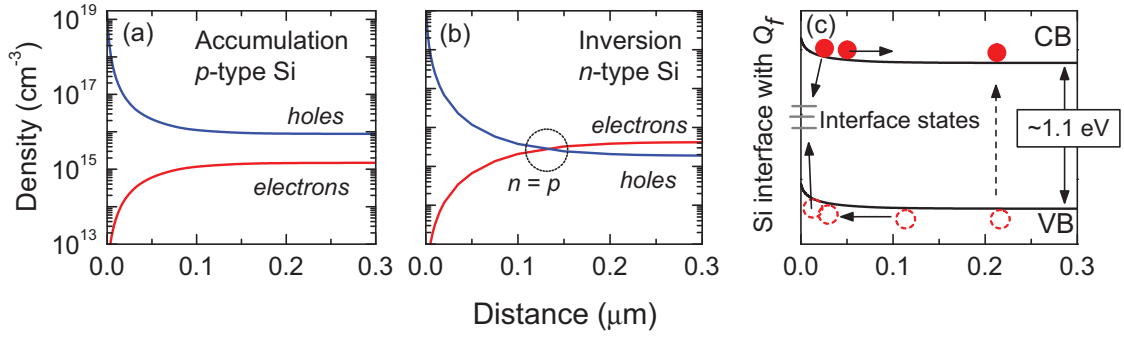


Figure 2.8 (a) and (b) are the density of electron (red line) and hole (blue line) at different depth from p-type c-Si surface affected by the fixed negative charge  $Q_f = 2 \times 10^{12} \text{ cm}^{-2}$  in the  $\text{Al}_2\text{O}_3$  film after the  $\text{Al}_2\text{O}_3$  deposited on the c-Si surface. (c) is the c-Si band bending under influence of  $Q_f$ . Data is obtained by simulation using PC1D for a 2 Ωcm c-Si wafer under illumination. Reprinted from Ref. [74]. Please refer to Appendix B: Reprint Permission for Copyright 2012, with permission from AIP Publishing.

Figure 2.8 is an example of  $\text{Al}_2\text{O}_3$  with negative fixed charge,  $Q_f$ ,  $2 \times 10^{12} \text{ cm}^{-2}$  and how this  $\text{Al}_2\text{O}_3$  influences the p-type c-Si and n-type c-Si respectively [74]. For p-type c-Si capped with  $\text{Al}_2\text{O}_3$  passivation layer, as seen in Figure 2.8 (a), the increased majority carrier density leads to a accumulation condition; however in Figure 2.8 (b) it becomes inverted. The  $\text{Al}_2\text{O}_3$  deposited on n-type c-Si surface forms a inversion condition, and may cause shunting problem. Although the electron density on the surface is reduced in both (a) accumulation and (b) inversion cases. However, the electron density and hole density becomes equal at a distance away from the interface, therefore the recombination rate in the subsurface area can be expected to enhance when bulk defects are present. The band bending in Figure 2.8 (c) caused by negative fixed charge in  $\text{Al}_2\text{O}_3$  film indicates that the electrons will be hindered and holes

collection will be assisted, hence the field effect passivation by  $\text{Al}_2\text{O}_3$  with its negative  $Q_f$  is more suitable for p layer.

#### **2.2.2.4 Hydrogenated Amorphous Silicon Nitride (a-SiN<sub>x</sub>:H)**

The commercialized homojunction c-Si solar cell in the PV industry has standard a-SiN<sub>x</sub>:H for front surface passivation using PECVD at processing temperature of about 400°C~450°C [81], [82]. Record low SRV of 4 cm/sec has been obtained on 1  $\Omega\text{cm}$  p-type Si wafers by a-SiN<sub>x</sub>:H using remote PECVD or high-frequency (13.56 MHz) direct PECVD [83]. The passivation effect of a-SiN<sub>x</sub>:H is primarily provided by the positive fixed charge in the a-SiN<sub>x</sub>:H film [84], and the amount of the  $Q_f$  is estimated to be around  $10^{12}/\text{cm}^2$  [73]. Positive  $Q_f$  makes the a-SiN<sub>x</sub>:H layer suitable for n-type c-Si surface passivation forming accumulation layer, instead of p-type which would cause parasitic shunting due to inversion layer [85]. This is because the positive  $Q_f$  can effectively shield the hole, which is the minority carrier in the n-type Si, away from the c-Si surface. Therefore the recombination rate being reduced due to the decreasing concentration of hole. Not only being a promising passivation dielectric material, a-SiN<sub>x</sub>:H refractive index can be flexibly adjusted to become ARC on c-Si solar cells. Therefore a-SiN<sub>x</sub>:H has been widely applied on p-type front diffused junction solar cell for the n<sup>+</sup> emitter layer passivation and anti-reflection [86], [87].

### 2.3 Review of Multicrystalline Si Bulk Defect Passivation

Cast mc-Si is broadly used for c-Si based solar cell due to its inexpensive characteristic. From Figure 2.9 it can be clearly seen the percentage of annual production by mc-Si is increasing year by year [8].

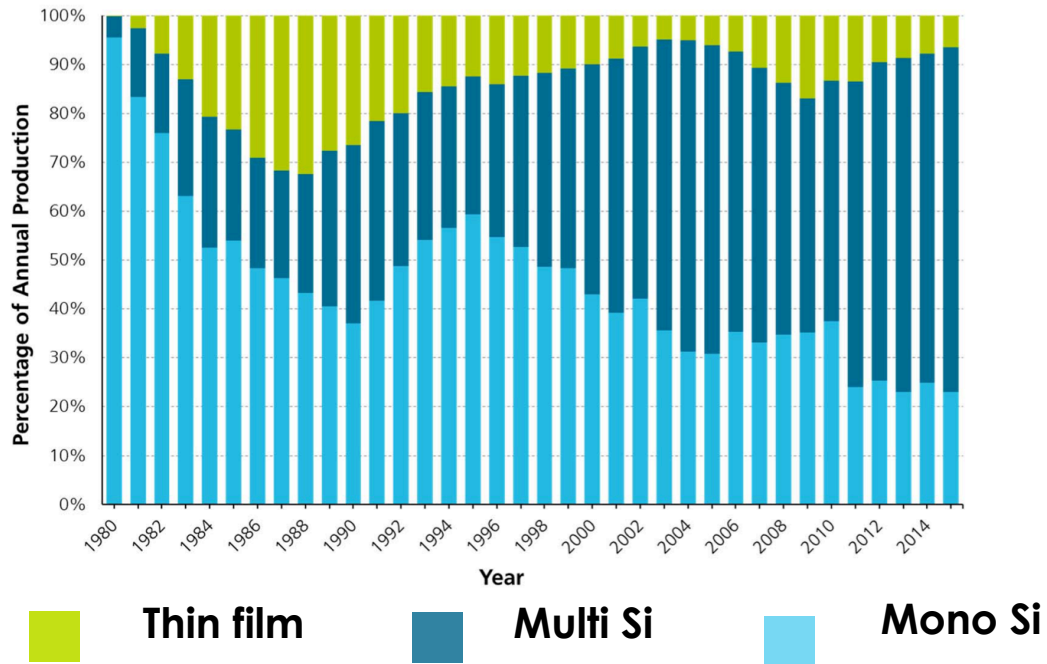


Figure 2.9 The percentage of annual production for thin film, mc-Si, and mono c-Si solar cell in photovoltaics field from 1980 to 2016 [8].

The record mc-Si cell efficiency is 21.9% by Fraunhofer ISE [88]. The main disadvantage of using mc-Si is its bulk defects including metal impurities, dislocation, and grain boundaries that reduce the device performance since those carriers may act as recombination centers and reduce its  $\tau_{\text{eff}}$  [89]. Using different approaches to remove



or reduce the defects in mc-Si has been studied by scientists for several years. Up to date, researchers are still striving and dedicating to the passivation of mc-Si bulk, to improve its bulk quality, enhance the solar cell efficiency, and reduce the cost. The mc-Si passivation process can be roughly divided into two steps. The first step is gettering metal impurities at a higher temperature usually above 950°C [4], [5]. The second step is hydrogen diffusion to passivate crystallographic defects such as dislocation and grain boundaries [90]. Using hydrogen to terminate dangling bonds along the grain boundaries has becoming a mature and well developed technology in mc-Si solar cell industry today.

### **2.3.1 Types of Bulk Defect**

There are three different types of defects in mc-Si limiting the efficiency of mc-Si solar cell. The first type is metal impurities such as Fe, Au, Cu, and Ni, which are caused by casting, the common growing process for mc-Si [91]. The concentrations of metal impurities exist in the mc-Si can be as high as  $10^{14} - 10^{16} \text{ cm}^{-3}$ , as seen in Figure 2.10. Those impurities may affect the efficiencies of mc-Si solar cells in a variety of ways, including bulk recombination, leakage current, and direct shunting. The second type of defect is a crystallographic one, such as dislocation. Dislocations are mainly generated during crystal growth including cooling process as a result of thermal stress or different crystal orientations [92], [93]. Some researchers have found that impurities in the mc-Si may precipitate at dislocations when the density of dislocation is above a threshold number of about  $10^6 \text{ cm}^{-2}$  and cause the ineffective impurity removal, and therefore can dramatically decrease the  $\tau_{\text{eff}}$  limiting the device performance [94], [95]. The third type of defect is dangling bonds along the

grain boundaries, which is the dominant one in a mc-Si wafer [96]-[98]. Different types of defect need different passivation approaches to remove or terminate them.

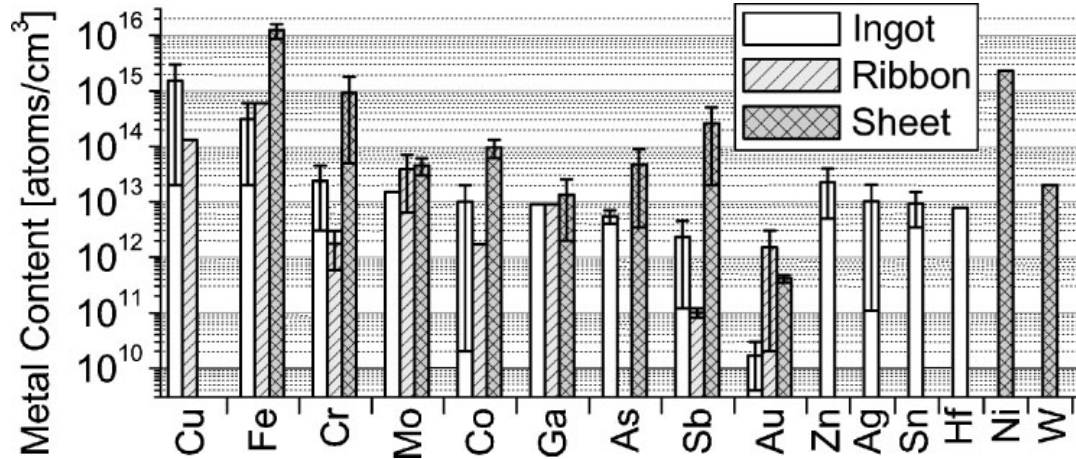


Figure 2.10 Neutron activation analysis data of total metal content in ingot-grown, ribbon, and sheet mc-Si materials, as determined from published data. Reprinted from Ref. [91]. Please refer to Appendix B: Reprint Permission for Copyright 2006, with permission from John Wiley and Sons.

### 2.3.2 Traditional Bulk Defect Passivation Methods

Two main bulk defect passivation techniques are mainly used to remove or reduce the impacts of defects and hence enhance the mc-Si solar cell performance. The first one is “gettering” at high temperature typically above 950°C to remove metal impurities in the mc-Si materials [99]-[102]. The critical point of the gettering process is that it concentrates impurities in a specific region of a wafer, typically is the surface, followed by chemical etching to remove those impurities. Different gettering resource

and process may have different gettering effectiveness to each metal impurity. Solute diffusion gettering by phosphorous is the most efficient one among different gettering materials such as boron, antimony, and arsenic [4]. The second passivation technique is making atomic hydrogen diffuse into mc-Si bulk and reduce the crystal defect density [90] where the hydrogen is typically provided by a-SiN<sub>x</sub>:H coating layer [103]-[106].

However it has been observed that hydrogen passivation might be insufficient for a high dislocation density material and also metal impurities and precipitates trapped in the high density of dislocations cannot be directly and effectively removed during gettering process [107], [108]. Hence, it has become critical to develop alternative approaches to remove dislocations. Many studies have been proposed to develop different approaches to suppress the dislocation generation during crystal growth or to annihilate the dislocation through post heat treatment. The generation of dislocations can be suppressed by diminishing the thermal stress or by managing its crystal structure during crystal growth by adjusting process conditions [109]-[111]. Researchers have found that dislocation mobility increases with temperature and stress. The post annealing above 1000°C with different heating rates and cooling rates has been found by several groups to reduce the density of dislocation, which is also consistent with the Peierls-Nabarro model [112]-[115]. Further investigations demonstrate that the driving forces, such as high temperature via thermal annealing or high stresses via mechanical stress application, are required for dislocations to overcome a certain amount of activation energy to be mobile [95], [116], [117]. Therefore in an environment with higher temperature, lower activation energy, and

higher stresses may cause an increase of the dislocation velocity and the rate of reduction of the dislocation density.

Grain boundaries are the main type of defects in mc-Si material limiting the efficiency of mc-Si solar cell. Hydrogen has great potential in the electrical passivation of grain boundaries, and is widely used to improve the quality of mc-Si and therefore device performance [118]-[120]. The potential impact of hydrogen on mc-Si solar cell was first time realized in 1979 at Sandia National Labs using direct current hydrogen plasma [121]. Later in a follow up report, they reported an improved diode characterization result for a hydrogen-passivated mc-Si solar cell [122]. Multiple processing approaches such as hydrogen plasma, ion implantation, and a-SiN<sub>x</sub>:H deposition followed by H diffusion have ability to introduce atomic hydrogen into mc-Si bulk to terminate dangling bonds along grain boundaries. The advantage and disadvantage of each approach will be discussed in chapter 7. In chapter 7 we will be focusing on mc-Si passivation in H<sub>2</sub>S reaction and demonstrated the passivation effect via the reduction of traps and recombination states.

## **Chapter 3**

### **EXPERIMENTAL TECHNIQUES**

#### **3.1 Fabrication**

The fabrication discussed in this work includes wafer cleaning, etching, thin film deposition, surface reaction, photolithography, and electron beam evaporation. The wafer cleaning process includes solvent cleaning to remove dust and grease, piranha oxidation to remove hydrocarbon and form oxidation layer on the surface, and HF etch to remove the oxide and form H-terminated surface. Two etchants for etching c-Si are mainly involved in this dissertation, one is tetramethyl-ammonium hydroxide (TMAH) for anisotropic etching, and another is HNA, which is composed of  $\text{HNO}_3$  and HF, for isotropic etching. Multi-chamber PECVD and custom-built sulfurization / selenization system at IEC will be introduced. Photolithography is used for the back surface patterning process for IBC-SHJ solar cell in this dissertation. Electron beam evaporation was used to deposit metal film for solar cell metal contact.

##### **3.1.1 Wafer Cleaning Process**

There are multiple cleaning steps from solvent cleaning, piranha oxidation, to HF etching. Solvents used in the wafer cleaning process include acetone, isopropanol, and methanol. All the solvent cleanings are with ultrasonic agitation. Starting with 5 min in acetone solution in 55°C ultrasonic tank, followed by isopropanol flush and 5

min DI water rinse. Acetone is mainly used to remove the grease on the wafer surface. After acetone, the wafers need to be cleaned in methanol in the ultrasonic tank with agitation at 55°C for 5 min. Isopropanol flush followed by 5 min DI water rinse is carried out after methanol.

After grease and all dusts on the wafer surface being cleaned by solvents, piranha, which is a mixture of  $\text{H}_2\text{SO}_4$  and  $\text{H}_2\text{O}_2$  in 3:1 ratio, is then used to remove organic residues on the c-Si surface by two chemical reactions occurring: dehydration and oxidation. In the dehydration reaction, hydrogen and oxygen as a unit of water are removed by the concentrated  $\text{H}_2\text{SO}_4$ . This dehydration reaction will also carbonize any organic materials on the c-Si wafer surfaces, such as hydrocarbon. Then, in the oxidation reaction,  $\text{H}_2\text{O}_2$  is converted from a normally mild oxidizing agent into an aggressive state by  $\text{H}_2\text{SO}_4$ , to dissolve elemental carbon on the c-Si surface. As a result, any organic residues on the c-Si surface can be completely removed in piranha aqueous solution.

After piranha, the samples need to be rinsed in flowing DI water for at least 5 min. The final cleaning step is HF etching to remove the oxide on the c-Si surface and form H-terminated Si surface by replacing surface OH groups with H surface bonds. The H-terminated surfaces need to be formed right before loading the samples into PECVD chamber for further processing. Figure 3.1 summarizes the sequential chemical reactions happen on the c-Si surface during these cleaning steps from solvent cleaning, to piranha oxidation, and then to HF dip.

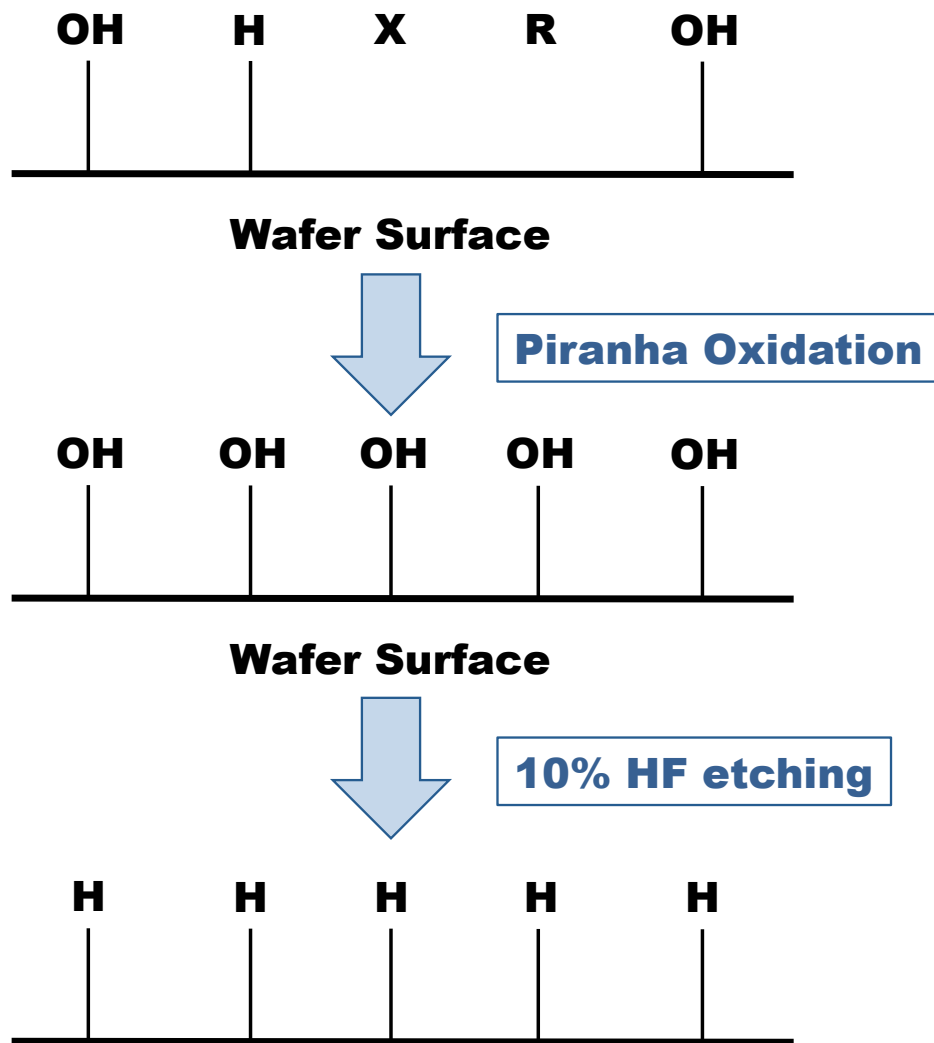
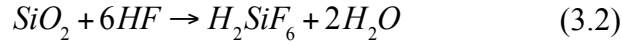
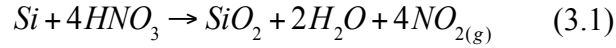


Figure 3.1 The schematic of the c-Si surface reactions during the cleaning processes in piranha oxidation and HF etch. X and R represent the impurities and organic residues on the c-Si surfaces.

### 3.1.2 Wet Chemical Etching: HNA & TMAH

HNA or TMAH are required during the cleaning process for wafers that need to be etched back, textured, or smoothed. HNA is used to etch off both c-Si and a-

Si:H, and the etching rate varies with different etching targets where the HNA is composed of  $\text{HNO}_3$  and HF. The reaction mechanism consists of reaction equations 3.1 and 3.2 where  $\text{HNO}_3$  oxides Si, forming  $\text{SiO}_2$ , which is removed by HF [123].



The etching rate does not vary with etching material and depends on the HNA concentration, which can be controlled by the diluent DI water or acetic acid. There were detailed studies comparing the etching rate and mechanism, which may be different between DI water and acetic acid. Using acetic acid to dilute HNA makes the solution has greater tolerance since  $\text{HNO}_3$  has less ionization in acetic acid than in DI water, and therefore the etching rate can be more controllable in acetic acid.

TMAH, tetramethylammonium hydroxide  $(\text{CH}_3)_4\text{NOH}$ , is another chemical used to texture or polish c-Si surface [124], [125]. Comparing to anisotropic etching by KOH or isotropic etching by NaOH, which have been traditionally used in PV industry, etching by TMAH aqueous solution avoids any metal ions contamination such as  $\text{K}^+$  and  $\text{Na}^+$ . TMAH provides highly anisotropic etching for Si since the bonding energy of Si atoms is different for each crystal plane, and therefore leads to pyramidal structures on the surface. Moreover, TMAH solution hardly attacks  $\text{SiO}_2$ , which can be used as an etching mask during the processing. For Si (100) used in this dissertation, the Si (100) etch rates generally increase with temperature and decrease with increasing TMAH concentration. The etched Si (100) surface roughness



decreases with increasing TMAH concentration, and mirror-polish surfaces can be obtained by high concentration, ~22%, TMAH solution.

In our lab, we primarily use two different etching concentrations for TMAH processing. Low concentration 1% is used to texture c-Si wafer surface forming random pyramid structure on originally polish surface, and 5% to smooth c-Si wafer surface, which was pre-textured by SunPower Corp having large ( $10\text{ }\mu\text{m} - 20\text{ }\mu\text{m}$ ) square pits with depth  $5\text{ }\mu\text{m} - 7\text{ }\mu\text{m}$  all over the surface and small random pyramids with depth  $2\text{ }\mu\text{m} - 3\text{ }\mu\text{m}$ . Both TMAH texturing and smoothing are at solution temperature  $70 - 80^\circ\text{C}$  in the beaker, by setting the ultrasonic tank water at  $\sim 150^\circ\text{C}$ .

### **3.1.3 Plasma Enhanced Chemical Vapor Deposition System (PECVD)**

At IEC, the multi-chamber (MC) system is used for PECVD to deposit i. a-Si:H, doped a-Si:H, a-SiN<sub>x</sub>:H, and a-SiC:H at low temperature  $175^\circ\text{C} - 300^\circ\text{C}$  for HJ Si solar cell processing. Right before loading samples into PECVD chamber for deposition, substrates are dipped in 10% HF for 1 min to make c-Si surfaces H-terminated and fully hydrophobic. PECVD is a deposition technique to deposit thin films from a gas phase precursor to solid phase on the substrates at low temperature. Since the main chemical reactions occurring during PECVD are initiated by plasma, high temperature can be avoided during the process. In our system, the chamber temperature is controlled between  $150^\circ\text{C}$  and  $300^\circ\text{C}$ . The plasma is generated by direct current (DC) or radio frequency (RF) glow discharge between two electrodes, which have the space normally  $1.7\text{ cm} - 1.8\text{ cm}$ . The chamber wall and the substrate plate are both grounded for our system configuration. The composition of the reactive gases is controlled by mass flow controller (MFC) prior to entering the deposition chamber. In

the chamber, plasma converts the gas mixture into reactive radicals, ions, electrons, neutral atoms, molecules, and other highly excited species. All these different type of particles are accelerated by the potential between the two electrodes and interact with substrate surfaces. The chamber pressure is usually maintained at a low pressure, which is at about 1 Torr through a throttle valve to maintain a balance between the gas flow rate and the pumping speed. The reaction begins when the species collide and successfully adsorb on the substrate surface with plasma striking when the chamber is uniformly filled reactive gas mixture with low chamber pressure. The low chamber pressure in PECVD needs to be maintained because the chemical reactions and the energetic species are formed by the collision of the gas particles. Species will either replace nearby Si-H bonds and then release the hydrogen or diffuse to vacancy region and therefore saturate the Si dangling bonds. High concentration of hydrogen will be created near the substrate surface, which enhances the surface reaction by increasing the surface mobility of the adsorbed species. The by-product of hydrogen must be desorbed and transported away from the substrate surfaces to allow the continuing film growth.

To summarize, a general PECVD process includes seven steps:

- (1) The transport of precursor gases to the chamber
- (2) Ignition of plasma to generate reactive species
- (3) Diffusion of the reactive species to the substrate surface
- (4) Surface reactions between radicals at the surface of the substrate
- (5) Desorption of gaseous by-products
- (6) Transport of by-products away from the surface of the substrate

(7) Transport of by-products and unreacted gas from the reactor

Step 1 and step 7 are more related to the design of the chamber, and step 2 to step 6 determine the film growth because plasma reaction and substrate surface reaction are both included.

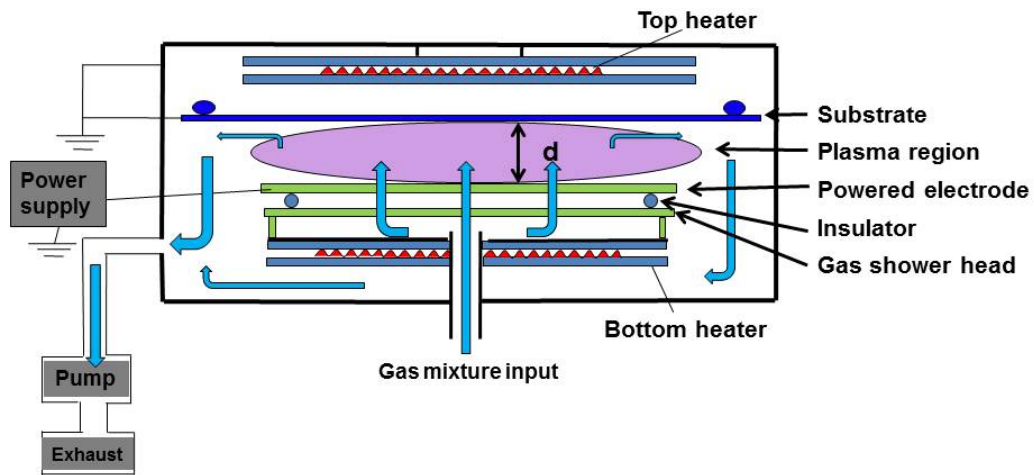


Figure 3.2 Schematic of cross-section of the PECVD system at IEC.

Figure 3.2 illustrates the design of PECVD chamber at IEC. Mixture of processing gas enters the chamber from the bottom of the chamber and being pumped out through a turbo pump, which is backed by a mechanical pump. The purple region is the plasma stroked in the chamber, generated between the two electrodes having the potential formed by the power source DC or RF power. Two heaters on the top and at

the bottom of substrate carriers control the substrate temperature up to about 300°C in our system.

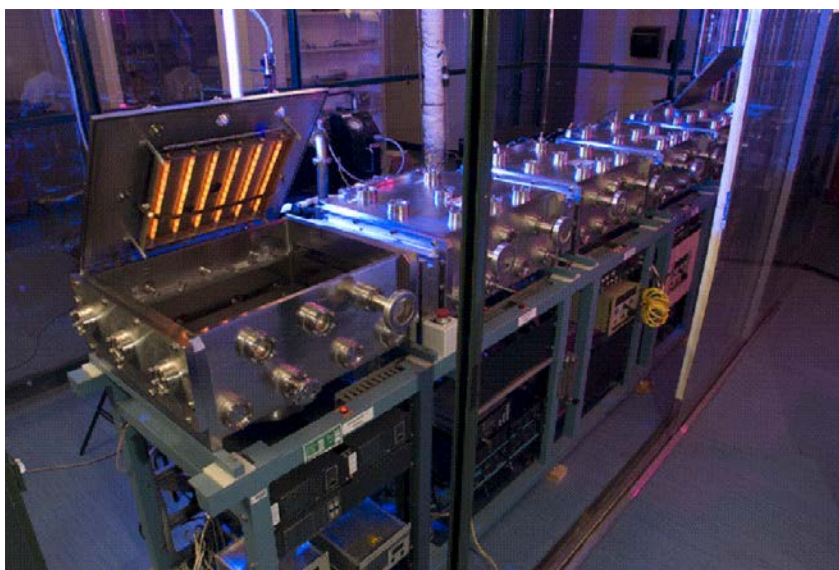


Figure 3.3 Multi-chamber (MC) in-line PECVD system at IEC, in which the PECVD processes in this dissertation were conducted.

The depositions completed in this dissertation were conducted by using a high vacuum multi-chamber in-line system at IEC, with four reaction chambers and two loading / unloading chamber at two sides, as shown in Figure 3.3. Each of the four reaction chamber has the similar structure as shown in Figure 3.2. Intrinsic, p-type, and n-type materials are deposited in different chambers of the MC system in Figure 3.3 to prevent any possible cross contamination. Silane ( $\text{SiH}_4$ ) and hydrogen ( $\text{H}_2$ ) are the gases for i. a-Si:H and also the basic gases for all other thin films. Diborane ( $\text{B}_2\text{H}_6$ )

is used for p. a-Si:H; phosphine ( $\text{PH}_3$ ) is used for n. a-Si:H; ammonia ( $\text{NH}_3$ ) is used for a-SiN<sub>x</sub>:H; methane ( $\text{CH}_4$ ) is used for a-SiC:H. A customized sample flipper was designed and installed in one of the loading chamber of our MC system. The flipper can be used to flip over the sample for both-side deposition, without breaking the vacuum and especially enhancing the c-Si surface passivation quality.

The process design of PECVD in our MC system has three stages: 1) reactive gas diffusing uniformly into the chamber; 2) plasma initiation and film growth; 3) purging reaction chamber with inert gas Ar. The flushing time of reaction gases in stage 1) and inert gas in stage 3) are both 3 min, which is based on the calculation between the chamber size and gas flow rate. Film deposition time in stage 2) is decided based on the film growth rate and thickness required. The growth rate can be tuned by deposition parameters, including substrate temperature, chamber pressure, supplied power type and magnitude, reaction gases, and each of their concentration.

#### **3.1.4 Photolithography**

Photolithography technology [126] is a technique widely used in microelectron fabrication for defining patterns. A designed pattern can be transferred from a photomask to a photo-sensitive polymeric material via UV light, known as photoresist. A photoresist contains three components: 1) a resin or base material; 2) a photoactive component; 3) a solvent that controls the viscosity of the photoresist. Photoresist can be categorized into two different types: positive photoresist and negative photoresist. For positive photoresist, its photoactive component behaves as an inhibitor before exposing to the UV light, which reduces the dissolve rate when immersing in a base solution called developer. The exposure of positive photoresist makes the photoresist

become soluble in the developer, while the area being covered by the mask will leave the photoresist film on the substrate surface. For negative photoresist, it contains a crosslink, which would be activated during the light exposure and become non-dissolvable in the developer. We choose positive photoresist Shipley S1827 for our patterning work in this dissertation. The advantage of positive photoresist is that resin material is fairly resistant to chemical attack and developer. Therefore the photoresist pattern can be a good mask for subsequent chemical etching during the IBC-SHJ solar cell fabrication. Optional post bake is used to make the film more resistant to chemical etching process.

For the whole photolithography process, sample cleanliness is critical. Any dust and particle on the sample surfaces before applying photoresist will affect the resist spin coating and film uniformity and adhesion. The equipment mask aligner for photolithography at IEC is shown in Figure 3.4. N<sub>2</sub> gun was used to blow off any dust and particle on the samples will provide a good starting of photolithography process. After N<sub>2</sub> blowing off, 120°C baking for 2 min on a hot plate assured complete dehydration of c-Si samples and therefore improved photoresist film adhesion. After cooling down, the samples were then placed on the spin coater one piece at a time. In the static state, positive photoresist Shipley S1827 was applied on the 1 inch by 1 inch wafer surface area fully, followed by ramping up to 3000 rpm within 10 sec, dwelling at 3000 rpm for 50 sec, and then ramping down within another 10 sec. The 3000-rpm spinning speed will generate ~ 3μm thick of resist film uniformly covering the entire surface of the substrate. The substrate was then transferred to the hot plate for soft baking at 120°C for 3 min, to remove most of the solvent in the resist film. The well-coated and after-soft-bake sample was then exposed under UV light through the

desired photomask in the mask aligner. The photomask is an opaque plate with partial transparencies, which has the pattern allowing UV light to shine through. Before using the photomask, make sure the mask is clean. The mask can be cleaned through N<sub>2</sub> gun to remove the dust; or can also be cleaned by acetone to remove any photoresist residue on the mask. The mask can only be dried through N<sub>2</sub> gun, because any of the wipes may cause scratches on the mask surface. After cleaning the mask, it was loaded with its brown side facing down onto the vacuum chuck and then being locked in its place. The sample stage needs to be placed at close contact before UV light exposure. After exposure, the sample was placed in the developer MF319, which contains low concentration of TMAH, to etch off the exposed region of positive photoresist. 5 min of DI water rinse was required after develop to completely remove all the solvent and TMAH on the sample, followed by hard bake at 140°C for 5 min to increase the thermal, chemical, and physical stability if more subsequent etching steps needed.



Figure 3.4 Karl Suss MJB standard 3 mask aligner used at IEC.

The basic photolithography process for patterning can be more easily understood in Figure 3.5. After the pattern completed in developer, sequential processing could be etching or thin film deposition, and the patterned photoresist film could be removed or leaved on the surface for further processing. All these depend on the device fabrication process and patterning approaches developed at IEC, which will be more detailed described in chapter 4.



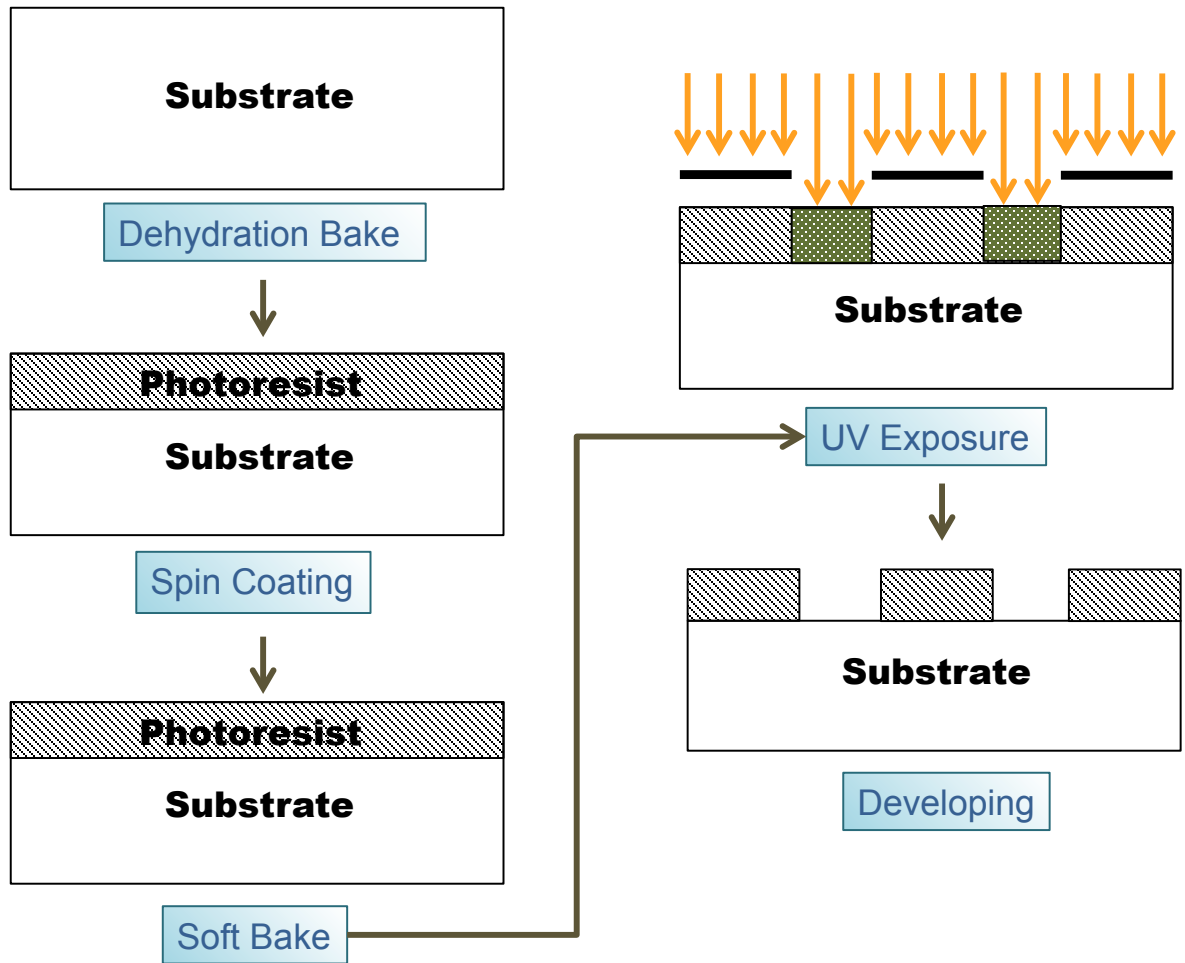


Figure 3.5 General photolithography process flow.

### 3.1.5 Custom-Built Sulfurization / Selenization System

At IEC there is a custom-built sulfurization / selenization system, as shown in Figure 3.6. Also, Figure 3.7 presents a simplified schematic of the reactor with the major components labeled.

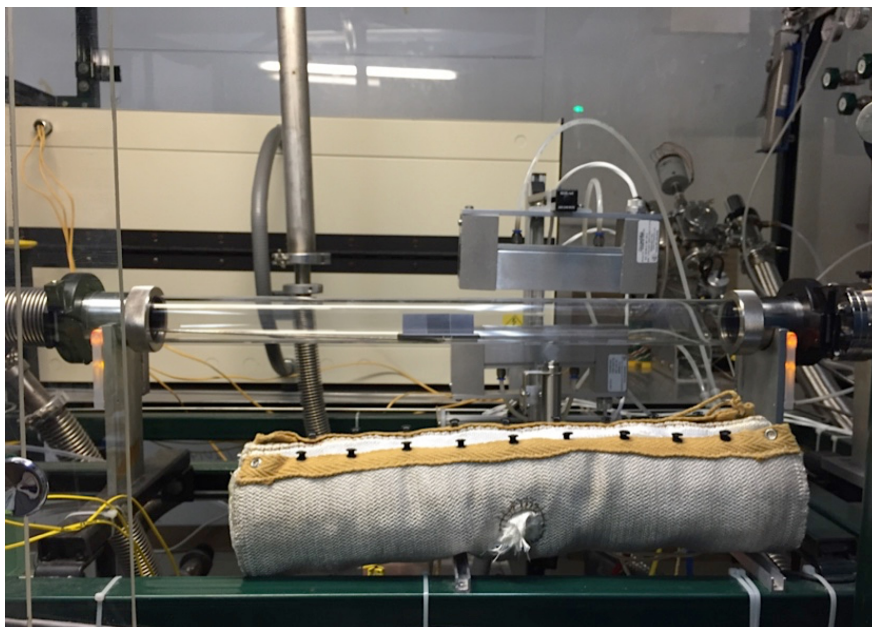


Figure 3.6 The custom-built sulfurization / selenization system at IEC, with the heating jacket for heating up the reactor.

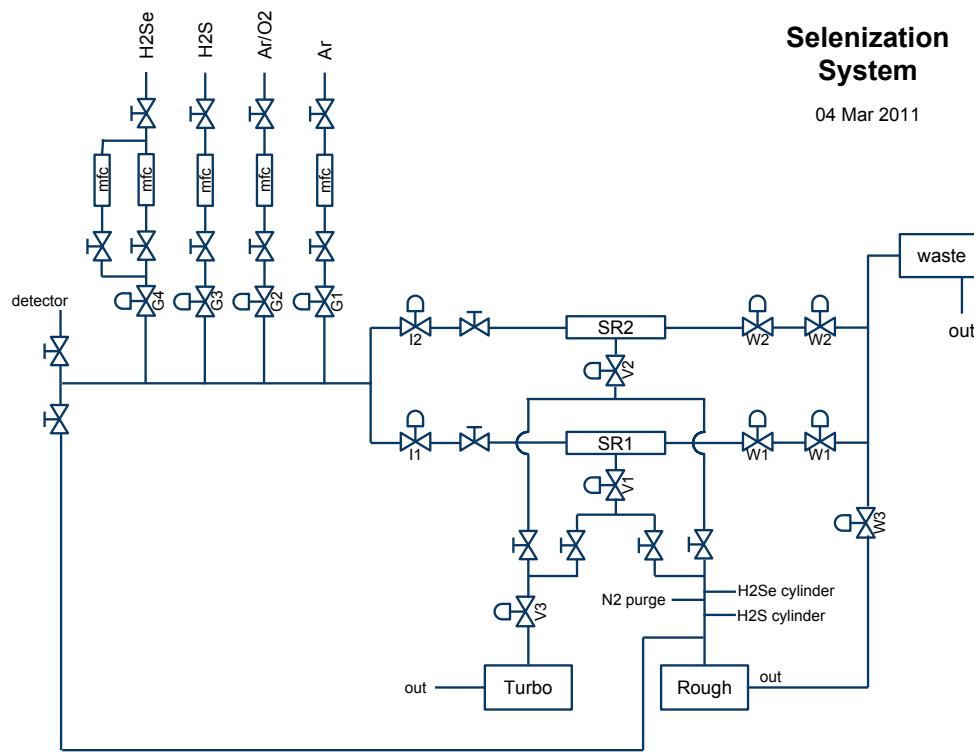


Figure 3.7 Schematic of the reactor with the major components labeled.

The full system incorporates two tube reactors: SR1 is a 5 cm inner - diameter (ID) quartz tube with a heating jacket for temperature control, shown in Figure 3.6. SR2 is a 15 cm ID quartz tube semi-permanently mounted in a tube furnace. The two tubes cannot be operated simultaneously, but the same reactions may be performed in either. SR1 is typically used to react one, two, or three square samples with sides 2.5

cm long, while SR2 can accommodate a 10 cm square sample, or a grid of 16 of the 2.5 cm size.

The heating jacket with SR1 has temperature capability up to 700°C, and a maximum temperature ramping speed of 40°C / min. The gas flow rate is quite low and therefore making considerable amount of convection inside the tube, as evidenced by the condensation of elemental selenium on the inside wall of the tube. Ar and H<sub>2</sub>S gases are supplied in pure form. The purity of Ar is 6N level, and the impurity level of H<sub>2</sub>S will be discussed in more details in chapter 6. H<sub>2</sub>Se is diluted and stored as 14% H<sub>2</sub>Se in Ar. The O<sub>2</sub> / Ar source shown in Figure 3.7 is used in CIGSSe production, where a small amount of oxygen presenting during the reaction has been found to surface characteristics, specifically to prevent “islanding” of indium during the heat ramping.

In this dissertation, the SR1 system was used for c-Si surface and / or bulk passivation in H<sub>2</sub>S. The bare Si wafer had final cleaning step in HF (10%, 1 min) dip forming H-terminated surface, and then got transferred to the reactor immediately. The turbo pump in the system has capability to pump down the system to 1E-6 torr within 10 min, to make sure the H-terminated c-Si surface can be preserved in the reactor. The reaction gases started to flow into the reactor after the vacuum level reaches below 1E-6 torr. The flow reaction proceeded at one atmosphere. The static reaction, also called “charge and react” was processed at the pressure slightly lower than one atmosphere. The reaction gas was initially charged to about 520 Torr at room temperature. And then all the valves were closed to make the reactor tube in an isolated environment. The scrubber pump was turned on due to safety concern. In the isolated environment, the pressure may increase to about 650 Torr after the system

temperature reached the target temperature 550°C ~ 650°C. After the reaction completed, heating jacket was turned off and the cooling down process may take ~ 20 min from reaction temperature to 250°C. The reactor can be pressurized by Ar to slightly higher than one atmosphere, and then the gas flow formed immediately when the valves were opened.

### **3.1.6 Electron Beam Metallization**

The IBC-SHJ solar cells studied in this dissertation (chapter 4) had metal contact formed by electron beam evaporation. All the metal contacts on the IBC-SHJ solar cells were directly deposited on the photoresist films. The metal films have the tendency to break at the edges of the photoresist so that when the photoresist is dissolved during the lift off process, the metal films on top of the photoresist can be easily removed.

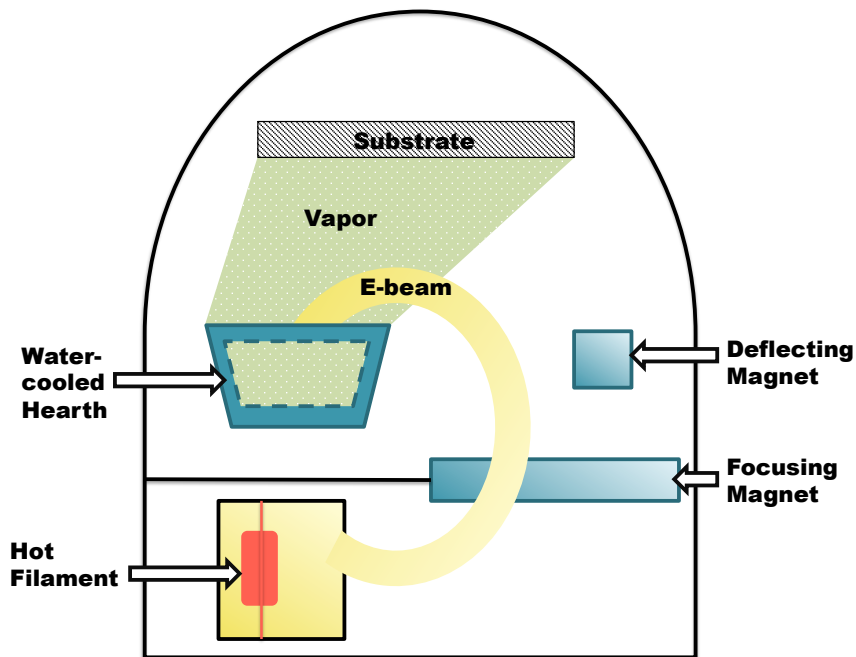


Figure 3.8 Schematic of electron beam evaporation system.

In the electron beam evaporation system, the chamber pressure is maintained at high vacuum level of  $1\text{E-}5$  Torr pumped down through diffusion pump. The target metal materials are placed in the crucible that are cooled down by flowing water. The high flux of electron beam is emitted from electron gun, and then accelerated to high kinetic energy and focused into the crucible by a magnetic system, as seen in Figure 3.8. When the electrons strike the crucible, most of their kinetic energy would be released and converted to thermal energy, causing a very high temperature on the surface. When the vacuum level is sufficient high and the temperature of the crucible region is high enough, the metal inside the crucible will be melted, vaporized, and then deposited on the substrate surface to form the metal film. A shutter is placed above the

crucible and is kept at close position before the deposition starts. The metal deposition rates are tunable in the range of 2 – 4 nm /sec by controlling the electron beam energy.

### **3.2 Material Characterization**

Material characterizations introduced in this section include X-ray photoelectron spectroscopy (XPS), Fourier transform infrared spectroscopy (FTIR), and photoluminescence imaging (PL imaging). XPS was used to study the surface bonding states and compositions of mono c-Si surface after passivation in H<sub>2</sub>S reaction. Core level electron of the element hydrogen cannot be evaluated by XPS, therefore FTIR was used to evaluate if there was any Si-H<sub>x</sub> bond on the passivated c-Si surface after reaction in H<sub>2</sub>S. For mc-Si wafer passivation in H<sub>2</sub>S reaction, the contrast of PL imaging was used to investigate the uniformity of bulk passivation and the distribution of defect.

#### **3.2.1 X-ray Photoelectron Spectroscopy**

X-ray photoelectron spectroscopy (XPS) is a technique used to analyze the surface chemistry of a sample by collecting its core level electrons and analyzing through the binding energy of those core level electrons. XPS can measure the surface elemental composition, empirical formula, chemical state, and electronic state of the elements within a material. XPS spectra are obtained by irradiating a solid surface with a beam of X-rays while simultaneously measuring the kinetic energy and core level electrons that are emitted from the top 1 – 10 nm of the material being analyzed. The actual sampling depth varies among different analyzing materials. A

photoelectron spectrum is recorded by counting ejected electrons over a range of electron kinetic energies. Peaks appear in the spectrum from atoms emitting electrons of a particular characteristic energy, which is primarily presented as binding energy to identify elements. In other words, the binding energy of photoelectrons at core-level orbitals of each element is unique, allowing the identification of element and its chemical states, based on values found in such as the NIST X-ray photoelectron spectroscopy database. By measuring the kinetic energy of the emitted electrons, it is possible to determine which elements are near the analyzed material's surface, their chemical states and the binding energy of the electron. The binding energy depends upon a number of factors, including the following:

- 1) The element from which the electron is emitted
- 2) The orbital from which the electron is ejected
- 3) The chemical environment of the atom from which the electron was emitted

Figure 3.9 is the illustration of XPS from Thermal Scientific K Alpha and shows its working mechanism.



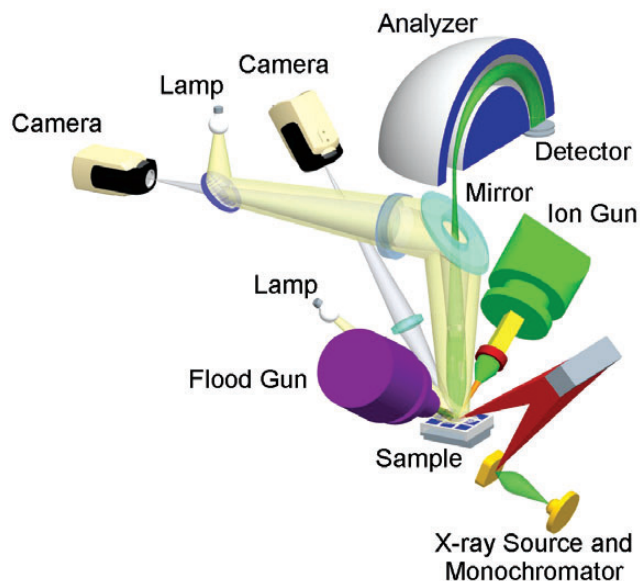


Figure 3.9 The internal geometry of the analytical components in Thermo Scientific K-Alpha [127].

In the XPS instruments, X-rays are generated by bombarding a metallic anode with high energy electrons. The energy of emitted X-rays depends on the anode material and beam intensity depends on the electron current striking the anode and its energy. Early XPS instruments were fitted with non-monochromatic X-ray sources because the sensitivity of the early instruments was low. Sensitivity and monochromator design now have improved, and most XPS instruments include monochromators as standard equipment and non-monochromatic sources are optional. The standard X-ray source is supplied with aluminum (Al) and magnesium (Mg)

anodes. Table 3.1 shows the energy and line width of available anode materials to produce X-rays.

Table 3.1 The energy and line widths of available anode materials [128].

<b>Anode</b>	<b>Radiation</b>	<b>Photo Energy (eV)</b>	<b>Line Width (eV)</b>
Mg	K $\alpha$	1253.6	0.7
Al	K $\alpha$	1486.6	0.85
Zr	L $\alpha$	2042.4	1.6
Ag	L $\alpha$	2984.3	2.6
Ti	K $\alpha$	4510.9	2.0
Cr	K $\alpha$	5417	2.1

The XPS instrument used in this dissertation is from Thermo Scientific, with the model name K alpha. The X-ray source is monochromatic, emitted by the anode Al K alpha with its energy 1486.6 eV and line width 0.85 eV. For the monochromators fitted to Thermo Scientific XPS instruments, the radius of curvature is different in each direction, allowing the X-rays to be focused and monochromated, as seen in Figure 3.10.

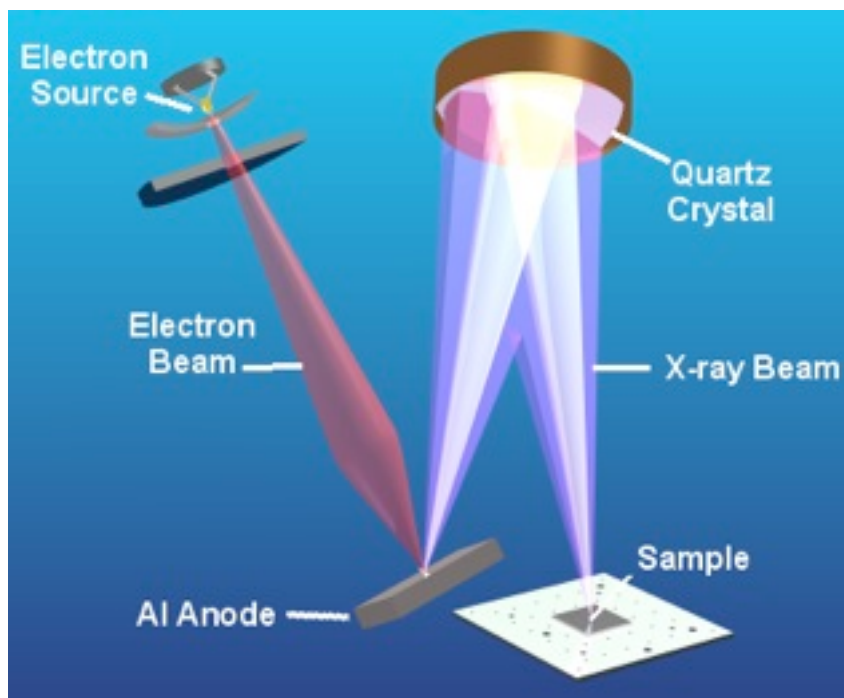


Figure 3.10 Schematic of the focusing X-ray monochromator used on Thermo Scientific XPS Instruments [127].

For the photoemission process, when an atom or molecule absorbs an X-ray photon, an electron can be ejected. The kinetic energy (KE) of the electron depends upon the photon energy of the incoming X-rays ( $h\nu$ ) and the binding energy (BE) of the electron. Binding energy can be understood as the energy required to remove the electron from the surface. The overall photoemission process is presented in Figure 3.11. For a more accurate calculation, the binding energy of the emitted photoelectrons can be calculated as  $BE = h\nu - KE - \phi_s$ , where  $\phi_s$  is the work function of the spectrometer. Figure 3.12 provides a more detailed explanation of how the spectrometer work function being correlated to the binding energy calculation.

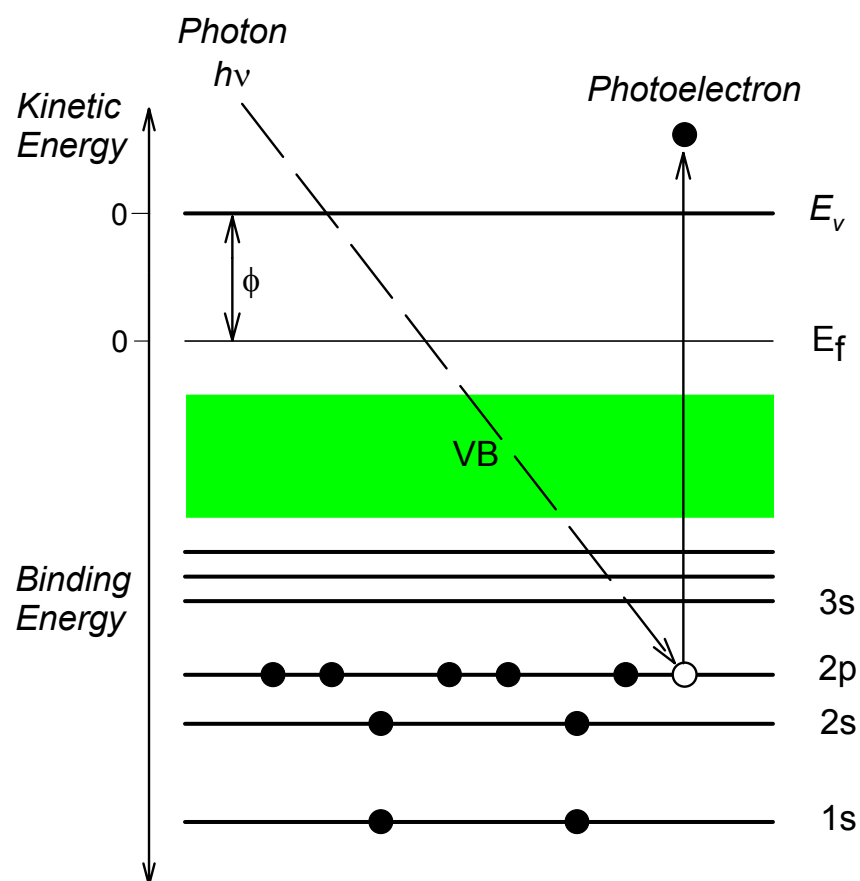


Figure 3.11 The photoemission process involved for XPS surface analysis. The discs represent electrons and the bars represent energy levels within the material being analyzed. The equation governing the process is:  $KE = h\nu - BE$  [129].

## Binding Energy Reference

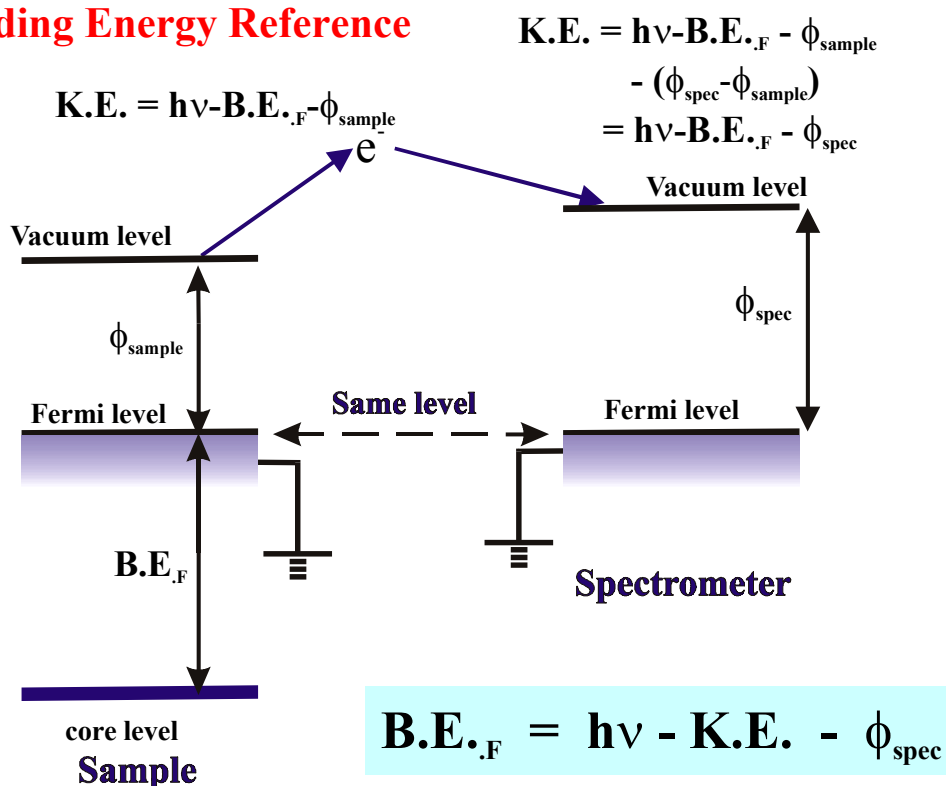


Figure 3.12 The binding energy reference [129]

The software CasaXPS was used for XPS data analysis [130]. Peaks in photoelectron spectra were fit by a Shirley background and a pseudo-Voigt Gaussian / Lorentzian product function, with peak separation and areas constrained by relevant spin orbital splitting. Element composition was calculated based on the peak area and the relative sensitivity factor of each element. The relative sensitivity factor can be affected by the instrument configuration, analyzer transmission function, and also depends upon different element and different chemical state. Overall, the relative sensitivity factor is used to correct (normalize) the actual amount of photoelectron

being collected by the detector. The efficiency of the photoelectron being emitted by the X-ray and the efficiency of photoelectron being collected by the detector are both different between different elements and different states. Therefore, each photoelectron has their own “characteristic” relative sensitivity factor. There are multiple libraries of relative sensitivity factor and the one used in this dissertation is most likely empirical, and is based on the Scottfield library, with the magic angle  $\sim 54.7^\circ$  for the X-ray incident angle.

To calculate the atomic percentage of each element on the surface, which is also commonly defined as the concentration of each element, the total amount of the photoelectrons are considered as 100%. For example, if there are three elements being defined from the survey spectrum, then, three fine scans (high resolution scans) for these three elements are processed. The photoelectron number of each element with their characteristic electronic state can therefore be defined by the peak area corrected with relative sensitivity factor. The total number of photoelectron is considered as 100%, and atomic percentage of each element is defined by the portion of the each of their photoelectron number.

### **3.2.2 Fourier Transform Infrared Spectroscopy (FTIR)**

FTIR is a technique used to identify the chemical bonding states through their molecule bond vibration modes after absorbing specific IR frequencies that are characteristic of their structure. These absorptions are resonant frequencies, which means the frequency of the absorbed radiation matches the transition energy of the chemical bond that vibrates. The energies are determined by the shape of the molecule

potential energy surfaces, the associated vibration coupling, and the masses of the atoms. Therefore, each of the absorbed frequency is the characteristic of a particular bond vibration mode and a particular bond type. The resulting spectrum represents the molecular absorption and transmission, creating a molecular fingerprint of the sample. Just like a fingerprint, no two unique molecular structures produce the same infrared spectrum. This makes the infrared spectroscopy useful for several types of analysis. The overall idea of how FTIR works can be understood in Figure 3.13. Hence, the information can be provided by FTIR includes: 1) Identify unknown materials; 2) Determine the quality or consistency of a sample; 3) Determine the amount of components in a mixture.

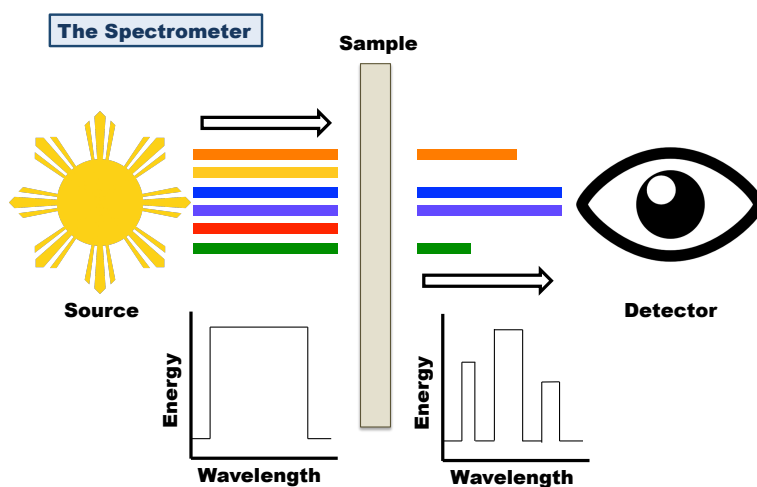


Figure 3.13 The characteristic frequencies in IR match the molecule absorption energies and being absorbed with the molecule vibration, providing the resulting spectrum represents the molecule absorption and transmission, creating a molecule fingerprint of the sample.

The most important characteristic needs to be addressed in FTIR introduction is the employment of a very simple optical device called “interferometer”, used to accelerate the slow scanning process by measuring all of the infrared frequencies simultaneously rather than individually. The interferometer produces a unique type of signal which has all of the infrared frequencies “encoded” into it. The signal can be measured in a very short time, typically on the order of seconds.

As seen in Figure 3.14, most interferometers employ a beam splitter, which takes the incoming infrared beam and divides it into two optical beams. One beam reflects off of a flat mirror, which is fixed in place. Another beam reflects off a moving mirror and also reflected back to the beam splitter. The two beams then refocus at the beam splitter and then pass towards the sample. Beam transmits through the sample and being collected by the detector. Because the path that one beam travels is a fixed length and the other is constantly changing as its mirrors moves, the signal exiting the interferometer is the result of these two beams “interfering” with each other. The resulting signal is called an interferogram, which has the unique property of every data point. Each data point is a function of the moving mirror position. A set of data points make up the signal, including the information of every infrared frequency that comes from the source.



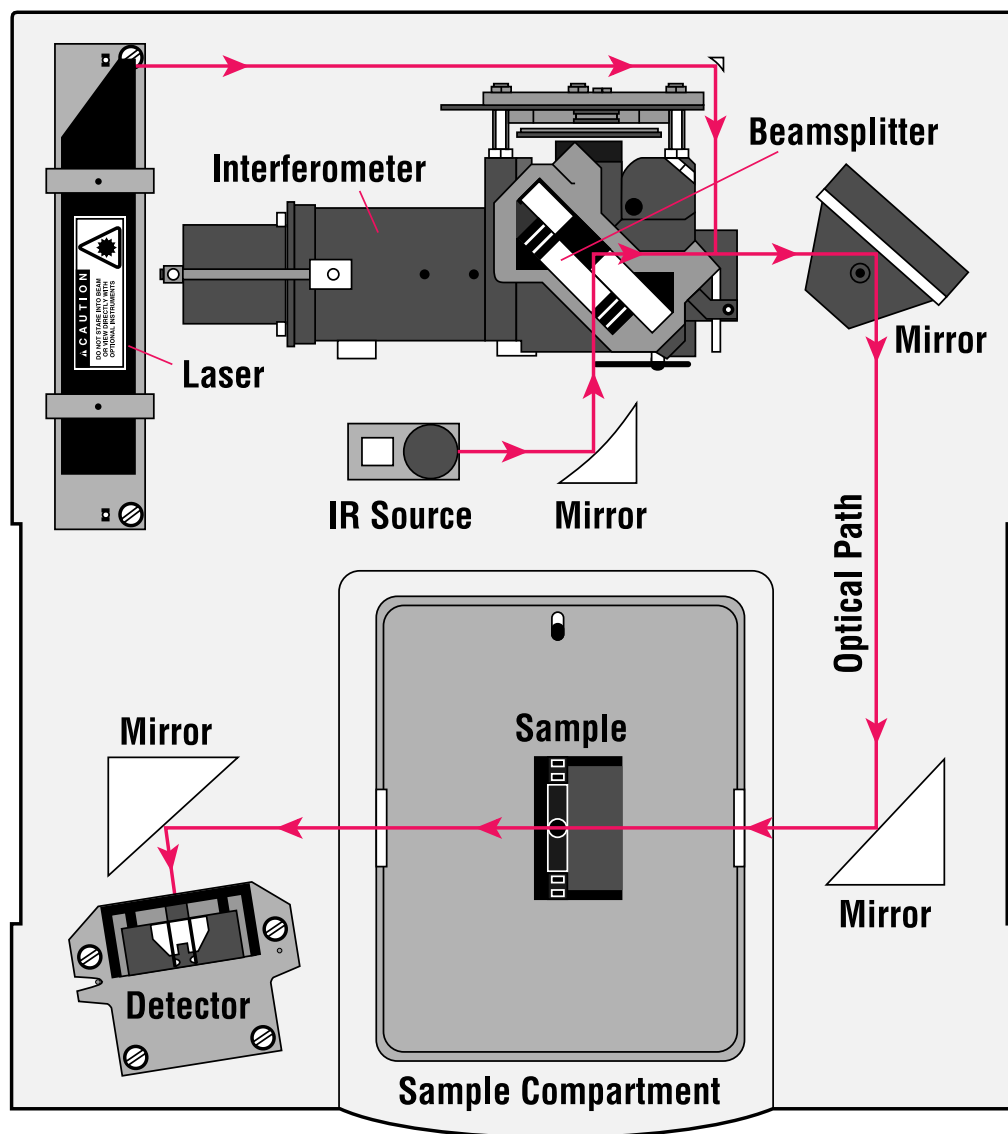


Figure 3.14 A simple spectrometer layout provided by Thermo Nicolet Corporation [131].

Why do we need Fourier transformation in the analysis? Because the measurement result is a frequency spectrum, which is a plot of the intensity at each

individual frequency, and the measured interferogram signal cannot be interpreted directly. A method of “decoding” the individual frequencies is required. This can be completed through a well-known mathematical technique called the “Fourier transformation”. This transformation is processed by the computer. The whole analysis process includes:

- 1) The source: Infrared light is emitted from a glowing black-body source. The beam passes through an aperture, controlling the amount of energy presented to the sample.
- 2) The interferometer: The beam enters the sample compartment, where it is transmitted through or reflected off of the surface of the sample, depending on the type (transmission or reflection) of analysis being accomplished. This is where the specific frequencies of the light source, which can be understood as the uniquely characteristic of the sample, are absorbed.
- 3) The detector: The beam finally passes through the detector for the final measurement. The detectors used here are specially designed for the measurement of the special interferogram signal.
- 4) The computer: The measured signal is digitized and sent to the computer where the Fourier transformation takes place. The final result (infrared spectrum) is then presented to the user.

The instrument FTIR is used to identify whether there is any Si-H<sub>x</sub> bond on the c-Si surface contributing to surface passivation after reaction in H<sub>2</sub>S. The sample chamber needs to be purged for a while before the measurement, and also for the

whole measurement process to make sure the absorption peak from  $\text{CO}_{2(g)}$  and  $\text{H}_2\text{O}_{(g)}$  can be avoided. The background spectrum needs to be measured because a relative scale for the absorption intensity is required. In this work, we used a bare polish wafer with H-terminated surface by HF dip for the background measurement. This technique results in a spectrum with all of the instrumental characteristics removed. Therefore, all the spectral features presented in the data are strictly from the sample. A single background measurement can be used for multiple sample measurements since this spectrum is characteristic of the instrument itself.

### **3.2.3 Photoluminescence Image**

The emission of photoluminescence (PL) radiation is caused by the transition of electrons from higher occupied electronic states into lower unoccupied states, under the emission of photons if the transition is dipole-allowed. PL imaging was used to evaluate the c-Si wafer bulk passivation effect and defect uniformity after reaction with  $\text{H}_2\text{S}$  in this dissertation, and how it corresponded to the  $\tau_{\text{eff}}$ . The laser beam used to produce the PL image has wavelength 690 nm, with its diameter 1 mm. An expander for the laser beam with its magnitude 20X was used in the measurement. When the laser light is applied on the mc-Si wafer, the electron-hole pairs generated by the photons recombine, causing PL emission. This PL emission is then detected by a SiGe detector, and a spatial map of the solar cell overall performance and recombination regions can be captured. The characterization of PL imaging shown in chapter 7 was assisted by Nuha Ahmed at IEC.

Unlike the electroluminescence (EL) imaging, which relies on the detection of relatively bright signals and can only be employed at the final stage of solar cell

manufacturing since metal contact is required for EL characterization, low-signal PL imaging can be implemented throughout the entire manufacturing process. PL imaging has great potential as an in-line monitoring tool. The ability to utilize this highly sensitive imaging technique during the early stages of the manufacturing process has significant ramifications, as PL images of ingots, bricks, and as-cut wafers can be predictive of final solar cell efficiency.

### **3.3 Optical and Electrical Characterization**

The main optical characterization used in this dissertation is variable angle spectroscopic ellipsometry. Ellipsometry uses polarized light to characterize thin film and bulk materials. The light undergoes a change in polarization as it interacts with the sample structure. The material properties of interest are determined by analyzing the polarization change, expressed by two measurement data, amplitude ratio,  $\psi$ , and phase difference,  $\delta$ . The electrical measurements in this dissertation includes  $\tau_{\text{eff}}$  by monitoring of photoconductance decay mainly to evaluate surface passivation quality, current-voltage measurement to determine solar cell performance, quantum efficiency to analyze the efficiency of carriers being collected by the photon illuminated on the solar cell, and laser beam induced current imaging to investigate the degree of uniformity through the spacial mapping of photocurrent. Among all these electrical characterizations,  $\tau_{\text{eff}}$  measurement is a contactless and non-destructive measurement, which can be used to monitor the wafer surface/bulk change during the device fabrication. Rest of the measurements, current-voltage, quantum efficiency, and laser beam induced current, all require complete device for the measurement and study.

### **3.3.1 Variable Angle Spectroscopic Ellipsometry (VASE)**

Ellipsometry measures a change in polarization as light reflects or transmits from a material structure. The polarization change is represented as an amplitude ratio  $\psi$ ,  $\Psi$ , and the phase difference  $\delta$ ,  $\Delta$ . The measured polarization change is determined by the optical properties and thickness of individual materials. Hence, ellipsometry is primarily used to determine the film thickness and its optical constants such as  $n$  &  $k$ , with the advantage of non-destructive, sensitive and precise. It can also be applied to characterize composition, crystallinity, roughness doping concentration, and other material properties related to a change in optical response.

Spectroscopic ellipsometry (SE) uses a broad band light source, covering a certain spectral range in the infrared, visible, or ultraviolet spectral region. With SE, the complex optical constants in the corresponding region can be obtained. Moreover, the accuracy of the ellipsometry result has been further improved with the use of variable angle, and this is exactly what being used in this dissertation, VASE. The combination of variable angle of incidence and spectroscopic measurements allows the user to acquire large amounts of data from a given sample. More importantly, the spectral acquisition range and the incident angle required may be optimized according to the sample material and other parameters, such as film thickness.

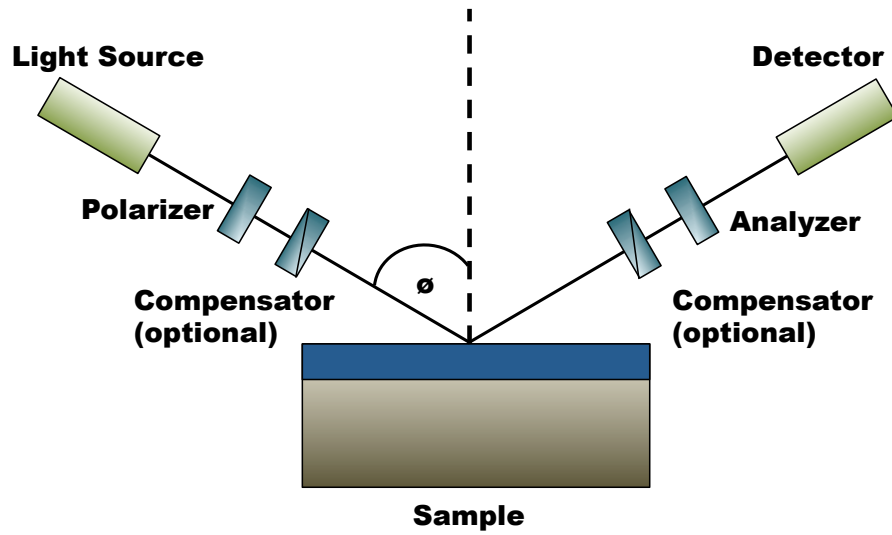


Figure 3.15 The configuration of variable angle spectroscopic ellipsometer [132].

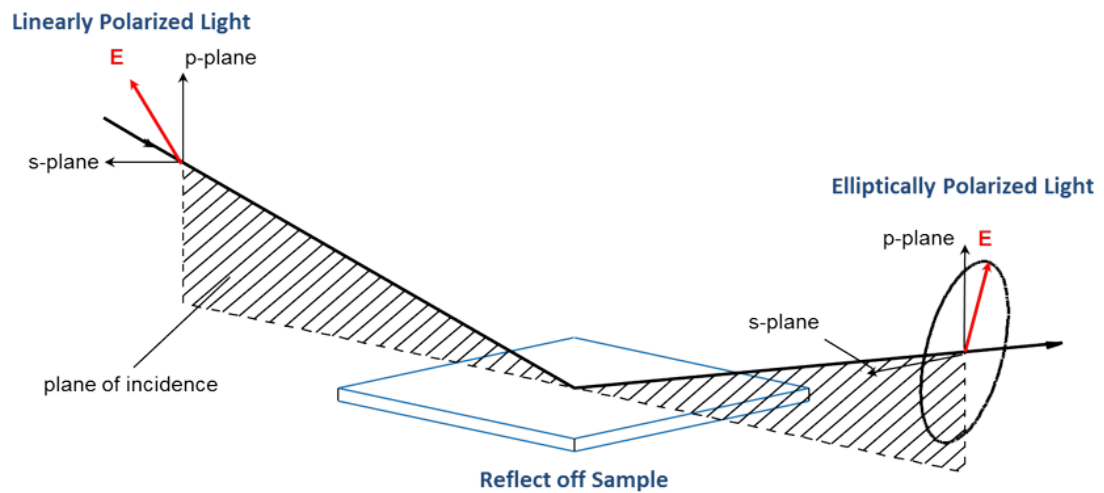


Figure 3.16 The linear polarized electromagnetic radiation emits and gets reflected by the sample, forming reflected elliptically polarized light, which includes the information (thickness, refractive index...etc.) of the characterized sample [133].

Figure 3.15 is the configuration of an variable angle spectroscopic ellipsometer [132]. The input light source is linearly polarized. The polarization is defined as the orientation p- and s- planes, as seen is Figure 3.16 [133], where the s component is oscillating perpendicular to the plane of incident and parallel to the sample surface, and the p component is oscillating parallel to the plane of incident. Before reaching the surface, the light passes through an optional compensator. This compensator is also called retarder, patented by J. A. Wollam, can convert linearly polarized light to circularly polarized light by introducing the phase delay between p-wave and s-wave due to the optical anisotropy of compensator. The combination of rotatable compensator and polarizer can convert and unpolarized light into any elliptical polarization. After being reflected from the sample, the light passes another compensator and a second polarizer, called analyzer, before reaching the detector.

As mentioned earlier, the VASE characterization relies on the change of the polarization between the radiation before and after being reflected by the sample, as shown in Figure 3.16. The polarization change is represented as an amplitude ratio, psi ( $\Psi$ ), and the phase difference, delta ( $\Delta$ ). A more direct parameter  $\rho$ , defined as the complex reflectance ratio of the system, which can be parameterized by the amplitude  $\Psi$  and the phase difference  $\Delta$ . As seen in Figure 3.16, both the incident light and the reflected light can be decomposed into s- and p- directions, respectively. The s- and p-component of reflected beam can be normalized to the initial value (s- and p-component of incident beam) and denoted by  $\gamma_s$  and  $\gamma_p$ , which can be presented by the equation 3.3:

$$\rho = \frac{\gamma_p}{\gamma_s} = \tan(\Psi)e^{i\Delta} \quad (3.3)$$

Equation 3.3 indicates that ellipsometry is measuring the ratio of these two quantities, rather than the absolute values of either of them. This makes the ellipsometry characterization more accurate and reproducible. This also makes the measurement less sensitive to light scattering or fluctuations, and hence there is no need any reference sample or reference beam for the measurement.

The general procedure of ellipsometry experiments is shown in Figure 3.17 [133]. Normally the measurement provides only an indirect result, where the film thickness, optical constants, or other desired information of the sample require further modeling and fitting.



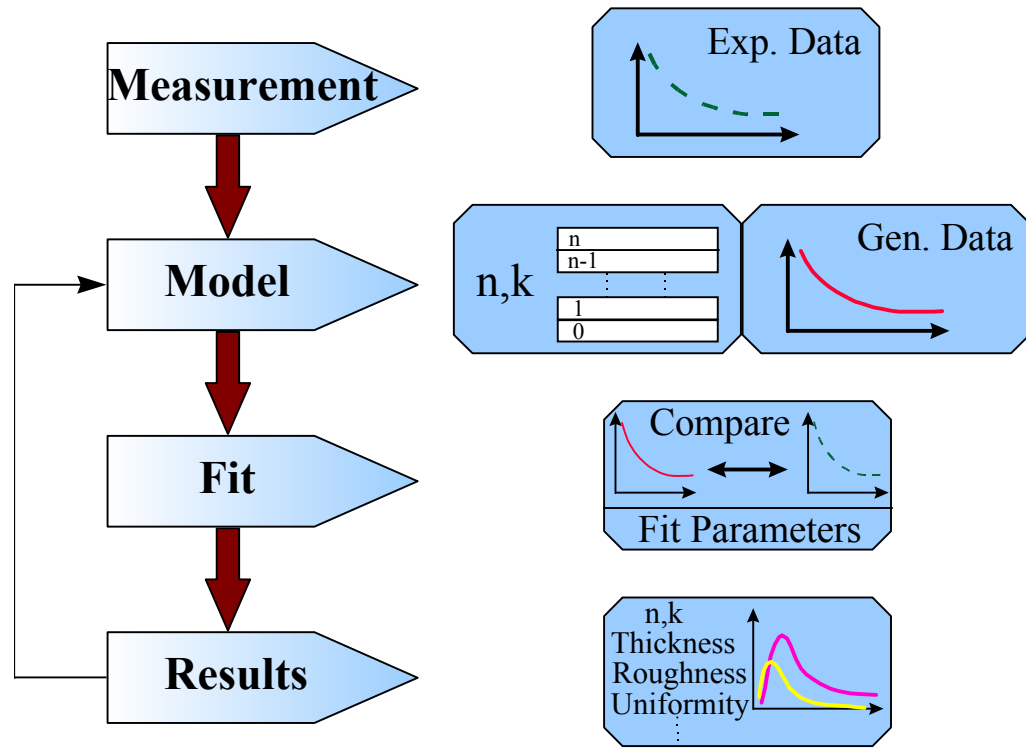


Figure 3.17 General procedure used in optical measurement, which is also the standard procedure in ellipsometry measurements to determine the material properties from experimental data [133].

With acquired  $\Psi$  and  $\Delta$  from the measurement, a model needs to be constructed to predict the desired parameters of the film, which contains some known parameters, such as the wavelength of the incident light, the incident beam polarization state, and the angle of the incident beam. After a model is developed, the unknown physical parameters can be varied to generate multiple sets of data until a set of optimized parameters is found that closely matches the measured optical data. Regression analysis is used since no exact equation can be written. Mean squared error (MSE) is used to quantify the difference between calculated curve and measured

curve. When this optimized set of parameters are unique, physically reasonable and not strongly correlated, the result can be considered as the best-fit model, representing the physical reality of the sample, with MSE typically less than 6.

Film thickness and the optical constants,  $n$  &  $k$ , determined from the VASE measurement, were used to evaluate the passivation layer on top of c-Si surface by reaction in  $H_2S$ . An increasing separation between the surface reflected light and the light traveling through the film is shown in Figure 3.18 [133], which is caused by an increasing film thickness. This will make a phase delay, which relates not only to the physical thickness but also to the refraction index. In another word, estimated thickness is not independent of the optical constants. The film thickness affects the path length of light traveling through the film, but the index determines the light waves' velocity and refracted angle. Therefore, both the film thickness and optical constants contribute to the delay between surface reflection and light traveling through the film.

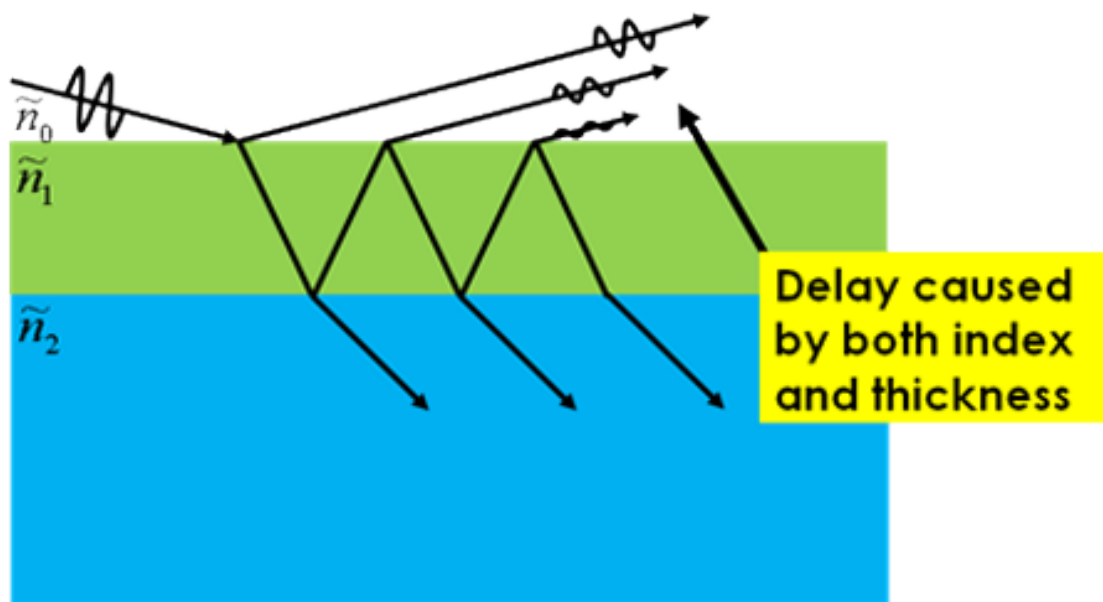


Figure 3.18 The phase delay between the reflected beam and the beam traveling through the film can be caused by both the film thickness and the refractive index [133].

The film thickness is determined by interference between the light reflected from the surface and the light traveling through the film. Depending on the relative phase of the rejoining light to the surface reflection, interference can be defined as constructive or destructive. The interference involves both amplitude and phase information. The phase information from  $\Delta$  is very sensitive to films down to sub-monolayer thickness. Take  $\text{SiO}_2$  as an example, Figure 3.19 shows the  $\Psi$  curve for a series of thin  $\text{SiO}_2$  films of different thicknesses. As the thickness ( $T$ ) increases, the interference oscillations shift toward longer wavelengths.

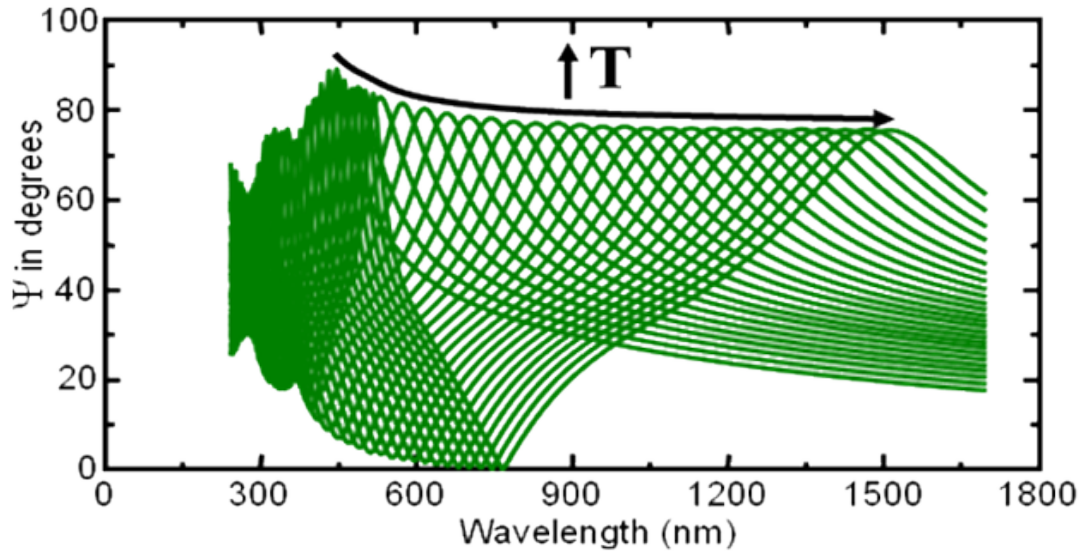


Figure 3.19 The  $\Psi$  curve for a series of  $\text{SiO}_2$  films of different thicknesses [133].

Moreover, thickness measurements also require a portion of the light travel through the entire film and then return to the surface, therefore thickness measurements by optical instruments is limited to thin, semi-opaque layers. This limitation can be circumvented by targeting measurements to a spectral with lower absorption. For example, organic film may strongly absorb UV and IR light, but be able to remain transparent at mid-visible wavelengths. For metals, the maximum thickness can be determined by ellipsometry is typically about 100 nm because metal strongly absorbs at all wavelength. Overall, different materials have their own suitable wavelength range for the characterization depending on their optical properties.

In addition to the thickness information, the shape of the data oscillation is dependent on the film optical constants because the index determines the light wave's

velocity and refracted angle. Optical constants including both  $n$  and  $k$  values must be known or determined along with the thickness to obtain the correct results from the optical measurement. For both the film thickness and optical constants, an iterative procedure using least-squares minimization can be applied to extract thickness and/or optical constants with the best matching of  $\Psi$  and  $\Delta$  to the experimental data. All ellipsometric measurements in this dissertation were performed with VASE from J. A. Woollam Corp. and the data was processed in the software CompleteEase. Figure 3.20 is the schematic of VASE system with their patented AutoRetarder from J. A. Woollam.

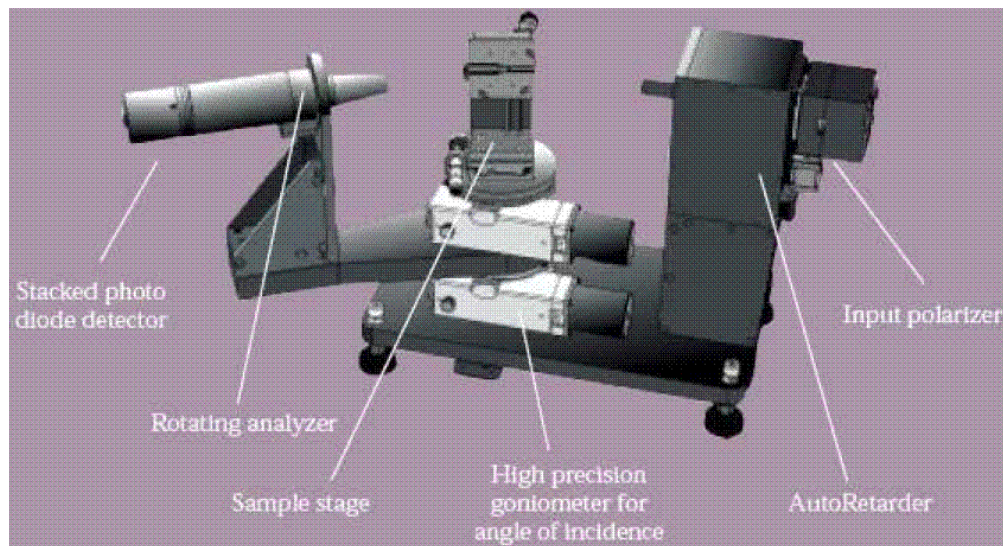


Figure 3.20 Variable angle spectroscopic ellipsometer (VASE) with AutoRetarder from J. A. Woollam [133].

### 3.3.2 Effective Minority Carrier Lifetime Measurement

Effective minority carrier lifetime ( $\tau_{\text{eff}}$ ) is commonly used in c-Si solar cell fabrication to monitor of how long a carrier is likely to stay around before recombination. The measured parameter,  $\tau_{\text{eff}}$ , which is the net result of summing up all the recombination losses that occurs in the different regions of a c-Si wafer or a solar cell, and it can be decomposed to bulk lifetime ( $\tau_b$ ) and surface lifetime ( $\tau_s$ ) as seen in Equation 3.4:

$$\frac{1}{\tau_{\text{eff}}} = \frac{1}{\tau_b} + \frac{1}{\tau_s} \quad (3.4)$$

From Equation 3.4  $\tau_{\text{eff}}$  is commonly used to evaluate the whole passivation level and predict the solar cell performance, especially for surface passivation quality when the wafer bulk quality is excellent and the term of bulk lifetime is negligible.

The  $\tau_{\text{eff}}$  in this work is measured by Sinton lifetime tester WCD-100, using the method of photoconductance decay, which measures the time dependent of photoconductance decay resulting from light pulse [134]. The WCD-100 is shown in Figure 3.21. When the sample is under illumination, the photoconductance will change as the result of excess carrier density,  $\Delta n$ , and the photoconductance decay is essentially the excess carrier decay inside the sample after pulse light illumination.  $\tau_{\text{eff}}$  can be calculated at each individual excess carrier density with known photogenerated carrier density. The change of photoconductance for a wafer of thickness  $W$  is given by:

$$\Delta\sigma_L = qW(\mu_n + \mu_p)\Delta n \quad (3.5)$$

Where  $\mu_n$  and  $\mu_p$  are electron and hole mobilities respectively, and the photoconductance  $\Delta\sigma_L$  can be measured in a contactless fashion by using an inductor.



Figure 3.21 The completed system should look like this. The calibration wafer covers the sensor coil but cannot cover the small blue light sensor (standard solar cell).

There are two types of measurement being studied in this dissertation, quasi-steady-state photoconductance (QSSPC) method [135] and transient mode [136]. These two measurements of lifetime both follow the generalized data analysis proposed in Equation 3.6 [137].

$$\tau_{eff} = \frac{\Delta n(t)}{G(t) - \frac{dn(t)}{dt}} \quad (3.6)$$

In QSSPC, the sample is flashed with the light, and then the decay of the light and the photoconductance are monitored during the flash. Data is acquired throughout a flash pulse from maximum intensity as it decays to zero. In more detail, the light intensity versus time is determined during a long, exponentially decaying light pulse. Then, the sample sheet conductivity versus time is measured and the conductivity is converted to carrier density. The  $\tau_{eff}$  is then evaluated from the carrier density through the equation below:

$$\tau_{eff} = \frac{\Delta n(t)}{G(t)} \quad (3.7)$$

where  $G(t)$  is the generation rate, which is measured using a photo-detector, a calibrated solar cell installed in the WCT-100. QSSPC mode works off the assumption that the lifetime of the flash is much greater than the lifetime of the sample, which means that the intensity of the flash changes sufficiently slowly so that the carrier populations in the sample are always at steady state. Thus, Equation 3.6 can be



simplified to Equation 3.7. With this assumption, the sample lifetime should be less than 200  $\mu$ s. For samples with lifetimes greater than 200  $\mu$ s, there will be error introduced into the measurement if measured in QSSPC mode making the assumption invalid.

In the transient mode, the sample is illuminated and then the photoconductance decay is monitored once the flash is cut off and no light used in the analysis. Thus, the equation presented transient mode can be simplified from Equation 3.6 QSSPC mode, as shown Equation 3.8 below:

$$\tau_{eff} = \frac{\Delta n(t)}{-\frac{dn(t)}{dt}} = -\frac{t}{\ln(\Delta n)} \quad (3.8)$$

For the transient mode, the change of wafer conductivity overtime is measured after the light being flashed on the sample and cut off, and the wafer conductivity is then converted to excess carrier density. The  $\tau_{eff}$  of each carrier density (injection level) can be determined through the derivative of the excess carrier density. The pulse of the light is only to excite the carriers and is off during the carrier density monitoring and measurement, therefore the term  $G(t)$  becomes zero. Based on the assumption in transient mode that the lifetime of the sample is greater than the lifetime of the flash, requiring the sample's  $\tau_{eff}$  to be greater than 100  $\mu$ sec for this mode since the cutoff time of the flash bulk is about 50  $\mu$ sec.

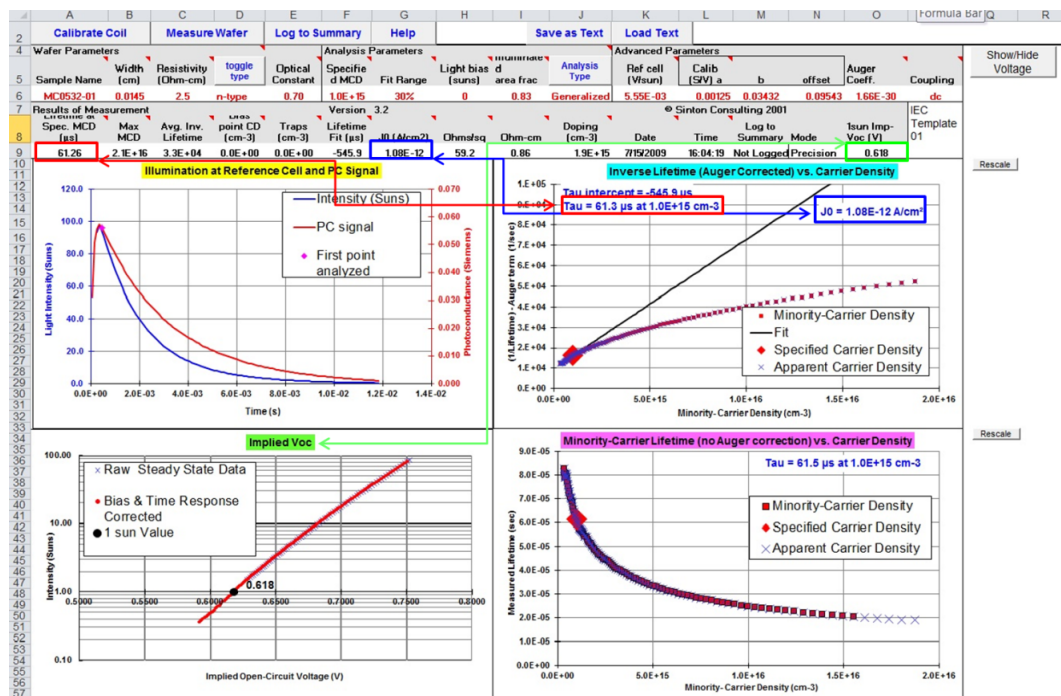


Figure 3.22 The screen shot of QSSPC mode  $\tau_{\text{eff}}$  measurement by Sinton Lifetime Tester WCT-100. The upper left plot: The decay overtime of illumination at reference cell and photoconductance signal. The upper right plot: Inverse lifetime after Auger correction at different carrier density (injection level). The lower left plot: Implied Voc calculated from lifetime measurement. The lower right plot: minority carrier lifetime without Auger correction at different carrier density (injection level). In this measurement, the  $\tau_{\text{eff}}$  (highlighted in red box), saturate current density (highlighted in blue box), and implied Voc at 1-sun intensity (highlighted in green box) can be calculated from the photoconductance decay.

Surface recombination velocity (SRV), which can be more directly and intuitively describe the quality of surface passivation, can be calculated from  $\tau_{\text{eff}}$ . SRV is in the unit of cm/sec, and can be understood as the speed of carriers move towards the surface. If a surface has no recombination site, the movement of carriers towards

the surface is zero, and therefore the SRV is zero. The  $\tau_{\text{eff}}$  can be presented as a combination of  $\tau_b$  and  $\tau_s$ , as previously describe in Equation 3.5. In the solar cell manufacturing, the absorber, c-Si wafer, usually has high  $\tau_b$  of several milliseconds. Hence, the bulk lifetime term in Equation 3.5 can be neglected and the Equation 3.5 can be simplified as  $1 / \tau_{\text{eff}} \sim 1 / \tau_s$ . To correlate the measured  $\tau_{\text{eff}}$  to SRV, Equation 3.9 to Equation 3.13 are a series of approximate solutions for several different cases, with the definition of S1 and S2 as seen in Figure 3.23 [138].

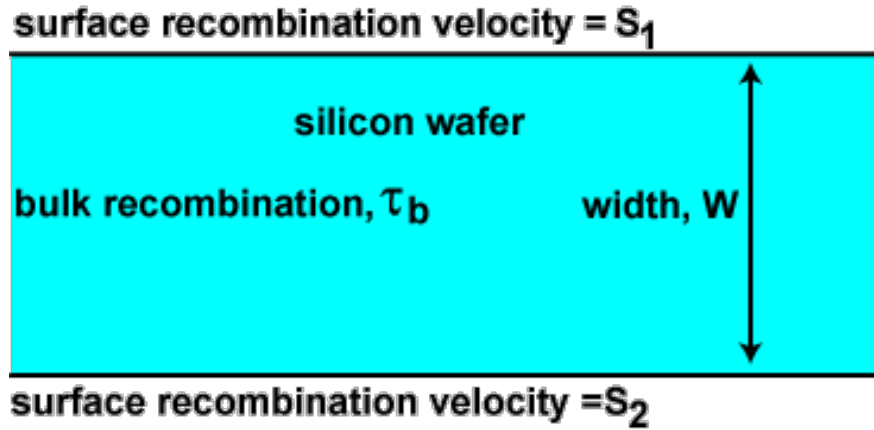


Figure 3.23 A schematic of a c-Si wafer with its front and back surface recombination velocity, S1 and S2 respectively.

The surface are identical, so  $S = S1 = S2$ .

$$\tau_s = \frac{W}{2S} + \frac{1}{D} \left( \frac{W}{\pi} \right)^2 \quad (3.9)$$

One surface is perfectly passivated, so  $S_2 = 0$

$$\tau_s = \frac{W}{S_1} + \frac{4}{D} \left( \frac{W}{\pi} \right)^2 \quad (3.10)$$

Both surfaces are perfectly passivated, so  $S_1 = S_2 = 0$

$$\tau_s = \infty \quad (3.11)$$

Both surfaces have high recombination, so  $S_1$  and  $S_2$  are both high

$$\tau_s = \frac{1}{D} \left( \frac{W}{\pi} \right)^2 \quad (3.12)$$

One surface has a high recombination and the other has a low recombination,  
so  $S_1 = 0$  and  $S_2 = \infty$

$$\tau_s = \frac{4}{D} \left( \frac{W}{\pi} \right)^2 \quad (3.13)$$

### 3.3.3 Current-Voltage Analysis

Current-Voltage analysis is used to evaluate solar cell performance, typically referred to J-V measurement and Figure 3.24 shows the schematic setup of a J-V tester. An artificial light source simulating the sunlight spectrum illuminates the solar cell. The current between the probes is recorded as a function of the applied voltage. During the measurement, the solar cell is cooled with a fan or water, and the temperature of the solar cell is monitored with the thermometer.

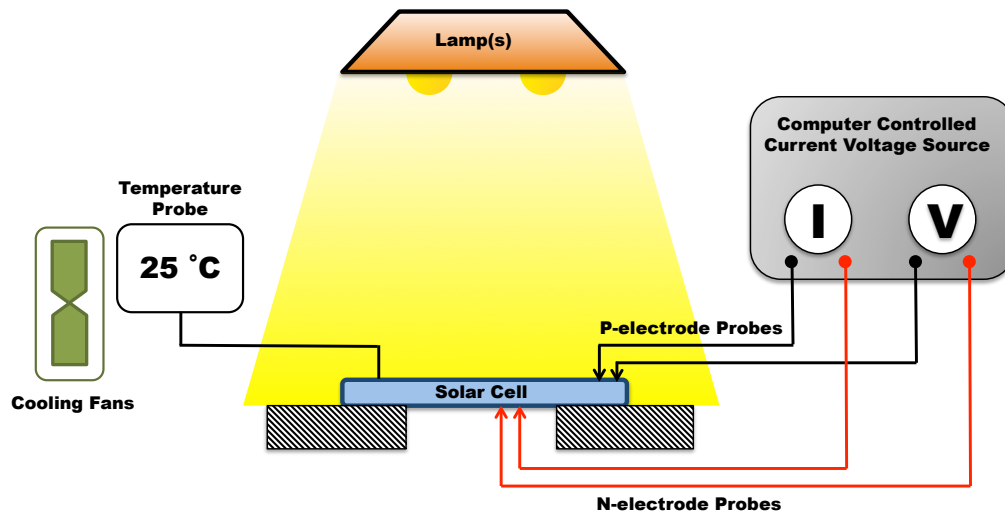


Figure 3.24 The schematic setup for current (density) – voltage measurement.

A standard solar cell tester should satisfy the following conditions: 1) Air mass 1.5 spectrum (AM1.5) for terrestrial cells and Air mass 0 spectrum (AM0) for space cells (Please refer to Appendix A for the definition and details of AM1.5 and AM0); 2) Intensity of  $100 \text{ mW/cm}^2$  or  $1\text{kW/m}^2$ , which is one-sun of illumination; 3) Cell

temperature at 25°C; 4) Four point probe to remove the effect of contact resistance between the probe and the device.

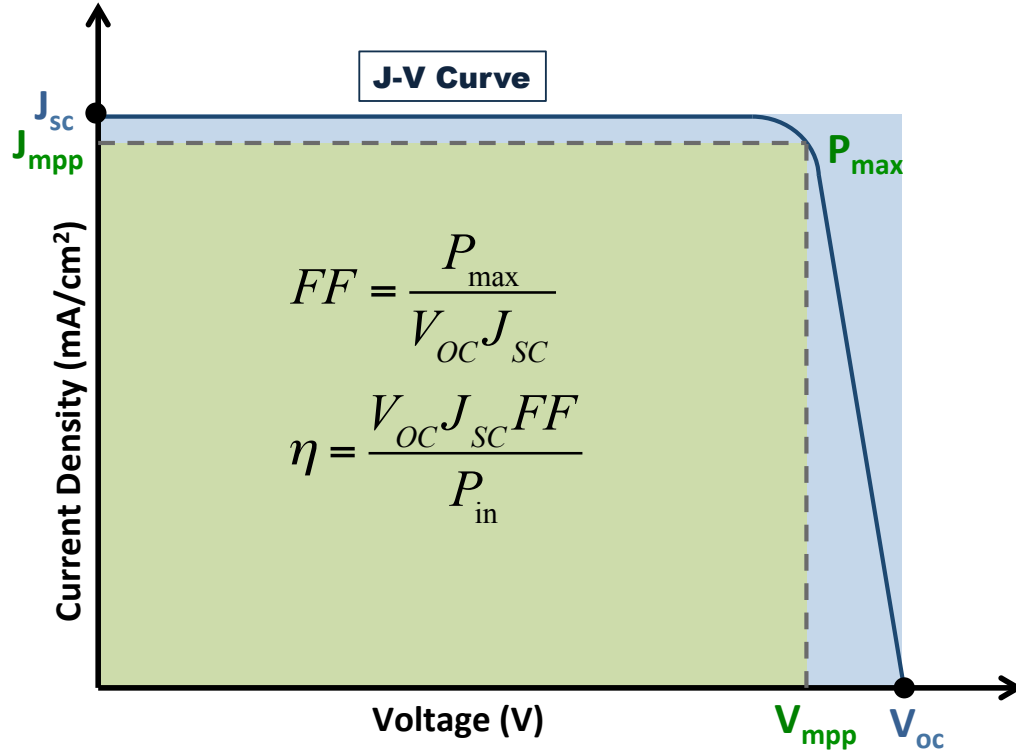


Figure 3.25 Example of a J-V curve and the characteristic parameters calculated from it:  $V_{OC}$ ,  $J_{SC}$ ,  $FF$ , and efficiency  $\eta$ .

From the J-V measurement, some basic parameters can be extracted that characterize the solar cell performance [34]. Figure 3.25 is an example of a J-V curve and the characteristic parameters from it, including short circuit current density ( $J_{SC}$ ), open circuit voltage ( $V_{OC}$ ), fill factor ( $FF$ ), and efficiency ( $\eta$ ).

The  $J_{SC}$  is the current density through the solar cell when the voltage across the solar cell is zero, which is due to the generation and collection of light-generated carriers. For an ideal solar cell, the  $J_{SC}$  and the light-generated current density ( $J_L$ ) are identical. Hence, the  $J_{SC}$  is the largest current density which may be drawn from the solar cell.  $J_{SC}$  can be affected by the number of photons, the spectrum of the incident light, the optical properties, and the collection probability. The collection probability describes the probability that a light-generated carrier absorbed in a certain region of the solar cell will be collected by its p-n junction before they recombine and therefore contribute to the light-generated current.

The  $V_{OC}$  is the maximum voltage in a solar cell, occurring at zero current. Equation 3.14 for  $V_{OC}$  is found by setting the net current equal to zero:

$$V_{OC} = \frac{nkT}{q} \ln \left( \frac{J_L}{J_0} + 1 \right) \quad (3.14)$$

Equation 3.14 shows that  $V_{OC}$  depends on the saturation current density ( $J_0$ ) of the solar cell and the  $J_L$ . Since  $J_L$  typically has a small variation, the key effect on  $V_{OC}$  is the  $J_0$ , which may vary by orders of magnitude for different solar cells depending on the recombination in the solar cell. Therefore,  $V_{OC}$  can be considered as a measure of the amount of recombination in the device.

$J_{SC}$  and  $V_{OC}$  can be obtained directly from the J-V measurement. The power output of a solar cell for any operating point can be expressed as the rectangle area in the J-V curve, as the green area indicated in Figure 3.25. There exists one particular operating point  $P_{max}$  at  $(V_{mpp}, J_{mpp})$ , maximizing the power output. The FF is a parameter related to the maximum power from a solar cell. It is a measurement of the

“squareness” of the J-V curve, and is defined as the ratio of maximum power density  $P_{\max}$  to the product of  $J_{SC} \times V_{OC}$ , as the equation shown below:

$$FF = \frac{P_{\max}}{J_{SC} \times V_{OC}} = \frac{J_{mpp} \times V_{mpp}}{J_{SC} \times V_{OC}} \quad (3.15)$$

The most important and commonly used parameter to compare the performance of solar cells, device conversion efficiency ( $\eta$ ), determined as the fraction of incident power ( $P_{\text{light}}$ ) which is converted to electricity output ( $P_{\max}$ ), as seen in Equation 3.16 below:

$$\eta = \frac{P_{\max}}{P_{\text{light}}} = \frac{FF \times J_{SC} \times V_{OC}}{P_{\text{light}}} \quad (3.16)$$

In addition to reflecting the performance of the solar cell itself, the efficiency depends on the spectrum and intensity of the incident sunlight and the temperature of the solar cell as well. Hence, conditions under which efficiency is measured must be carefully controlled in order to compare the performance of one solar cell to another. Terrestrial solar cells are measured under AM1.5 conditions and at temperature of 25°C.

### 3.3.4 Quantum Efficiency Measurement

Quantum efficiency (QE) [139] is defined as the ratio of the number of carriers being collected by the solar cell to the incident of photons by a given energy



(wavelength) incident on the solar cell. If all the photons of a particular wavelength are absorbed and the generated minority carriers are all collected, then the QE at that particular wavelength would be defined as one. The ideal QE curve has a rectangular shape, because QE for photons with energy below the material bandgap transmit through the cell is zero. However, most of the cases are not ideal, not rectangular shape. Figure 3.26 shows a typical QE curve, which has various recombination effect losses and additional losses such as reflection loss at illuminating side involved.

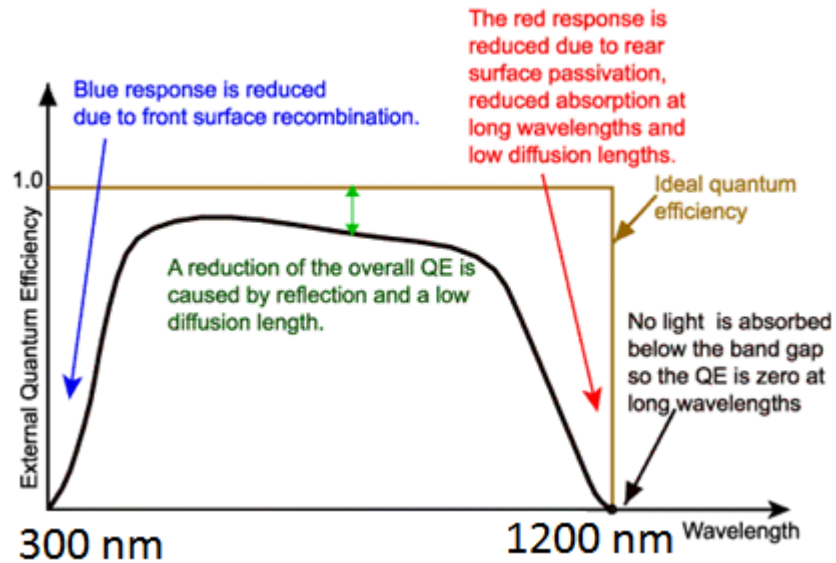


Figure 3.26 Typical quantum efficiency curve of a c-Si solar cell [138].

Figure 3.26 is a typical QE spectrum of a c-Si solar cell, where the measurement range is from 300 nm to 1200 nm, determined by solar spectrum AM 1.5

and the bandgap of c-Si, 1.12 eV [138]. Both electrical loss and optical loss in the device make the QE curve varies from the ideal rectangular shape. The collection loss in the short wavelength region (blue response region) is most likely due to the front surface recombination loss (electrical part) and reflection loss (optical part) along with the losses from the front passivation layer and the front emitter. Therefore, QE loss in the short wavelength region can be reduced by the optimization of the front surface layers for: 1) surface passivation to reduce carrier recombination; 2) anti-reflection to maximize the number of photons reaching the absorber; 3) the thickness and bandgap of the passivation and emitter to minimize the number of photons being absorbed before reaching the c-Si material. QE loss in the long wavelength region (red response region) is caused by the back surface recombination and reduced photon absorption near c-Si bandgap 1.12 eV where overall reduction of QE is due to the optical reflections and the short diffusion lengths of the carriers. For a well-behaved device, the integration of QE through Equation 3.16 will be in agreement with short circuit current  $J_{SC}$  measured under the same spectrum.  $\Phi(\lambda)$  is the photon flux at a given wavelength under AM 1.5 spectrum.

$$J_{ph} = q \int \phi(\lambda) QE(\lambda) d\lambda \quad (3.17)$$

So far all the descriptions about QE are external QE, which has all the optical losses in the device being considered. Internal QE, corrects all these optical losses such as grid line covering loss, total reflection loss of the device, absorption loss from the front passivation layer, front emitter, and anti-reflection coating. Equation 3.18 expresses the simplified correlation between external QE and internal QE of the cells

within the same cell configuration, including absorption loss from the front surface layers. This analysis approach is commonly used in the discussion of QE.

$$IQE(\lambda) = \frac{EQE(\lambda)}{1 - R_F(\lambda)} \quad (3.18)$$

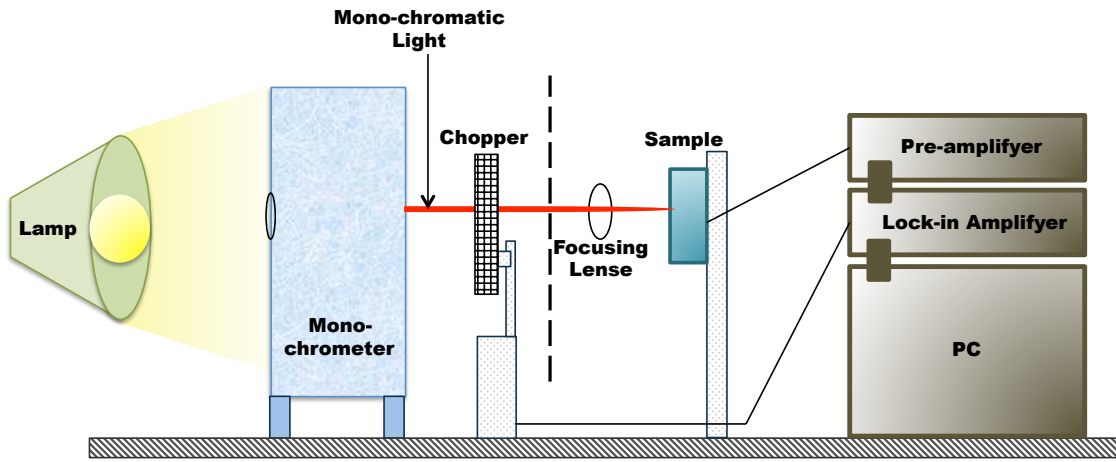


Figure 3.27 Configuration of quantum efficiency measurement [140].

Figure 3.27 is the schematic of the QE measurement setup, which includes a solar simulator to create a stabilized light source, a monochromator, and a chopper. The chopper and monochromator are used to make a chopped monochromatic probe beam. The current gets generated when the monochromatic light beam refocuses on the sample. The generated current signal passes through a pre-amplifier to be amplified, and then gets phase-sensitively detected by a lock-in amplifier. The lock-in

technique is used in QE measurement is phase-sensitive and therefore has capability to detect only the AC signal from the chopped probe beam, where any DC signal from the light bias would be rejected. The purpose of having this lock-in technique is to separate AC signal from any other DC signal bias, making the measurement even more accurate for those small current signals generated by weak chopped monochromatic light beam [140].

### **3.3.5 Laser Beam Induced Current Scanning**

Laser beam induced current (LBIC) is characterized by illuminating a small area of the device, and then the resulting photogenerated current is measured. Hence if the laser beam is scanned, either line scan or the whole sample mapping, the localized defects can be identified. The spatial mapping of photocurrent provides the degree of uniformity of the whole device. Here the measurement of LBIC line scan was used to study the spatial dependence of current collection and further to evaluate the FF loss in two dimensional IBC-SHJ solar cells. Traced back to the 1970's, LBIC has been widely used to analyze the processing techniques and related device performances since then [141].

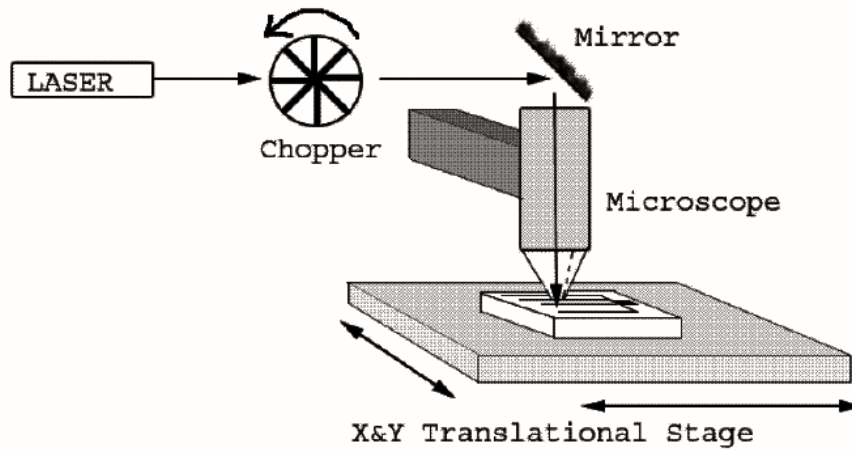


Figure 3.28 The LBIC system setup [142].

The LBIC system setup is shown in Figure 3.28. Normally the incident laser light is modulated into a pulse AC signal through a mechanical chopper, hence the laser-induced photocurrent can be generated while the sample is under illumination with a constant light bias. The laser beam is fixed on the sample surface, which is a typical setup as shown in Figure 3.28. During the measurement, the sample stage is moving to complete the scan. However, at IEC the design of the beam and stage is reversed. We have the sample stage fixed while the beam is free to move to complete the scan and mapping across the sample, which increases the range of measuring area from hundreds of square microns to over one square meter. Moreover, the LBIC system at IEC provides a DC light bias ranging from 0.001 sun to 1 sun, and a DC voltage bias from -5 V to +5 V. The LBIC system at IEC uses a laser beam with 633 nm, approximately 50  $\mu\text{m}$  spot size, and 50  $\mu\text{m}$  step size.

## Chapter 4

### THE ROLE OF BACK CONTACT PATTERNING ON STABILITY AND PERFORMANCE OF SI IBC HETEROJUNCTION SOLAR CELLS

The contents of this dissertation chapter have been adapted from a manuscript published in *IEEE 40<sup>th</sup> Photovoltaic Specialists Conference*: U. Das, **H.Y. Liu**, J. He, and S. Hegedus, “The Role of Back Contact Patterning on Stability and Performance of Si IBC Heterojunction Solar Cells” *40<sup>th</sup> IEEE Photovolt. Spec. Conf.*, 2014, pp. 0590-0593. Please refer to Appendix B: Reprint Permission for Copyright 2014, IEEE. The IEEE does not require individuals working on a thesis to obtain a formal reuse license.

#### 4.1 Summary

The initial performance and stability over time of IBC-SHJ solar cell exhibits a critical dependence on the patterning processes, especially in defining the gap structure between emitter and base contacts. Original patterning processes using photoresist (PR) resulted in device performance of only 15% which degraded even with dark storage in a dry environment over days while a newly developed patterning approach using a-SiN<sub>x</sub>:H for patterning yielded higher performance of 17.9% with the first time fabrication and was stable over months. The use of photoresist as a mask in PECVD to form interdigitated contacts resulted in a gap that was insufficiently passivated and the possible PR outgassing in PECVD chamber may cause

contamination to the interface and bulk of intrinsic and/or doped a-Si:H. However, use of a-SiN<sub>x</sub>:H as a mask allows for a clean deposition in PECVD with a multi-layer gap structure which improves the cell performance and stability. The laser fired contact (LFC) reduces  $V_{OC}$  slightly due to increased recombination loss, but does not cause additional instability. In this chapter, we reported a first time stable efficiency of 17.9% achieved in an IBC-SHJ solar cell using all low temperature processes that incorporated a multi-layer gap passivation structure. With more careful sample handling and device fabrication process, the highest performance of 20.2% was reached in our lab with this device structure.

## 4.2 Introduction

IBC-SHJ solar cells [143] combine the advantage of the IBC cell design - high  $J_{SC}$  due to lack of front shading loss – with the advantage of SHJ cell process - high  $V_{OC}$  due to improved low temperature surface passivation by a-Si:H. Recently, Kaneka announced a world record efficiency of 26.7% for a Si solar cell using IBC-SHJ structure with improved FF of 83.8% by improving surface passivation and series resistance [3]. The back surface of an IBC-SHJ cell has alternatively patterned p- and n-type a-Si:H strips with a gap between them. The cell performance is influenced by the entire back surface passivation quality, which is inherently inter-related to the bulk and interface quality of the interdigitated p- and n-a-Si:H pattern deposition and the gap [144]. The method of patterning the doped a-Si:H layers influences the HJ and contact behavior due to strong sensitivity of each hetero-interface to interface defects, contamination, and heterojunction formation [145]. In this work, we fabricated IBC-SHJ solar cells with two different patterning approaches; (a) using PR and (b) using a-

SiN<sub>x</sub>:H as a mask for depositing the interdigitated pattern. The two different processes lead to different gap composition and structures, together with varying cleanliness of different interfaces. The solar cell performance and stability were found to be critically dependent on the patterning process.

### 4.3 Experimental Section

All the c-Si wafers used in this work were 150  $\mu\text{m}$  Fz polish wafers having textured front surfaces. Wafer cleaning steps include: 1) solvent cleaning with agitation to remove dust and grease; 2) 5 min Piranha, which is a mixture of H<sub>2</sub>SO<sub>4</sub> : H<sub>2</sub>O<sub>2</sub> (3:1) to remove hydrocarbon; 3) Oxide removal in 10% HF, to make surface H-terminated. To make the front surface texturing, wafers were loaded into PECVD chamber right after HF dip for one-side a-SiN<sub>x</sub>:H deposition. With one side protected by a-SiN<sub>x</sub>:H, the other side was textured in 1% TMAH solution at  $\sim 75^\circ\text{C}$  for 20 min with agitation followed by 10 min static status. After one-side texturing, the wafer was cleaned by the solvent again, followed by a-SiN<sub>x</sub>:H removal in HF. Final clean Piranha (5 min) and 10% HF (1 min) were performed right before a-Si:H layers deposition through PECVD.

The IBC-SHJ solar cells with different back surface patterning approaches had front texturing surfaces passivated by a 8 nm i. a-Si:H layer, followed by ARC composed of 75 nm a-SiN<sub>x</sub>:H and 20 nm a-SiC:H. The a-SiC:H is mainly for protecting the front surface during rear surface etching processes, which was developed by Brent Shu in our group years ago [146]. These front stack layers provide a well-passivated anti-reflection surface, which enables an independent investigation of the back surface patterning process [144]. A continuous 8 nm a-Si:H layer is first



deposited on the back surface. The back surface interdigitated patterns are composed of a p-type a-Si:H strip, which is 20 nm thick and 1.4 mm wide, and a n-type a-Si:H strip, which is 30 nm thick and 0.25 mm wide. All a-Si:H layers are deposited by direct current PECVD at 175-250°C. Two patterning approaches will be discussed in this chapter. The original one using PR as patterning mask was developed previously in our group shown in Figure 4.1 (a). Newly developed back surface patterning approach for IBC-SHJ solar cells using a-SiN<sub>x</sub>:H as a patterning mask is shown in Figure 4.1 (b). Table 4.1 (a) and (b) show the sequence of a-Si:H and its alloy deposition for IBC-SHJ solar cell processing, including both front and back surface deposition, for PR mask and a-SiN<sub>x</sub>:H mask respectively.

PR-mask patterning process in Figure 4.1 (a) had the back surface initially passivated by stack layers composed of 8 nm i. a-Si:H capped with ~80 nm a-SiN<sub>x</sub>:H. The first photolithography defined the p strip opening where 2% HF was used to completely remove a-SiN<sub>x</sub>:H since a-Si:H cannot be etched off by HF and the p region remained hydrophobic. Lower concentration of HF (2%) was used to remove a-SiN<sub>x</sub>:H because lower concentration provides less severe etching process and therefore can better protect the photoresist film on the sample. The sample was loaded into PECVD chamber for p. a-Si:H deposition right after HF. After p. a-Si:H deposition, metallization was performed followed by lift off. Then the second photolithography was processed for n strip opening, followed by 2% HF etch to completely remove a-SiN<sub>x</sub>:H on the n strip. The 25µm gap between p. a-Si:H strip and n. a-Si:H strip are passivated by stack layers composed of i. a-Si:H and a-SiN<sub>x</sub>:H. However, no a-SiN<sub>x</sub>:H was observed under the optical microscope after removal of a-SiN<sub>x</sub>:H on n strip, which is possibly due to the high lateral etching speed of HF on a-

$\text{SiN}_x\text{:H}$ . After removing  $\text{a-SiN}_x\text{:H}$  on the n strip, n.  $\text{a-Si:H}$  was deposited, followed by metallization and then lift off, to complete the IBC-SHJ solar cell.

The new patterning process using 100 nm  $\text{a-SiN}_x\text{:H}$  as mask is shown in Figure 4.1 (b) where the back surface was initially passivated by stack layers composed of i.  $\text{a-Si:H}$  / n.  $\text{a-Si:H}$  /  $\text{a-SiN}_x\text{:H}$ . The first photolithography opened p strip, followed by  $\text{a-SiN}_x\text{:H}$  removal using 2% HF. The i.  $\text{a-Si:H}$  and n.  $\text{a-Si:H}$  under  $\text{a-SiN}_x\text{:H}$  were then etched off by HNA solution for 1 min, which is composed of 100:1  $\text{HNO}_3$  : HF. HNA can also etch of c-Si, therefore a trench was formed by HNA when the etching condition was optimized. After HNA etch, the photoresist film on the n strip was then removed in acetone. After photoresist removal, the sample was cleaned again by Piranha and 5% HF right before loading into PECVD chamber for i.  $\text{a-Si:H}$  and p.  $\text{a-Si:H}$  (emitter) deposition. The reason using 5% HF instead of 10% HF is because  $\text{a-SiN}_x\text{:H}$  here cannot be completely removed during the HF process. At least part of  $\text{a-SiN}_x\text{:H}$  is required to act as a mask for further patterning process. The second photolithography was processed for n strip opening. After n opening, HNA was used again to remove p.  $\text{a-Si:H}$  and i.  $\text{a-Si:H}$  on the n strip. The duration of HNA etching was controlled by observation of re-appearance of  $\text{a-SiN}_x\text{:H}$  color. After HNA, 2% HF was then used to completely remove  $\text{a-SiN}_x\text{:H}$  on the n strip, followed by metallization and lift off to complete the n metal contact. The third photolithography was performed for the p metal contact.

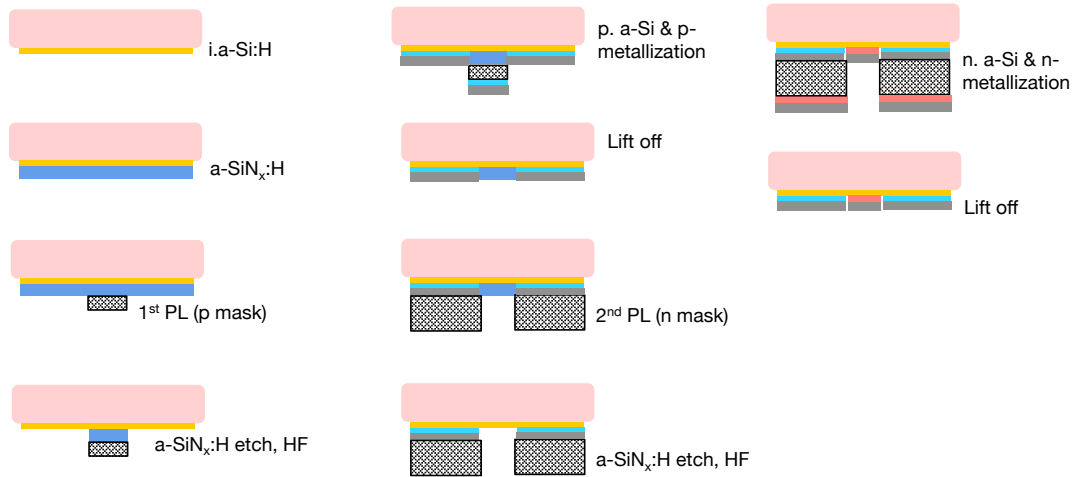


Figure 4.1 (a) Back surface patterning by PR: Process flow of back surface of IBC-SHJ solar cell using PR as a patterning mask with 2 steps photolithography

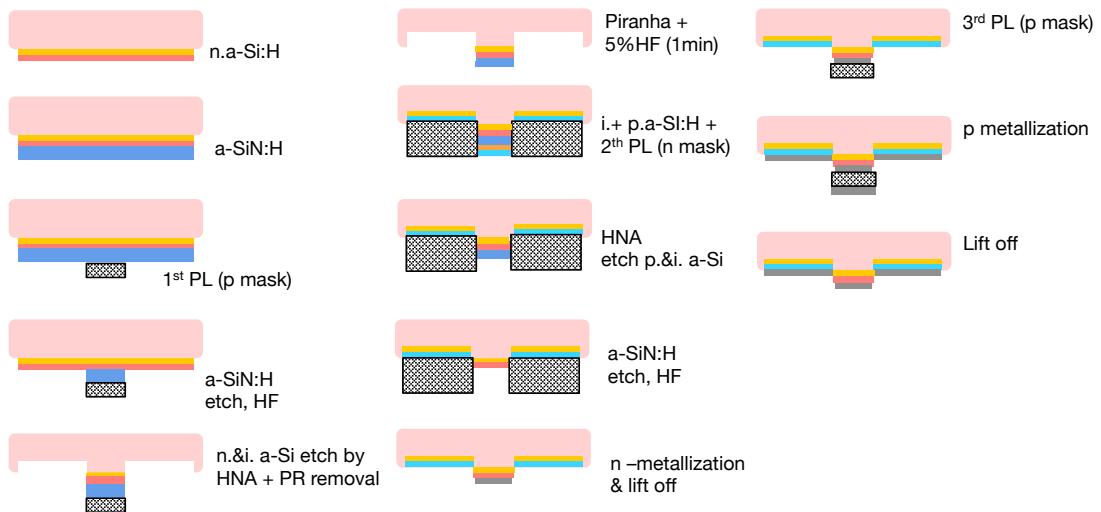


Figure 4.1 (b) Back surface patterning by a-SiN<sub>x</sub>:H: Process flow of back surface of IBC-SHJ solar cell using a-SiN<sub>x</sub>:H as a patterning mask with 3 steps photolithography

Table 4.1 (a) Back surface patterning by PR: The sequence of all a-Si:H layers and its alloy deposition, and their each deposition conditions used for IBC-SHJ solar cells, including both front and back surfaces

Sequence	Film	Temp. (°C)	Pressure (Torr)	SiH <sub>4</sub> (sccm)	H <sub>2</sub> (sccm)	Other (sccm)	Thickness (nm)
1	i-a-Si:H (front)	225	1.25	10	25	N/A	8
2	i-a-Si:H (back)	225	1.25	10	25	N/A	8
3	a-SiN <sub>x</sub> :H (back)	300	1.00	10	50	NH <sub>3</sub> -82	80
4	a-SiN <sub>x</sub> :H (front)	300	1.00	10	50	NH <sub>3</sub> -82	75
5	a-SiC <sub>x</sub> :H (front)	200	0.50	5	60	CH <sub>4</sub> -28	20
<b>Process: 1<sup>st</sup> photolithography and p region etch off</b>							
6	p-a-Si:H (back)	175	1.25	20	120	B <sub>2</sub> H <sub>6</sub> -15	20
7	n-a-Si:H (back)	175	1.25	20	120	PH <sub>3</sub> -10	30

Table 4.1 (b) Back surface patterning by a-SiN<sub>x</sub>:H: The sequence of all a-Si:H layers and its alloy deposition, and their each deposition conditions used for IBC-SHJ solar cells, including both front and back surfaces

Sequence	Film	Temp. (°C)	Pressure (Torr)	SiH <sub>4</sub> (sccm)	H <sub>2</sub> (sccm)	Other (sccm)	Thickness (nm)
1	i-a-Si:H (front)	225	1.25	10	25	N/A	8
2	i-a-Si:H (back)	225	1.25	10	25	N/A	8

3	n-a-Si:H (back)	250	1.25	20	120	PH <sub>3</sub> -10	30
4	a-SiN <sub>x</sub> :H (back)	300	1.00	10	50	NH <sub>3</sub> -30	100
5	a-SiN <sub>x</sub> :H (front)	300	1.00	10	50	NH <sub>3</sub> -82	75
6	a-SiC <sub>x</sub> :H (front)	200	0.50	5	60	CH <sub>4</sub> -28	20
<b>Process: 1<sup>st</sup> photolithography and p region etch off</b>							
7	i-a-Si:H (back)	225	1.25	20	25	N/A	8
8	p-a-Si:H (back)	200	1.25	20	120	B <sub>2</sub> H <sub>6</sub> -15	20

The emitter contact is Al and base contact is a metal stack of Ti – Sb – Al that allows an optional formation of LFC) on n-type wafers [147]. Two different patterning approaches result in different gap structures and compositions, which are schematically shown in Figure 4.2.

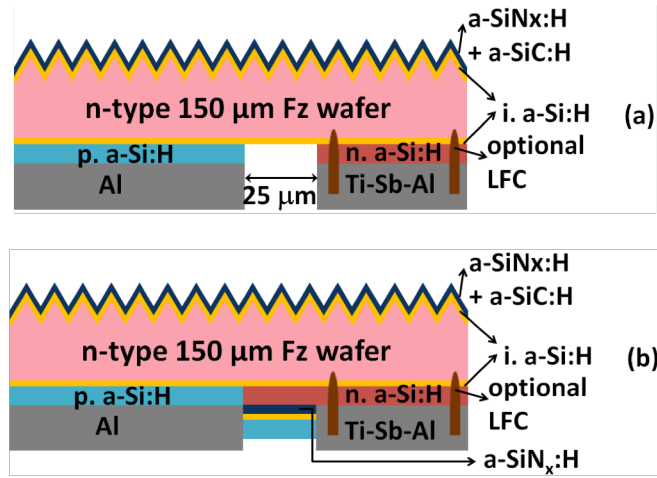


Figure 4.2 Schematic structure of IBC-SHJ solar cell using (a) PR and (b) a-SiNx:H as masks for forming the interdigitated pattern. Note that two processes lead to different gap structures.

In summary, in patterning process (a) [Figure 4.1 (a)], photoresist was used as a mask (PR mask) for interdigitated p.a-Si:H/Al and n.a-Si:H/Ti-Sb-Al strip formation using two photolithography steps [Figure 4.2 (a)]. This process leads to the presence of photoresist in the PECVD chamber at a temperature of  $\sim 175^{\circ}\text{C}$  resulting in impurity outgassing which could contaminate the bulk doped a-Si:H layers and/or the i/doped layer interfaces. Also, the deposition temperature,  $175^{\circ}\text{C}$  for p. and n. a-Si:H, is lower than our optimized temperature, which should be  $200^{\circ}\text{C}$  for p. a-Si:H and  $250^{\circ}\text{C}$  for n. a-Si:H [Table 4.2 (b)]. The slightly lower temperature of  $175^{\circ}\text{C}$  is because the photoresist cannot sustain a higher temperature of  $200^{\circ}\text{C}$ . This approach also leads to a 25 mm gap structure between each p- and n-strip that is passivated only

by the 8 nm i.a-Si:H layer. The effect of gap composition and gap passivation on device performance and stability will be further discussed later. In patterning process (b), a  $\sim 100$  nm a-SiN<sub>x</sub>:H layer was used as a mask (SiN<sub>x</sub> mask) to form an interdigitated p. a-Si:H strip and n. a-Si:H strip pattern [Figure 4.2 (b)]. Worth noting is that the back a-SiN<sub>x</sub>:H had deposition condition slightly different from the front a-SiN<sub>x</sub>:H. This is because the back a-SiN<sub>x</sub>:H needs to be more resistant to HF etch, which results a lower etching rate, for better processing control. This approach contains three photolithography steps, but avoids baking the photoresist at 150 °C - 200 °C in the PECVD chamber and therefore avoids any possible outgassing and contamination. Without the photoresist in the PECVD chamber, the optimized condition for each a-Si:H layer can be carried out. The resulting gap structure between the p- and n-strips is passivated by a 5-layer stack (i. / n. a-Si:H / a-SiN<sub>x</sub>:H / i. / p. a-Si:H) as shown in Figure 4.2(b). The thicker multilayer stack in the gap of the SiN<sub>x</sub>-mask process and clean deposition in PECVD chamber results in improved performance and stability, compared to a single thin a-Si:H layer as results from the PR-mask process.

Optional LFC, details of which are described elsewhere [147], [148], were used on the n-strip to investigate its influence on cell performance. The solar cells were tested in the dark and under AM 1.5 illumination (Please refer to Appendix A) with masks of either 2.50 or 1.57 cm<sup>2</sup> area at 25°C. The cells were stored in a desiccator in N<sub>2</sub> ambient and were tested over 6 months for stability. Occasionally, some cells were annealed at 200°C for 5 min in air ambient, which was found to be the optimum annealing condition for such IBC-SHJ cells. The LBIC line scan across the

interdigitated pattern was characterized by a position sensitive 632 nm laser beam with width of  $\sim 30$   $\mu\text{m}$ .

#### 4.4 Results and Discussions

Figure 4.3 shows the cell efficiency over time for different back surface patterning approaches of three  $2.5\text{ cm}^2$  IBC-SHJ solar cells. The IBC-SHJ solar cell fabricated with PR mask with LFC (PR / LFC) degraded  $\sim 20\%$  compared to the cells fabricated with  $\text{SiN}_x$  mask ( $\text{SiN}_x$  / LFC &  $\text{SiN}_x$ ) which only degraded by  $\sim 2 - 4\%$ . The cell using  $\text{SiN}_x$  / LFC resulted in lower efficiency, primarily due to reduced  $V_{OC}$  by  $\sim 40\text{ mV}$  compared to the cell without the LFC, but does not cause additional instability. A similar decrease in  $V_{OC}$  due to LFC has been seen in the past and is attributed to higher recombination loss at the LFC spots [145]. Therefore, the degradation of the cell with PR / LFC is believed to be due to the PR-mask patterning process rather than introduced by LFC. Heat treatments can only partially recover the PR / LFC cell efficiency, which exhibits  $\sim 9\%$  degradation (PR / LFC / HT in Figure 4.3). As shown in the structure schematic in Figure 4.2 (a), the cell with PR / LFC has the  $0.025\text{ mm}$  gap passivated by only  $8\text{ nm}$  thick i-layer, which we have shown leads to unstable passivation quality as exhibited by a decrease in  $\tau_{eff}$  over time [149]. Contamination at the i / doped a-Si:H interface in this process may occur due to the presence of PR during deposition in the PECVD chamber [150]. However, if the gap consists of a multi-layer stack structure, as is the result for the cells fabricated with  $\text{SiN}_x$  as a mask, the cell does not show any appreciable degradation due to its stable passivation quality and elimination of any interface impurities. Such stable passivation



quality has been demonstrated when the c-Si surface is passivated by a stack layer of a-Si:H, as thin as 2 nm, capped with a-SiN<sub>x</sub>:H [146].

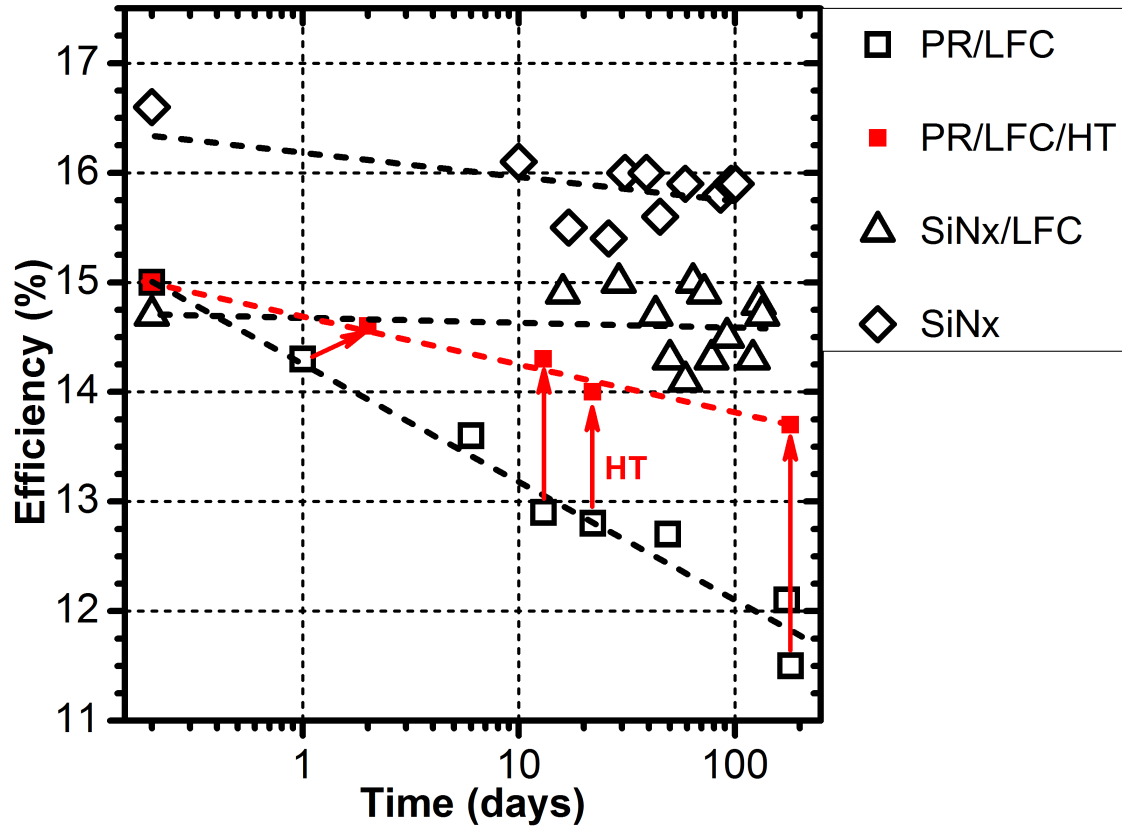


Figure 4.3 Cell efficiencies over time of 2.5 cm<sup>2</sup> IBC-SHJ solar cells fabricated with PR or SiN<sub>x</sub> as a mask. Note that two cells had an optional laser fired contact (LFC). The red arrows indicate days where the device was given 200 °C heat treatment and retested.

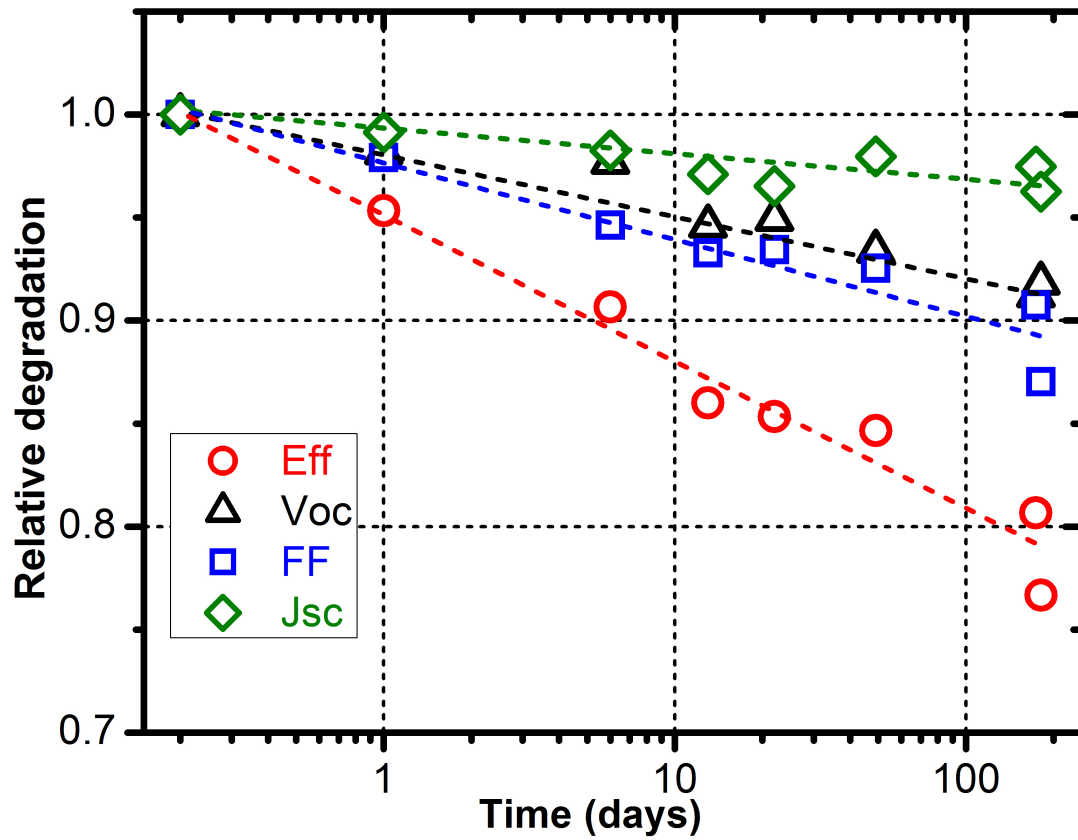


Figure 4.4 Relative cell parameter degradation for an IBC-SHJ solar cell fabricated with PR mask (PR / LFC).

In order to comprehend the performance decrease of the PR mask cell, we plotted the relative degradation of the PR / LFC cell parameters in Figure 4.4. It is clearly seen that the efficiency degrades primarily due to degradation of  $V_{OC}$  and FF, while  $J_{SC}$  drops by less than 5%.  $V_{OC}$  degradation results from poor gap passivation on the back and is in accordance with the passivation instability of the single intrinsic a-Si:H layer over time

[146], [149]. To understand the FF degradation, we have measured the LBIC line scan across the interdigitated strips with 0 V (short circuit) and maximum power point voltage ( $V_{mp}$ ) bias. The ratio of the LBIC signal at  $V_{mp}$  to 0V  $[(LBIC)_{V_{mp}} / (LBIC)_{0V}]$  is indicative of the spatial current loss at maximum power point and, thus, related to FF of the cell. Figure 4.5 shows the LBIC ratio of the three cells fabricated with PR and  $SiN_x$  mask. The PR mask cell was heat treated prior to LBIC measurement. The figure clearly shows that the  $SiN_x$  mask cell without any LFC has near uniform current collection loss, while the LFC formation on similarly processed cell ( $SiN_x$  / LFC) exhibits additional current collection loss (lateral dimension of  $\sim 100 \mu m$ ) from the n-strip presumably due to passivation damage on the LFC spots. However, the PR / LFC / HT cell suffers severe collection loss not only from the LFC spots on n-strips but also from much wider lateral regions ( $>500 \mu m$ ), which suggests a much inferior gap passivation provided by the single 8 nm i. a-Si:H layer. This confirms that the primary degradation of the PR mask cell arises from the unstable gap passivation, which leads to instability in  $V_{OC}$  and FF.

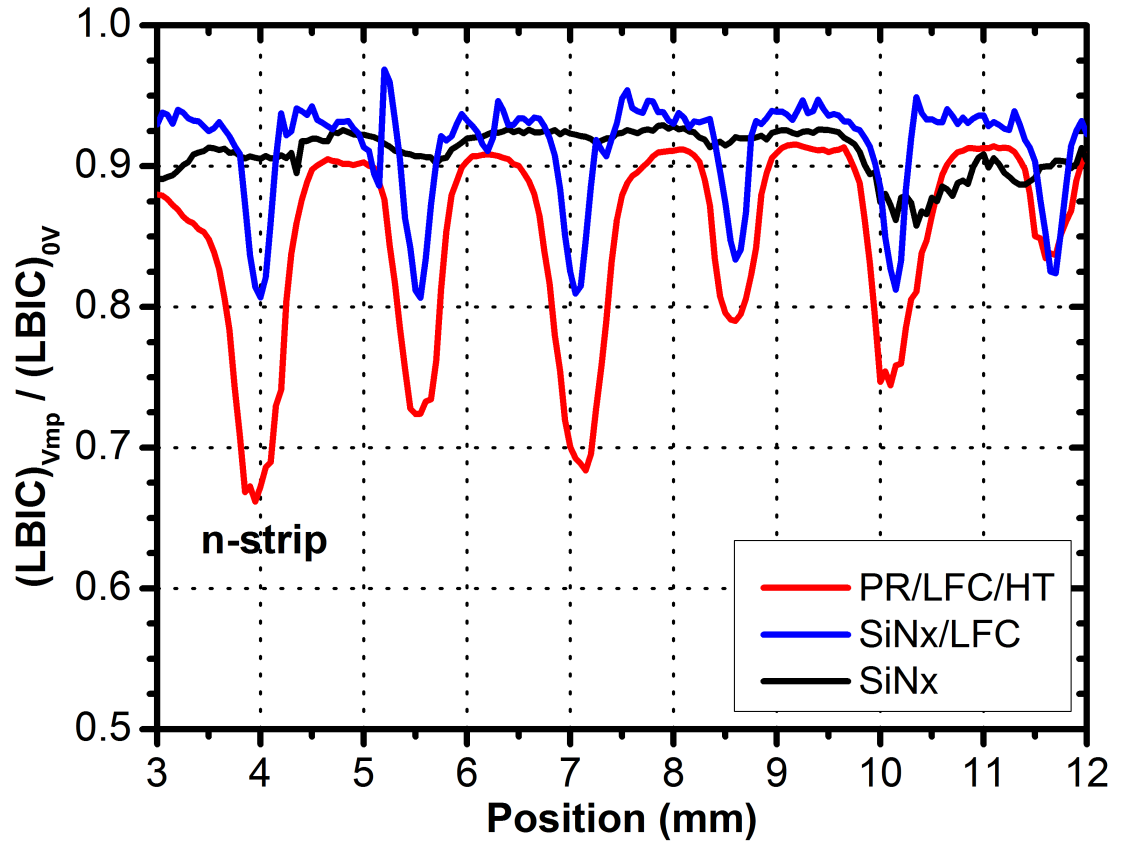


Figure 4.5 The ratio of LBIC line scan at  $V_{mp}$  to 0V biases of IBC-SHJ solar cells with three different patterning processes (PR/LFC/HT,  $\text{SiN}_x$ /LFC and  $\text{SiN}_x$ ).

Table 4.2 lists the performance parameters for this device (PR mask) in the initial, degraded (180 days storage), and post-heat treatment condition. Also shown are the series resistance ( $R_s$ ), ideality ( $n$ ), and recombination current density ( $J_0$ ) extracted from the light JV curves assuming a single diode model.  $R_s$  increases but is restored to its original value with annealing, while the parameters  $n$  and  $J_0$ , which are determined by the junction recombination, also increase but are not fully annealed to their original

values after heat treatment. The recovery of  $R_s$  indicates it is metastable, while the degradation in diode recombination ( $n$ ,  $J_0$ ) is only partially recovered with annealing. Note that  $n$  increases to 2.5, suggesting other losses in addition to standard deep defect recombination ( $n=2.0$ ). We have analyzed numerous IBC devices and find only those with the PR mask occasionally have  $n>2$  confirming that they have complex loss mechanisms beyond standard recombination. Values of  $n>2$  in Si solar cells can be attributed to various losses such as current crowding, non-uniform resistance and collection (as seen in Figure 4.5), barrier modification, or conductivity modulation. The rapidity of the partial recovery ( $< 5$  minutes annealing) and the fact that impervious metal layers cover  $>95\%$  of the rear surface implies that the gap region is responsible for the fast degradation and recovery. The LBIC characterization and detailed device analysis in Table 4.2 were performed by Dr. Ujjwal Das.

Table 4.2 Illuminated JV performance and model parameters for the cell processed with PR/LFC; Initial, degraded (180 days) and post-heat treatment. Area =  $2.5 \text{ cm}^2$ .

State	$V_{OC}$ (V)	$J_{SC}$ (mA/cm <sup>2</sup> )	FF (%)	Eff (%)	$R_s$ (Ohm-cm <sup>2</sup> )	$n$	$J_0$ (mA/cm <sup>2</sup> )
Initial	0.649	34.4	67.0	15.0	1.7	1.8	2E-04
180 days	0.595	33.2	58.4	11.5	2.2	2.5	7E-03
HT	0.630	33.1	65.4	13.7	1.7	2.0	4E-04

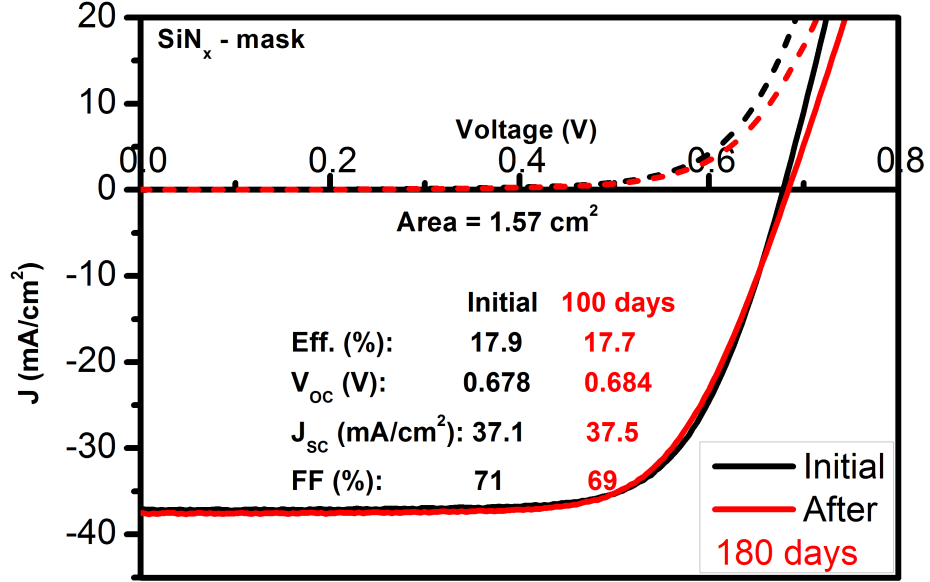


Figure 4.6 Dark and light JV curves of 1.57 cm<sup>2</sup> IBC-SHJ solar cell showing a stable efficiency of ~17.9% fabricated by SiN<sub>x</sub> mask with no LFC.

Figure 4.6 shows the J-V curve for the best stable IBC-SHJ with efficiency of 17.9% measured with an aperture area of 1.57 cm<sup>2</sup> processed using SiN<sub>x</sub> as a mask without the LFC. The device shows negligible degradation after 180 days without any heat treatment. Excellent back surface passivation by intrinsic a-Si:H capped with doped a-Si:H and a-SiN<sub>x</sub>:H is proven to provide stable  $V_{OC}$ . For comparison to the PR-masked cell of Table 4.2, this device has  $R_s=1.5$  Ohm-cm<sup>2</sup>,  $n=1.8$ , and  $J_0=3E-5$  mA/cm<sup>2</sup>. Thus, the better performance results from lower  $J_0$ , not lower  $R_s$  or a different recombination mechanism ( $n$ ). This is consistent with the assumption that the SiN<sub>x</sub>-masked cells have less contamination and less interface state defects. We note that our best front heterojunction cells have FF=77% and  $R_s=1.0$  Ohm-cm<sup>2</sup>,

suggesting that the IBC cells have additional  $R_s$ . After correcting for  $R_s$  losses, both can have similar FF ~80%.

#### **4.5 Conclusion**

Based on all the characterizations and device analysis with the newly developed back surface patterning approach using an a-SiN<sub>x</sub>:H as a mask, it is shown that the back surface patterning processes of IBC-SHJ solar cells are critical not only for initial solar cell performance but also its stability over time, even in the absence of any illumination. When the gap between p- and n-strips is passivated by a single thin i. a-Si:H layer, the initial performance is reduced and degradation over time is increased due to the insufficient and unstable passivation quality. An improved patterning approach was developed in my work utilizing a-SiN<sub>x</sub>:H as a PR mask for the PECVD process of interdigitated doped layers which resulted in a well passivated gap structure comprised of thin intrinsic a-Si:H capped by doped a-Si:H and a-SiN<sub>x</sub>:H layers. A stable efficiency of 17.9% was achieved for a cell aperture area of 1.57 cm<sup>2</sup>. Additionally, our group achieved a 20.2% IBC-SHJ device utilizing this process describe above.

## Chapter 5

### DIFFERENT FRONT STACK LAYER PASSIVATION FOR APPLICATION IN IBC-SHJ SOLAR CELLS

#### 5.1 Summary

The effect of  $n^+$  phosphorous diffusion layer forming front surface field (FSF) on the IBC-SHJ solar cells to improve surface passivation and FF by increased lateral current transport has been evaluated jointly with professor Buonassisi's group at MIT. MIT performed  $n^+$  phosphorus diffusion on the c-Si wafers cleaned and supplied by us, and we performed Si HJ solar cell fabrication, device measurements and analysis. Four sets of c-Si wafers evaluated where the front surface was passivated by either: 1) i. a-Si:H; 2)  $n^+$  diffusion / i. a-Si:H; 3) i. a-Si:H / n. a-Si:H; and 4) n. a-Si:H. Although  $n^+$  diffusion sample showed slightly better surface passivation, the front surface passivated by only i. a-Si:H exhibited the highest efficiency of 20.2% with FF~75%, comparing to efficiency of 19.6% and similar FF by  $n^+$  FSF sample. Front surface passivated by i. a-Si:H capped with n. a-Si:H for FSF didn't exhibit any improvement from n. a-Si:H; instead, light absorption loss caused by n. a-Si:H reduces the device  $J_{sc}$ . Front surface passivated by only n. a-Si:H is insufficient and therefore caused poor  $\tau_{eff}$  and device  $V_{oc}$ . The solar cell with front surface passivated by this under-optimized n. a-Si:H showed efficiency only 15.4%. No measureable difference of series resistance ( $R_s$ ) analyzed from J-V data among these four front surface structures, suggesting that  $R_s$  was not reduced by the FSF developed in this project.



## 5.2 Introduction

The effect of front surface field, FSF, on n-type c-Si back-contact back-junction solar cells has become a critical topic for enhancing the device performance where FSF provides improvements in front surface passivation level [151]-[153], lateral carrier transport, and therefore the  $R_s$  loss [154]-[156]. For c-Si solar cell, which is typically fabricated on wafers that are  $> 100$  microns, most of the carriers are generated within a few micrometers of the front surface [157]. Thus, the front surface passivation level becomes important since electrons and holes need to be able to reach the back surface and be collected by either the base or the emitter. The FSF induces an accumulation layer which forms high-low junction  $n^+np^+$  structure [158], [159], enhancing carrier separation, and hence improving the front surface passivation quality, which can be characterized through  $\tau_{eff}$ .

Additionally, the FSF enhances the lateral carrier transport [155], [156], where the lateral carrier transport is the main resistance loss mechanism reducing the device performance with increased  $R_s$  and decreased fill factor FF. The idea of using FSF with its higher conductivity to enhance the carrier lateral transport on back-junction back-contact Si solar cell can be understood in Figure 5.1 [155].

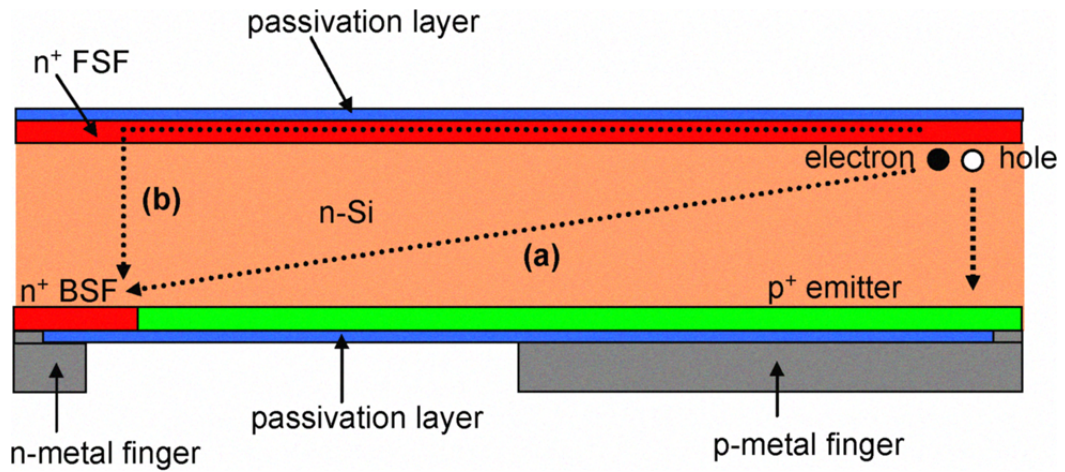


Figure 5.1 Schematic drawing of the effect of the enhanced lateral current transport of the majority carriers via the front surface field (FSF). The lateral current transport through the FSF (b) can be seen as an additional transport path to the base lateral resistance (a). Reprinted from Ref. [155], with Copyright 2008 IEEE. (IEEE does not require individuals working on a thesis to obtain a formal reuse license.)

For the back-junction back-contact c-Si solar cell, the emitter coverage on the rear surface needs to be as high as possible [160] to reduce the required diffusion path for the light-generated minority carrier to reach the p-n junction and be collected by the emitter contact. However, the increased emitter coverage on the rear surface means the reduction of the base coverage. The high emitter fraction makes the majority carriers transport laterally to a larger distance to reach the base contact, where the resistance loss from the base material (c-Si wafer) becomes more significant to increase the device  $R_s$  with reduced FF, and therefore lower its performance. As seen in Figure 5.1, when a highly-doped  $n^+$  FSF is present, the lateral transport of the electrons (majority carriers) can be enhanced via route (b) due to the higher

conductivity of FSF, reducing the  $R_s$  loss caused by the base material c-Si wafer and thus improving the FF when comparing to route (a). The contribution of FSF will be more significant in the case of high resistivity wafer or larger lateral distance [156].

## 5.3 Experimental

### 5.3.1 Wafer Cleaning and Preparation

The back surface patterning and structure of IBC-SHJ solar cells discussed in this chapter are all the same as discussed in chapter 4, using a-SiN<sub>x</sub>:H as the patterning mask. 145  $\mu$ m SunPower Cz texturing wafers with resistivity 8-10  $\Omega$ cm were used to study the effect of different front stack layers on IBC-SHJ solar cells performance. Samples without n<sup>+</sup> phosphorus diffusion (bare wafer) were cleaned using the following steps: 1) solvent cleaning with ultrasonic agitation to remove all the dust and grease due to sample handling and transferring; 2) piranha oxidation in a mixture of H<sub>2</sub>SO<sub>4</sub> and H<sub>2</sub>O<sub>2</sub> (3:1) to remove hydrocarbon; 3) 10% HF to remove surface oxide; 4) 20sec HNA (acid mixture of HF: HNO<sub>3</sub> = 1 : 100) etch back.

For samples with n<sup>+</sup> phosphorus diffusion, the wafers were sent to MIT for phosphorus diffusion, which is commonly used to form FSF in PV industry and laboratory and then followed by the wafer cleaning and etching processes at IEC [161], [162]. The first part of cleaning after diffusion is the same as “no diffusion sample”, including step one to step four. After all these cleaning steps, the samples had piranha oxidation followed by 10% HF right before a-SiN<sub>x</sub>:H deposition to protect one side of n<sup>+</sup> diffused surface. With well-protected n<sup>+</sup> diffused front surface,

the back  $n^+$  diffused surface was completely etched off and slightly polished by 22% TMAH at 90°C, followed by 5min of 10% HF to remove the front surface a-SiN<sub>x</sub>:H.

Before depositing intrinsic & doped a-Si:H, a-SiN<sub>x</sub>:H, and a-SiC:H by PECVD, all the wafers were again cleaned by 5 min piranha oxidation and 1 min 10% HF forming H-terminated surface, including both with  $n^+$  diffusion wafer and without  $n^+$  diffusion wafer. Four sets of front surface stack layers were discussed through passivation quality and IBC-SHJ solar cell analysis to evaluate the contribution of FSF forming by either  $n^+$  phosphorous diffusion or n. a-Si:H deposition. The four different front stack layers include 1) i. a-Si:H; 2)  $n^+$  diffusion / i. a-Si:H; 3) i. a-Si:H / n. a-Si:H; and 4) n. a-Si:H.

### 5.3.2 Front Stack: i. a-Si:H / a-SiN<sub>x</sub>:H / a-SiC:H (control sample)

Table 5.1 The sequence of all a-Si:H layers and its alloy deposition, and their each deposition conditions used for IBC-SHJ solar cells with their front stack layers i. a-Si:H / a-SiN<sub>x</sub>:H / a-SiC:H

Sequence	Film	Temp. (°C)	Pressure (Torr)	SiH <sub>4</sub> (sccm)	H <sub>2</sub> (sccm)	Other (sccm)	Thickness (nm)
1	i.a-Si:H (front)	225	1.25	10	25	N/A	8
2	i.a-Si:H (back)	225	1.25	10	25	N/A	8
3	n.a-Si:H (back)	250	1.25	20	120	PH <sub>3</sub> -10	30
4	a-SiN <sub>x</sub> :H (back)	300	1.00	10	50	NH <sub>3</sub> -30	170
5	a-SiN <sub>x</sub> :H (front)	300	1.00	10	50	NH <sub>3</sub> -82	75

6	a-SiC <sub>x</sub> :H (front)	200	0.50	5	60	CH <sub>4</sub> -28	20
<b>Process: 1<sup>st</sup> photolithography and p region etch off</b>							
7	i-a-Si:H (back)	225	1.25	20	25	N/A	8
8	p-a-Si:H (back)	200	1.25	20	120	B <sub>2</sub> H <sub>6</sub> -15	20

### 5.3.3 Front Stack: n<sup>+</sup> diffusion / i. a-Si:H (8nm) / a-SiN<sub>x</sub>:H / a-SiC:H

Table 5.2 The sequence of all a-Si:H layers and its alloy deposition, and their each deposition conditions used for IBC-SHJ solar cells with their front stack layers n<sup>+</sup> diffusion / i. a-Si:H / a-SiN<sub>x</sub>:H / a-SiC:H

Sequence	Film	Temp. (°C)	Pressure (Torr)	SiH <sub>4</sub> (sccm)	H <sub>2</sub> (sccm)	Other (sccm)	Thickness (nm)
1	i.a-Si:H (front)	225	1.25	10	25	N/A	8
2	i.a-Si:H (back)	225	1.25	10	25	N/A	8
3	n.a-Si:H (back)	250	1.25	20	120	PH <sub>3</sub> -10	30
4	a-SiN <sub>x</sub> :H (back)	300	1.00	10	50	NH <sub>3</sub> -30	170
5	a-SiN <sub>x</sub> :H (front)	300	1.00	10	50	NH <sub>3</sub> -82	75
6	a-SiC <sub>x</sub> :H (front)	200	0.50	5	60	CH <sub>4</sub> -28	20
<b>Process: 1<sup>st</sup> photolithography and p region etch off</b>							
7	i-a-Si:H (back)	225	1.25	20	25	N/A	8
8	p-a-Si:H (back)	200	1.25	20	120	B <sub>2</sub> H <sub>6</sub> -15	20

#### 5.3.4 Front Stack: i. a-Si:H (8nm) / n. a-Si:H (20nm) / a-SiN<sub>x</sub>:H / a-SiC:H

Table 5.3 The sequence of all a-Si:H layers and its alloy deposition, and their each deposition conditions used for IBC-SHJ solar cells with their front stack layers i. a-Si:H / n. a-Si:H / a-SiN<sub>x</sub>:H / a-SiC:H

Sequence	Film	Temp. (°C)	Pressure (Torr)	SiH <sub>4</sub> (sccm)	H <sub>2</sub> (sccm)	Other (sccm)	Thickness (nm)
1	i.a-Si:H (front)	225	1.25	10	25	N/A	8
2	n.a-Si:H (front)	250	1.25	20	120	PH <sub>3</sub> -10	20
3	i.a-Si:H (back)	225	1.25	10	25	N/A	8
4	n.a-Si:H (back)	250	1.25	20	120	PH <sub>3</sub> -10	30
5	a-SiN <sub>x</sub> :H (back)	300	1.00	10	50	NH <sub>3</sub> -30	170
6	a-SiN <sub>x</sub> :H (front)	300	1.00	10	50	NH <sub>3</sub> -82	75
7	a-SiC <sub>x</sub> :H (front)	200	0.50	5	60	CH <sub>4</sub> -28	20
<b>Process: 1<sup>st</sup> photolithography and p region etch off</b>							
8	i.a-Si:H (back)	225	1.25	10	25	N/A	8
9	p-a-Si:H (back)	200	1.25	20	120	B <sub>2</sub> H <sub>6</sub> -15	20

### 5.3.5 Front Stack: n. a-Si:H (40nm) / a-SiN<sub>x</sub>:H / a-SiC:H

Table 5.4 The sequence of all a-Si:H layers and its alloy deposition, and their each deposition conditions used for IBC-SHJ solar cells with their front stack layers n. a-Si:H / a-SiN<sub>x</sub>:H / a-SiC:H

Sequence	Film	Temp. (°C)	Pressure (Torr)	SiH <sub>4</sub> (sccm)	H <sub>2</sub> (sccm)	Other (sccm)	Thickness (nm)
1	n.a-Si:H (front)	250	1.25	20	120	PH <sub>3</sub> -10	40
2	i.a-Si:H (back)	225	1.25	10	25	N/A	8
3	n.a-Si:H (back)	250	1.25	20	120	PH <sub>3</sub> -10	30
4	a-SiN <sub>x</sub> :H (back)	300	1.00	10	50	NH <sub>3</sub> -30	170
5	a-SiN <sub>x</sub> :H (front)	300	1.00	10	50	NH <sub>3</sub> -82	75
6	a-SiC <sub>x</sub> :H (front)	200	0.50	5	60	CH <sub>4</sub> -28	20
<b>Process: 1<sup>st</sup> photolithography and p region etch off</b>							
7	i.a-Si:H (back)	225	1.25	10	25	N/A	8
8	p-a-Si:H (back)	200	1.25	20	120	B <sub>2</sub> H <sub>6</sub> -15	20

## 5.4 Results and Discussion

### 5.4.1 Stack Layer Passivation Level

The purpose of having FSF is to improve the front surface passivation, and device performance attributed to reduced  $R_s$  loss and therefore improved FF. Table 5.5 showed the  $\tau_{eff}$  of stack layer passivation, including both front and back surfaces

passivation (Table 5.1 to Table 5.4). From Table 5.5 it is found that only n. a-Si:H sample got insufficient surface passivation, and other three front structures provided very decent passivation level.  $N^+$  diffusion sample showed slightly higher  $\tau_{\text{eff}}$ , which might be contributed by the effect of FSF. Front surface passivation by 20 nm of n. a-Si:H on top of i. a-Si:H didn't show better passivation level, which may indicate that the condition of n. a-Si:H used in this work is under optimized and could not provide the effect of FSF.

Table 5.5  $\tau_{\text{eff}}$  of stack layer passivation, comparing between different front stack layers.

Front stack layers	$\tau_{\text{eff}}$ ( $\mu\text{sec}$ )	SRV (cm/sec)
i. a-Si:H / a-SiN <sub>x</sub> :H / a-SiC:H	3365	2.2
$N^+$ diff / i. a-Si:H / a-SiN <sub>x</sub> :H / a-SiC:H	4420	1.6
i. a-Si:H / n. a-Si:H / a-SiN <sub>x</sub> :H / a-SiC:H	1995	3.6
n. a-Si:H / a-SiN <sub>x</sub> :H / a-SiC:H	650	11.2

#### 5.4.2 J-V and QE Measurements and Analysis

IBC-SHJ solar cells were fabricated based on four different front stack layers discussed in chapter 5.3. Solar cell performances are shown in Figure 5.2 and Table 5.6.



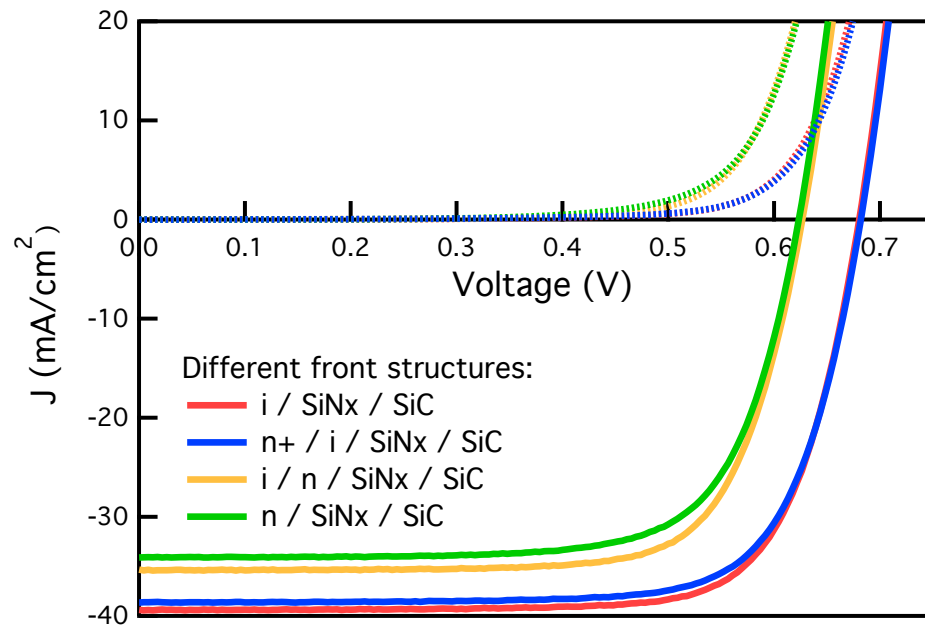


Figure 5.2: IBC-SHJ solar cell performances by J-V curves of four different front structures. Cell area  $1.61 \text{ cm}^2$

Table 5.6: IBC-SHJ solar cell performances including parameters  $V_{OC}$ ,  $J_{SC}$ , FF, and Efficiency ( $\eta$ ). Cell area  $1.61 \text{ cm}^2$

Front structure	$V_{OC}$ (V)	$J_{SC}$ (mA / $\text{cm}^2$ )	FF (%)	$R_s$ (ohm- $\text{cm}^2$ )	$\eta$ (%)
i (8 nm) / $\text{SiN}_x$ / SiC	0.680	39.4	75.2	0.3	20.2
$n^+$ diff/ i (8 nm) / $\text{SiN}_x$ / SiC	0.682	38.6	74.5	0.3	19.6
i (8 nm) / n (20 nm) / $\text{SiN}_x$ / SiC	0.627	35.4	74.0	0.4	16.4
n (40 nm) / $\text{SiN}_x$ / SiC	0.623	34.1	72.3	0.2	15.4

From the IBC-SHJ solar cell performance with different front structure, it is found that standard cell structure with front surface: i. a-Si:H (8 nm) / a-SiN<sub>x</sub>:H / a-

SiC showed the highest efficiency 20.2%. The  $n^+$ -diffused layer for the FSF processed at MIT was expected to reduce  $R_s$  and therefore improve FF due to better lateral transport; however no any expected improvement was observed. The lower  $J_{SC}$  of IBC-SHJ solar cell with front surface layer: i (8 nm) / n (20 nm) /  $SiN_x$  / SiC had  $J_{SC}$  of only  $35.4 \text{ mA/cm}^2$ , which is most likely due to more absorption loss caused by n. a-Si:H on the front surface. Single n. a-Si:H is not sufficient for high level surface passivation, which can be seen on the cell performance only 15.4%, with all the parameters  $V_{OC}$ ,  $J_{SC}$ , and FF are relatively lower.

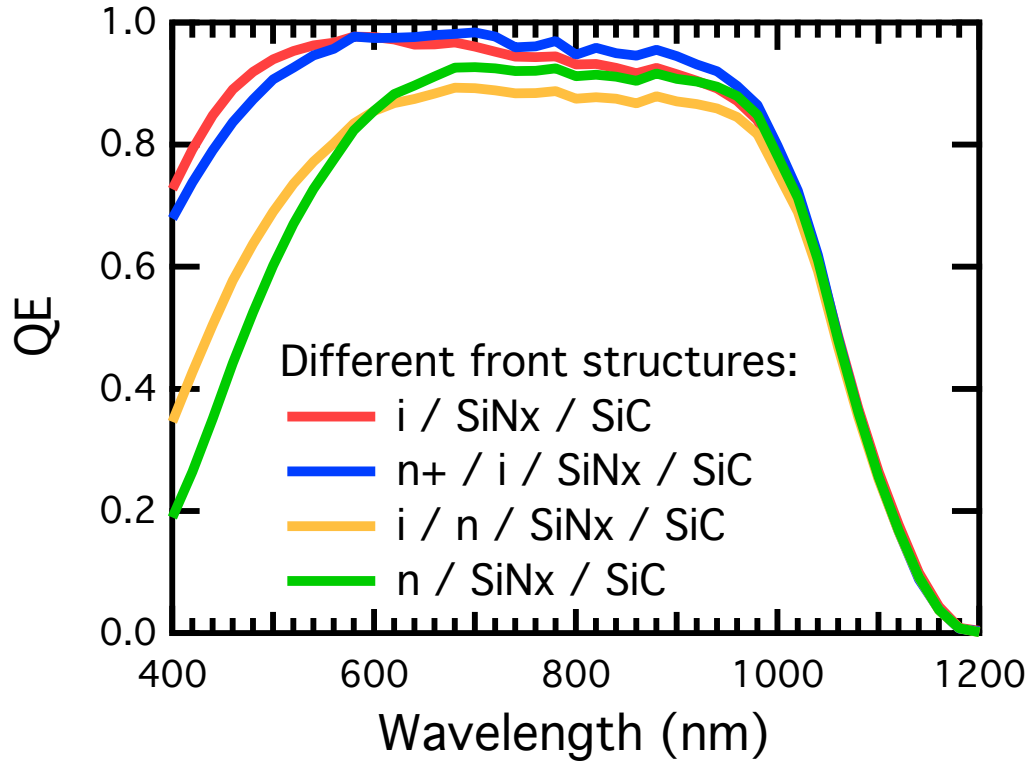


Figure 5.3: QE of SHJ-IBC solar cells with different front structures

QE measurements provide a better understanding of the current loss on each sample. The cell with i (8 nm) / n (20 nm) / SiN<sub>x</sub> / SiC had poor blue response because of absorption loss mainly in the 20 nm n. a-Si:H layer. The cell with n (40 nm) / SiN<sub>x</sub> / SiC also had poor blue response due to insufficient front surface passivation and absorption loss by single n. a-Si:H layer. Phosphorous-diffused n<sup>+</sup> for FSF did not give a measureable difference from J-V and QE measurements.

No significant improvement attributed to FSF was observed may suggest that the conditions of phosphorous-diffused n<sup>+</sup> and n. a-Si:H are under optimized and need further study. Besides this, some discussions in the literatures can be learned to explain our observations. As shown in Figure 5.4, the simulations in PC1D exhibits the influence of the front surface recombination velocity ( $SRV_{front}$ ) on the performance of back-junction back-contact n-type c-Si solar cell, with and without FSF[155]. Comparing to the one without FSF, the existence of FSF has the device efficiency reach the same high level in a very wide range of  $SRV_{front}$ , which makes the contribution of FSF more effective at poor surface passivation level. No significant difference of device efficiency is shown between with and without FSF when the  $SRV_{front}$  is about below 10 cm/sec, which is also the range that the four samples being studied in our work shown in Table 5.5, with the assumption that front and back surface passivation level are identical ( $SRV_{front} = SRV_{back}$ ).

Thus, the application of the FSF enables a high solar cell efficiency especially for unsatisfied surface passivation quality, where the FSF makes cell performance insensitive to the SRV up to 5000 cm/sec [158]. This characteristic of the FSF makes it more important for the manufacturing of the high-efficiency solar cells in industrial

processing environment, where the perfect surface passivation with low SRV is more difficult to reach than in a laboratory environment. This might be one of the reasons to explain the results we obtained in our project.

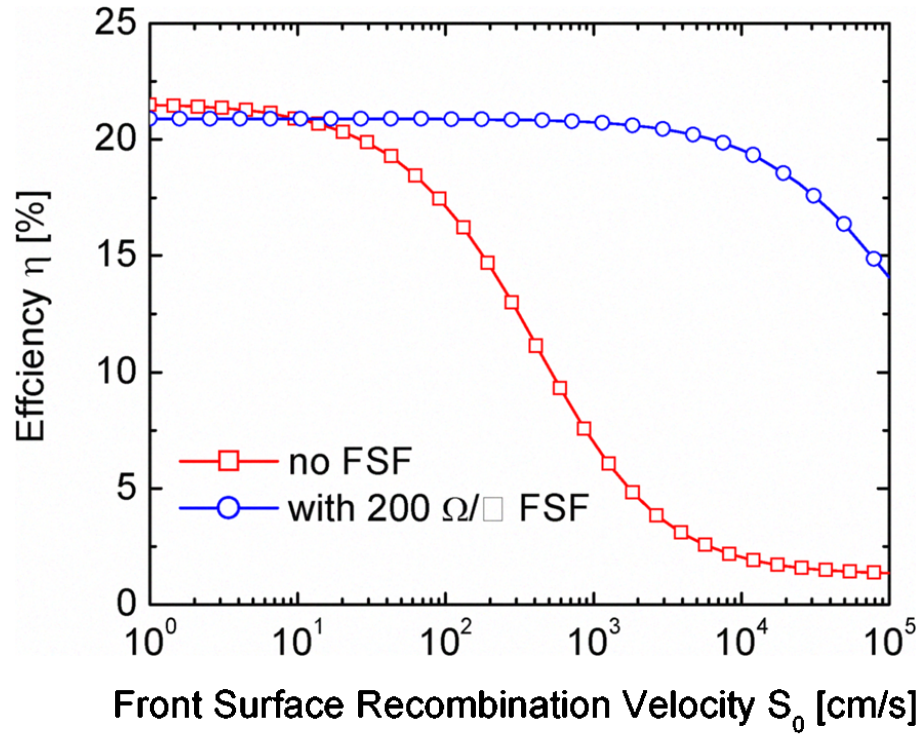


Figure 5.4 PC1D simulations [163] of the influence of the front surface recombination velocity on the efficiency of back-junction back-contact n type c-Si solar cells with and without the FSF. Device structure shown in Figure 5.6. Reprinted from Ref. [155], with Copyright 2008 IEEE. (IEEE does not require individuals working on a thesis to obtain a formal reuse license.)

Another thing can be learned is the effect of base material resistivity and pitch dimension on FSF contribution, where the definition of pitch can be seen on Figure

5.5 [155]. The device structure shown in Figure 5.5 was used for further simulations and discussions presented in Figure 5.6 about the influence of base material resistivity and pitch dimension on device performances, for the cases with and without FSF [155]. The improvement provided by FSF was found more significant with a higher resistivity c-Si wafer and larger pitch size, as seen in Figure 5.6. A higher resistivity wafer makes more  $R_s$  loss in route (b) in Figure 5.1 and hence large reduction of  $R_s$  loss can be found with the lateral carrier transport via route (a), with a more conductive FSF. Figure 5.6 indicated that the impact of the FSF on the FF [Figure 5.6 (a)] and the  $R_s$  loss [Figure 5.6 (b)] is more pronounced for the device with 8  $\Omega\text{cm}$  of wafer resistivity comparing to 1  $\Omega\text{cm}$  of wafer resistivity.

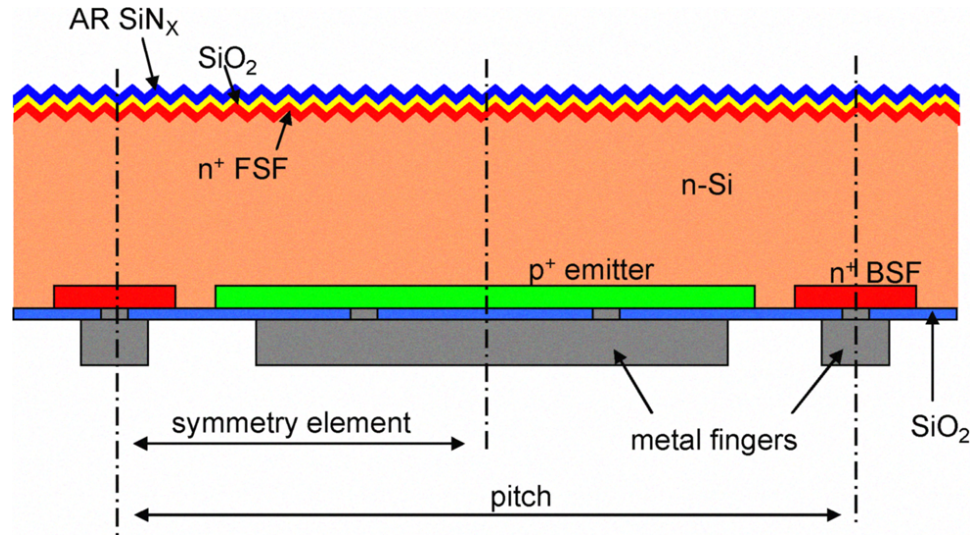
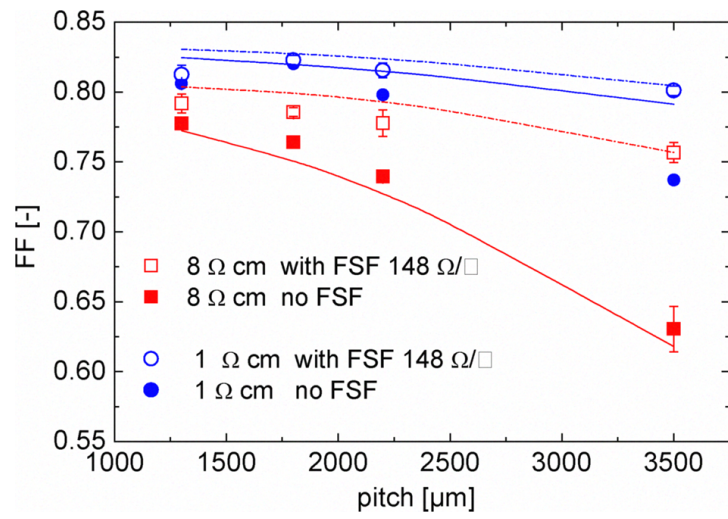
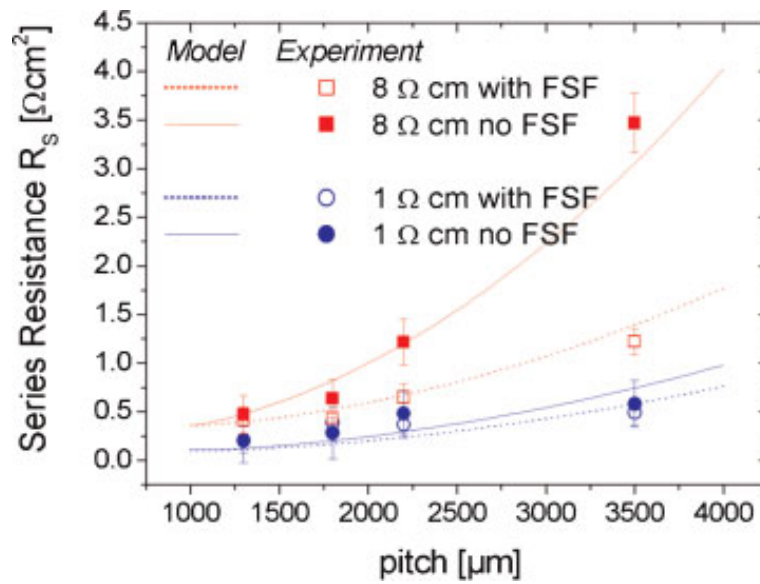


Figure 5.5 Schematic cross-section of the n-type back-junction back-contact Si solar cell. Reprinted from Ref. [155], with Copyright 2008 IEEE. (IEEE does not require individuals working on a thesis to obtain a formal reuse license)



(a)



(b)

Figure 5.6 Two-dimensional numerical simulations and measured values of the (a) FF & (b) series resistance on the back-junction back-contact Si solar cells as a function of the pitch size for two different base material c-Si wafer resistivities reveal the effect of FSF. (a) Reprinted from Ref. [155], Copyright 2008 IEEE. (b) Reprinted from Ref. [156], with Copyright 2008 John Wiley and Sons. (IEEE does not require individuals working on a thesis to obtain a formal reuse license)

Not only wafer resistivity, pitch dimension is another factor where the effect of FSF to enhance lateral current transport is stronger for larger pitches, since the base lateral resistance dominates the resistance loss of the device and the larger pitch size makes longer carrier transport distance. With a larger pitch size, the  $R_s$  increased and therefore the FF decreased due to the increase of lateral resistance in the base material. The pitch size of the IBC-SHJ solar cell in our work is 850  $\mu\text{m}$ , therefore the reduction of  $R_s$  and improvement of FF with FSF contributed by enhanced lateral carrier transport in our IBC-SHJ solar cell may not be obvious according to the simulation and experimental results presented in Figure 5.6.

## 5.5 Conclusion

In this work, three different FSF structures have been studied to improve surface passivation and device performance, mainly focusing on the improvement of lateral carrier transport and therefore FF by the reduction of  $R_s$ . These three front structures are: 1)  $n^+$  diffusion /  $\text{SiNx}$  /  $\text{SiC}$ ; 2)  $i$  (8nm) /  $n$  (20nm) /  $\text{SiNx}$  /  $\text{SiC}$ ; 3)  $n$  (40nm) /  $\text{SiNx}$  /  $\text{SiC}$ , which were all compared to standard structure  $i$  (8nm) /  $\text{SiNx}$  /  $\text{SiC}$ . However, no any significant improvements have been identified using these three FSF studies, although the  $n^+$  - diffused sample showed higher  $\tau_{\text{eff}}$  after the deposition of all stack layers (Table 5.5). The best cell performance of 20.2% in our work has the standard front structure  $i$  (8nm) /  $\text{SiNx}$  /  $\text{SiC}$ . The original surface passivation level before FSF, the wafer resistivity, and the pitch size are all possible factors influencing the magnitude of FSF effect on device performance that we need to consider in our experiments. Moreover, the front structures using  $n$ .  $a\text{-Si:H}$  had lower  $J_{\text{SC}}$ , and the loss

of  $J_{SC}$  was due to lower blue response caused by the absorption loss and insufficient surface passivation.



## Chapter 6

### SURFACE DEFECT PASSIVATION AND REACTION OF C-SI IN H<sub>2</sub>S

The contents of this dissertation chapter have been adapted from a manuscript published in *Langmuir*: **H.Y. Liu**, U. Das, R. Birkmire, “Surface Defect Passivation and Reaction of c-Si in H<sub>2</sub>S” *Langmuir*, vol. 33, no. 51, pp. 14580–14585, Dec. 2017. Copyright 2017 American Chemical Society. Reprint permission is granted for individuals working on a thesis / dissertation.

#### 6.1 Summary

A unique passivation process of Si surface dangling bonds through reaction with H<sub>2</sub>S is demonstrated and presented in this chapter. The passivation level of  $\tau_{\text{eff}} > 2000$   $\mu\text{sec}$  corresponding to a SRV of  $< 3$  cm/sec was achieved over a temperature range of 550 – 650 °C using H<sub>2</sub>S treatment. XPS confirmed the bonding states of Si and S, and provided insights to the reaction pathway of Si with H<sub>2</sub>S and other impurity elements both during and after the reaction. Quantitative analysis of XPS spectra showed that the  $\tau_{\text{eff}}$  increases with an increase in surface S content up to  $\sim 3.5\%$  and stabilizes thereafter, which is indicative of surface passivation by mono-layer coverage of S on the Si surface. However, S passivation of the Si surface is highly unstable due to thermodynamically favorable reaction with atmospheric H<sub>2</sub>O and O<sub>2</sub>. This

instability was eliminated by capping the S-passivated Si surface with a protective thin film such as low temperature deposited a-SiN<sub>x</sub>:H.

## 6.2 Introduction

The trend of the PV industry is towards thinner c-Si wafers and higher solar cell efficiency, which makes the passivation of the c-Si surface an extremely critical issue [37]. Excellent surface passivation quality with low SRV below 10 cm/sec has been achieved by primarily by two distinct mechanisms: 1) reduction of surface dangling bonds using either SiO<sub>2</sub> or a-Si:H, and 2) inducing a surface field to repel one type of carrier from the surface using either Al<sub>2</sub>O<sub>3</sub>, or a-SiN<sub>x</sub>:H.

SiO<sub>2</sub> passivation is the most popular and widely accepted method and is achieved by dry oxidation at temperature ~1050 °C or by wet oxidation at lower temperature ~850 °C where the oxygen reacts with Si surface reducing the number of dangling bonds [40], [164], [165]. a-SiN<sub>x</sub>:H passivation is performed at temperature ~450 °C using PECVD, which not only passivates the surface but also acts as a front surface anti-reflection coating [166], [167]. The passivation using a-SiN<sub>x</sub>:H is attributed to the presence of positive fixed charge, making it suitable for n-type c-Si [82], [167]. Al<sub>2</sub>O<sub>3</sub>, which is commonly processed by ALD, also passivates the Si surface by field effect where a negative fixed charge is formed and is appropriate for passivation of p-type c-Si [72], [168]-[170]. The thin, below 10 nm layer of i. a-Si:H deposited by PECVD at low temperature (< 250 °C) provides excellent surface passivation in a-Si/c-Si HJ cell but cannot withstand downstream process temperatures higher than 300 °C [62], [171], [172]. Additionally, efficient light absorption in the a-Si:H introduces optical loss when used as a front surface passivation layer [24].

The theoretical calculation reported by Kaxiras [173] indicated that group VI chalcogen elements, S and Se, can act as proper valence mending adsorbates for Si surface restoration. Several experimental studies have reported the possibility of using a monolayer of S to terminate Si dangling bonds and restore Si (100) surface by S residing at the bridge position of Si-Si, which were mainly characterized by low energy electron diffraction and Auger electron spectroscopy [174]-[177]. Ali et al [178] have evaluated the potential of S to reduce Si surface defects using S-containing chemicals in a mixture of ammonium hydroxide and ammonium sulfide. The ammonium hydroxide removes silicon oxide in-situ from the Si surface exposing a clean Si (100) surface, which is then passivated by ammonium sulfide. The reduction of surface defect states was evaluated by forming Schottky barriers contacts, which were characterized by current-voltage, capacitance-voltage, and activation energy [179]. Zhang [180] later published similar approaches using S for n-type and p-type Si (100) surface passivation through chemical vapor deposition at 750 °C using H<sub>2</sub>, HCl, and H<sub>2</sub>S gas mixture. A similar characterization strategy was used in Zhang's work, where metals were deposited on S-passivated Si surface for Schottky barrier height characterization. The Schottky barriers exhibited a higher sensitivity to the work function due to reduced Si surface states. However, there is no direct experimental evidence that demonstrates the effectiveness of S passivation for c-Si where  $\tau_{\text{eff}}$  and SRV were measured.

In this chapter, the c-Si surface is passivated by the reaction with H<sub>2</sub>S as a precursor gas at a temperature range of 550 - 650 °C. The  $\tau_{\text{eff}}$  and SRV were used to evaluate surface passivation quality and XPS was performed to determine the Si

surface bonding states before and after reaction. Additionally, the stability of S-passivated Si surface is also discussed.

### 6.3 Experimental

150  $\mu\text{m}$  8-10  $\Omega\cdot\text{cm}$  n-type Cz Si (100) wafers with both planar and textured surfaces were used to evaluate the sulfur passivation. Prior to  $\text{H}_2\text{S}$  reaction, the wafer surfaces were cleaned and prepared using the following steps: 1) Solvent with ultrasonic agitation; 2) 5 min in a mixture of  $\text{H}_2\text{SO}_4$  :  $\text{H}_2\text{O}_2$  (3:1) to remove hydrocarbon; 3) Oxide removal in 10% HF; 4) Surface etching by reaction in HNA, a mixture of HF and  $\text{HNO}_3$  (1:100); 5) formation of H-terminated surface by immersion in a 10% solution of HF for 1 min.

The reaction was performed in a custom-built quartz tube (5 cm diameter) CVD reactor using  $\text{H}_2\text{S}$  gas with 99.5% purity (Table 6.3). The primary impurities in  $\text{H}_2\text{S}$  source gas consist of: nitrogen, water vapor, and hydrocarbon. The concentration of  $\text{H}_2\text{S}$  was controlled by dilution in argon (Ar). A heating jacket surrounding the quartz tube controlled the reaction temperature. A sheathed K-type thermocouple was used for temperature monitoring and was positioned inside the tube, under the sample holder. The Si wafers were held vertically on a graphite holder so that both surfaces of the wafer were passivated simultaneously in  $\text{H}_2\text{S}$  reaction.

The Si wafers were loaded into the reactor immediately after the HF dip, and the system was pumped down to below  $10^{-6}$  Torr. The reactor was filled with  $\text{H}_2\text{S}/\text{Ar}$  gas to 525 Torr at room temperature. The temperature of the quartz tube reactor was then ramped up in 30 min to the set point for temperatures ranging from 450 to 650  $^{\circ}\text{C}$  and the wafers were reacted for 30 to 240 min. The system was then cooled down in

the H<sub>2</sub>S/Ar to 250 °C, followed by purging in Ar flow to cool the reactor to room temperature before unloading.

The Si surface passivation quality was characterized by measuring  $\tau_{\text{eff}}$  using the photoconductance decay (PCD) method where all values of  $\tau_{\text{eff}}$  are reported at minority carrier density of  $10^{15} \text{ cm}^{-3}$ . The SRV was then calculated from Equation (6.1) using the measured  $\tau_{\text{eff}}$ . The  $1/\tau_b$  term was neglected in the calculation since bulk lifetime,  $\tau_b$  is much larger than the surface lifetime,  $\tau_s$  due to the high quality of the c-Si wafer. The  $1/\tau_s$  term was approximated as  $2S/W$  where  $S$  is the SRV and  $W$  is the wafer thickness.

$$\frac{1}{\tau_{\text{eff}}} = \frac{1}{\tau_b} + \frac{1}{\tau_s} \cong \frac{2S}{W} \quad (6.1)$$

To evaluate the Si surface composition, the surface chemical states were characterized using XPS to measure the binding energy using Al K- $\alpha$  monochromatic source at 1486.6 eV with a spot size of 100  $\mu\text{m}$  and a takeoff angle of 90°. The samples were transferred in a vacuum-sealed vessel without exposing the sample to air from H<sub>2</sub>S reactor to XPS instrument. Sequential Ar<sup>+</sup> ion sputtering was used for profiling, where the ion gun beam voltage used was 1 keV with a sputter raster size of 1×1 mm. The average etch rate was calculated from the depth measurement by atomic-force microscopy (AFM) and the sputtering depth was thereafter estimated from etch rate for any duration of sputtering. Wide surveys and regional fine scans were used for elemental and chemical state identification, where all deconvolution and fitting of measured data were processed in CasaXPS [130] using general forms of Gaussian and Lorentzian line shapes (GL), with a standard Shirley background

subtraction. For quantification of each element on the analyzed area, relative concentrations of the various constituents were presented, which had 100% representing the sum of all the detected elements, and the concentration of each element was determined by the fraction of its peak areas corrected by relative sensitivity factor [128], [181].

## **6.4 Results and Discussion**

### **6.4.1 Effect of Reaction Temperature on $\tau_{\text{eff}}$**

The change in  $\tau_{\text{eff}}$  of planar and textured c-Si measured after reaction in  $\text{H}_2\text{S}$  at temperatures from 450 to 650 °C for 30 min are shown in Figure 6.1, measured in the initial state, immediately after reaction. The  $\tau_{\text{eff}}$  is consistently lower for the textured wafers most likely due to the greater exposed surface area. However, both follow similar trends reaching a maximum  $\tau_{\text{eff}}$  of  $\sim 2000$   $\mu\text{sec}$  for the planar and  $\sim 1300$   $\mu\text{sec}$  for the textured with SRV of 3.2 cm/sec and 5.4 cm/sec respectively. These passivation levels are comparable to those we typically achieved with 10 nm of i. a-Si:H using similar wafers and surface cleaning [146]. The SRV values are also comparable to the SRV reported by others using a-SiN<sub>x</sub>:H [82], [167], AlO<sub>x</sub> [169], [182]-[184], and SiO<sub>2</sub> [40], [164], [185].

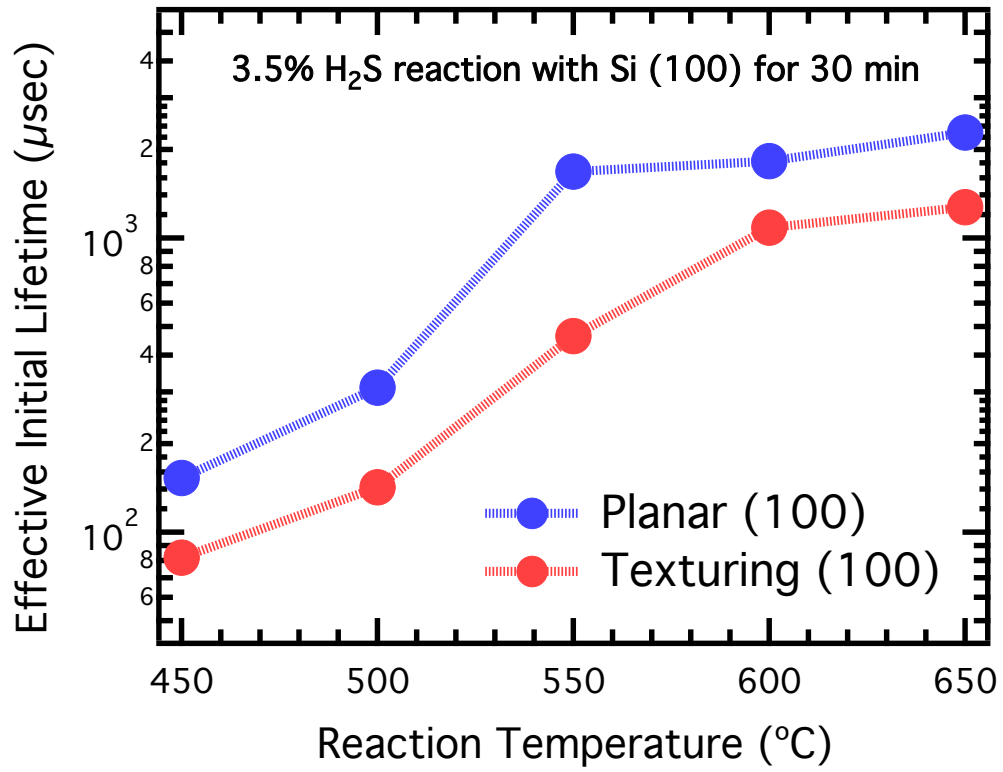


Figure 6.1 Initial  $\tau_{\text{eff}}$  at minority carrier density of  $10^{15} \text{ cm}^{-3}$  on planar and textured Si (100) wafers right after reaction with 3.5%  $\text{H}_2\text{S}$  diluted in Ar at different temperatures for 30 min.

#### 6.4.2 Surface Bonding States

The Si 2p, S 2p, and O 1s regions of XPS spectra of the c-Si surface after cleaning, after annealing in Ar at 550°C, and after reaction in  $\text{H}_2\text{S}$  at 550°C are shown in Figure 5.2. Bonding states associated with Si, S, and O were identified.

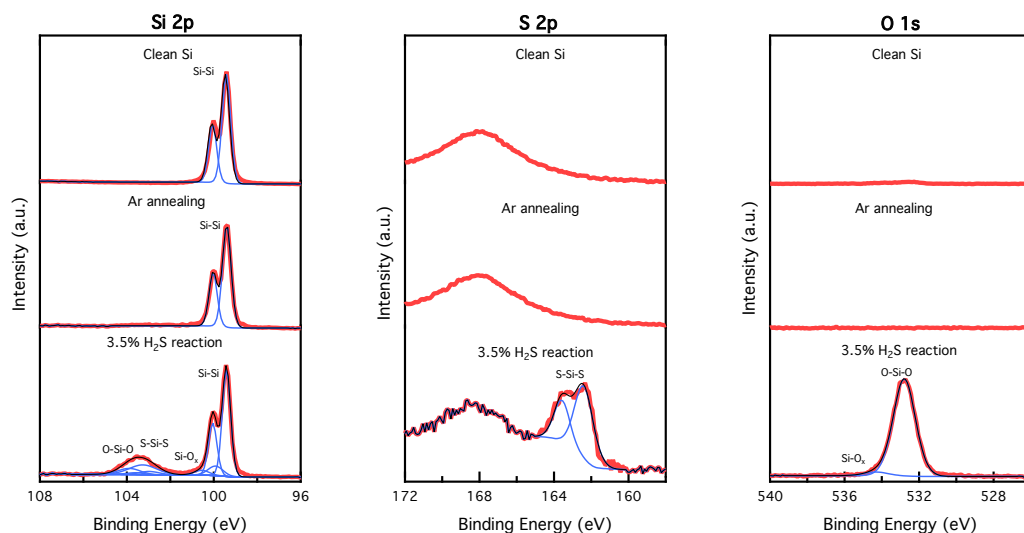


Figure 6.2 XPS measurements for three elements detected on the surface: Si, S, and O for three Si surfaces; (i) clean Si (top row), (ii) clean Si reacted in 100% Ar at 550°C for 30 min (middle row), and (iii) clean Si reacted in 3.5% H<sub>2</sub>S diluted in Ar at 550°C for 30 min (bottom row). Red, blue, and black lines represent measured XPS data, deconvoluted spectra and composite spectra respectively.

For the clean c-Si wafer with a H-terminated surface only the Si-Si 2p bonding states at 99.4 eV were observed [128], [186], verifying the “cleanliness” of Si surface. H-terminated clean Si surface was annealed in Ar at 550°C for 30 min using the same reaction parameters as H<sub>2</sub>S reaction in Ar dilution. Only the Si-Si 2p chemical states were detected in the XPS scan, verifying the “cleanliness” of Si surface and ensuring that the surface did not change upon annealing in Ar atmosphere.

After the reaction of the c-Si wafer with a H-terminated surface with H<sub>2</sub>S at 550 °C for 30 min, multiple peaks in Si 2p spectrum were observed. In addition to Si-Si peaks at 99.4 eV [128], [186], other peaks corresponding to SiO<sub>x</sub> [187], SiO<sub>2</sub> [186], and SiS<sub>2</sub> [188] were identified. SiS<sub>2</sub> peaks have binding energy only 0.3 eV lower than



SiO<sub>2</sub> peaks in Si 2p spectrum, making peak deconvolution challenging. However, the corresponding bonding state of SiS<sub>2</sub> is observed in the S 2p spectrum with binding energy of 162.4 eV [189]. Additionally, in O 1s spectrum, two bonding states of O to Si were observed for SiO<sub>2</sub> and SiO<sub>x</sub> [190], which are expected since these two chemical states were concurrent with those identified in Si 2p spectrum. The observed O on Si surface implied the existence of oxygen source in the reaction system.

To determine whether the passivation was controlled by S or by O, a Si wafer with the cleaning process discussed above was annealed in 4% O<sub>2</sub> in Ar at a temperature and time same as the H<sub>2</sub>S reaction (550 °C, 30 min). XPS spectra in Figure 6.3 show the presence of O at the Si surface in both H<sub>2</sub>S reacted and O<sub>2</sub>/Ar reacted samples, and not surprisingly, no S peak is observed for the O<sub>2</sub>/Ar reacted sample. The results of the XPS quantitative analysis along with the measured  $\tau_{\text{eff}}$  are summarized in Table 6.1, demonstrating that S originating from the H<sub>2</sub>S reaction is required for Si surface passivation, achieving  $\tau_{\text{eff}} \sim 1500 \mu\text{sec}$ . No surface passivation was contributed by O<sub>2</sub> / Ar annealing although an adequate amount of surface oxide was formed. The existence of S-Si-S bonding state can also be confirmed by comparing the full width at half maximum (FWHM) of measurement peaks at 103~104 eV in Si spectra. In Figure 6.3, the measured S-Si-S / O-Si-O peak in Si spectrum from H<sub>2</sub>S reaction sample had FWHM 1.72, compared to the measured O-Si-O peak in Si spectrum from O<sub>2</sub> / Ar annealing sample had FWHM 1.45. Larger FWHM from H<sub>2</sub>S reaction sample indicated the presence of additional bonding states.

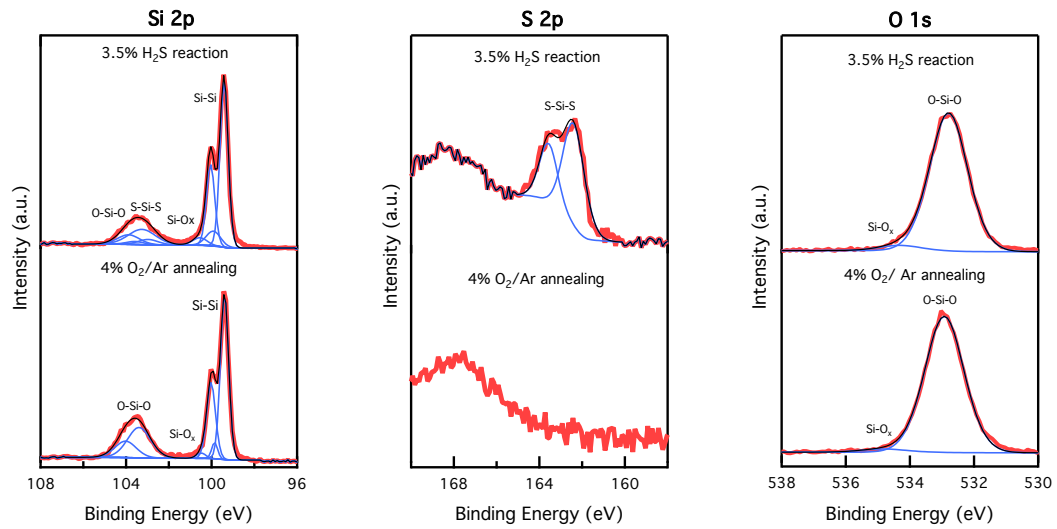


Figure 6.3 The comparison of Si surface by XPS measurements on Si wafers reacted in 3.5% H<sub>2</sub>S/Ar and 4% O<sub>2</sub>/Ar at 550°C for 30 min. Red, blue, and black lines represent measured XPS data, deconvoluted spectra and composite spectra respectively.

Table 6.1 XPS analysis of each component on Si surface and the passivation level after process indicates no passivation effect after O<sub>2</sub>/Ar annealing.

Process	Si%	S%	O%	$\tau_{\text{eff}}(\mu\text{sec})$
3.5% H <sub>2</sub> S/Ar	68.0	4.6	27.4	1497
4% O <sub>2</sub> /Ar	52.9	0.0	47.1	4

### 6.4.3 Origin of Oxygen

To identify the origin of oxygen, a series of experiments were performed. The XPS spectra in Figure 6.2 for clean Si sample and Ar annealing sample indicated the

cleanliness of c-Si surface and the vacuum level of the chamber is able to maintain the initial status of c-Si surface without forming any oxide upon Ar annealing. Further, to realize the possible source of oxygen, experiments with different temperature, time, and H<sub>2</sub>S% in Ar dilution. The concentrations of three elements Si, S, and O in each reaction run are listed in Table 6.2.

Table 6.2 Concentration of Si, S, and O on c-Si surface after H<sub>2</sub>S reactions, studies include different temperature, duration, and H<sub>2</sub>S concentration.

Temperature	Time	H <sub>2</sub> S%	XPS		
			Si	S	O
550 °C	0.5 hr	100%	57.3%	2.5%	40.2%
600 °C	0.5 hr	100%	48.8%	1.7%	49.5%
550 °C	0.5 hr	26%	60.0%	5.7%	34.3%
550 °C	2 hr	100%	21.1%	0.6%	78.3%
550 °C	4 hr	100%	19.9%	~0%	80.1%
550 °C	17 hr	100%	17.7%	0%	82.3%

From Table 6.2 it is clear shown that the higher reaction temperature, longer reaction duration, and higher H<sub>2</sub>S% (100% means without Ar dilution) resulted in higher concentration of O. These observations indicated that oxidation happened during the reaction, instead of before or after the reaction. Higher reaction temperature made oxidation more active. Longer reaction duration forming more oxide on the surface suggested that more and more O replaced S which is originally bonded to Si over time. H<sub>2</sub>S reaction without any Ar dilution caused more oxide on the surface. All these may indicate O in the reaction system came from H<sub>2</sub>S cylinder, which is highly possibly from the impurity in the cylinder. This conclusion is consistent with what has

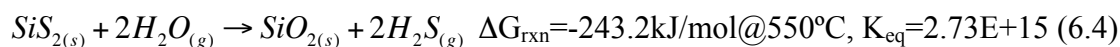
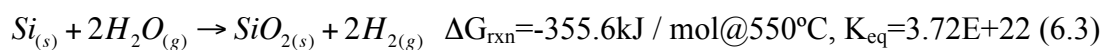
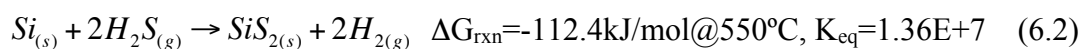
been found from the comparison between H<sub>2</sub>S reacted wafer and O<sub>2</sub> annealed wafer. The XPS spectra of H<sub>2</sub>S reacted wafer and O<sub>2</sub> annealed wafer also suggested that the impurities in the H<sub>2</sub>S are likely the origin of the oxide. The certificate of analyses in Table 6.3 for the H<sub>2</sub>S source gas indicated as much as 500 ppm of water vapor (H<sub>2</sub>O<sub>(g)</sub>) is present, which cannot be safely and completely eliminated.

Table 6.3 Certificate of Analyses showed impurity level in H<sub>2</sub>S cylinder

N <sub>2</sub>	H <sub>2</sub> O	CO <sub>2</sub>	THC
< 500 ppm	< 500 ppm	< 500 ppm	< 3000 ppm

#### 6.4.4 Reaction Pathways for Si Surface Passivation

The possible reactions of the c-Si surface with H<sub>2</sub>S were evaluated as equilibrium reactions to provide relative estimates of the Gibbs free energies,  $\Delta G_{\text{rxn}}$ , calculated at 550 °C for Equations 6.2 – 6.4:

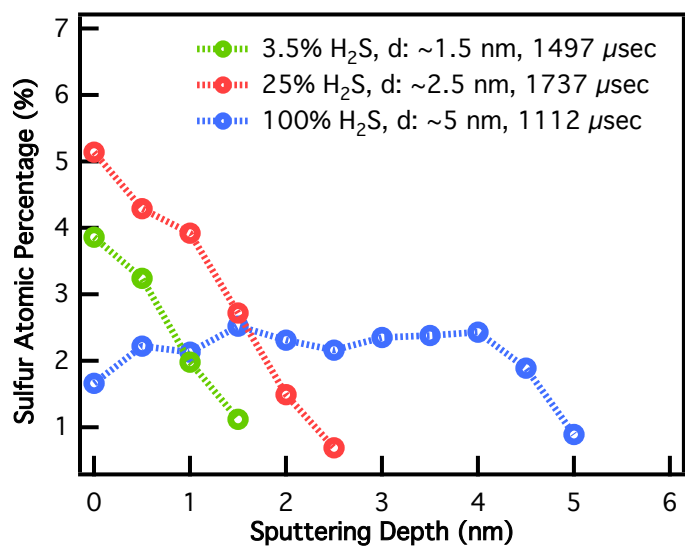


On the basis of the Gibbs free energy of reaction, both the H<sub>2</sub>S<sub>(g)</sub> and H<sub>2</sub>O<sub>(g)</sub> are thermodynamically favored to react with Si, where a negative  $\Delta G_{\text{rxn}}$  is indicative of favorable reaction kinetics. Further, the product, SiS<sub>2(s)</sub>, from the reaction between Si

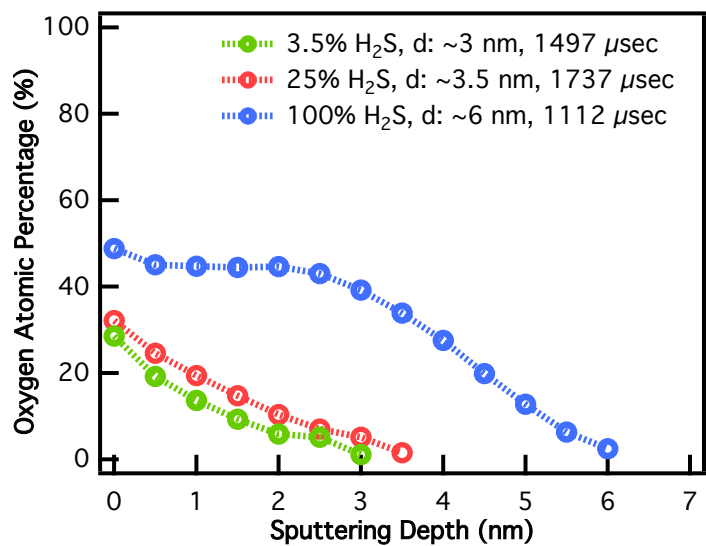
and  $\text{H}_2\text{S}_{(\text{g})}$  can easily be oxidized in presence of any  $\text{H}_2\text{O}_{(\text{g})}$  in the reactor [Equation 6.4]. As the reaction proceeds, the Si surface is converted to  $\text{SiS}_{2(\text{s})}$  and  $\text{SiO}_{2(\text{s})}$  following reactions 6.2 and 6.3. The reaction between  $\text{SiS}_{2(\text{s})}$  and  $\text{H}_2\text{O}_{(\text{g})}$  continues until all the  $\text{SiS}_{2(\text{s})}$  is converted to  $\text{SiO}_{2(\text{s})}$ . Thus even the small concentration of  $\text{H}_2\text{O}_{(\text{g})}$  in the source  $\text{H}_2\text{S}_{(\text{g})}$  ( $< 500$  ppm) can lead to much higher concentration of O at the Si surface as detected in the XPS spectra.

#### **6.4.5 Effect of Sulfur, Oxygen, and Hydrogen on Passivation Level**

Figure 6.4 shows the XPS concentration profiles for S and O obtained by sequential  $\text{Ar}^+$  ion sputtering for c-Si wafers reacted at  $550^\circ\text{C}$  for 30 min using different  $\text{H}_2\text{S}$  concentration in Ar. The  $\tau_{\text{eff}}$  evaluated immediately after the reaction is also included in the figure representing the initial passivation level along with the estimated thickness,  $d$ , of the Si-S layer.



(a)

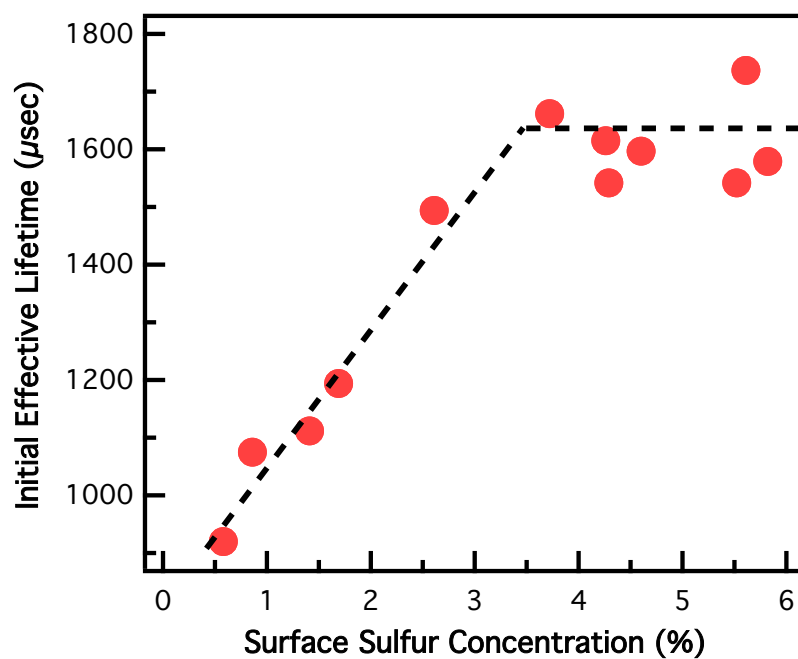


(b)

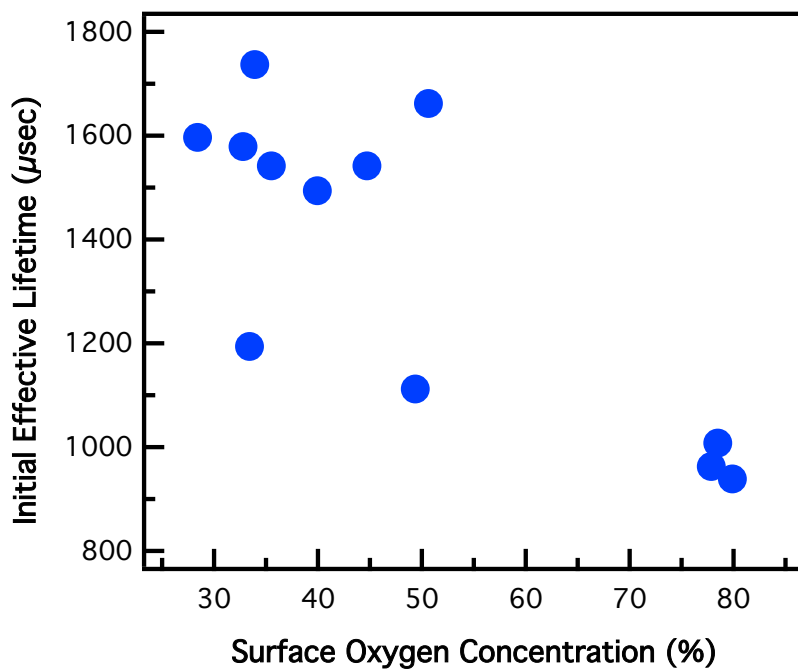
Figure 6.4 S and O depth profiles determined from XPS characterization with sequential Ar sputtering for the samples reacted at 550°C for 30 min in different H<sub>2</sub>S concentration in Ar. Measured initial  $\tau_{\text{eff}}$  and d values are listed in the legend.

The reaction with 25% H<sub>2</sub>S has the highest S concentration at the surfaces ~5.5% while the wafer reacted with 100% H<sub>2</sub>S had below 2% of S on Si surface. The lower S concentration in 100% compared to 25% H<sub>2</sub>S results from 1) the reaction of H<sub>2</sub>O<sub>(g)</sub> directly with the Si surface to form SiO<sub>2(s)</sub>, which has a  $\Delta G$  of -355.6 kJ/mol with an equilibrium constant  $> 10^{22}$  [Equation 6.3] and 2) the H<sub>2</sub>S reacts with Si to form SiS<sub>2(s)</sub>, which then reacts with H<sub>2</sub>O<sub>(g)</sub> to form SiO<sub>2(s)</sub> [Equations 6.2 and 6.4]. Thus, there were competing reactions occurring during the 30 min reactions that are dependent on the H<sub>2</sub>S concentration. Sequential Ar<sup>+</sup> ion sputtering showed that the depth of S in Si is thicker for the reaction with 100% H<sub>2</sub>S, ~5 nm, compared to the depth of ~1.5 nm for 3.5% H<sub>2</sub>S and ~2.5 nm for 25% H<sub>2</sub>S reactions. The O depth profiles were nearly identical for the wafers reacted in 3.5% and 25% H<sub>2</sub>S, where the estimated depth, *d*, were 3 and 3.5 nm respectively. The depth of the O for the 100% H<sub>2</sub>S reaction was ~6 nm compared to the sulfur depth of ~5 nm.

No correlation between  $\tau_{\text{eff}}$  and surface O% was found in Figure 6.4 (b), indicating that the O% does not play a significant role in the surface passivation. Further, there is a correlation between  $\tau_{\text{eff}}$  and surface S% for the different H<sub>2</sub>S reaction concentrations in Figure 6.4 (a), where a higher concentration of S at the surface results in an increase in  $\tau_{\text{eff}}$ , indicating a better surface passivation quality. A definitive relationship between surface S% and  $\tau_{\text{eff}}$  was found for the samples reacted at different reaction conditions including temperatures, times, and H<sub>2</sub>S concentrations, and the results are shown in Figure 6.5 (a). However, no similar correlation between surface O% and  $\tau_{\text{eff}}$  in Figure 6.5 (b) can be found from the same batch of samples reacted at different temperatures, times, and H<sub>2</sub>S concentrations.



(a)



(b)



Figure 6.5 The variation of initial  $\tau_{\text{eff}}$  with the surface S% (a) / O% (b) estimated from XPS. The S% / O% was varied by  $\text{H}_2\text{S}$  reactions at different temperatures, times, and concentrations.

Hydrogen arising from dissociation of  $\text{H}_2\text{S}$  can also potentially passivate Si surface, which cannot be detected by XPS. Therefore, Figure 6.6 showed FTIR measurements of the  $\text{H}_2\text{S}$  reacted samples were carried out in a  $\text{N}_2$  purged spectrometer, but no Si-H<sub>x</sub> bonding peaks were detected, which would be at 2000~2200  $\text{cm}^{-1}$ . The absence of any Si-H<sub>x</sub> bond is likely due to the reaction temperature of  $> 450^\circ\text{C}$ , at which H is known to desorb out from Si lattice [189], [191]. It also has been reported that the reaction of  $\text{H}_2\text{S}$  with Si at the temperature range  $525^\circ\text{C}\sim 625^\circ\text{C}$  leads to  $\text{H}_2$  desorption accompanied by diffusion of S into Si crystal [192]. The range of IR absorption peaks of  $\text{SiS}_2$  has the highest possibility between 800  $\text{cm}^{-1}$  and 1200  $\text{cm}^{-1}$ , which is correspondent with our observation in the FTIR work [193].

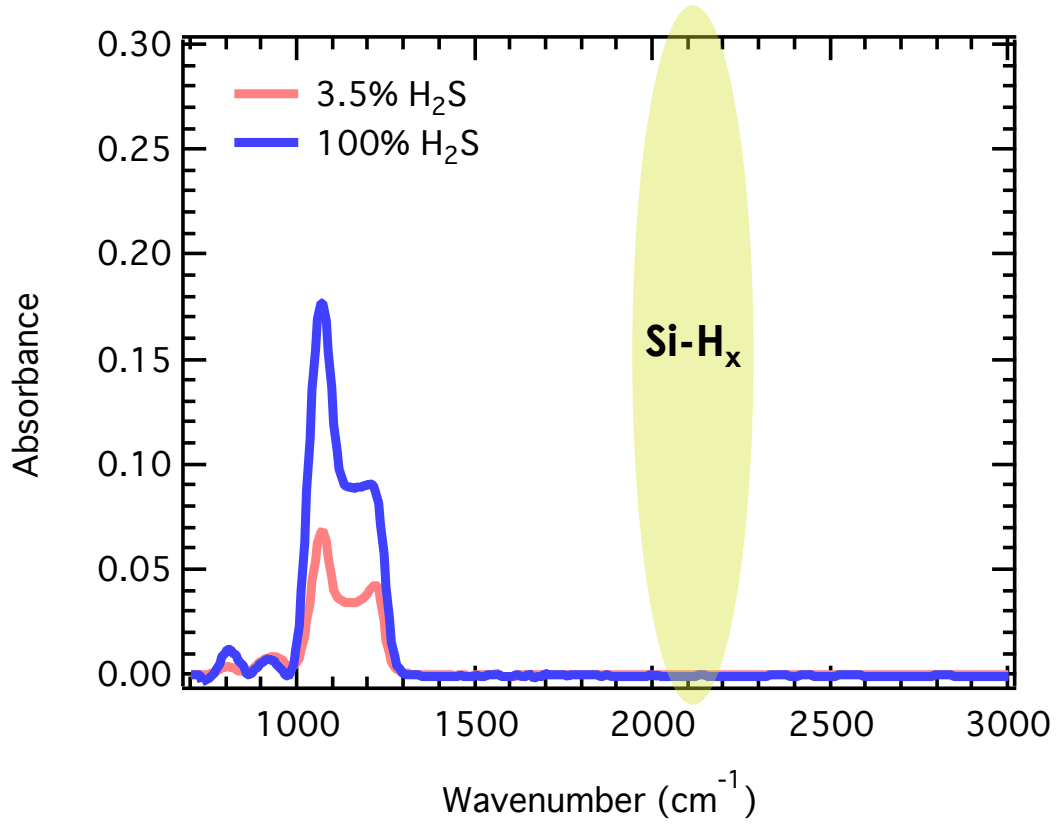


Figure 6.6. FTIR observation of H<sub>2</sub>S-reacted Si sample, demonstrating no Si-H<sub>x</sub> on the reacted Si surface contributing to surface passivation.

#### 6.4.6 Degradation and Stability of Surface Passivation

The stability of SiS<sub>2</sub> passivation layer was evaluated for c-Si wafers after exposure in air for extended periods of time and Figure 6.7 shows the change in  $\tau_{\text{eff}}$  after the air exposure. It is clearly seen that the  $\tau_{\text{eff}}$  of S-passivated Si degrades appreciably by air exposure.

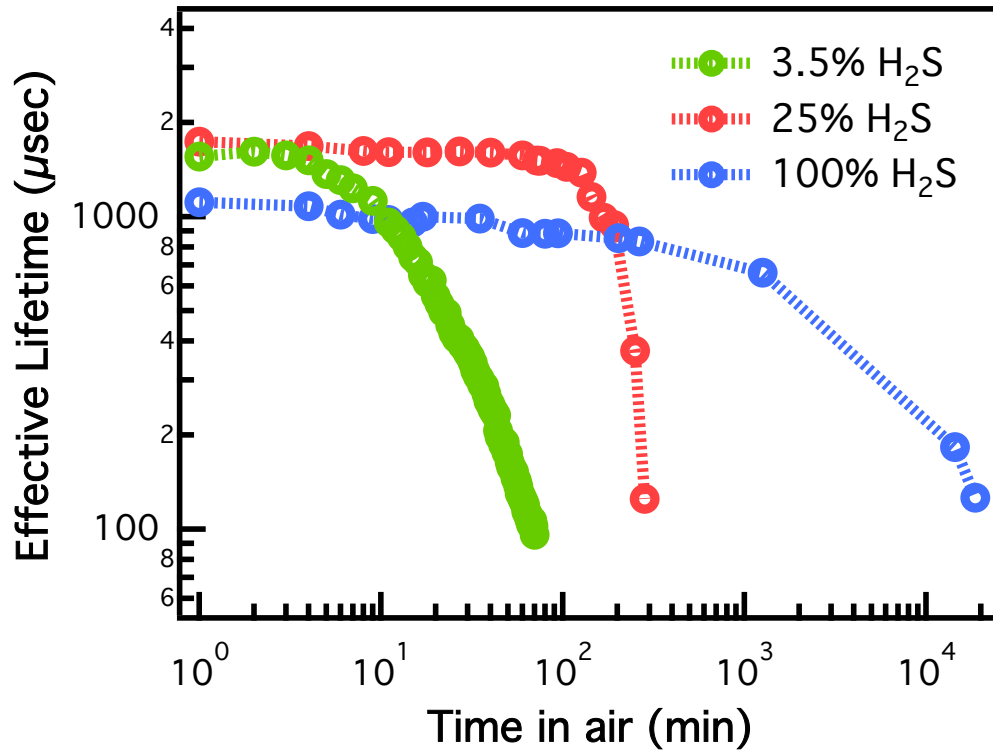
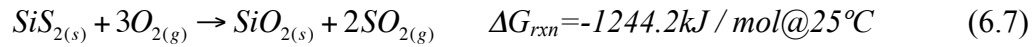


Figure 6.7 The stability of surface passivation evaluated by change in  $\tau_{\text{eff}}$  with storage time in air.

Comparing Figures 6.4 (a) and Figure 6.7, the change in  $\tau_{\text{eff}}$  with time directly correlates with the depth of S in Si. For the 3.5% H<sub>2</sub>S reaction with S depth of  $\sim 1.5$  nm, the  $\tau_{\text{eff}}$  degraded from 1497  $\mu\text{sec}$  to  $\sim 100$   $\mu\text{sec}$  in only 70 min and for the wafer reacted in 25% H<sub>2</sub>S degraded from 1737  $\mu\text{sec}$  to  $\sim 100$   $\mu\text{sec}$  in 300 min. However, the wafer reacted in 100% H<sub>2</sub>S resulting in a SiS<sub>2</sub> thickness of  $\sim 5$  nm took ten days to degrade from 1112  $\mu\text{sec}$  to  $\sim 100$   $\mu\text{sec}$  confirming that the higher concentration of H<sub>2</sub>S, which increases the thickness of the SiS<sub>2</sub>, provides improved stability over time. Such degradation of  $\tau_{\text{eff}}$  can be explained by considering the unstable nature of SiS<sub>2</sub> in air,

which converts to SiO<sub>2</sub>. The reaction pathways for the formation of SiO<sub>2</sub> are thermodynamically favored for SiS<sub>2</sub> with both H<sub>2</sub>O<sub>(g)</sub> and O<sub>2(g)</sub> [194], [195] at room temperature having ΔG<sub>rxn</sub> of:



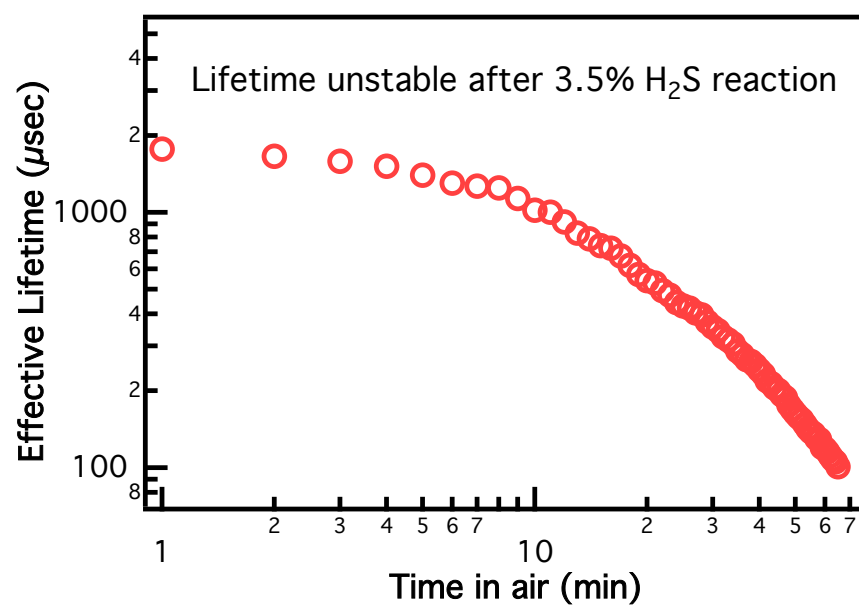
In Table 6.4, the bond association energies for Si with Si, H, O, and S indicate the strongest bonding is between Si and O.

Table 6.4 Bond association energies (kJ/mol) among elements Si, O, S, and H.

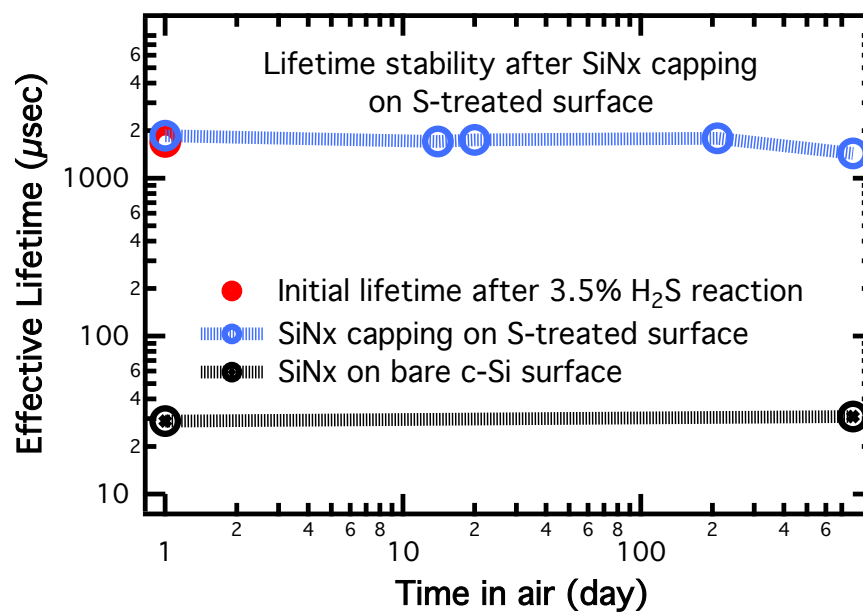
Si-Si	Si-S	Si-O	Si-H	S-O	S-S
327	619	798	298	522	429

A simple mitigation strategy to eliminate the passivation degradation was achieved by capping the SiS<sub>2</sub> passivation layer using a low temperature deposited thin a-SiN<sub>x</sub>:H films. An 80 nm thick a-SiN<sub>x</sub>:H film was deposited by PECVD at 300 °C to protect the SiS<sub>2</sub> from exposure to air. Figure 6.8 shows the change in τ<sub>eff</sub> as a function of time for wafers with and without the a-SiN<sub>x</sub>:H protective layer. The initial τ<sub>eff</sub> was ~2000 μsec for both samples and τ<sub>eff</sub> degraded to ~100 μsec in 65 min for the unprotected SiS<sub>2</sub> layer [Fig. 6.8 (a)], while the wafer capped with a-SiN<sub>x</sub>:H after H<sub>2</sub>S

reaction remained stable for months with no degradation [Fig. 6.8 (b)]. The a-SiN<sub>x</sub>:H layer alone deposited at 300 °C on c-Si surface provide a surface passivation with  $\tau_{\text{eff}}$  of 30  $\mu\text{sec}$  due to the low deposition temperature, which was also observed in our previous work [196]. The  $\tau_{\text{eff}}$  of symmetric a-SiN<sub>x</sub>:H deposited on clean c-Si surface was stable over time [Fig. 6.8 (b)]. Thus, the surface passivation achieved from the reaction of H<sub>2</sub>S by forming SiS<sub>2</sub> on the c-Si surface can be stabilized by depositing a thin a-SiN<sub>x</sub>:H layer. The a-SiN<sub>x</sub>:H layer can also be used as antireflection coating by controlling the thickness of the layer which is widely used in Si solar cells [86].



(a)



(b)

Figure 6.8. (a) Degradation of  $\tau_{\text{eff}}$  of a S-passivated Si with time in air ( $\tau_{\text{eff}} \sim 2000$   $\mu\text{sec}$  degraded to  $< 100$   $\mu\text{sec}$  in 70 min). (b) Change in  $\tau_{\text{eff}}$  with time in air for a S-passivated Si coated with 80 nm a-SiN<sub>x</sub>:H deposited at 300 °C exhibits stable passivation level over time. A low ( $\tau_{\text{eff}} \sim 30$   $\mu\text{sec}$ ) but stable  $\tau_{\text{eff}}$  is also observed for the Si passivated by only a-SiN<sub>x</sub>:H layer.

## 6.5 Conclusion

The reaction of c-Si in H<sub>2</sub>S gas at temperatures ranging from 550 to 650 °C provides excellent surface passivation for c-Si associated with the formation of SiS<sub>2</sub> surface layer resulting in  $\tau_{\text{eff}}$  of  $\sim 2000$   $\mu\text{sec}$  and SRV below 3 cm/sec. XPS analysis shows a surface concentration of S  $> 3.5\%$  is required, however, presence of significant amount of O was also found associated O impurity in the gas H<sub>2</sub>S. A separate reaction in O<sub>2</sub>/Ar gas mixture produced a similar level of surface O content, confirmed by XPS, but did not provide any surface passivation of the c-Si. Therefore, we conclude that the Si surface passivation is due to H<sub>2</sub>S, where the bonding state S-Si-S reduces the Si surface states. Degradation of the  $\tau_{\text{eff}}$  from air exposure of SiS<sub>2</sub> due to hydrolysis and oxidation was eliminated by capping the Si surface with a-SiN<sub>x</sub>:H deposited by low temperature PECVD.

## Chapter 7

### A NOVEL DEFECT PASSIVATION FOR MULTICRYSTALLINE SI WAFER BY H<sub>2</sub>S REACTION

The contents of this dissertation chapter have been adapted from a manuscript published in *IEEE 44<sup>th</sup> Photovoltaic Specialists Conference*: **H.Y. Liu**, U. Das, and R. Birkmire, “A Novel Defect Passivation Method for Multicrystalline Si Wafer by H<sub>2</sub>S Reaction” 44<sup>th</sup> *IEEE Photovolt. Spec. Conf.*, 2017. Please refer to Appendix B: Reprint Permission for Copyright 2017, IEEE. The IEEE does not require individuals working on a thesis to obtain a formal reuse license.

#### 7.1 Summary

The passivation of mc-Si wafers by reaction in H<sub>2</sub>S is discussed where the  $\tau_{\text{eff}}$  was measured to evaluate the improvements of the bulk quality. Mc-Si  $\tau_{\text{eff}}$  improved to >200  $\mu\text{sec}$  due to bulk and surface passivation by H<sub>2</sub>S reaction, compared to 40~60  $\mu\text{sec}$  with only surface passivation by quinhydrone-methanol (QHY/ME) or a-Si:H, two well-developed surface passivation methods for mono c-Si. Injection level dependent  $\tau_{\text{eff}}$  showed the reduction of both trap and recombination states for mc-Si passivation in H<sub>2</sub>S.  $\tau_{\text{eff}} > 250 \mu\text{sec}$  was yielded through surface repassivation in QHY/ME after removal of H<sub>2</sub>S reaction-formed surface layer by wet chemical etching. This indicates the passivated bulk quality by H<sub>2</sub>S reaction was not affected even after a series of wet chemistry treatments.



## 7.2 Introduction

Deployment of mc-Si wafer solar cells has expanded in recent years due to much lower cost compared to mono c-Si wafer solar cells. The greatest challenge in mc-Si wafer solar cell is to improve the device performance that is primarily limited by traps and recombination states along the grain boundaries. These recombination defects are detrimental to the  $\tau_{\text{eff}}$  and cell efficiency [197].

Hydrogen passivation of mc-Si bulk defects at the grain boundaries is the most common method to improve mc-Si solar cell performance [90]. Several methods have been used to diffuse hydrogen into Si bulk for passivation such as: hydrogen plasma [119], low energy hydrogen implantation [198], and PECVD of a-SiN<sub>x</sub>:H [104]. Hydrogen plasma and hydrogen implantation have inherent limitation due to ion damage, making a-SiN<sub>x</sub>:H the most common method for hydrogen diffusion to reduce bulk defects in mc-Si.

In this work, a new approach for mc-Si bulk defect passivation is presented using H<sub>2</sub>S reaction. We have previously reported that sulfur can passivate Si surface defects and improve  $\tau_{\text{eff}}$  in mono c-Si through reaction with H<sub>2</sub>S [199], [200]. The concept of Si surface passivation by H<sub>2</sub>S is based on theoretical arguments that sulfur can be a suitable valence mending **adsorbate** to restore silicon surface [173]. Besides being a proper candidate for Si surface restoration, sulfur has the highest diffusivity in Si among all group VI elements and the potential for bulk defect passivation. Han et.al. [192] reported that reaction of H<sub>2</sub>S with Si (100) surface consisted of H<sub>2</sub> desorption accompanied by diffusion of sulfur into bulk Si at elevated temperature. Comparing to hydrogen, the double valence of sulfur could passivate double dangling

bond sites along grain boundaries, while hydrogen can only passivate single dangling bond sites.

Saha et al. reported the passivation of mc-Si bulk using H<sub>2</sub>S reaction [201], with the best passivation results leading to  $\tau_{\text{eff}} \sim 25 \mu\text{sec}$  at H<sub>2</sub>S reaction temperature 525°C, followed by post-annealing at 500°C. However, the apparent  $\tau_{\text{eff}}$  curve as a function of minority carrier density ( $\Delta n$ ) displayed an obvious trap effect at low injection level, which implies presence of significant number of traps in the bulk.

### 7.3 Experimental

N-type 190  $\mu\text{m}$  mc-Si wafers with resistivity 3.0  $\Omega\text{-cm}$  were cleaned using the following sequential steps: 1) solvent cleaning with ultrasonic agitation; 2) piranha oxidation in a mixture of H<sub>2</sub>SO<sub>4</sub> and H<sub>2</sub>O<sub>2</sub> (3:1); 3) removal of surface oxide layer in 10% HF; 4) 2-3  $\mu\text{m}$  of Si etching in an acid mixture of HF : HNO<sub>3</sub> = 1 : 100 (HNA); and 5) formation of a H-terminated surface using 10% HF dip for 60 sec just prior to loading into the H<sub>2</sub>S reactor. N-type 145  $\mu\text{m}$  monocrystalline Cz wafers with resistivity 5.0  $\Omega\text{-cm}$  were used as control samples, where the cleaning procedure was same as mc-Si wafers.

The H<sub>2</sub>S reaction was carried out in a custom-built quartz tube CVD reactor, where the reaction temperature was controlled by a heating jacket and monitored by K-type thermocouple positioned beneath the sample holder. The tube reactor was evacuated to 10<sup>-6</sup> Torr after loading the H-terminated Si samples, and then pressurized to 520 Torr with H<sub>2</sub>S gas at room temperature, followed by temperature ramp-up to the set point. All reactions were done in a static H<sub>2</sub>S environment at temperature

between 600°C - 675°C for 30 minutes. After the reaction was completed, the system was cooled down in static H<sub>2</sub>S to 250°C, and then to room temperature in flowing Ar.

Si defect passivation was also studied by two other methods for comparison using QHY/ME and a-Si:H. H-terminated Si wafers after the last cleaning (step 5) were immersed in QHY/ME solution that is known to passivate surface defects by organic **adsorbates** [202]. In another method, a thin (10 nm) a-Si:H layer was deposited on both sides of clean wafers at 200°C by PECVD as discussed elsewhere [171].

The passivation quality was evaluated by measuring injection level dependent  $\tau_{\text{eff}}$  using a Sinton tester by PCD method. The  $\tau_{\text{eff}}$  values reported in the text are at a minority carrier density of  $1 \times 10^{15} \text{ cm}^{-3}$ . PL images were used to evaluate the uniformity of surface passivation where the image was captured using silicon germanium detector. XPS characterization was performed on control monocrystalline Cz wafer with its surface passivated in H<sub>2</sub>S reaction where the samples were transferred to XPS without exposing to air using a vacuum-sealed transport vessel.

## **7.4 Results and Discussion**

### **7.4.1 Injection Level Dependent Minority Carrier Effective Lifetime**

Figure 7.1 (a) and (b) shows the  $\tau_{\text{eff}}$  as a function of  $\Delta n$  of monocrystalline Cz wafer and mc-Si wafer, respectively with three different passivation approaches. Excellent defect passivation for Cz wafers was achieved using all three methods: QHY/ME, deposited a-Si:H, and H<sub>2</sub>S reaction, where the  $\tau_{\text{eff}} > 2000 \text{ } \mu\text{sec}$  were achieved as shown in Figure 7.1 (a). Monocrystalline Cz wafers used in this work

have high bulk quality, and therefore the passivation on Cz wafers can be considered as surface passivation only. Figure 7.1 (b), however, shows that the defect passivation levels are different for three different methods. Moreover, the shape of the  $\tau_{\text{eff}}$  curve for QHY/ME and a-Si:H passivated wafers are very different from the H<sub>2</sub>S passivated wafer. The anomalous increase in  $\tau_{\text{eff}}$  at low injection level ( $< 1 \times 10^{15} \text{ cm}^{-3}$ ) for QHY/ME and a-Si:H passivated samples indicate presence of trap states as commonly observed in poorly passivated mc-Si due to presence of dislocation and grain boundaries [203], [204]. At a low injection level, the excess carrier density becomes comparable to the trap states density [203], [205]. This increases the photo conductance and hence the carrier lifetime estimated from PCD [204]. The H<sub>2</sub>S passivated wafer shows significant suppression of this apparent increase in  $\tau_{\text{eff}}$  at low injection level due to efficient passivation of trap states. It also improves  $\tau_{\text{eff}}$  at high injection ( $> 1 \times 10^{15} \text{ cm}^{-3}$ ), which is indicative of efficient passivation of recombination states. Therefore we conclude that QHY/ME and deposited a-Si:H layer can not effectively passivate the trap and recombination states in mc-Si, while H<sub>2</sub>S reaction reduces both types of defects.

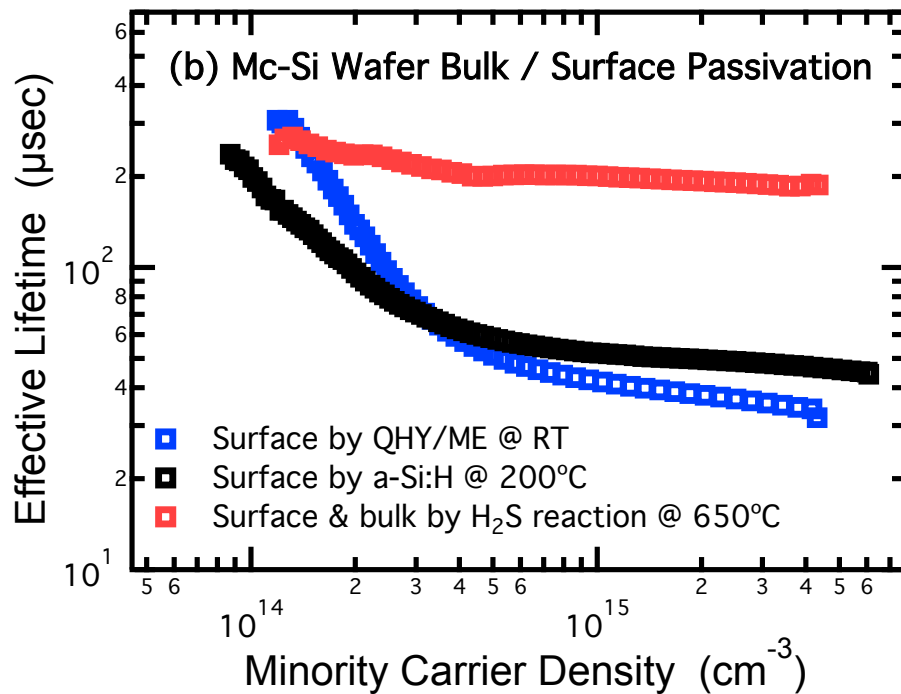
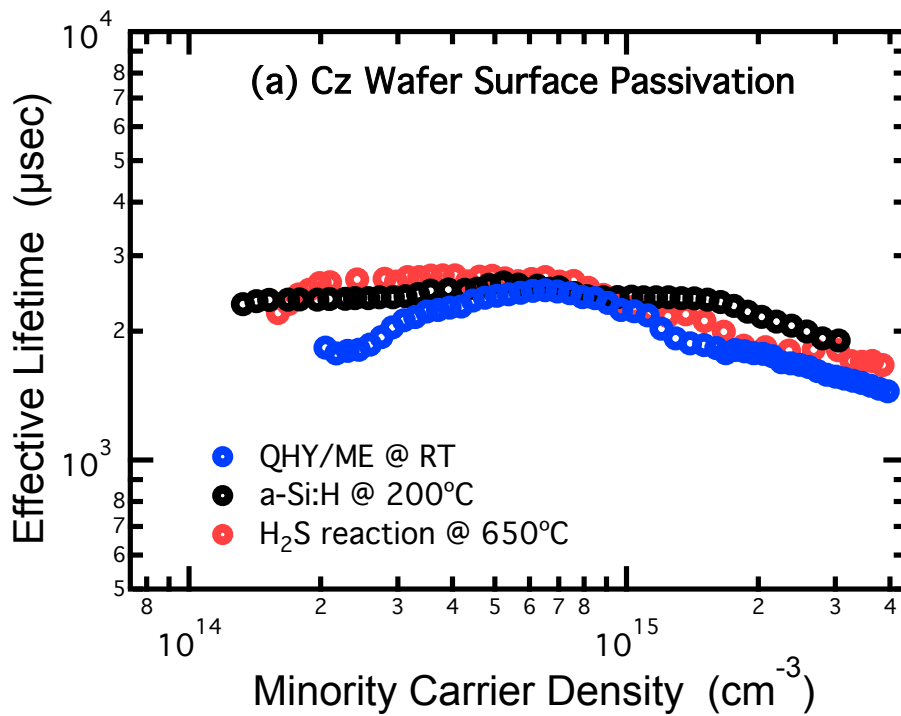


Figure 7.1 (a)  $\tau_{\text{eff}}$  as a function of  $\Delta n$  of monocrystalline Cz wafers comparing three different Si surface passivation methods; (b)  $\tau_{\text{eff}}$  as a function of  $\Delta n$  of mc-Si wafers with the same passivation methods as with Cz wafers demonstrating QHY/ME and a-Si:H can not passivate trap and recombination states in mc-Si effectively, while  $\text{H}_2\text{S}$  reaction passivates both types of defects.

#### 7.4.2 Passivation Stability and Reasons Causing Degradation

The stability of the  $\tau_{\text{eff}}$  for the Cz wafers after reaction with  $\text{H}_2\text{S}$  was inferior compared to the mc-Si wafers. This unstable surface passivation level is within expectation since the surface passivating  $\text{SiS}_2$  is unstable in air due to ease of hydrolysis and oxidation [195]. Figure 7.2 shows the degradation of  $\tau_{\text{eff}}$  of a Cz wafer after passivation in  $\text{H}_2\text{S}$ , where the initial  $\tau_{\text{eff}}$  is  $\sim 2000 \mu\text{sec}$  and degraded to below  $100 \mu\text{sec}$  within 70 minutes. The mc-Si wafer has relatively better stability comparing to Cz wafers, as seen in Figure 7.2. The slightly degraded  $\tau_{\text{eff}}$  on mc-Si is most likely caused by the instability of surface passivation level, which can be further understood in the next surface removal and repassivation work.

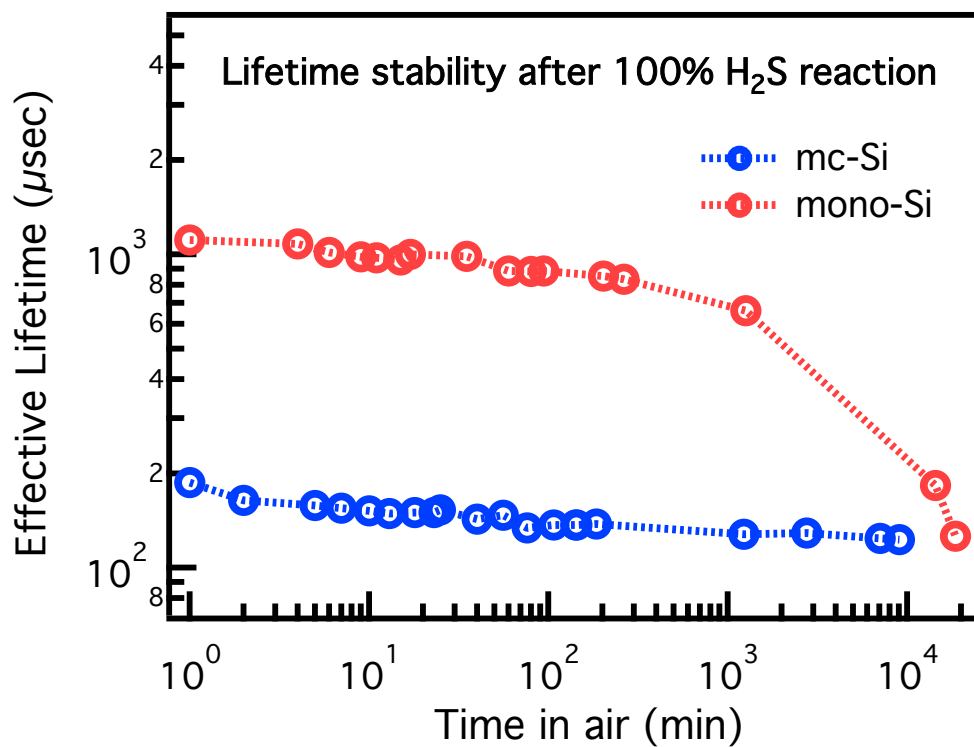


Figure 7.2 Comparison of the passivation stability after 100% H<sub>2</sub>S reaction: The Cz wafer  $\tau_{\text{eff}}$  degraded from initial ~2000 μsec to below 100 μsec in ~18 days with storage in air; the mc-Si wafer was relatively stable over time.

XPS analysis of S 2p peak was performed on Cz wafers after reaction with H<sub>2</sub>S at 650°C to compare the sulfur concentration and  $\tau_{\text{eff}}$  before and after degradation is shown in Figure 7.3. The concentration of sulfur on Si surface decreased from 4.4% to 1.6% concurrent with the change in  $\tau_{\text{eff}}$  from ~2000 μsec to below 100 μsec.

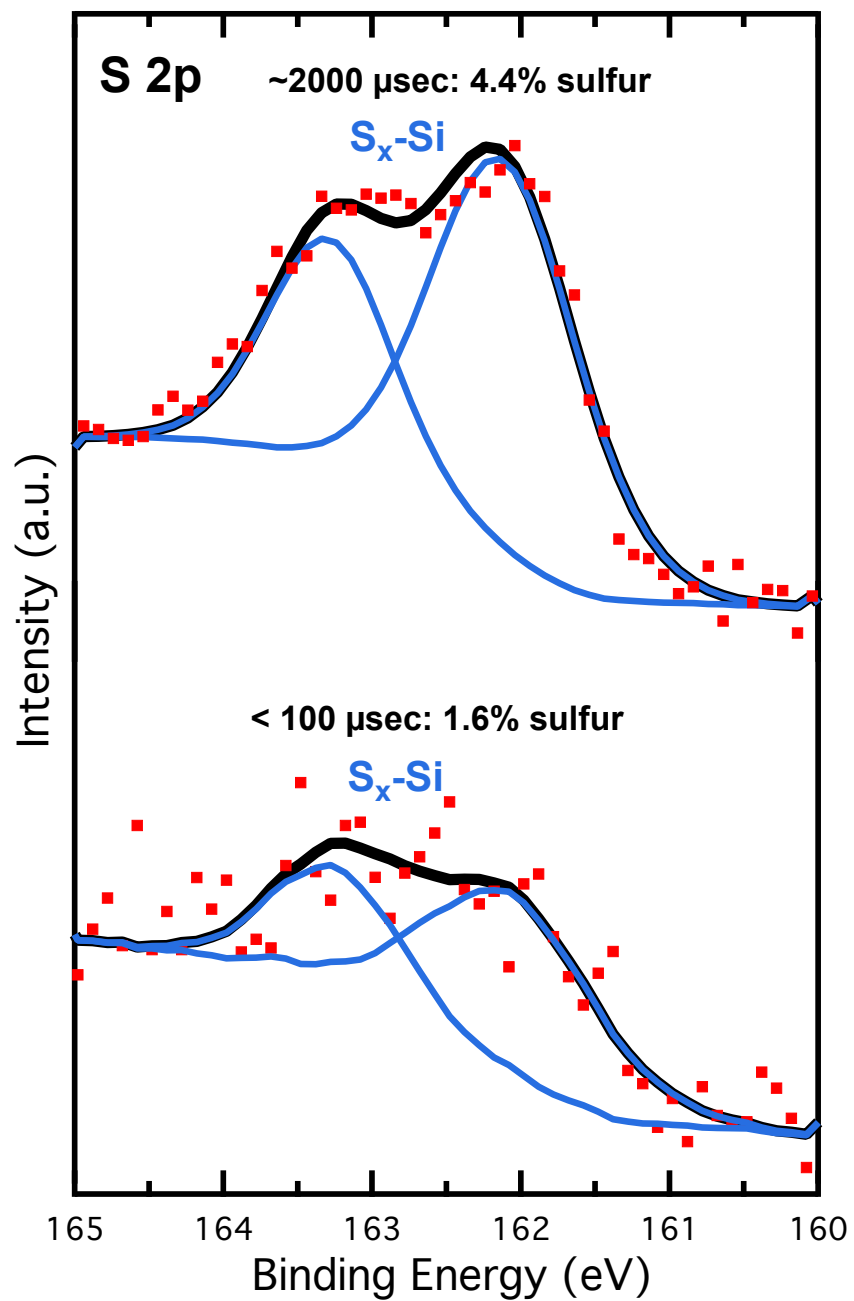


Figure 7.3 XPS spectra of S 2p on a Cz Si surface after reaction with H<sub>2</sub>S at 650°C: comparison of the sulfur concentration before and after degradation where the initial  $\tau_{\text{eff}}$  is ~2000  $\mu$ sec and the degraded  $\tau_{\text{eff}}$  is below 100  $\mu$ sec.



### 7.4.3 Wet Chemistry Process: Surface Removal and Repassivation

To further separate the effect of surface and bulk passivation and instability in  $\tau_{\text{eff}}$ , a series of wet chemistry treatments for surface removal and repassivation was studied as shown in Figure 7.4 (a). A mc-Si wafer cleaned in HF had an initial  $\tau_{\text{eff}}$  of only 25  $\mu\text{sec}$  before  $\text{H}_2\text{S}$  reaction, which increased to 208  $\mu\text{sec}$  after reaction in  $\text{H}_2\text{S}$  at 650°C for 30 minutes and is attributed to reduction of both traps and recombination states. The passivated mc-Si wafer was then etched in HNA solution to remove  $\sim 2$   $\mu\text{m}$  Si layer from both surfaces and  $\tau_{\text{eff}}$  after surface removal dropped down to 62  $\mu\text{sec}$ . QHY/ME was then used to repassivate the surface, resulting a  $\tau_{\text{eff}}$  of 252  $\mu\text{sec}$ . This indicates  $\text{H}_2\text{S}$  reaction passivates bulk defects in mc-Si and the bulk passivation remains unaffected even after a series of wet chemical etching and cleaning.

Figure 7.4 (b) exhibits the injection level dependent  $\tau_{\text{eff}}$  after each processing step. Removal of surface layer on both sides after  $\text{H}_2\text{S}$  reaction (blue curve) resulted in unpassivated surfaces, but the bulk passivation effect still can be seen when comparing with clean bare mc-Si wafer (black curve). The reduction in trap states and recombination states after  $\text{H}_2\text{S}$  reaction (red curve) and after surface repassivation in QHY/ME (green curve) demonstrates the bulk passivation quality is unaffected and preserved during a series of wet chemistry treatments. Therefore the results in Figure 7.4 indicate: i)  $\text{H}_2\text{S}$  reaction provides both bulk and surface defect passivation effectively; ii)  $\text{H}_2\text{S}$ -passivated bulk quality is stable over time, and the unstable  $\tau_{\text{eff}}$  is due to degradation of surface passivation, similar to Cz wafer; and iii) the passivated surface can be restored and repassivated with few simple wet chemical steps without affecting the bulk passivation provided by  $\text{H}_2\text{S}$ . This developed wet chemical process will allow the fabrication of surface sensitive high efficiency Si solar cell structures, such as a-Si/c-Si HJ solar cells on mc-Si wafer that has  $\text{H}_2\text{S}$ -passivated bulk using a-

Si:H as a surface passivation layer. The completion of device will provide approaches to investigate other electrical properties, such as diffusion length, emitter saturation current density and suitability for high efficiency solar cell structure on mc-Si with bulk passivated by  $\text{H}_2\text{S}$  reaction.

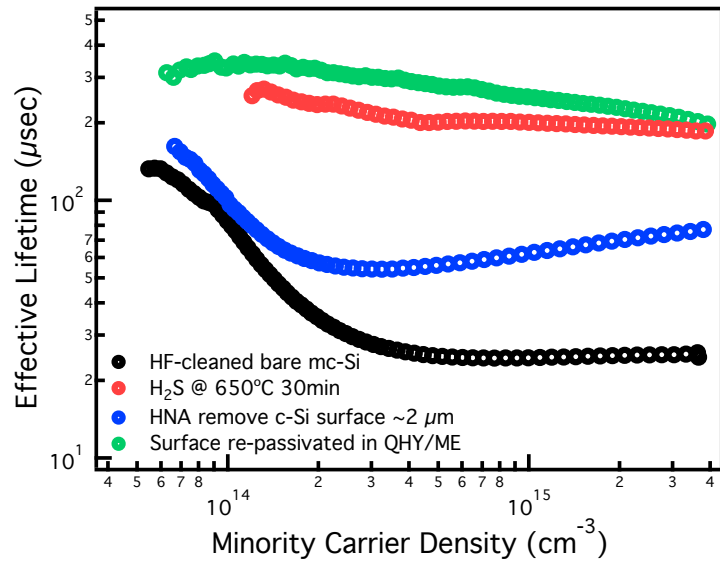
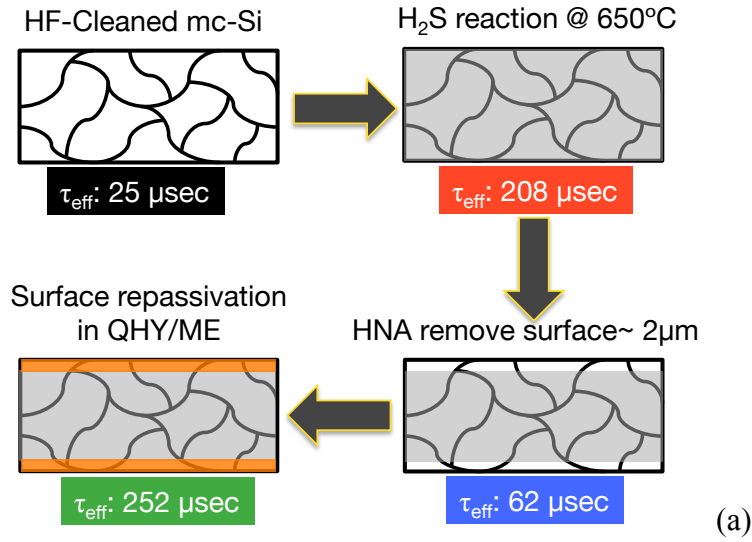


Figure 7.4 (a) Graphic depiction of processing on mc-Si starting from HF-cleaned bare wafer, followed by  $\text{H}_2\text{S}$  reaction for bulk and surface passivation. After  $\text{H}_2\text{S}$  reaction, surface was removed by HNA and then repassivated by QHY/ME. Each step has  $\tau_{\text{eff}}$  reported at  $10^{15} \text{ cm}^{-3}$ . (b) Injection level dependent  $\tau_{\text{eff}}$  after each step of processing, verifying the bulk passivation quality can be maintained with trap effect eliminated during surface removal and repassivation in wet chemistry.

#### 7.4.4 Photoluminescence Images Demonstrate Improved mc-Si Bulk Quality

The PL images of the unreacted and H<sub>2</sub>S reacted mc-Si are shown in Figure 7.5. The bare mc-Si with  $\tau_{\text{eff}}$  7  $\mu\text{sec}$  does not display any luminescence. However, for the mc-Si wafer processed in H<sub>2</sub>S at 650°C with an initial  $\tau_{\text{eff}} = 208 \mu\text{sec}$ , there is a well-defined PL image, demonstrating the improved bulk and surface quality after reaction in H<sub>2</sub>S.

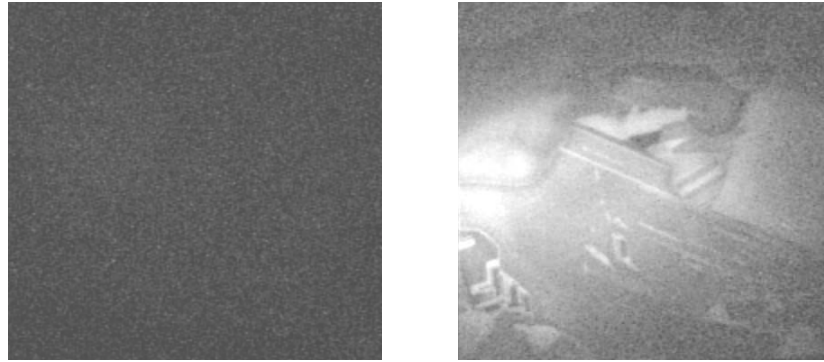


Figure 7.5 PL images on clean bare mc-Si wafer (left) shows no luminescence and (right) 650°C H<sub>2</sub>S-passivated mc-Si wafer with a clear defined PL image.

#### 7.5 Conclusion

H<sub>2</sub>S reaction with mc-Si provides both surface and bulk passivation where the  $\tau_{\text{eff}}$  increased from 7  $\mu\text{sec}$  to  $> 200 \mu\text{sec}$  and was directly observed by PL imaging. The mc-Si wafer had an anomalous increase of  $\tau_{\text{eff}}$  at low injection level caused by trap effect that no longer existed after passivation in H<sub>2</sub>S. The surface passivation

using  $\text{H}_2\text{S}$  reaction degrades due to the unstable Si-S compound in air, which was confirmed by evaluating the  $\text{H}_2\text{S}$  passivation on Cz wafers and XPS analysis. The  $\text{H}_2\text{S}$ -passivated surface layer on mc-Si wafer can be completely removed without damaging the bulk passivation, and surface passivation can be restored using a-Si:H or QHY/ME solution. This approach confirms the stability of bulk passivation over time and not affected by wet chemical processing, and therefore provides a pathway to fabricate HJ solar cells on mc-Si wafers with surface passivated by a-Si:H and bulk passivated by  $\text{H}_2\text{S}$ .

## Chapter 8

### SUMMARY AND FUTURE PROSPECT

#### 8.1 Summary

Several topics have been investigated in this thesis, including the back contact patterning and front surface field of IBC-SHJ solar cell, new c-Si surface passivation method using  $\text{H}_2\text{S}$  reaction, and the mc-Si bulk passivation by sulfur in  $\text{H}_2\text{S}$  reaction:

(1) A new patterning approach for the back contact of IBC-SHJ solar cell was developed to enhance the cell performance and improve its stability. Photoresist was used as the patterning mask in the original patterning method, where the photoresist was baked in PECVD chamber during deposition which caused the photoresist to outgassing and contaminated the interface between c-Si and a-Si:H layer and other interface as well as the bulk. Additionally, the original patterning method formed a single intrinsic a-Si:H for gap passivation which was insufficient. Thus, the insufficient gap passivation and contamination in PECVD chamber resulted in IBC-SHJ cell efficiencies of only 15%, and degraded to 14.3% within a day. However, with the new patterning method, using a-SiN<sub>x</sub>:H instead of photoresist as the patterning mask which avoided contamination in the PECVD chamber resulted in a clean deposition process. Moreover, with the new patterning design, the gap was passivated by multiple layers including intrinsic a-Si:H, doped a-Si:H, and a-SiN<sub>x</sub>:H, allowing sufficient gap passivation, which contributes to the stability of the cell performance.

Thus with the patterning method using a-SiN<sub>x</sub>:H for the patterning mask, the highest performance reached in our group is 20.2% and was stable overtime.

(2) Front surface field (FSF) was evaluate as another method to apply on IBC-SHJ solar cell to improve the front surface passivation and also reduce its series resistance attributed to the better conductivity in n<sup>+</sup> FSF layer. N<sup>+</sup> phosphorous diffusion for FSF was processed at MIT and the Cz wafers were provided by IEC. The wafer cleaning and device fabrication were all completed in our group. The back contact patterning process in device fabrication was the same as prescribed in chapter 4. The front surface stack layer structures included: a) i. a-Si:H / ARC (control sample), b) n<sup>+</sup> FSF / i. a-Si:H / ARC, c) i. a-Si:H / n. a-Si:H / ARC, d) n. a-Si:H / ARC. The only improvement was observed for the higher  $\tau_{\text{eff}}$  on sample (b) which indicates the better passivation level attributed to n<sup>+</sup> FSF. Unfortunately, no obvious enhancement was obtained from the device analysis after the completed device fabrication. This suggests the subtle improvement of front surface passivation by n<sup>+</sup> FSF cannot stand out among all other factors derived from the device fabrication process.

(3) A new c-Si surface passivation scheme using H<sub>2</sub>S reaction was developed and demonstrated to be comparable to the state-of-the-art surface passivation technology, reaching an  $\tau_{\text{eff}} > 2000 \mu\text{sec}$  corresponding to  $\text{SRV} < 5 \text{ cm/sec}$  over the optimized temperature range of 550°C ~ 650°C. The c-Si surface bonding state was evaluated via XPS and the results explained the passivation mechanism. The higher sulfur concentration on c-Si surface provided higher  $\tau_{\text{eff}}$  and deeper sulfur diffusion into c-Si wafer which resulted in better stability. The best passivation process required 3.5% of sulfur on the c-Si surface using the reaction parameters at a temperature

450°C ~ 650°C for a duration 0.5 hr ~ 4 hr, It is found that the passivation level after H<sub>2</sub>S reaction degraded from original passivation level with  $\tau_{\text{eff}} \sim 2000 \mu\text{sec}$  to below 100  $\mu\text{sec}$  corresponding to SRV from 3.2 cm / sec to above 70 cm / sec in couple of hours storage in air. This instability is believed due to the ease of oxidation and hydrolysis of silicon disulfide (SiS<sub>2</sub>) in atmosphere. The instability can be eliminated by a capping layer a-SiN<sub>x</sub>:H on top of sulfurized c-Si surface and the surface passivation quality was stabilized in air even after two years. The capping using a-SiN<sub>x</sub>:H on top of sulfurized c-Si surface can be compatible to the front surface structure of IBC-SHJ solar cell. Hence using H<sub>2</sub>S reaction to passivate c-Si front surface on IBC-SHJ solar cell can be utilized for high efficiency cells with a minimum absorption loss due to monolayer thickness of passivation layer and high bandgap of SiS<sub>2</sub>.

(4) With H<sub>2</sub>S reaction, we demonstrated the capability of having sulfur terminated c-Si surface defects, and observed the sulfur diffusion into Si. This suggested using H<sub>2</sub>S to passivate both bulk and surface defects in mc-Si wafers. To make sulfur drive-in, we used 100% H<sub>2</sub>S without Ar dilution and increased the temperature to 650°C. The original bare mc-Si wafer had  $\tau_{\text{eff}}$  only 25  $\mu\text{sec}$  after our standard wafer cleaning process, and the  $\tau_{\text{eff}}$  was enhanced to above 200  $\mu\text{sec}$  after H<sub>2</sub>S reaction. From the injection level dependent  $\tau_{\text{eff}}$ , it was observed that the density of traps and recombination states are both reduced using the H<sub>2</sub>S reaction. Additionally, a wet chemistry process was developed where the  $\tau_{\text{eff}}$  was monitored after each chemical step for the H<sub>2</sub>S-passivated of the mc-Si wafer, to differentiate the information between its bulk and surface. We found that the mc-Si surface passivated in H<sub>2</sub>S could be removed by wet chemical etching in HNA without affecting the



passivated bulk quality. The H<sub>2</sub>S-passivated bulk was preserved during surface removal and the surface could be re-passivated and restored by commonly used surface passivation layers such as quinhydrone methanol. Thus, the will give us feasibility to fabricate heterojunction solar cell with mc-Si wafer, should be possible.

## 8.2 Future Prospects

Using H<sub>2</sub>S reaction to passivate c-Si surface defect opens a whole new topic in c-Si surface passivation field. We have already demonstrated its feasibility by promising result of  $\tau_{\text{eff}} > 2000 \mu\text{sec}$  corresponding to SRV  $< 5 \text{ cm/sec}$ , and found the correlation between  $\tau_{\text{eff}}$  and S-Si-S bond to explain the passivation mechanism. However, there was always an oxidation reaction due to the impurity level in the H<sub>2</sub>S gas cylinder dominating over sulfurization reaction and limiting the amount of sulfur bonds to Si. So far we had found that more and more oxide formed with longer reaction duration. With the current heating system using heating jacket, the time required to reach setting temperature is about 30 min and there is no way to avoid the competition between sulfurization and oxidation within this 30 min. Finding a different heating method to minimize the heat-up time should minimize the effect of oxidation in the system and allow us to obtain much clearer information about sulfurization, which is ideally the only reaction in the system. The alternative heat-up system can be considered to be built up for H<sub>2</sub>S reaction is rapid thermal annealing. Another possible method to exclude the effect from oxygen is using a different source of sulfur, such as using sulfur powder evaporation to create gas phase of atomic sulfur for c-Si surface passivation. Moreover, in this dissertation we have only explored the chemical passivation mechanism – making sulfur terminate c-Si surface defects

demonstrated by the surface bonding state confirmed by XPS. Capacitance- voltage (CV) measurement will give us a more quantitative result of the density of interface state ( $D_{it}$ ).  $D_{it}$  can also tell the possibility of another passivation mechanism – field-effect passivation via the measurement of  $Q_f$ , which is quite important especially when there is already a publication reporting the additional field-effect passivation provided by the additional negative charge from sulfur, which is induced at the interface between surface passivation layer  $Al_2O_3$  and nanostructured Si [206]. Another important future prospect after we have better understanding of passivation mechanism is fabricating IBC-SHJ solar cell and using  $H_2S$  reaction to replace original front surface passivation layer i. a-Si:H. The main target is to reduce absorption loss at illuminating side by  $H_2S$  reaction [207], meanwhile, maintain the same passivation level as i. a-Si:H could provide.

Although we observed a drastic bulk quality improvement of mc-Si after reaction in  $H_2S$ , there is still not clear enough about the passivation mechanism and what exactly being changed during the reaction [208]. Some literatures had found the correlation between the density of dislocation and trap defect and reported different models to quantify actual number of dislocation before and after passivation process from the injection level dependent  $\tau_{eff}$  measurement and analysis [209]-[211]. Another work needs to be continued in the future prospects is PL characterization, to obtain more ideas about the effect of grain boundaries on carrier recombination, which can be learned from the contrast of PL image and the change of  $\tau_{eff}$ . The last and the most important future prospect is to fabricate mc-Si solar cell with its bulk passivated in  $H_2S$  reaction. The enhancement of cell efficiency and the QE curve may tell us how does the improved bulk quality contribute to device performance especially carrier

collection. At IEC we have capability of making low temperature processing heterojunction solar cell, and this will also be the first time using mc-Si wafer for heterojunction solar cell in photovoltaic field.

## REFERENCES

- [1] S. Hegedus and A. Luque, “Achievements and challenges of solar electricity from photovoltaics,” in *Handbook of Photovoltaic Science and Engineering*, John Wiley & Sons, Ltd, 2011, pp. 1–38.
- [2] R. R. King, A. Boca, W. Hong, X. -Q. Liu, D. Bhusari, D. Larrabee, K. M. Edmondson, D. C. Law, C.M. Fetzer, S. Mesropian, and N. H. Karam, “Band-gap-engineered architectures for high-efficiency multijunction concentrator solar cells,” *24<sup>th</sup> EU PVSEC*, Sep. 2009.
- [3] K. Yoshikawa, H. Kawasaki, W. Yoshida, T. Irie, K. Konishi, K. Nakano, T. Uto, D. Adachi, M. Kanematsu, H. Uzu, and K. Yamamoto, “Silicon heterojunction solar cell with interdigitated back contacts for a photoconversion efficiency over 26%,” *Nat. Energy*, vol. 2, no. 5, pp. 17032–8, Mar. 2017.
- [4] J. S. Kang and D. K. Schroder, “Gettering in silicon,” *J. Appl. Phys.*, vol. 65, no. 8, pp. 2974–2985, Apr. 1989.
- [5] N. Khedher, M. Hajji, M. Hassen, A. Ben Jaballah, B. Ouertani, H. Ezzaouia, B. Bessais, A. Selmi, and R. Bennaceur, “Gettering impurities from crystalline silicon by phosphorus diffusion using a porous silicon layer,” *Sol. Energ. Mater. Sol. Cells*, vol. 87, no. 1, pp. 605–611, May 2005.
- [6] B. Herzog, G. Hahn, M. Hofmann, and I. G. Romijn, “Bulk hydrogenation in mc-Si by PECVD SiNx deposition using direct and remote plasma,” *23<sup>rd</sup> EU PVSEC*, Sep. 2008.
- [7] “Renewables 2017 Global Status Report,” *REN 21*, 2017.
- [8] “Photovoltaics Report,” *Fraunhofer Institute for Solar Energy Systems*, ISE with support of PSE AG, Jul. 2017.
- [9] “APS NEWS,” *American Physical Society*, vol. 18, no. 4, Apr. 2009. ([www.aps.org/publications/apsnews](http://www.aps.org/publications/apsnews))

- [10] D. M. Chapin, C. S. Fuller, and G. L. Pearson, "A new silicon p-n junction photocell for converting solar radiation into electrical power," *J. Appl. Phys.*, vol. 25, no. 5, pp. 676–677, May 1954.
- [11] Y. Zhang, N. Stokes, B. Jia, S. Fan, and M. Gu, "Towards ultra-thin plasmonic silicon wafer solar cells with minimized efficiency loss," *Scientific Reports*, vol. 4, no. 1, May 2014.
- [12] S. De Wolf, A. Descoeur, Z. C. Holman, and C. Ballif, "High-efficiency silicon heterojunction solar cells: A Review," *green*, vol. 2, no. 1, Jan. 2012.
- [13] J. Melskens, B. W. H. van de Loo, B. Macco, L. E. Black, S. Smit, and W. M. M. Kessels, "Passivating contacts for crystalline silicon solar cells: from concepts and materials to prospects," *IEEE J. Photovolt.*, vol. 8, no. 2, pp. 373–388, Mar. 2018.
- [14] J. Bullock, Di Yan, A. Cuevas, B. Demarex, A. Hessler-Wyser, and S. De Wolf, "Passivated contacts to  $n^+$  and  $p^+$  silicon based on amorphous silicon and thin dielectrics," *40<sup>th</sup> IEEE Photovolt. Spec. Conf.*, 2014.
- [15] M. Taguchi, et al., "HITTM cells—high-efficiency crystalline Si cells with novel structure," *Prog. Photovolt: Res. Appl.*, vol. 8, no. 5, pp. 503–513, 2000.
- [16] J. I. Pankove and M. L. Tarng, "Amorphous silicon as a passivant for crystalline silicon," *Appl. Phys. Lett.*, vol. 34, no. 2, pp. 156–157, 1979.
- [17] A. Tomasi, et al., "Transparent electrodes in silicon heterojunction solar cells: Influence on contact passivation," *IEEE J. Photovolt.*, vol. 6, no. 1, pp. 17–27, Jan. 2016.
- [18] S. M. Iftiqar, Y. Lee, V. A. Dao, S. Kim, and J. Yi, "High efficiency heterojunction with intrinsic thin layer solar cell: A short review," *Materials and processes for energy: communicating current research and technological developments*, pp. 59–67, 2013.
- [19] A. Louwen, W. van Sark, R. Schropp, and A. Faaij, "A cost roadmap for silicon heterojunction solar cells," *Sol. Energy Mater. Sol. Cells*, vol. 147, pp. 295–314, Jan. 2016.
- [20] D. Adachi, J. L. Hernández, and K. Yamamoto, "Impact of carrier recombination on fill factor for large area heterojunction crystalline silicon solar cell with 25.1% efficiency," *Appl. Phys. Lett.*, vol. 107, no. 23, pp. 233506, Dec. 2015.

- [21] M. Hermle, F. Feldmann, J. Eisenlohr, J. Benick, A. Richter, B. Lee, P. Stradins, A. Rohatgi, and S. W. Glunz, "Approaching efficiencies above 25% with both sides-contacted silicon solar cells," *42<sup>nd</sup> IEEE Photovolt. Spec. Conf.*, 2015.
- [22] M. Taguchi, A. Yano, S. Tohoda, K. Matsuyama, Y. Nakamura, T. Nishiwaki, K. Fujita, and E. Maruyama, "24.7% record efficiency HIT solar cell on thin silicon wafer," *IEEE J. Photovolt.*, vol. 4, no. 1, pp. 96–99, Jan. 2014.
- [23] B. Paviet-Salomon, A. Tomasi, A. Descoeudres, L. Barraud, S. Nicolay, M. Despeisse, S. D. Wolf, and C. Ballif, "Back-contacted silicon heterojunction solar cells: Optical-loss analysis and mitigation," *IEEE J. Photovolt.*, vol. 5, no. 5, pp. 1293–1303, Sep. 2015.
- [24] Z. C. Holman, A. Descoeudres, L. Barraud, F. Z. Fernandez, J. P. Seif, S. De Wolf, and C. Ballif, "Current losses at the front of silicon heterojunction solar cells," *IEEE J. Photovolt.*, vol. 2, no. 1, pp. 7–15, Jan. 2012.
- [25] C. Reichel, F. Granek, M. Hermle, and S. W. Glunz, "Back-contacted back-junction n-type silicon solar cells featuring an insulating thin film for decoupling charge carrier collection and metallization geometry," *Prog. Photovolt: Res. Appl.*, vol. 21, pp. 1063–1076, Mar. 2012.
- [26] M. K. M. Desa, S. Sapeai, A. W. Azhari, K. Sopian, M. Y. Sulaiman, N. Amin, and S. H. Zaidi, "Silicon back contact solar cell configuration: A pathway towards higher efficiency," *Renew. Sust. Energ. Rev.*, vol. 60, pp. 1516–1532, Mar. 2016.
- [27] G. Lu, J. Wang, Z. Qian, and W. Shen, "Development of back-junction back-contact silicon solar cells based on industrial processes," *Prog. Photovolt: Res. Appl.*, vol. 25, no. 6, pp. 441–451, Mar. 2017.
- [28] M. D. Lammert and R. J. Schwartz, "The interdigitated back contact solar cell: A silicon solar cell for use in concentrated sunlight," *IEEE Trans. Electron Devices*, vol. 24, no. 4, pp. 337–341, Apr. 1977.
- [29] D. D. Smith, G. Reich, M. Baldrias, M. Reich, N. Boitnott, and G. Bunea, "Silicon solar cells with total area efficiency above 25 %," *43<sup>rd</sup> IEEE Photovolt. Spec. Conf.*, pp. 3351–3355, 2016.
- [30] M. Schmidt, H. Angermann, E. Conrad, L. Korte, A. Laades, K. Maydell, C. Schubert, and R. Stangl, "Physical and technological aspects of a-Si:H/c-Si hetero-junction solar cells," *Conference Record of the 2006 IEEE 4<sup>th</sup> World Conference on Photovoltaic Energy Conversion*, vol. 2, pp. 1433–1438.

- [31] A. G. Aberle, "Surface passivation of crystalline silicon solar Cells: A review," *Prog. Photovolt: Res. Appl.*, vol. 8, pp. 473–487, May 2000.
- [32] P. Škarvada, P. Tománek, P. Koktavý, R. Macků, J. Šicner, M. Vondra, D. Dallaeva, S. Smith, and L. Grmela, "A variety of microstructural defects in crystalline silicon solar cells," *Appl. Surf. Sci.*, vol. 312, pp. 50–56, May. 2014.
- [33] C. T. Sah, R. N. Noyce, W. Shockley, "Carrier generation and recombination in p-n junctions and p-n junction characteristics," *Proceeding of the IRE*, pp. 1228–1243, 1957.
- [34] Martin A. Green, "Solar cells: Operating principles, technology and system applications," Prentice-Hall, Inc., Englewood Cliffs, N. J. 07632, 1982
- [35] W. Shockley and J. W T Read, "Statistics of the recombinations of holes and electrons," *Phys. Rev.*, vol. 87, no. 5, pp. 835–842, Sep. 1952.
- [36] K. Zweibel, P. Hersch, and Solar Energy Research Institute (SERI), "Basic Photovoltaic Principles and Methods," the University of Michigan, Van Nostrand Reinhold, 1984.
- [37] M. Z. Rahman and S. I. Khan, "Advances in surface passivation of c-Si solar cells," *Mater. Renew. Sust. Energ.*, vol. 1, no. 1, Oct. 2012.
- [38] J. Schmidt, F. Werner, B. Veith, D. Zielke, S. Steingrube, P. P. Altermatt, S. Gatz, T. Dullweber, and R. Brendel, "Advances in the surface passivation of silicon solar cells," *Energy Procedia*, vol. 15, pp. 30–39, Jan. 2012.
- [39] A. G. Aberle, S. Glunz, and W. Warta, "Impact of illumination level and oxide parameters on Shockley–Read–Hall recombination at the Si–SiO<sub>2</sub> interface," *J. Appl. Phys.*, vol. 71, no. 9, pp. 4422–4431, May 1992.
- [40] M. J. Kerr and A. Cuevas, "Very low bulk and surface recombination in oxidized silicon wafers," *Semicond. Sci. Technol.*, vol. 17, pp. 35–38, Dec. 2001.
- [41] H. Jin, K. J. Weber, N. C. Dang, and W. E. Jellett, "Defect generation at the Si–SiO<sub>2</sub> interface following corona charging," *Appl. Phys. Lett.*, vol. 90, no. 26, pp. 262109, Jun. 2007.
- [42] P. E. Gruenbaum, R. A. Sinton, and R. M. Swanson, "Stability problems in point contact solar cells," *Conference Record of the Twentieth IEEE Photovolt. Spec. Conf.*, 1988.

- [43] A. Rohatgi, P. Doshi, J. Moschoner, T. Lauinger, A. G. Aberle, and D. S. Ruby, "Comprehensive study of rapid, low-cost silicon surface passivation technologies," *IEEE Trans. Electron Devices*, vol. 47, no. 5, pp. 987–993, May 1977.
- [44] T. Lauinger, J. Schmidt, A. G. Aberle, and R. Hezel, "Surface passivation properties of silicon/silicon oxide/silicon nitride structures for solar cells," *13<sup>th</sup> EU PVSEC*, Oct. 1995.
- [45] E. Yablonovitch, T. Gmitter, R. M. Swanson, and Y. H. Kwark, "A 720 mV open circuit voltage  $\text{SiO}_x\text{:c-Si:SiO}_x$  double heterostructure solar cell," *Appl. Phys. Lett.*, vol. 47, no. 11, pp. 1211–1213, Sep. 1985.
- [46] N. E. Grant and K. R. McIntosh, "Passivation of a (100) silicon surface by silicon dioxide grown in nitric acid," *IEEE Electron Device Lett.*, vol. 30, no. 9, pp. 922–924, Sep. 2009.
- [47] V. D. Mihailetschi, Y. Komatsu, and L. J. Geerligs, "Nitric acid pretreatment for the passivation of boron emitters for n-type base silicon solar cells," *Appl. Phys. Lett.*, vol. 92, no. 6, pp. 063510, Feb. 2008.
- [48] A. H. Mahan, "Hot wire chemical vapor deposition of Si containing materials for solar cells," *Sol. Energ. Mater. Sol. Cells*, vol. 78, no. 1, pp. 299–327, Jul. 2003.
- [49] R. E. Rocheleau, S. C. Jackson, S. S. Hegedus, and B. N. Baron, "Properties of a-Si:H and a-SiGe:H films deposited by photo-assisted CVD," *Mat. Res. Soc. Symp. Proc.*, vol. 70, pp. 37–42, 1986.
- [50] C. S. McCormick, C. E. Webe, and J. R. Abelson, "An amorphous silicon thin film transistor fabricated at 125°C by dc reactive magnetron sputtering," *Mat. Res. Soc. Symp. Proc.*, vol. 424, pp. 53–57, 1997.
- [51] D. J. Barber, "The physics of hydrogenated amorphous silicon I," *Optica Acta: International J. Optics*, vol. 31, no. 11, pp. 1207, Nov. 1984.
- [52] W. Beyer and H. Wagner, "The role of hydrogen in a-Si: H - results of evolution and annealing studies," *J. Non-Crystalline Solids*, vol. 59, pp. 161–168, 1983.
- [53] C. J. Fang, K. J. Gruntz, L. Ley, M. Cardona, "The hydrogen content of a-Ge: H and a-Si:H as determined by IR spectroscopy, gas evolution and nuclear reaction techniques," *J. Non-Crystalline Solids*, vol. 35, pp. 255–260, 1980.



- [54] D. G. Cahill, M. Katiyar, and J. R. Abelson, "Thermal conductivity of a-Si:H thin films," *Phys. Rev. B*, vol. 50, no. 9, pp. 6077–6081, Sep. 1994.
- [55] D. K. Biegelsen, R. A. Street, C. C. Tsai, and J. C. Knights, "Hydrogen evolution and defect creation in amorphous Si:H alloys," *Phys. Rev. B*, vol. 20, no. 12, pp. 4839–4846, Dec. 1979.
- [56] R. A. Street, "Hydrogen chemical potential and structure of a-Si:H," *Phys. Rev. B*, vol. 43, no. 3, pp. 2454–2457, Jan. 1991.
- [57] L. Korte, E. Conrad, H. Angermann, R. Stangl, and M. Schmidt, "Advances in a-Si:H/c-Si heterojunction solar cell fabrication and characterization," *Sol. Energ. Mater. Sol. Cells*, vol. 93, no. 6, pp. 905–910, Dec. 2008.
- [58] A. Descoeudres, L. Barraud, S. De Wolf, B. Strahm, D. Lachenal, C. Guerin, Z. C. Holman, F. Zicarelli, B. Demareux, J. Seif, J. Holovsky, and C. Ballif, "Improved amorphous/crystalline silicon interface passivation by hydrogen plasma treatment," *Appl. Phys. Lett.*, vol. 99, no. 12, pp. 123506, 2011.
- [59] S. De Wolf and M. Kondo, "Nature of doped a-Si:H/c-Si interface recombination," *J. Appl. Phys.*, vol. 105, no. 10, pp. 103707, May 2009.
- [60] J.-C. Hsiao, C.-H. Chen, C.-C. Lin, D.-C. Wu, and P. Yu, "Effect of hydrogen dilution on the intrinsic a-Si:H film of the heterojunction silicon-based solar cell," *J. Electrochem. Soc.*, vol. 158, no. 9, pp. H876–H878, Jul. 2011.
- [61] J.-W. A. Schüttauf, K. H. M. van der Werf, I. M. Kielen, Wilfried. G. J. H. M. van Sark, J. K. Rath, and R. E. I. Schropp, "High quality crystalline silicon surface passivation by combined intrinsic and n-type hydrogenated amorphous silicon," *Appl. Phys. Lett.*, vol. 99, no. 20, pp. 203503, Nov. 2011.
- [62] M. Z. Burrows, U. K. Das, R. L. Opila, S. De Wolf, and R. W. Birkmire, "Role of hydrogen bonding environment in a-Si:H films for c-Si surface passivation," *J. Vac. Sci. Technol. A*, vol. 26, no. 4, pp. 683–687, Jul./Aug. 2008.
- [63] B. Rech, H. Wagner, "Potential of amorphous silicon for solar cells," *Appl. Phys. A*, vol. 69, pp. 155–167, Jun. 1999.
- [64] L. Korte, A. Laades, and M. Schmidt, "Electronic states in a-Si:H/c-Si heterostructures," *J. Non-Crystalline Solids*, vol. 352, no. 9, pp. 1217–1220, Mar. 2006.

- [65] C. Leendertz, N. Mingirulli, T. F. Schulze, J. P. Kleider, B. Rech, and L. Korte, "Discerning passivation mechanisms at a-Si:H/c-Si interfaces by means of photoconductance measurements," *Appl. Phys. Lett.*, vol. 98, no. 20, pp. 202108, May 2011.
- [66] C. Leendertz, R. Stangl, T. F. Schulze, M. Schmidt, and L. Korte, "A recombination model for a-Si:H/c-Si heterostructures," *Phys. Status Solidi C*, vol. 7, no. 3–4, pp. 1005–1010, Jan. 2010.
- [67] A. Froitzheim, K. Brendel, L. Elstner, W. F. J. O. Non, 2002, "Interface recombination in heterojunctions of amorphous and crystalline silicon," *J. Non-Crystalline Solids*, vol. 299–302, pp. 663–667, Apr. 2002.
- [68] D. L. Staebler and C. R. Wronski, "Reversible conductivity changes in discharge-produced amorphous Si," *Appl. Phys. Lett.*, vol. 31, no. 4, pp. 292–294, Jun. 1977.
- [69] M. Stutzmann, W. B. Jackson, and C. C. Tsai, "Light-induced metastable defects in hydrogenated amorphous silicon: A systematic study," *Phys. Rev. B*, vol. 32, no. 1, pp. 23–47, Jul. 1985.
- [70] S. De Wolf, B. Demareux, A. Descoeurdes, and C. Ballif, "Very fast light-induced degradation of a-Si:H/c-Si(100) interfaces," *Phys. Rev. B*, vol. 83, no. 23, pp. 233301, Jun. 2011.
- [71] B. Hoex, S. B. S. Heil, E. Langereis, M. C. M. van de Sanden, and W. M. M. Kessels, "Ultralow surface recombination of c-Si substrates passivated by plasma-assisted atomic layer deposited  $\text{Al}_2\text{O}_3$ ," *Appl. Phys. Lett.*, vol. 89, no. 4, pp. 042112, Jul. 2006.
- [72] G. Agostinelli, A. Delabie, P. Vitanov, Z. Alexieva, H. F. W. Dekkers, S. De Wolf, and G. Beaucarne, "Very low surface recombination velocities on p-type silicon wafers passivated with a dielectric with fixed negative charge," *Sol. Energ. Mater. Sol. Cells*, vol. 90, no. 18, pp. 3438–3443, Aug. 2006.
- [73] R. Hezel and K. Jaeger, "Low-temperature surface passivation of silicon for solar cells," *J. Electrochem. Soc.*, vol. 136, no. 2, pp. 518–523, Feb. 1989.
- [74] G. Dingemans and W. M. M. Kessels, "Status and prospects of  $\text{Al}_2\text{O}_3$ -based surface passivation schemes for silicon solar cells," *J. Vac. Sci. Technol. A*, vol. 30, no. 4, pp. 040802, 2012.

- [75] J. Schmidt, A. Merkle, R. Brendel, B. Hoex, M. C. M. V. de Sanden, and W. M. M. Kessels, "Surface passivation of high-efficiency silicon solar cells by atomic-layer-deposited  $\text{Al}_2\text{O}_3$ ," *Prog. Photovolt: Res. Appl.*, vol. 16, no. 6, pp. 461–466, Sep. 2008.
- [76] B. Hoex, J. Schmidt, R. Bock, P. P. Altermatt, M. C. M. van de Sanden, and W. M. M. Kessels, "Excellent passivation of highly doped p-type Si surfaces by the negative-charge-dielectric  $\text{Al}_2\text{O}_3$ ," *Appl. Phys. Lett.*, vol. 91, no. 11, pp. 112107, Sep. 2007.
- [77] B. Hoex, J. Gielis, and M. Van De Sanden, "On the c-Si surface passivation mechanism by the negative-charge-dielectric  $\text{Al}_2\text{O}_3$ ," *J. Appl. Phys.*, vol. 104, no. 11, pp. 113703, Dec. 2008.
- [78] B. Hoex, J. Schmidt, P. Pohl, M. C. M. van de Sanden, and W. M. M. Kessels, "Silicon surface passivation by atomic layer deposited  $\text{Al}_2\text{O}_3$ ," *J. Appl. Phys.*, vol. 104, no. 4, pp. 44903, Aug. 2008.
- [79] S. Bordihn, P. Engelhart, V. Mertens, G. Kesser, D. Köhn, G. Dingemans, M. M. Mandoc, J. W. Müller, and W. M. M. Kessels, "High surface passivation quality and thermal stability of ALD  $\text{Al}_2\text{O}_3$  on wet chemical grown ultra-thin  $\text{SiO}_2$  on silicon," *Energy Procedia*, vol. 8, pp. 654–659, 2011.
- [80] J. Benick, B. Hoex, M. C. M. van de Sanden, W. M. M. Kessels, O. Schultz, and S. W. Glunz, "High efficiency n-type Si solar cells on  $\text{Al}_2\text{O}_3$ -passivated boron emitters," *Appl. Phys. Lett.*, vol. 92, no. 25, pp. 253504, Jun. 2008.
- [81] C. Leguijt, et al., "Low temperature surface passivation for silicon solar cells," *Sol. Energ. Mater. Sol. Cells*, vol. 40, no. 4, pp. 297–345, Aug. 1996.
- [82] A. Cuevas, M. J. Kerr, and J. Schmidt, "Passivation of crystalline silicon using silicon nitride," *3<sup>rd</sup> World Conference on Photovoltaic Energy Conversion*, May 2003.
- [83] T. Lauinger, J. Schmidt, A. G. Aberle, and R. Hezel, "Record low surface recombination velocities on 1  $\Omega$  cm p-silicon using remote plasma silicon nitride passivation," *Appl. Phys. Lett.*, vol. 68, no. 9, pp. 1232–1234, Feb. 1996.
- [84] S. Dauwe, J. Schmidt, A. Metz, and R. Hezel, "Fixed charge density in silicon nitride films on crystalline silicon surfaces under illumination," *Conference Record of the Twenty-Ninth IEEE Photovolt. Spec. Conf.*, 2002.

- [85] J. R. Elmiger and M. Kunst, "Investigation of charge carrier injection in silicon nitride/silicon junctions," *Appl. Phys. Lett.*, vol. 69, no. 4, pp. 517–519, May 1996.
- [86] J. Hofstetter, C. del Canizo, S. Ponce-Alcantara, and A. Luque, "Optimisation of SiNx:H anti-reflection coatings for silicon solar cells," *Spanish Conference on Electron Devices*, 2007.
- [87] H. Nagel, A. G. Aberle, and R. Hezel, "Optimised antireflection coatings for planar silicon solar cells using remote PECVD silicon nitride and porous silicon dioxide," *Prog. Photovolt: Res. Appl.*, vol. 7, no. 4, pp. 245–260, Jul. 1999.
- [88] J. Benick, et al., "High-efficiency n-Type HP mc silicon solar cells," *IEEE J. Photovolt.*, vol. 7, no. 5, pp. 1171–1175, Sep. 2017.
- [89] B. Michl, M. Rüdiger, J. A. Giesecke, M. Hermle, W. Warta, and M. C. Schubert, "Efficiency limiting bulk recombination in multicrystalline silicon solar cells," *Sol. Energ. Mater. Sol. Cells*, vol. 98, pp. 441–447, Mar. 2012.
- [90] C. E. Dube and J. I. Hanoka, "Hydrogen passivation of multicrystalline silicon," *Conference Record of the Thirty-first IEEE Photovolt. Spec. Conf.*, 2005.
- [91] T. Buonassisi et al., "Chemical natures and distributions of metal impurities in multicrystalline silicon materials," *Prog. Photovolt: Res. Appl.*, vol. 14, no. 6, pp. 513–531, 2006.
- [92] S. Woo, M. Bertoni, K. Choi, S. Nam, S. Castellanos, D. M. Powell, T. Buonassisi, and H. Choi, "An insight into dislocation density reduction in multicrystalline silicon," *Sol. Energ. Mater. Sol. Cells*, vol. 155, pp. 88–100, Oct. 2016.
- [93] B. Sopori and P. Sheldon, P. Rupnowski, and D. Balzer "Dislocation generation by thermal stresses in Si: Modeling and experiments," *presented at the 2005 DOE Solar Energy Technologies*.
- [94] B. P. Uberuaga, L. J. Vernon, E. Martinez, and A. F. Voter, "The relationship between grain boundary structure, defect mobility and grain boundary sink efficiency," *Sci Rep*, vol. 5, no. 1, Mar. 2015.
- [95] K. Hartman, M. Bertoni, J. Serdy, and T. Buonassisi, "Dislocation density reduction in multicrystalline silicon solar cell material by high temperature annealing," *Appl. Phys. Lett.*, vol. 93, no. 12, pp. 122108, Sep. 2008.

- [96] H. C. Sio, S. P. Phang, H. T. Nguyen, D. Yan, T. Trupke, and D. Macdonald, "Comparison of recombination activity of grain boundaries in various multicrystalline silicon materials," *31<sup>st</sup> EU PVSEC*, 2015.
- [97] M. I. Bertoni, D. P. Fenning, M. Rinio, V. Rose, M. Holt, J. Maser, and T. Buonassisi, "Nanoprobe X-ray fluorescence characterization of defects in large-area solar cells," *Energy Environ. Sci.*, vol. 4, no. 10, pp. 4252–4257, 2011.
- [98] J. Chen, T. Sekiguchi, D. Yang, F. Yin, K. Kido, and S. Tsunekawa, "Electron-beam-induced current study of grain boundaries in multicrystalline silicon," *J. Appl. Phys.*, vol. 96, no. 10, pp. 5490–5495, Nov. 2004.
- [99] S. A. McHugo, H. Hieslmair, and E. R. Weber, "Gettering of metallic impurities in photovoltaic silicon," *Appl. Phys. A*, vol. 64, no. 2, pp. 127–137, Jan. 1997.
- [100] P. Manshanden and L. J. Geerligs, "Improved phosphorous gettering of multicrystalline silicon," *Sol. Energ. Mater. Sol. Cells*, vol. 90, no. 7, pp. 998–1012, Jul. 2005.
- [101] I. Périchaud, "Gettering of impurities in solar silicon," *Sol. Energ. Mater. Sol. Cells*, vol. 72, no. 1–4, pp. 315–326, Apr. 2002.
- [102] D. Macdonald, A. Cuevas, A. Kinomura, and Y. Nakano, "Phosphorus gettering in multicrystalline silicon studied by neutron activation analysis," *Conference Record of the Twenty-Ninth IEEE Photovolt. Spec. Conf.*, 2002.
- [103] J. Hong et al., "Bulk passivation of multicrystalline silicon solar cells induced by high-rate-deposited ( $> 1$  nm/s) silicon nitride films," *Prog. Photovolt: Res. Appl.*, vol. 11, no. 2, pp. 125–130, 2003.
- [104] F. Duerinckx and J. Szlufcik, "Defect passivation of industrial multicrystalline solar cells based on PECVD silicon nitride," *Sol. Energ. Mater. Sol. Cells*, vol. 72, no. 1–4, pp. 231–246, Apr. 2002.
- [105] J. -F. Lelièvre, E. Fourmond, A. Kaminski, O. Palais, D. Ballutaud, and M. Lemitte, "Study of the composition of hydrogenated silicon nitride  $\text{SiN}_x\text{:H}$  for efficient surface and bulk passivation of silicon," *Sol. Energ. Mater. Sol. Cells*, vol. 93, no. 8, pp. 1281–1289, Mar. 2009.
- [106] M. Lipiński, P. Panek, S. Klusak, P. Zięba, A. Szyszka, and B. Paszkiewicz, "Defect passivation of multicrystalline silicon solar cells by silicon nitride coatings," *Materials Science-Poland*, vol. 24, no. 4, 2006.

- [107] T. Buonassisi, A. A. Istratov, M. D. Pickett, M. A. Marcus, T. F. Ciszek, and E. R. Weber, "Metal precipitation at grain boundaries in silicon: Dependence on grain boundary character and dislocation decoration," *Appl. Phys. Lett.*, vol. 89, no. 4, pp. 042102, Jul. 2006.
- [108] M. Seibt, R. Khalil, V. Kveder, and W. Schröter, "Electronic states at dislocations and metal silicide precipitates in crystalline silicon and their role in solar cell materials," *Appl. Phys. A*, vol. 96, no. 1, pp. 235–253, Dec. 2008.
- [109] Y. Nose, I. Takahashi, W. Pan, N. Usami, K. Fujiwara, and K. Nakajima, "Floating cast method to realize high-quality Si bulk multicrystals for solar cells," *J. Cryst. Growth*, vol. 311, no. 2, pp. 228–231, Jan. 2009.
- [110] T. Y. Wang, S. L. Hsu, C. C. Fei, K. M. Yei, W. C. Hsu, and C. W. Lan, "Grain control using spot cooling in multi-crystalline silicon crystal growth," *Journal of Crystal Growth*, vol. 311, no. 2, pp. 263–267, Jan. 2009.
- [111] H. J. Choi, M. I. Bertoni, J. Hofstetter, D. P. Fenning, D. M. Powell, S. Castellanos, and T. Buonassisi, "Dislocation density reduction during impurity gettering in multicrystalline silicon," *IEEE J. Photovolt.*, vol. 3, no. 1, pp. 189–198, Jan. 2013.
- [112] C.-X. Li, Q.-Y. Meng, G. Li, and L.-J. Yang, "Atomistic simulation of the 60° dislocation mobility in silicon crystal," *Superlattices and Microstructures*, vol. 40, no. 2, pp. 113–118, Aug. 2006.
- [113] B. Joós, Q. Ren, and M. S. Duesbery, "Peierls-Nabarro model of dislocations in silicon with generalized stacking-fault restoring forces," *Phys. Rev. B*, vol. 50, no. 9, pp. 5890–5898, Sep. 1994.
- [114] A. H. Cottrell, "Theory of dislocations" *Progress in Metal Physics*, vol. 4, pp. 205–264, Jan. 1953.
- [115] J. D. Eshelby, "Supersonic dislocations and dislocations in dispersive media," *Proc. Phys. Soc. B*, vol. 69, no. 10, pp. 1013–1019, Oct. 1956.
- [116] M. Bertoni, C. Colin, and T. Buonassisi, "Dislocation engineering in multicrystalline silicon," *Solid State Phenomena*, vol. 156–158, pp. 11–18, Oct. 2009.
- [117] J. Samuels and S. G. Roberts, "The brittle-ductile transition in silicon. I. Experiments," *Proc. Royal Society A: Mathematical, Physical and Engineering Sciences*, vol. 421, no. 1860, pp. 1–23, Jan. 1989.

- [118] M. Sheoran, A. Upadhyaya, and A. Rohatgi, "Bulk lifetime and efficiency enhancement due to gettering and hydrogenation of defects during cast multicrystalline silicon solar cell fabrication," *Solid-State Electronics*, vol. 52, no. 5, pp. 612–617, May 2008.
- [119] S. Rattanapan, H. Yamamoto, S. Miyajima, T. Sato, and M. Konagai, "Hydrogen plasma treatment for improving bulk passivation quality of c-Si solar cells," *Current Appl. Phys.*, vol. 10, no. S, pp. S215–S217, Mar. 2010.
- [120] R. Einhaus et al., "Hydrogen passivation of newly developed EMC-multi-crystalline silicon," *Mater. Sci. Eng. B*, vol. 58, no. 1-2, pp. 81–85, Feb. 1999.
- [121] C. H. Seager and D. S. Ginley, "Passivation of grain boundaries in polycrystalline silicon," *Appl. Phys. Lett.*, vol. 34, no. 5, pp. 337–340, Mar. 1979.
- [122] C. H. Seager, D. S. Ginley, and J. D. Zook, "Improvement of polycrystalline silicon solar cells with grain-boundary hydrogenation techniques," *Appl. Phys. Lett.*, vol. 36, no. 10, pp. 831–833, May 1980.
- [123] H. Robbins and B. Schwartz, "Chemical etching of silicon II. The system HF, HNO<sub>3</sub>, H<sub>2</sub>O, and HC<sub>2</sub>H<sub>3</sub>O<sub>2</sub>," *J. Electrochem. Soc.*, vol. 107, no. 2, pp. 108–111, Feb. 1960.
- [124] O. Tabata, R. Asahi, H. Funabashi, K. Shimaoka, and S. Sugryama, "Anisotropic etching of silicon in TMAH solutions," *Sensors and Actuators A*, vol. 34, pp. 51–57, 1992.
- [125] M. Sekimura, "Anisotropic etching of surfactant-added TMAH solution," *IEEE International MEMS 99 Conference*, 1999.
- [126] S. A. Campbell, "The science and engineering of microelectronic fabrication 2<sup>nd</sup> version," Oxford University Press, 2001.
- [127] "Thermo Scientific XPS: <https://xpssimplified.com/whatisxps.php>
- [128] J. F. Moudler, W. F. Stickle, P. E. Sobol, and K. D. Bomben, "Handbook of X-ray photoelectron spectroscopy," Perkin-Elmer, 1992.
- [129] R. Smart, S. McIntyre, M. Bancroft, I. Bello, and Friends, "Lecture: X-ray Photoelectron Spectroscopy," prepared by Dept. of Physics and Materials Science, City University of Hong Kong, Surface Science Western, UWO.

- [130] “CasaXPS Manual 2.3.15,” published by Casa Software Ltd. (<http://www.casaxps.com/ebooks/OrangeBookRev1.3ebook.pdf>)
- [131] “Introduction to Fourier Transform Infrared Spectrometry,” prepared by Thermo Nicolet Corporation, 2001.
- [132] H. G. Tompkins and W. A. McGahan, “Spectroscopic Ellipsometry and Reflectometry: A User's Guide,” Wiley, 1999.
- [133] “Guide to Using WVASE 32,” manual prepared by J. A. Woollam Co., Inc. (<https://www.jawoollam.com/resources/ellipsometry-tutorial>)
- [134] R. A. Sinton and A. Cuevas, “Contactless determination of current–voltage characteristics and minority-carrier lifetimes in semiconductors from quasi-steady-state photoconductance data,” *Appl. Phys. Lett.*, vol. 69, no. 17, pp. 2510–2512, Oct. 1996.
- [135] R. A. Sinton and A. Cuevas, “Quasi-steady-state photoconductance, a new method for solar cell material and device characterization,” *25<sup>th</sup> IEEE Photovolt. Spec. Conf.*, May 1996.
- [136] C. Berge, J. Schmidt, B. Lenkeit, H. Nagel, and A. G. Aberle, “Comparison of effective carrier lifetimes in silicon determined by transient and quasi-steady-state photoconductance measurements,” *2<sup>nd</sup> World Conference and Exhibition on Photovoltaic Solar Energy Conversion*, Vienna, 1998.
- [137] H. Nagel, C. Berge, and A. G. Aberle, “Generalized analysis of quasi-steady-state and quasi-transient measurements of carrier lifetimes in semiconductors,” *J. Appl. Phys.*, vol. 86, no. 11, pp. 6218–6221, Dec. 1999.
- [138] C. Honsberg and S. Bowden, “Surface Recombination,” *PVEDUCATION.ORG*. (<http://www.pveducation.org/pvcdrom/characterisation/surface-recombination>)
- [139] A. Goetzberger, J. Knobloch, and B. Voss, “Crystalline Silicon Solar Cells,” John Wiley & Sons, Ltd, 2014.
- [140] S. S. Hegedus and W. N. Shafarman, “Thin-film solar cells: Device measurements and analysis,” *Prog. Photovolt: Res. Appl.*, vol. 12, no. 23, pp. 155–176, Mar. 2004.
- [141] B. C. Plunkett, P. G. Lasswell, “Laser scanning of experimental solar cells,” *Proc. SPIE 0248, Role of Electro-Optics in Photovoltaic Energy Conversion*, Nov. 1980.



- [142] J. M. Frey Master Thesis, University of Delaware, 2005.
- [143] M. Lu, S. Bowden, U. Das, and R. Birkmire, "Interdigitated back contact silicon heterojunction solar cell and the effect of front surface passivation," *Appl. Phys. Lett.*, vol. 91, no. 6, pp. 063507, 2007.
- [144] Z. Shu, U. Das, J. Allen, R. Birkmire, and S. Hegedus, "Experimental and simulated analysis of front versus all-back-contact silicon heterojunction solar cells: effect of interface and doped a-Si:H layer defects," *Prog. Photovolt: Res. Appl.*, vol. 23, no. 1, pp. 78–93, Jun. 2013.
- [145] U. Das, J. He, Z. Shu, L. Zhang, C. Thompson, R. Birkmire, and S. Hegedus, "Sensitivity of surface passivation and interface quality in IBC-SHJ solar cells to patterning process," *39<sup>th</sup> IEEE Photovolt. Spec. Conf.*, 2013.
- [146] B. Shu, U. Das, O. Jani, S. Hegedus, and R. Birkmire, "Low temperature front surface passivation of interdigitated back contact silicon heterojunction solar cell," *34<sup>th</sup> IEEE Photovolt. Spec. Conf.*, 2009.
- [147] J. He, S. Hegedus, U. Das, Z. Shu, M. Bennett, L. Zhang, and R. Birkmire, "Laser-fired contact for n-type crystalline Si solar cells," *Prog. Photovolt: Res. Appl.*, vol. 23, no. 9, pp. 1091–1099, Jun. 2014.
- [148] J. He, S. Hegedus, U. Das, Z. Shu., M. Bennett, and R. Birkmire, "Laser fired contact for n-type crystalline Si solar cell," *39<sup>th</sup> IEEE Photovolt. Spec. Conf.*, 2013.
- [149] S. Bowden, U. Das, S. Herasimenka, and R. Birkmire, "Stability of amorphous/crystalline silicon heterojunctions," *33<sup>rd</sup> IEEE Photovolt. Spec. Conf.*, 2008.
- [150] L. Zhang, B. Shu, R. Birkmire, S. Hegedus, and U. Das, "Impact of back surface patterning process on FF in IBC-SHJ," *38<sup>th</sup> IEEE Photovolt. Spec. Conf.*, 2012.
- [151] P. E. Gruenbaum, R. R. King, and R. M. Swanson, "Photoinjected hot-electron damage in silicon point-contact solar cells," *J. Appl. Phys.*, vol. 66, no. 12, pp. 6110–6114, Dec. 1989.
- [152] R. R. King, R. A. Sinton, and R. M. Swanson, "Front and back surface fields for point-contact solar cells," *Conference Record of the Twentieth IEEE Photovolt. Spec. Conf.*, 1988.

- [153] F. Granek, C. Reichel, M. Hermle, D. M. Huljić, O. Schultz, S. W. Glunz, "Front surface passivation of n-type high-efficiency back-junction silicon solar cells using front surface field," *22<sup>nd</sup> EU PVSEC*, Sep. 2007.
- [154] M. Bivour, M. Rüdiger, C. Reichel, K.-U. Ritzau, M. Hermle, and S. W. Glunz, "Analysis of the diffused front surface field of n-type silicon solar cells with a-Si/c-Si heterojunction rear emitter," *Energy Procedia*, vol. 8, pp. 185–192, Apr. 2011.
- [155] F. Granek, M. Hermle, C. Reichel, A. Grohe, O. Schultz-Wittmann, and S. Glunz, "Positive effects of front surface field in high-efficiency back-contact back-junction n-type silicon solar cells," *33<sup>rd</sup> IEEE Photovolt. Spec. Conf.*, 2008.
- [156] F. Granek, M. Hermle, D. M. Huljić, O. Schultz-Wittmann, and S. W. Glunz, "Enhanced lateral current transport via the front N<sup>+</sup> diffused layer of n-type high-efficiency back-junction back-contact silicon solar cells," *Prog. Photovolt: Res. Appl.*, vol. 17, no. 1, pp. 47–56, Jan. 2009.
- [157] C. S. Solanki and H. K. Singh, "Anti-reflection and light trapping in c-Si solar cells," Springer Singapore, 2017.
- [158] D. Diouf, J. P. Kleider, T. Desrues, P. -J. Ribeyron, "Effects of the front surface field in n-type interdigitated back contact silicon heterojunctions solar cells," *Energy Procedia*, vol. 2, pp. 59–64, 2010.
- [159] C. T. Sah and F. A. Lindholm, and J. G. Fossum, "A high-low junction emitter structure for improving silicon solar cell efficiency," *IEEE Trans. on Electron Devices*, vol. ed-25, no. 1, pp. 66–67, Jan. 1978.
- [160] J. Haschke, Y.-Y. Chen, R. Gogolin, M. Mews, N. Mingirulli, L. Korte, and B. Rech, "Approach for a Simplified Fabrication Process for IBC-SHJ Solar Cells with High Fill Factors," *Energy Procedia*, vol. 38, pp. 732–736, 2013.
- [161] R. Keding, M. Hendrichs, D. Stüwe, M. Jahn, C. Reichel, D. Borchert, A. Wolf, H. Reinecke, D. Biro, "POCL3-based co-diffusion process for n-type back-contact back-junction solar cells," *29<sup>th</sup> EU PVSEC*, Sep. 2014.
- [162] A. Kimmerle, R. Woehl, A. Wolf, and D. Biro, "Simplified front surface field formation for back contacted silicon solar cells," *Energy Procedia*, vol. 38, pp. 278–282, 2013.

- [163] D. A. Clugston, P. A. Basore, "PC1D version 5: 32-bit solar cell modeling on personal computers," *Conference Record of the Twenty-Sixth IEEE Photovolt. Spec. Conf.*, 1997.
- [164] A. G. Aberle, S. W. Glunz, and A. W. Stephens, "High-efficiency silicon solar cells: Si/SiO<sub>2</sub> interface parameters and their impact on device performance," *Prog. Photovolt: Res. Appl.*, vol. 2, no. 4, pp. 265–273, Oct. 1994.
- [165] J. Benick, K. Zimmermann, J. Spiegelman, M. Hermle, and S. W. Glunz, "Rear side passivation of PERC-type solar cells by wet oxides grown from purified steam," *Prog. Photovolt: Res. Appl.*, vol. 19, no. 3, pp. 361–365, Jul. 2010.
- [166] A. G. Aberle, "Overview on SiN surface passivation of crystalline silicon solar cells," *Sol. Energ. Mater. Sol. Cells*, vol. 65, no. 1–4, pp. 239–248, Jan. 2001.
- [167] Y. Wan, K. R. McIntosh, and A. F. Thomson, "Characterisation and optimisation of PECVD SiN<sub>x</sub> as an antireflection coating and passivation layer for silicon solar cells," *AIP Advances*, vol. 3, no. 3, p. 032113, 2013.
- [168] W.-C. Wang, C.-W. Lin, H.-J. Chen, C.-W. Chang, J.-J. Huang, M.-J. Yang, B. Tjahjono, J.-J. Huang, W.-C. Hsu, and M.-J. Chen, "Surface passivation of efficient nanotextured black silicon solar cells using thermal atomic layer deposition," *ACS Appl. Mater. Interfaces*, vol. 5, no. 19, pp. 9752–9759, Sep. 2013.
- [169] G. Dingemans, R. Seguin, P. Engelhart, M. C. M. van de Sanden, and W. M. M. Kessels, "Silicon surface passivation by ultrathin Al<sub>2</sub>O<sub>3</sub> films synthesized by thermal and plasma atomic layer deposition," *Physica Status Solidi-Rapid Research Letters*, vol. 4, no. 1, pp. 10–12, Feb. 2010.
- [170] D. K. Simon, P. M. Jordan, T. Mikolajick, and I. Dirnstorfer, "On the Control of the Fixed Charge Densities in Al<sub>2</sub>O<sub>3</sub>-Based Silicon Surface Passivation Schemes," *ACS Appl. Mater. Interfaces*, vol. 7, no. 51, pp. 28215–28222, Dec. 2015.
- [171] U. K. Das, M. Z. Burrows, M. Lu, S. Bowden, and R. W. Birkmire, "Surface passivation and heterojunction cells on Si (100) and (111) wafers using dc and rf plasma deposited Si:H thin films," *Appl. Phys. Lett.*, vol. 92, no. 6, pp. 063504, Feb. 2008.

- [172] W. Liu, F. Meng, X. Zhang, and Z. Liu, "Evolution of a Native Oxide Layer at the a-Si:H/c-Si Interface and Its Influence on a Silicon Heterojunction Solar Cell," *ACS Appl. Mater. Interfaces*, vol. 7, no. 48, pp. 26522–26529, Nov. 2015.
- [173] E. Kaxiras, "Semiconductor-surface restoration by valence-mending adsorbates: Application to Si(100):S and Si(100):Se," *Phys. Rev. B*, vol. 43, no. 8, pp. 6824–6827, Mar. 1991.
- [174] T. Hahn, H. Metzner, B. Plikat, and M. Seibt, "Epitaxial growth of CuInS<sub>2</sub> on sulphur terminated Si(001)," *Appl. Phys. Lett.*, vol. 72, no. 21, pp. 2733–2735, May 1998.
- [175] J. Roche, P. Ryan, and G. Hughes, "Core-level photoemission studies of the sulphur-terminated Si (100) surface," *Surf. Sci.*, vol. 465, n. 1–2, pp. 115–119, Oct. 2000.
- [176] J. P. Lacharme, N. Benazzi, and C. A. Sébenne, "Compositional and electronic properties of Si(001)2 x 1 upon diatomic sulfur interaction," *Surf. Sci.*, vol. 433, pp. 415–419, Aug. 1999.
- [177] A. Papageorgopoulos, A. Corner, M. Kamaratos, and C. A. Papageorgopoulos, "Adsorption of elemental S on Si(100)2×1: Surface restoration," *Phys. Rev. B*, vol. 55, no. 7, pp. 4435–4441, Feb. 1997.
- [178] M. Y. Ali and M. Tao, "Passivation of Si(100) surface by S from a solution and its effect on Schottky barrier height," *ECS Trans*, vol. 6, pp. 489–497, Jun. 2015.
- [179] M. Y. Ali and M. Tao, "Effect of sulfur passivation of silicon (100) on Schottky barrier height: Surface states versus surface dipole," *J. Appl. Phys.*, vol. 101, no. 10, pp. 103708, May 2007.
- [180] H.-F. Zhang, A. Saha, W.-C. Sun, and M. Tao, "Characterization of Al/Si junctions on Si(100) wafers with chemical vapor deposition-based sulfur passivation," *Appl. Phys. A*, vol. 116, no. 4, pp. 2031–2038, Mar. 2014.
- [181] G. C. Smith, "Surface Analysis by Electron Spectroscopy," Springer, Boston, MA, 1994.
- [182] A. Richter, J. Benick, M. Hermle, and S. W. Glunz, "Excellent silicon surface passivation with 5 Å thin ALD Al<sub>2</sub>O<sub>3</sub> layers: Influence of different thermal post-deposition treatments," *Phys. Status Solidi RRL*, vol. 5, no. 5–6, pp. 202–204, May 2011.

- [183] P. Saint-Cast, J. Benick, D. Kania, L. Weiss, M. Hofmann, J. Rentsch, R. Preu, and S. W. Glunz, "High-efficiency c-Si solar cells passivated with ALD and PECVD aluminum oxide," *IEEE Electron Device Lett.*, vol. 31, no. 7, pp. 695–697, Jul. 2010.
- [184] G. Dingemans, M. C. M. van de Sanden, and W. M. M. Kessels, "Influence of the deposition temperature on the c-Si surface passivation by  $\text{Al}_2\text{O}_3$  films synthesized by ALD and PECVD," *Electrochem. Solid-State Lett.*, vol. 13, no. 3, pp. H76–H79, Mar. 2010.
- [185] G. Dingemans, M. C. M. van de Sanden, and W. M. M. Kessels, "Excellent Si surface passivation by low temperature  $\text{SiO}_2$  using an ultrathin  $\text{Al}_2\text{O}_3$  capping film," *Phys. Status Solidi RRL*, vol. 5, no. 1, pp. 22–24, Jan. 2011.
- [186] "XPS Interpretation of Silicon," by Thermo Scientific.
- [187] F. J. Himpsel, F. R. McFeely, A. Taleb-Ibrahimi, J. A. Yarmoff, and G. Hollinger, "Microscopic structure of the  $\text{SiO}_2/\text{Si}$  interface," *Phys. Rev. B*, vol. 38, no. 9, pp. 6084–6096, Sep. 1988.
- [188] W. E. Morgan and J. R. Van Wazer, "Binding energy shifts in the x-ray photoelectron spectra of a series of related group IV-a compounds," *J. Phys. Chem.*, vol. 77, no. 7, 1973.
- [189] Y. -H. Lai, C. -T. Yeh, Y. -H. Lin, and W. -H. Hung, "Adsorption and thermal decomposition of  $\text{H}_2\text{S}$  on  $\text{Si}(100)$ ," *Surf. Sci.*, vol. 519, no. 1, pp. 150–156, 2002.
- [190] D. S. Jensen, S. S. Kanyal, N. Madaan, M. A. Vail, A. E. Dadson, M. H. Engelhard, and M. R. Linford, "Silicon (100)/ $\text{SiO}_2$  by XPS," *Surf. Sci. Spec.*, vol. 20, no. 1, pp. 36–42, Dec. 2013.
- [191] U. Höfer, L. Li, and T. F. Heinz, "Desorption of hydrogen from  $\text{Si}(100)2\times 1$  at low coverages: The influence of  $\pi$ -bonded dimers on the kinetics," *Phys. Rev. B*, vol. 45, no. 16, pp. 9485–9488, Apr. 1992.
- [192] M. Han, Y. Luo, N. Camillone, and R. M. Osgood Jr., "Reaction of  $\text{H}_2\text{S}$  with  $\text{Si}(100)$ ," *J. Phys. Chem. B*, vol. 104, no. 28, pp. 6576–6583, Jul. 2000.
- [193] G. F. Kraus, J. A. Nuth III, R. N. Nelson, "Is  $\text{SiS}_2$  the carrier of the unidentified 21 micron emission feature?" *Astron. Astrophys.*, vol. 328, pp. 419–425, Mar. 1997.

- [194] P. A. G. O'hare, "Thermochemistry of silicon-containing materials," *Pure Appl. Chem.*, vol. 71, no. 7, pp. 1243–1248, Jul. 1999.
- [195] A. Haas, "The chemistry of silicon-sulfur compounds," *Angewandte Chemie International Edition in English*, vol. 4, no. 12, pp. 1014–1023, Dec. 1965.
- [196] Zhan Shu Doctoral Dissertation, University of Delaware, 2013.
- [197] A. K. Ghosh, C. Fishman, and T. Feng, "Theory of the electrical and photovoltaic properties of polycrystalline silicon," *J. Appl. Phys.*, vol. 51, no. 1, pp. 446–454, Jan. 1980.
- [198] S. Ashok and S. A. Ringel, "Low-energy hydrogen implantation for silicon Schottky barrier modification," *Vacuum*, vol. 36, no. 11/12, pp. 917–920, 1986.
- [199] H.-Y. Liu, U. K. Das, S. Hegedus, Z. E. Voras, T. P. Beebe Jr., and R. Birkmire, "Si surface passivation by H<sub>2</sub>S reaction for c-Si solar cell ," *Electronic Materials Conf.*, Jun. 2016.
- [200] H. Y. Liu, U. K. Das, R. W. Birkmire, "Surface defect passivation and reaction of c-Si in H<sub>2</sub>S," *Langmuir*, vol. 33, no. 51, pp. 14580–14585, Dec. 2017.
- [201] A. Saha, H. Zhang, and W. C. Sun, "A new method for bulk passivation in multicrystalline-Si by sulfur," *42<sup>nd</sup> IEEE Photovolt. Spec. Conf.*, 2015.
- [202] B. Chhabra, S. Bowden, R. L. Opila, and C. B. Honsberg, "High effective minority carrier lifetime on silicon substrates using quinhydrone-methanol passivation," *Appl. Phys. Lett.*, vol. 96, no. 6, pp. 063502, Feb. 2010.
- [203] J. R. Haynes and J. A. Hornbeck, "Trapping of Minority Carriers in Silicon. II. n-Type Silicon," *Phys. Rev.*, vol. 100, no. 2, pp. 606–615, Oct. 1955.
- [204] D. Macdonald and A. Cuevas, "Trapping of minority carriers in multicrystalline silicon," *Appl. Phys. Lett.*, vol. 74, no. 12, pp. 1710–1712, Mar. 1999.
- [205] H. Y. FAN, "Effect of Traps on Carrier Injection in Semiconductors," *Phys. Rev.*, vol. 92, no. 6, pp. 1424–1428, Dec. 1953.
- [206] D. W. Kim, J.-W. Song, Y. M. Park, J.-H. Lee, and T. J. Park, "Novel field-effect passivation for nanostructured Si solar cells using interfacial sulfur incorporation," *Prog. Photovolt: Res. Appl.*, vol. 25, no. 5, pp. 376–383, Feb. 2017.

- [207] B. Shu, U. Das, J. Appel, B. McCandless, S. Hegedus, and R. Birkmire, "Alternative approaches for low temperature front surface passivation of interdigitated back contact silicon heterojunction solar cell," *35<sup>th</sup> IEEE Photovolt. Spec. Conf.*, 2010.
- [208] S. Joonwichien, S. Matsushima, and N. Usami, "Effects of crystal defects and their interactions with impurities on electrical properties of multicrystalline Si," *J. Appl. Phys.*, vol. 113, no. 13, pp. 133503, Apr. 2013.
- [209] D. Macdonald and A. Cuevas, "Understanding carrier trapping in multicrystalline silicon," *Sol. Energ. Mater. Sol. Cells*, vol. 65, no. 1–4, pp. 509–516, Jan. 2001.
- [210] A. Cuevas, M. Stocks, D. McDonald, M. Kerr, and C. Samundsett, "Recombination and trapping in multicrystalline silicon," *IEEE Trans. on Electron Devices*, vol. 46, no. 10, Oct. 1999.
- [211] P. Gundel, M. C. Schubert, and W. Warta, "Origin of trapping in multicrystalline silicon," *J. Appl. Phys.*, vol. 104, no. 7, pp. 73716, 2008.
- [212] Irradiation spectrum:  
<http://www.superstrate.net/pv/illumination/spectrum.html>.

## Appendix A

### SOLAR SPECTRAL IRRADIANCE: AM1.5 AND AM0

The solar cell efficiency  $\eta$  is defined as  $P_{\text{out}}/P_{\text{in}}$  where  $P_{\text{out}}$  is the electrical power generated per unit area and  $P_{\text{in}}$  is the power density of the solar irradiation. The value of  $P_{\text{in}}$  varies considerably for different applications and conditions, where it changes throughout the day and with locations. The standard reference spectra are defined to allow the comparison of PV device performances from different manufacturers and research laboratories.

The standard spectrum for space application is referred to as AM0, where the solar insolation is outside the earth's atmosphere. It has an integrated power of 1366.1 W/m<sup>2</sup>, presented as the red curve in Figure A.

Two standard spectra are defined for terrestrial usage at the earth's surface, with its radiation intensity reduced from AM0 due to scattering and absorption that occur in the atmosphere. The amount by which the radiation is reduced depends on the length of the optical path through the atmosphere varying by the sun's location in the sky, which is determined by the time of the day, time of the year, and latitude of the observer. When the sun is directly overhead at sea level and without clouds, the radiation will be at its maximum, which is referred to as air mass one (AM1) radiation. In other cases, the air mass (AM) is then defined as

$$\text{Air mass} = 1 / \cos\theta$$



where  $\theta = 0$  corresponds to the sun being directly overhead.

For terrestrial applications, AM1.5 (48° from overhead) has been established as the standard solar irradiation, which corresponds to a power density  $P_{in}$  of 100 mW/cm<sup>2</sup> or 1000W/m<sup>2</sup>.

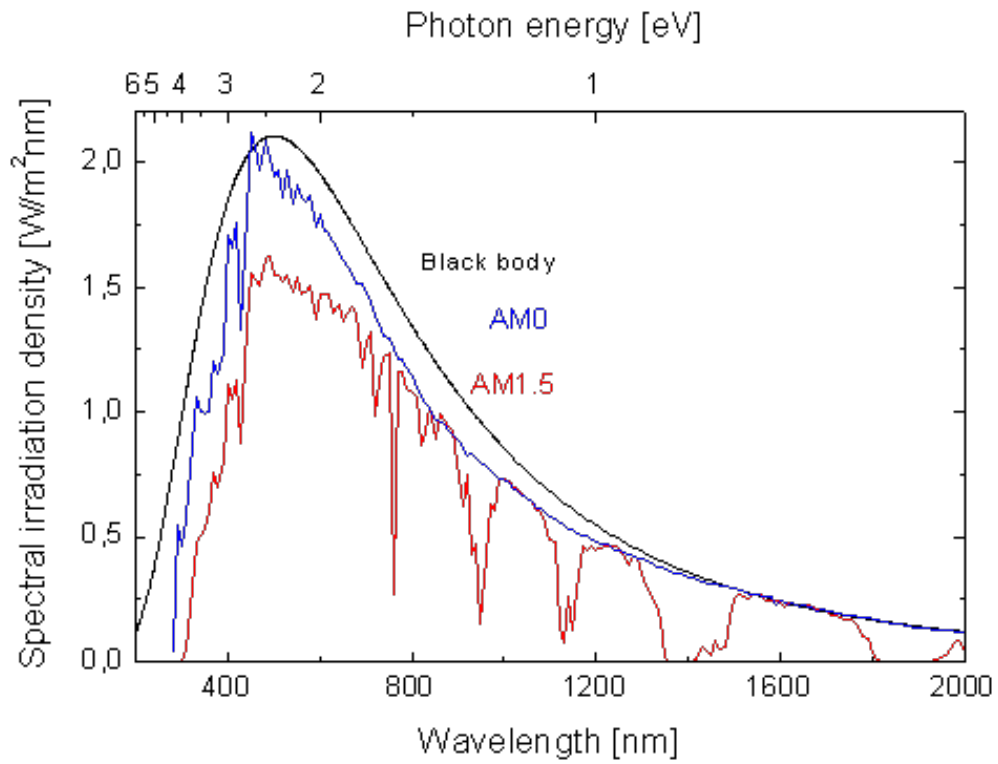


Figure A.1 Spectral distribution of sunlight for the cases AM1.5 and AM0, with the ideal black body radiation at 5800 K for comparison [212].



## Appendix B


### REPRINT PERMISSION LETTERS


#### Reprint permission for Figure 2.4

Rightslink® by Copyright Clearance Center

4/1/18, 8:09 PM



[Home](#) [Account Info](#) [Help](#) 



**Title:** Approaching efficiencies above 25% with both sides-contacted silicon solar cells

**Conference Proceedings:** Photovoltaic Specialist Conference (PVSC), 2015 IEEE 42nd

**Author:** Martin Hermle

**Publisher:** IEEE

**Date:** June 2015

Copyright © 2015, IEEE

Logged in as:  
Hsiang-Yu Liu

[LOGOUT](#)

#### Thesis / Dissertation Reuse

**The IEEE does not require individuals working on a thesis to obtain a formal reuse license, however, you may print out this statement to be used as a permission grant:**

*Requirements to be followed when using any portion (e.g., figure, graph, table, or textual material) of an IEEE copyrighted paper in a thesis:*

- 1) In the case of textual material (e.g., using short quotes or referring to the work within these papers) users must give full credit to the original source (author, paper, publication) followed by the IEEE copyright line © 2011 IEEE.
- 2) In the case of illustrations or tabular material, we require that the copyright line © [Year of original publication] IEEE appear prominently with each reprinted figure and/or table.
- 3) If a substantial portion of the original paper is to be used, and if you are not the senior author, also obtain the senior author's approval.

*Requirements to be followed when using an entire IEEE copyrighted paper in a thesis:*

- 1) The following IEEE copyright/ credit notice should be placed prominently in the references: © [year of original publication] IEEE. Reprinted, with permission, from [author names, paper title, IEEE publication title, and month/year of publication]
- 2) Only the accepted version of an IEEE copyrighted paper can be used when posting the paper or your thesis on-line.
- 3) In placing the thesis on the author's university website, please display the following message in a prominent place on the website: In reference to IEEE copyrighted material which is used with permission in this thesis, the IEEE does not endorse any of [university/educational entity's name goes here]'s products or services. Internal or personal use of this material is permitted. If interested in reprinting/republishing IEEE copyrighted material for advertising or promotional purposes or for creating new collective works for resale or redistribution, please go to [http://www.ieee.org/publications\\_standards/publications/rights/rights\\_link.html](http://www.ieee.org/publications_standards/publications/rights/rights_link.html) to learn how to obtain a License from RightsLink.

If applicable, University Microfilms and/or ProQuest Library, or the Archives of Canada may supply single copies of the dissertation.

[BACK](#)

[CLOSE WINDOW](#)

Copyright © 2018 Copyright Clearance Center, Inc. All Rights Reserved. [Privacy statement](#). [Terms and Conditions](#).  
Comments? We would like to hear from you. E-mail us at [customer@copyright.com](mailto:customer@copyright.com)

## Reprint Permission for Figure 2.5

RightsLink Printable License

4/1/18, 8:44 PM

### SPRINGER NATURE LICENSE TERMS AND CONDITIONS

Apr 01, 2018

This Agreement between Hsiang ("You") and Springer Nature ("Springer Nature") consists of your license details and the terms and conditions provided by Springer Nature and Copyright Clearance Center.

License Number	4320490376528
License date	Apr 01, 2018
Licensed Content Publisher	Springer Nature
Licensed Content Publication	Nature Energy
Licensed Content Title	Silicon heterojunction solar cell with interdigitated back contacts for a photoconversion efficiency over 26%
Licensed Content Author	Kunta Yoshikawa, Hayato Kawasaki, Wataru Yoshida, Toru Irie, Katsunori Konishi et al.
Licensed Content Date	Mar 20, 2017
Licensed Content Volume	2
Licensed Content Issue	5
Type of Use	Thesis/Dissertation
Requestor type	academic/university or research institute
Format	print and electronic
Portion	figures/tables/illustrations
Number of figures/tables/illustrations	1
High-res required	no
Will you be translating?	no
Circulation/distribution	<501
Author of this Springer Nature content	no
Title	Silicon Defect Passivation by H <sub>2</sub> S Reaction and Patterning Process of Interdigitated Back Contact Silicon Heterojunction (IBC-SHJ) Solar Cell
Instructor name	Robert Birkmire
Institution name	Institute of Energy Conversion
Expected presentation date	May 2018
Portions	Figure 1, used in the "Literature Review" chapter in my thesis, stating that the current world record cell of IBC-SHJ structure is achieved by Kaneka.
Requestor Location	Hsiang-Yu Liu 451 Wyoming Rd  NEWARK, DE 19716 United States Attn: Hsiang-Yu Liu
Billing Type	Invoice
Billing Address	Hsiang-Yu Liu 451 Wyoming Rd  NEWARK, DE 19716 United States Attn: Hsiang-Yu Liu
Total	0.00 USD
Terms and Conditions	

#### Springer Nature Terms and Conditions for RightsLink Permissions

**Springer Customer Service Centre GmbH (the Licensor)** hereby grants you a non-exclusive, world-wide licence to reproduce the material and for the purpose and requirements specified in the attached copy of your order form, and for no other use, subject to the conditions below:

1. The Licensor warrants that it has, to the best of its knowledge, the rights to license reuse of this material. However, you should ensure that the material you are requesting is original to the Licensor and does not carry the copyright of another entity (as credited in the published version).

If the credit line on any part of the material you have requested indicates that it was reprinted or adapted with permission from another source, then you should also seek permission from that source to reuse the material.

2. Where **print only** permission has been granted for a fee, separate permission must be obtained for any additional electronic re-use.

3. Permission granted **free of charge** for material in print is also usually granted for any electronic version of that work, provided that the material is incidental to your work as a whole and that the electronic version is essentially equivalent to, or substitutes for, the print version.
4. A licence for 'post on a website' is valid for 12 months from the licence date. This licence does not cover use of full text articles on websites.
5. Where '**reuse in a dissertation/thesis**' has been selected the following terms apply: Print rights for up to 100 copies, electronic rights for use only on a personal website or institutional repository as defined by the Sherpa guideline ([www.sherpa.ac.uk/romeo/](http://www.sherpa.ac.uk/romeo/)).
6. Permission granted for books and journals is granted for the lifetime of the first edition and does not apply to second and subsequent editions (except where the first edition permission was granted free of charge or for signatories to the STM Permissions Guidelines <http://www.stm-assoc.org/copyright-legal-affairs/permissions/permissions-guidelines/>), and does not apply for editions in other languages unless additional translation rights have been granted separately in the licence.
7. Rights for additional components such as custom editions and derivatives require additional permission and may be subject to an additional fee. Please apply to [Journalpermissions@springernature.com](mailto:Journalpermissions@springernature.com) or [bookpermissions@springernature.com](mailto:bookpermissions@springernature.com) for these rights.
8. The Licensor's permission must be acknowledged next to the licensed material in print. In electronic form, this acknowledgement must be visible at the same time as the figures/tables/illustrations or abstract, and must be hyperlinked to the journal/book's homepage. Our required acknowledgement format is in the Appendix below.
9. Use of the material for incidental promotional use, minor editing privileges (this does not include cropping, adapting, omitting material or any other changes that affect the meaning, intention or moral rights of the author) and copies for the disabled are permitted under this licence.
10. Minor adaptations of single figures (changes of format, colour and style) do not require the Licensor's approval. However, the adaptation should be credited as shown in Appendix below.

#### **Appendix — Acknowledgements:**

##### **For Journal Content:**

Reprinted by permission from [the Licensor]: [Journal Publisher (e.g. Nature/Springer/Palgrave)] [JOURNAL NAME] [REFERENCE CITATION (Article name, Author(s) Name), [COPYRIGHT] (year of publication)]

##### **For Advance Online Publication papers:**

Reprinted by permission from [the Licensor]: [Journal Publisher (e.g. Nature/Springer/Palgrave)] [JOURNAL NAME] [REFERENCE CITATION (Article name, Author(s) Name), [COPYRIGHT] (year of publication), advance online publication, day month year (doi: 10.1038/sj.[JOURNAL ACRONYM].)]

##### **For Adaptations/Translations:**

Adapted/Translated by permission from [the Licensor]: [Journal Publisher (e.g. Nature/Springer/Palgrave)] [JOURNAL NAME] [REFERENCE CITATION (Article name, Author(s) Name), [COPYRIGHT] (year of publication)]

##### **Note: For any republication from the British Journal of Cancer, the following credit line style applies:**

Reprinted/adapted/translated by permission from [the Licensor]: on behalf of Cancer Research UK: : [Journal Publisher (e.g. Nature/Springer/Palgrave)] [JOURNAL NAME] [REFERENCE CITATION (Article name, Author(s) Name), [COPYRIGHT] (year of publication)]

##### **For Advance Online Publication papers:**

Reprinted by permission from The [the Licensor]: on behalf of Cancer Research UK: [Journal Publisher (e.g. Nature/Springer/Palgrave)] [JOURNAL NAME] [REFERENCE CITATION (Article name, Author(s) Name), [COPYRIGHT] (year of publication), advance online publication, day month year (doi: 10.1038/sj.[JOURNAL ACRONYM].)]

##### **For Book content:**

Reprinted/adapted by permission from [the Licensor]: [Book Publisher (e.g. Palgrave Macmillan, Springer etc)] [Book Title] by [Book author(s)] [COPYRIGHT] (year of publication)

#### **Other Conditions:**

Version 1.0

Questions? [customercare@copyright.com](mailto:customercare@copyright.com) or +1-855-239-3415 (toll free in the US) or +1-978-646-2777.

## Reprint Permission for Figure 2.8

RightsLink Printable License

4/1/18, 8:58 PM

### AIP PUBLISHING LICENSE TERMS AND CONDITIONS

Apr 01, 2018

This Agreement between Hsiang ("You") and AIP Publishing ("AIP Publishing") consists of your license details and the terms and conditions provided by AIP Publishing and Copyright Clearance Center.

License Number	4320491407960
License date	Apr 01, 2018
Licensed Content Publisher	AIP Publishing
Licensed Content Publication	Journal of Vacuum Science & Technology A
Licensed Content Title	Status and prospects of Al <sub>2</sub> O <sub>3</sub> -based surface passivation schemes for silicon solar cells
Licensed Content Author	G. Dingemans, W. M. M. Kessels
Licensed Content Date	Jul 1, 2012
Licensed Content Volume	30
Licensed Content Issue	4
Type of Use	Thesis/Dissertation
Requestor type	Student
Format	Print and electronic
Portion	Figure/Table
Number of figures/tables	1
Title of your thesis / dissertation	Silicon Defect Passivation by H <sub>2</sub> S Reaction and Patterning Process of Interdigitated Back Contact Silicon Heterojunction (IBC-SHJ) Solar Cell
Expected completion date	May 2018
Estimated size (number of pages)	1
Requestor Location	Hsiang-Yu Liu 451 Wyoming Rd  NEWARK, DE 19716 United States Attn: Hsiang-Yu Liu
Billing Type	Invoice
Billing Address	Hsiang-Yu Liu 451 Wyoming Rd

NEWARK, DE 19716  
United States  
Attn: Hsiang-Yu Liu

Total 0.00 USD

#### Terms and Conditions

##### American Vacuum Society -- Terms and Conditions: Permissions Uses

American Vacuum Society ("AVS") hereby grants to you the non-exclusive right and license to use and/or distribute the Material according to the use specified in your order, on a one-time basis, for the specified term, with a maximum distribution equal to the number that you have ordered. Any links or other content accompanying the Material are not the subject of this license.

1. You agree to include the following copyright and permission notice with the reproduction of the Material: "Reprinted with permission from [FULL CITATION]. Copyright [PUBLICATION YEAR], American Vacuum Society." For an article, the copyright and permission notice must be printed on the first page of the article or book chapter. For photographs, covers, or tables, the copyright and permission notice may appear with the Material, in a footnote, or in the reference list.
2. If you have licensed reuse of a figure, photograph, cover, or table, it is your responsibility to ensure that the material is original to AVS and does not contain the copyright of another entity, and that the copyright notice of the figure, photograph, cover, or table does not indicate that it was reprinted by AVS, with permission, from another source. Under no circumstances does AVS, purport or intend to grant permission to reuse material to which it does not hold copyright.
3. You may not alter or modify the Material in any manner. You may translate the Material into another language only if you have licensed translation rights. You may not use the Material for promotional purposes. AVS reserves all rights not specifically granted herein.
4. The foregoing license shall not take effect unless and until AVS or its agent, Copyright Clearance Center, receives the Payment in accordance with Copyright Clearance Center Billing and Payment Terms and Conditions, which are incorporated herein by reference.
5. AVS or the Copyright Clearance Center may, within two business days of granting this license, revoke the license for any reason whatsoever, with a full refund payable to you. Should you violate the terms of this license at any time, AVS, American Vacuum Society, or Copyright Clearance Center may revoke the license with no refund to you. Notice of such revocation will be made using the contact information provided by you. Failure to receive such notice will not nullify the revocation.
6. AVS makes no representations or warranties with respect to the Material. You agree to indemnify and hold harmless AVS, American Vacuum Society, and their officers, directors, employees or agents from and against any and all claims arising out of your use of the Material other than as specifically authorized herein.
7. The permission granted herein is personal to you and is not transferable or assignable without the prior written permission of AVS. This license may not be amended except in a writing signed by the party to be charged.
8. If purchase orders, acknowledgments or check endorsements are issued on any forms containing terms and conditions which are inconsistent with these provisions, such inconsistent terms and conditions shall be of no force and effect. This document, including the CCC Billing and Payment Terms and Conditions, shall be the entire agreement between the parties relating to the subject matter hereof.

This Agreement shall be governed by and construed in accordance with the laws of the State of New York. Both parties hereby submit to the jurisdiction of the courts of New York County for purposes of resolving any disputes that may arise hereunder.

**Questions? [customercare@copyright.com](mailto:customercare@copyright.com) or +1-855-239-3415 (toll free in the US) or +1-978-646-2777.**

## Reprint Permission for Figure 2.10

### JOHN WILEY AND SONS LICENSE TERMS AND CONDITIONS

Apr 01, 2018

This Agreement between Hsiang ("You") and John Wiley and Sons ("John Wiley and Sons") consists of your license details and the terms and conditions provided by John Wiley and Sons and Copyright Clearance Center.

License Number	4320500237755
License date	Apr 01, 2018
Licensed Content Publisher	John Wiley and Sons
Licensed Content Publication	Progress in Photovoltaics
Licensed Content Title	Chemical natures and distributions of metal impurities in multicrystalline silicon materials
Licensed Content Author	T. Buonassisi, A. A. Istratov, M. D. Pickett, et al
Licensed Content Date	May 2, 2006
Licensed Content Volume	14
Licensed Content Issue	6
Licensed Content Pages	19
Type of use	Dissertation/Thesis
Requestor type	University/Academic
Format	Print and electronic
Portion	Figure/table
Number of figures/tables	1
Original Wiley figure/table number(s)	Figure 1.
Will you be translating?	No
Title of your thesis / dissertation	Silicon Defect Passivation by H <sub>2</sub> S Reaction and Patterning Process of Interdigitated Back Contact Silicon Heterojunction (IBC-SHJ) Solar Cell
Expected completion date	May 2018
Expected size (number of pages)	1
Requestor Location	Hsiang-Yu Liu 451 Wyoming Rd  NEWARK, DE 19716 United States Attn: Hsiang-Yu Liu

Publisher Tax ID EU826007151

Total 0.00 USD

[Terms and Conditions](#)

### TERMS AND CONDITIONS

This copyrighted material is owned by or exclusively licensed to John Wiley & Sons, Inc. or one of its group companies (each a "Wiley Company") or handled on behalf of a society with which a Wiley Company has exclusive publishing rights in relation to a particular work (collectively "WILEY"). By clicking "accept" in connection with completing this licensing transaction, you agree that the following terms and conditions apply to this transaction (along with the billing and payment terms and conditions established by the Copyright Clearance Center Inc., ("CCC's Billing and Payment terms and conditions"), at the time that you opened your RightsLink account (these are available at any time at <http://myaccount.copyright.com>).

#### Terms and Conditions

- The materials you have requested permission to reproduce or reuse (the "Wiley Materials") are protected by copyright.
- You are hereby granted a personal, non-exclusive, non-sub licensable (on a stand-alone basis), non-transferable, worldwide, limited license to reproduce the Wiley Materials for the purpose specified in the licensing process. This license, **and any CONTENT (PDF or image file) purchased as part of your order**, is for a one-time use only and limited to any maximum distribution number specified in the license. The first instance of republication or reuse granted by this license must be completed within two years of the date of the grant of this license (although copies prepared before the end date may be distributed thereafter). The Wiley Materials shall not be used in any other manner or for any other purpose, beyond what is granted in the license. Permission is granted subject to an appropriate acknowledgement given to the author, title of the material/book/journal and the publisher. You shall also duplicate the copyright notice that appears in the Wiley publication in your use of the Wiley Material. Permission is also granted on the understanding that nowhere in the text is a previously published source acknowledged for all or part of this Wiley Material. Any third party content is expressly excluded from this permission.
- With respect to the Wiley Materials, all rights are reserved. Except as expressly granted by the terms of the license, no part of the Wiley Materials may be copied, modified, adapted (except for minor reformatting required by the new Publication), translated, reproduced, transferred or distributed, in any form or by any means, and no derivative works may be made based on the Wiley Materials without the prior permission of the respective copyright owner. **For STM Signatory Publishers clearing permission under the terms of the [STM Permissions Guidelines](#) only, the terms of the license are extended to include subsequent editions and for editions in other languages, provided such editions are for the work as a whole in situ and does not involve the separate exploitation of the permitted figures or extracts,** You may not alter, remove or suppress in any manner any copyright, trademark or



other notices displayed by the Wiley Materials. You may not license, rent, sell, loan, lease, pledge, offer as security, transfer or assign the Wiley Materials on a stand-alone basis, or any of the rights granted to you hereunder to any other person.

- The Wiley Materials and all of the intellectual property rights therein shall at all times remain the exclusive property of John Wiley & Sons Inc, the Wiley Companies, or their respective licensors, and your interest therein is only that of having possession of and the right to reproduce the Wiley Materials pursuant to Section 2 herein during the continuance of this Agreement. You agree that you own no right, title or interest in or to the Wiley Materials or any of the intellectual property rights therein. You shall have no rights hereunder other than the license as provided for above in Section 2. No right, license or interest to any trademark, trade name, service mark or other branding ("Marks") of WILEY or its licensors is granted hereunder, and you agree that you shall not assert any such right, license or interest with respect thereto
- NEITHER WILEY NOR ITS LICENSORS MAKES ANY WARRANTY OR REPRESENTATION OF ANY KIND TO YOU OR ANY THIRD PARTY, EXPRESS, IMPLIED OR STATUTORY, WITH RESPECT TO THE MATERIALS OR THE ACCURACY OF ANY INFORMATION CONTAINED IN THE MATERIALS, INCLUDING, WITHOUT LIMITATION, ANY IMPLIED WARRANTY OF MERCHANTABILITY, ACCURACY, SATISFACTORY QUALITY, FITNESS FOR A PARTICULAR PURPOSE, USABILITY, INTEGRATION OR NON-INFRINGEMENT AND ALL SUCH WARRANTIES ARE HEREBY EXCLUDED BY WILEY AND ITS LICENSORS AND WAIVED BY YOU.
- WILEY shall have the right to terminate this Agreement immediately upon breach of this Agreement by you.
- You shall indemnify, defend and hold harmless WILEY, its Licensors and their respective directors, officers, agents and employees, from and against any actual or threatened claims, demands, causes of action or proceedings arising from any breach of this Agreement by you.
- IN NO EVENT SHALL WILEY OR ITS LICENSORS BE LIABLE TO YOU OR ANY OTHER PARTY OR ANY OTHER PERSON OR ENTITY FOR ANY SPECIAL, CONSEQUENTIAL, INCIDENTAL, INDIRECT, EXEMPLARY OR PUNITIVE DAMAGES, HOWEVER CAUSED, ARISING OUT OF OR IN CONNECTION WITH THE DOWNLOADING, PROVISIONING, VIEWING OR USE OF THE MATERIALS REGARDLESS OF THE FORM OF ACTION, WHETHER FOR BREACH OF CONTRACT, BREACH OF WARRANTY, TORT, NEGLIGENCE, INFRINGEMENT OR OTHERWISE (INCLUDING, WITHOUT LIMITATION, DAMAGES BASED ON LOSS OF PROFITS, DATA, FILES, USE, BUSINESS OPPORTUNITY OR CLAIMS OF THIRD PARTIES), AND WHETHER OR NOT THE PARTY HAS BEEN ADVISED OF THE POSSIBILITY OF SUCH DAMAGES. THIS LIMITATION SHALL APPLY NOTWITHSTANDING ANY FAILURE OF ESSENTIAL PURPOSE OF ANY LIMITED REMEDY PROVIDED

## HEREIN.

- Should any provision of this Agreement be held by a court of competent jurisdiction to be illegal, invalid, or unenforceable, that provision shall be deemed amended to achieve as nearly as possible the same economic effect as the original provision, and the legality, validity and enforceability of the remaining provisions of this Agreement shall not be affected or impaired thereby.
- The failure of either party to enforce any term or condition of this Agreement shall not constitute a waiver of either party's right to enforce each and every term and condition of this Agreement. No breach under this agreement shall be deemed waived or excused by either party unless such waiver or consent is in writing signed by the party granting such waiver or consent. The waiver by or consent of a party to a breach of any provision of this Agreement shall not operate or be construed as a waiver of or consent to any other or subsequent breach by such other party.
- This Agreement may not be assigned (including by operation of law or otherwise) by you without WILEY's prior written consent.
- Any fee required for this permission shall be non-refundable after thirty (30) days from receipt by the CCC.
- These terms and conditions together with CCC's Billing and Payment terms and conditions (which are incorporated herein) form the entire agreement between you and WILEY concerning this licensing transaction and (in the absence of fraud) supersedes all prior agreements and representations of the parties, oral or written. This Agreement may not be amended except in writing signed by both parties. This Agreement shall be binding upon and inure to the benefit of the parties' successors, legal representatives, and authorized assigns.
- In the event of any conflict between your obligations established by these terms and conditions and those established by CCC's Billing and Payment terms and conditions, these terms and conditions shall prevail.
- WILEY expressly reserves all rights not specifically granted in the combination of (i) the license details provided by you and accepted in the course of this licensing transaction, (ii) these terms and conditions and (iii) CCC's Billing and Payment terms and conditions.
- This Agreement will be void if the Type of Use, Format, Circulation, or Requestor Type was misrepresented during the licensing process.
- This Agreement shall be governed by and construed in accordance with the laws of the State of New York, USA, without regards to such state's conflict of law rules. Any legal action, suit or proceeding arising out of or relating to these Terms and Conditions or the breach thereof shall be instituted in a court of competent jurisdiction in New York County in the State of New York in the United States of America and each party

hereby consents and submits to the personal jurisdiction of such court, waives any objection to venue in such court and consents to service of process by registered or certified mail, return receipt requested, at the last known address of such party.

#### **WILEY OPEN ACCESS TERMS AND CONDITIONS**

Wiley Publishes Open Access Articles in fully Open Access Journals and in Subscription journals offering Online Open. Although most of the fully Open Access journals publish open access articles under the terms of the Creative Commons Attribution (CC BY) License only, the subscription journals and a few of the Open Access Journals offer a choice of Creative Commons Licenses. The license type is clearly identified on the article.

##### **The Creative Commons Attribution License**

The [Creative Commons Attribution License \(CC-BY\)](#) allows users to copy, distribute and transmit an article, adapt the article and make commercial use of the article. The CC-BY license permits commercial and non-

##### **Creative Commons Attribution Non-Commercial License**

The [Creative Commons Attribution Non-Commercial \(CC-BY-NC\) License](#) permits use, distribution and reproduction in any medium, provided the original work is properly cited and is not used for commercial purposes.(see below)

##### **Creative Commons Attribution-Non-Commercial-NoDerivs License**

The [Creative Commons Attribution Non-Commercial-NoDerivs License](#) (CC-BY-NC-ND) permits use, distribution and reproduction in any medium, provided the original work is properly cited, is not used for commercial purposes and no modifications or adaptations are made. (see below)

##### **Use by commercial "for-profit" organizations**

Use of Wiley Open Access articles for commercial, promotional, or marketing purposes requires further explicit permission from Wiley and will be subject to a fee.

Further details can be found on Wiley Online Library

<http://olabout.wiley.com/WileyCDA/Section/id-410895.html>

#### **Other Terms and Conditions:**

**v1.10 Last updated September 2015**

**Questions? [customercare@copyright.com](mailto:customercare@copyright.com) or +1-855-239-3415 (toll free in the US) or +1-978-646-2777.**

## Reprint Permission for Figure 5.1, 5.4, 5.5, and 5.6 (a)

Rightslink® by Copyright Clearance Center

4/1/18, 9:22 PM



RightsLink®

Home

Account  
Info

Help



**Title:** Positive effects of front surface field in high-efficiency back-contact back-junction n-type silicon solar cells

**Conference Proceedings:** Photovoltaic Specialists Conference, 2008. PVSC '08. 33rd IEEE

**Author:** Filip Granek

**Publisher:** IEEE

**Date:** May 2008

Copyright © 2008, IEEE

Logged in as:

Hsiang-Yu Liu

LOGOUT

### Thesis / Dissertation Reuse

**The IEEE does not require individuals working on a thesis to obtain a formal reuse license, however, you may print out this statement to be used as a permission grant:**

*Requirements to be followed when using any portion (e.g., figure, graph, table, or textual material) of an IEEE copyrighted paper in a thesis:*

- 1) In the case of textual material (e.g., using short quotes or referring to the work within these papers) users must give full credit to the original source (author, paper, publication) followed by the IEEE copyright line © 2011 IEEE.
- 2) In the case of illustrations or tabular material, we require that the copyright line © [Year of original publication] IEEE appear prominently with each reprinted figure and/or table.
- 3) If a substantial portion of the original paper is to be used, and if you are not the senior author, also obtain the senior author's approval.

*Requirements to be followed when using an entire IEEE copyrighted paper in a thesis:*

- 1) The following IEEE copyright/ credit notice should be placed prominently in the references: © [year of original publication] IEEE. Reprinted, with permission, from [author names, paper title, IEEE publication title, and month/year of publication]
- 2) Only the accepted version of an IEEE copyrighted paper can be used when posting the paper or your thesis on-line.
- 3) In placing the thesis on the author's university website, please display the following message in a prominent place on the website: In reference to IEEE copyrighted material which is used with permission in this thesis, the IEEE does not endorse any of [university/educational entity's name goes here]'s products or services. Internal or personal use of this material is permitted. If interested in reprinting/republishing IEEE copyrighted material for advertising or promotional purposes or for creating new collective works for resale or redistribution, please go to [http://www.ieee.org/publications\\_standards/publications/rights/rights\\_link.html](http://www.ieee.org/publications_standards/publications/rights/rights_link.html) to learn how to obtain a License from RightsLink.

If applicable, University Microfilms and/or ProQuest Library, or the Archives of Canada may supply single copies of the dissertation.

BACK

CLOSE WINDOW

Copyright © 2018 Copyright Clearance Center, Inc. All Rights Reserved. [Privacy statement](#). [Terms and Conditions](#).

## Reprint Permission for Figure 5.6 (b)

RightsLink Printable License

4/1/18, 9:25 PM

### JOHN WILEY AND SONS LICENSE TERMS AND CONDITIONS

Apr 01, 2018

This Agreement between Hsiang ("You") and John Wiley and Sons ("John Wiley and Sons") consists of your license details and the terms and conditions provided by John Wiley and Sons and Copyright Clearance Center.

License Number	4320501505996
License date	Apr 01, 2018
Licensed Content Publisher	John Wiley and Sons
Licensed Content Publication	Progress in Photovoltaics
Licensed Content Title	Enhanced lateral current transport via the front N+ diffused layer of n-type high-efficiency back-junction back-contact silicon solar cells
Licensed Content Author	Filip Granek, Martin Hermle, Dominik M. Huljić, et al
Licensed Content Date	Oct 29, 2008
Licensed Content Volume	17
Licensed Content Issue	1
Licensed Content Pages	10
Type of use	Dissertation/Thesis
Requestor type	University/Academic
Format	Print and electronic
Portion	Figure/table
Number of figures/tables	1
Original Wiley figure/table number(s)	Figure 6
Will you be translating?	No
Title of your thesis / dissertation	Silicon Defect Passivation by H <sub>2</sub> S Reaction and Patterning Process of Interdigitated Back Contact Silicon Heterojunction (IBC-SHJ) Solar Cell
Expected completion date	May 2018
Expected size (number of pages)	1
Requestor Location	Hsiang-Yu Liu 451 Wyoming Rd  NEWARK, DE 19716 United States Attn: Hsiang-Yu Liu

Publisher Tax ID EU826007151

Total 0.00 USD

[Terms and Conditions](#)

### TERMS AND CONDITIONS

This copyrighted material is owned by or exclusively licensed to John Wiley & Sons, Inc. or one of its group companies (each a "Wiley Company") or handled on behalf of a society with which a Wiley Company has exclusive publishing rights in relation to a particular work (collectively "WILEY"). By clicking "accept" in connection with completing this licensing transaction, you agree that the following terms and conditions apply to this transaction (along with the billing and payment terms and conditions established by the Copyright Clearance Center Inc., ("CCC's Billing and Payment terms and conditions"), at the time that you opened your RightsLink account (these are available at any time at <http://myaccount.copyright.com>).

#### Terms and Conditions

- The materials you have requested permission to reproduce or reuse (the "Wiley Materials") are protected by copyright.
- You are hereby granted a personal, non-exclusive, non-sub licensable (on a stand-alone basis), non-transferable, worldwide, limited license to reproduce the Wiley Materials for the purpose specified in the licensing process. This license, **and any CONTENT (PDF or image file) purchased as part of your order**, is for a one-time use only and limited to any maximum distribution number specified in the license. The first instance of republication or reuse granted by this license must be completed within two years of the date of the grant of this license (although copies prepared before the end date may be distributed thereafter). The Wiley Materials shall not be used in any other manner or for any other purpose, beyond what is granted in the license. Permission is granted subject to an appropriate acknowledgement given to the author, title of the material/book/journal and the publisher. You shall also duplicate the copyright notice that appears in the Wiley publication in your use of the Wiley Material. Permission is also granted on the understanding that nowhere in the text is a previously published source acknowledged for all or part of this Wiley Material. Any third party content is expressly excluded from this permission.
- With respect to the Wiley Materials, all rights are reserved. Except as expressly granted by the terms of the license, no part of the Wiley Materials may be copied, modified, adapted (except for minor reformatting required by the new Publication), translated, reproduced, transferred or distributed, in any form or by any means, and no derivative works may be made based on the Wiley Materials without the prior permission of the respective copyright owner. **For STM Signatory Publishers clearing permission under the terms of the [STM Permissions Guidelines](#) only, the terms of the license are extended to include subsequent editions and for editions in other languages, provided such editions are for the work as a whole in situ and does not involve the separate exploitation of the permitted figures or extracts,** You may not alter, remove or suppress in any manner any copyright, trademark or

other notices displayed by the Wiley Materials. You may not license, rent, sell, loan, lease, pledge, offer as security, transfer or assign the Wiley Materials on a stand-alone basis, or any of the rights granted to you hereunder to any other person.

- The Wiley Materials and all of the intellectual property rights therein shall at all times remain the exclusive property of John Wiley & Sons Inc, the Wiley Companies, or their respective licensors, and your interest therein is only that of having possession of and the right to reproduce the Wiley Materials pursuant to Section 2 herein during the continuance of this Agreement. You agree that you own no right, title or interest in or to the Wiley Materials or any of the intellectual property rights therein. You shall have no rights hereunder other than the license as provided for above in Section 2. No right, license or interest to any trademark, trade name, service mark or other branding ("Marks") of WILEY or its licensors is granted hereunder, and you agree that you shall not assert any such right, license or interest with respect thereto
- NEITHER WILEY NOR ITS LICENSORS MAKES ANY WARRANTY OR REPRESENTATION OF ANY KIND TO YOU OR ANY THIRD PARTY. EXPRESS, IMPLIED OR STATUTORY, WITH RESPECT TO THE MATERIALS OR THE ACCURACY OF ANY INFORMATION CONTAINED IN THE MATERIALS, INCLUDING, WITHOUT LIMITATION, ANY IMPLIED WARRANTY OF MERCHANTABILITY, ACCURACY, SATISFACTORY QUALITY, FITNESS FOR A PARTICULAR PURPOSE, USABILITY, INTEGRATION OR NON-INFRINGEMENT AND ALL SUCH WARRANTIES ARE HEREBY EXCLUDED BY WILEY AND ITS LICENSORS AND WAIVED BY YOU.
- WILEY shall have the right to terminate this Agreement immediately upon breach of this Agreement by you.
- You shall indemnify, defend and hold harmless WILEY, its Licensors and their respective directors, officers, agents and employees, from and against any actual or threatened claims, demands, causes of action or proceedings arising from any breach of this Agreement by you.
- IN NO EVENT SHALL WILEY OR ITS LICENSORS BE LIABLE TO YOU OR ANY OTHER PARTY OR ANY OTHER PERSON OR ENTITY FOR ANY SPECIAL, CONSEQUENTIAL, INCIDENTAL, INDIRECT, EXEMPLARY OR PUNITIVE DAMAGES, HOWEVER CAUSED, ARISING OUT OF OR IN CONNECTION WITH THE DOWNLOADING, PROVISIONING, VIEWING OR USE OF THE MATERIALS REGARDLESS OF THE FORM OF ACTION, WHETHER FOR BREACH OF CONTRACT, BREACH OF WARRANTY, TORT, NEGLIGENCE, INFRINGEMENT OR OTHERWISE (INCLUDING, WITHOUT LIMITATION, DAMAGES BASED ON LOSS OF PROFITS, DATA, FILES, USE, BUSINESS OPPORTUNITY OR CLAIMS OF THIRD PARTIES), AND WHETHER OR NOT THE PARTY HAS BEEN ADVISED OF THE POSSIBILITY OF SUCH DAMAGES. THIS LIMITATION SHALL APPLY NOTWITHSTANDING ANY FAILURE OF ESSENTIAL PURPOSE OF ANY LIMITED REMEDY PROVIDED

## HEREIN.

- Should any provision of this Agreement be held by a court of competent jurisdiction to be illegal, invalid, or unenforceable, that provision shall be deemed amended to achieve as nearly as possible the same economic effect as the original provision, and the legality, validity and enforceability of the remaining provisions of this Agreement shall not be affected or impaired thereby.
- The failure of either party to enforce any term or condition of this Agreement shall not constitute a waiver of either party's right to enforce each and every term and condition of this Agreement. No breach under this agreement shall be deemed waived or excused by either party unless such waiver or consent is in writing signed by the party granting such waiver or consent. The waiver by or consent of a party to a breach of any provision of this Agreement shall not operate or be construed as a waiver of or consent to any other or subsequent breach by such other party.
- This Agreement may not be assigned (including by operation of law or otherwise) by you without WILEY's prior written consent.
- Any fee required for this permission shall be non-refundable after thirty (30) days from receipt by the CCC.
- These terms and conditions together with CCC's Billing and Payment terms and conditions (which are incorporated herein) form the entire agreement between you and WILEY concerning this licensing transaction and (in the absence of fraud) supersedes all prior agreements and representations of the parties, oral or written. This Agreement may not be amended except in writing signed by both parties. This Agreement shall be binding upon and inure to the benefit of the parties' successors, legal representatives, and authorized assigns.
- In the event of any conflict between your obligations established by these terms and conditions and those established by CCC's Billing and Payment terms and conditions, these terms and conditions shall prevail.
- WILEY expressly reserves all rights not specifically granted in the combination of (i) the license details provided by you and accepted in the course of this licensing transaction, (ii) these terms and conditions and (iii) CCC's Billing and Payment terms and conditions.
- This Agreement will be void if the Type of Use, Format, Circulation, or Requestor Type was misrepresented during the licensing process.
- This Agreement shall be governed by and construed in accordance with the laws of the State of New York, USA, without regards to such state's conflict of law rules. Any legal action, suit or proceeding arising out of or relating to these Terms and Conditions or the breach thereof shall be instituted in a court of competent jurisdiction in New York County in the State of New York in the United States of America and each party



hereby consents and submits to the personal jurisdiction of such court, waives any objection to venue in such court and consents to service of process by registered or certified mail, return receipt requested, at the last known address of such party.

#### **WILEY OPEN ACCESS TERMS AND CONDITIONS**

Wiley Publishes Open Access Articles in fully Open Access Journals and in Subscription journals offering Online Open. Although most of the fully Open Access journals publish open access articles under the terms of the Creative Commons Attribution (CC BY) License only, the subscription journals and a few of the Open Access Journals offer a choice of Creative Commons Licenses. The license type is clearly identified on the article.

##### **The Creative Commons Attribution License**

The [Creative Commons Attribution License \(CC-BY\)](#) allows users to copy, distribute and transmit an article, adapt the article and make commercial use of the article. The CC-BY license permits commercial and non-

##### **Creative Commons Attribution Non-Commercial License**

The [Creative Commons Attribution Non-Commercial \(CC-BY-NC\) License](#) permits use, distribution and reproduction in any medium, provided the original work is properly cited and is not used for commercial purposes.(see below)

##### **Creative Commons Attribution-Non-Commercial-NoDerivs License**

The [Creative Commons Attribution Non-Commercial-NoDerivs License](#) (CC-BY-NC-ND) permits use, distribution and reproduction in any medium, provided the original work is properly cited, is not used for commercial purposes and no modifications or adaptations are made. (see below)

##### **Use by commercial "for-profit" organizations**

Use of Wiley Open Access articles for commercial, promotional, or marketing purposes requires further explicit permission from Wiley and will be subject to a fee.

Further details can be found on Wiley Online Library

<http://olabout.wiley.com/WileyCDA/Section/id-410895.html>

#### **Other Terms and Conditions:**

**v1.10 Last updated September 2015**

**Questions? [customer care@copyright.com](mailto:customer care@copyright.com) or +1-855-239-3415 (toll free in the US) or +1-978-646-2777.**

## Reprint Permission for excerpt in chapter 2.3.4

RightsLink Printable License

4/1/18, 9:15 PM

### ELSEVIER LICENSE TERMS AND CONDITIONS

Apr 01, 2018

This Agreement between Hsiang ("You") and Elsevier ("Elsevier") consists of your license details and the terms and conditions provided by Elsevier and Copyright Clearance Center.

License Number	4320500905083
License date	Apr 01, 2018
Licensed Content Publisher	Elsevier
Licensed Content Publication	Solar Energy Materials and Solar Cells
Licensed Content Title	An insight into dislocation density reduction in multicrystalline silicon
Licensed Content Author	Soobin Woo, Mariana Bertoni, Kwangmin Choi, Seungjin Nam, Sergio Castellanos, Douglas Michael Powell, Tonio Buonassisi, Hyunjoo Choi
Licensed Content Date	Oct 1, 2016
Licensed Content Volume	155
Licensed Content Issue	n/a
Licensed Content Pages	13
Start Page	88
End Page	100
Type of Use	reuse in a thesis/dissertation
Intended publisher of new work	other
Portion	excerpt
Number of excerpts	1
Format	both print and electronic
Are you the author of this Elsevier article?	No
Will you be translating?	No
Title of your thesis/dissertation	Silicon Defect Passivation by H <sub>2</sub> S Reaction and Patterning Process of Interdigitated Back Contact Silicon Heterojunction (IBC-SHJ) Solar Cell
Publisher of new work	Institute of Energy Conversion
Author of new work	Robert Birkmire
Expected completion date	May 2018
Estimated size (number of pages)	1

Requestor Location	Hsiang-Yu Liu 451 Wyoming Rd  NEWARK, DE 19716 United States Attn: Hsiang-Yu Liu
Publisher Tax ID	98-0397604
Total	0.00 USD
Terms and Conditions	

### INTRODUCTION

1. The publisher for this copyrighted material is Elsevier. By clicking "accept" in connection with completing this licensing transaction, you agree that the following terms and conditions apply to this transaction (along with the Billing and Payment terms and conditions established by Copyright Clearance Center, Inc. ("CCC"), at the time that you opened your Rightslink account and that are available at any time at <http://myaccount.copyright.com>).

### GENERAL TERMS

- Elsevier hereby grants you permission to reproduce the aforementioned material subject to the terms and conditions indicated.
- Acknowledgement: If any part of the material to be used (for example, figures) has appeared in our publication with credit or acknowledgement to another source, permission must also be sought from that source. If such permission is not obtained then that material may not be included in your publication/copies. Suitable acknowledgement to the source must be made, either as a footnote or in a reference list at the end of your publication, as follows:  
"Reprinted from Publication title, Vol /edition number, Author(s), Title of article / title of chapter, Pages No., Copyright (Year), with permission from Elsevier [OR APPLICABLE SOCIETY COPYRIGHT OWNER]." Also Lancet special credit - "Reprinted from The Lancet, Vol. number, Author(s), Title of article, Pages No., Copyright (Year), with permission from Elsevier."
- Reproduction of this material is confined to the purpose and/or media for which permission is hereby given.
- Altering/Modifying Material: Not Permitted. However figures and illustrations may be altered/adapted minimally to serve your work. Any other abbreviations, additions, deletions and/or any other alterations shall be made only with prior written authorization of Elsevier Ltd. (Please contact Elsevier at [permissions@elsevier.com](mailto:permissions@elsevier.com)). No modifications can be made to any Lancet figures/tables and they must be reproduced in full.
- If the permission fee for the requested use of our material is waived in this instance, please be advised that your future requests for Elsevier materials may attract a fee.
- Reservation of Rights: Publisher reserves all rights not specifically granted in the combination of (i) the license details provided by you and accepted in the course of this licensing transaction, (ii) these terms and conditions and (iii) CCC's Billing and Payment terms and conditions.
- License Contingent Upon Payment: While you may exercise the rights licensed immediately upon issuance of the license at the end of the licensing process for the transaction, provided that you have disclosed complete and accurate details of your proposed

use, no license is finally effective unless and until full payment is received from you (either by publisher or by CCC) as provided in CCC's Billing and Payment terms and conditions. If full payment is not received on a timely basis, then any license preliminarily granted shall be deemed automatically revoked and shall be void as if never granted. Further, in the event that you breach any of these terms and conditions or any of CCC's Billing and Payment terms and conditions, the license is automatically revoked and shall be void as if never granted. Use of materials as described in a revoked license, as well as any use of the materials beyond the scope of an unrevoked license, may constitute copyright infringement and publisher reserves the right to take any and all action to protect its copyright in the materials.

9. Warranties: Publisher makes no representations or warranties with respect to the licensed material.

10. Indemnity: You hereby indemnify and agree to hold harmless publisher and CCC, and their respective officers, directors, employees and agents, from and against any and all claims arising out of your use of the licensed material other than as specifically authorized pursuant to this license.

11. No Transfer of License: This license is personal to you and may not be sublicensed, assigned, or transferred by you to any other person without publisher's written permission.

12. No Amendment Except in Writing: This license may not be amended except in a writing signed by both parties (or, in the case of publisher, by CCC on publisher's behalf).

13. Objection to Contrary Terms: Publisher hereby objects to any terms contained in any purchase order, acknowledgment, check endorsement or other writing prepared by you, which terms are inconsistent with these terms and conditions or CCC's Billing and Payment terms and conditions. These terms and conditions, together with CCC's Billing and Payment terms and conditions (which are incorporated herein), comprise the entire agreement between you and publisher (and CCC) concerning this licensing transaction. In the event of any conflict between your obligations established by these terms and conditions and those established by CCC's Billing and Payment terms and conditions, these terms and conditions shall control.

14. Revocation: Elsevier or Copyright Clearance Center may deny the permissions described in this License at their sole discretion, for any reason or no reason, with a full refund payable to you. Notice of such denial will be made using the contact information provided by you. Failure to receive such notice will not alter or invalidate the denial. In no event will Elsevier or Copyright Clearance Center be responsible or liable for any costs, expenses or damage incurred by you as a result of a denial of your permission request, other than a refund of the amount(s) paid by you to Elsevier and/or Copyright Clearance Center for denied permissions.

#### LIMITED LICENSE

The following terms and conditions apply only to specific license types:

15. **Translation:** This permission is granted for non-exclusive world English rights only unless your license was granted for translation rights. If you licensed translation rights you may only translate this content into the languages you requested. A professional translator must perform all translations and reproduce the content word for word preserving the integrity of the article.

16. **Posting licensed content on any Website:** The following terms and conditions apply as follows: Licensing material from an Elsevier journal: All content posted to the web site must maintain the copyright information line on the bottom of each image; A hyper-text must be

included to the Homepage of the journal from which you are licensing at <http://www.sciencedirect.com/science/journal/xxxxx> or the Elsevier homepage for books at <http://www.elsevier.com>; Central Storage: This license does not include permission for a scanned version of the material to be stored in a central repository such as that provided by Heron/XanEdu.

Licensing material from an Elsevier book: A hyper-text link must be included to the Elsevier homepage at <http://www.elsevier.com>. All content posted to the web site must maintain the copyright information line on the bottom of each image.

**Posting licensed content on Electronic reserve:** In addition to the above the following clauses are applicable: The web site must be password-protected and made available only to bona fide students registered on a relevant course. This permission is granted for 1 year only. You may obtain a new license for future website posting.

17. **For journal authors:** the following clauses are applicable in addition to the above:

**Preprints:**

A preprint is an author's own write-up of research results and analysis, it has not been peer-reviewed, nor has it had any other value added to it by a publisher (such as formatting, copyright, technical enhancement etc.).

Authors can share their preprints anywhere at any time. Preprints should not be added to or enhanced in any way in order to appear more like, or to substitute for, the final versions of articles however authors can update their preprints on arXiv or RePEc with their Accepted Author Manuscript (see below).

If accepted for publication, we encourage authors to link from the preprint to their formal publication via its DOI. Millions of researchers have access to the formal publications on ScienceDirect, and so links will help users to find, access, cite and use the best available version. Please note that Cell Press, The Lancet and some society-owned have different preprint policies. Information on these policies is available on the journal homepage.

**Accepted Author Manuscripts:** An accepted author manuscript is the manuscript of an article that has been accepted for publication and which typically includes author-incorporated changes suggested during submission, peer review and editor-author communications.

Authors can share their accepted author manuscript:

- immediately
  - via their non-commercial person homepage or blog
  - by updating a preprint in arXiv or RePEc with the accepted manuscript
  - via their research institute or institutional repository for internal institutional uses or as part of an invitation-only research collaboration work-group
  - directly by providing copies to their students or to research collaborators for their personal use
  - for private scholarly sharing as part of an invitation-only work group on commercial sites with which Elsevier has an agreement
- After the embargo period
  - via non-commercial hosting platforms such as their institutional repository
  - via commercial sites with which Elsevier has an agreement

In all cases accepted manuscripts should:

- link to the formal publication via its DOI
- bear a CC-BY-NC-ND license - this is easy to do
- if aggregated with other manuscripts, for example in a repository or other site, be shared in alignment with our hosting policy not be added to or enhanced in any way to appear more like, or to substitute for, the published journal article.

**Published journal article (JPA):** A published journal article (JPA) is the definitive final record of published research that appears or will appear in the journal and embodies all value-adding publishing activities including peer review co-ordination, copy-editing, formatting, (if relevant) pagination and online enrichment.

Policies for sharing publishing journal articles differ for subscription and gold open access articles:

**Subscription Articles:** If you are an author, please share a link to your article rather than the full-text. Millions of researchers have access to the formal publications on ScienceDirect, and so links will help your users to find, access, cite, and use the best available version. Theses and dissertations which contain embedded PJAs as part of the formal submission can be posted publicly by the awarding institution with DOI links back to the formal publications on ScienceDirect.

If you are affiliated with a library that subscribes to ScienceDirect you have additional private sharing rights for others' research accessed under that agreement. This includes use for classroom teaching and internal training at the institution (including use in course packs and courseware programs), and inclusion of the article for grant funding purposes.

**Gold Open Access Articles:** May be shared according to the author-selected end-user license and should contain a [CrossMark logo](#), the end user license, and a DOI link to the formal publication on ScienceDirect.

Please refer to Elsevier's [posting policy](#) for further information.

18. **For book authors** the following clauses are applicable in addition to the above:

Authors are permitted to place a brief summary of their work online only. You are not allowed to download and post the published electronic version of your chapter, nor may you scan the printed edition to create an electronic version. **Posting to a repository:** Authors are permitted to post a summary of their chapter only in their institution's repository.

19. **Thesis/Dissertation:** If your license is for use in a thesis/dissertation your thesis may be submitted to your institution in either print or electronic form. Should your thesis be published commercially, please reapply for permission. These requirements include permission for the Library and Archives of Canada to supply single copies, on demand, of the complete thesis and include permission for Proquest/UMI to supply single copies, on demand, of the complete thesis. Should your thesis be published commercially, please reapply for permission. Theses and dissertations which contain embedded PJAs as part of the formal submission can be posted publicly by the awarding institution with DOI links back to the formal publications on ScienceDirect.

### **Elsevier Open Access Terms and Conditions**

You can publish open access with Elsevier in hundreds of open access journals or in nearly 2000 established subscription journals that support open access publishing. Permitted third party re-use of these open access articles is defined by the author's choice of Creative Commons user license. See our [open access license policy](#) for more information.

**Terms & Conditions applicable to all Open Access articles published with Elsevier:**

Any reuse of the article must not represent the author as endorsing the adaptation of the article nor should the article be modified in such a way as to damage the author's honour or reputation. If any changes have been made, such changes must be clearly indicated. The author(s) must be appropriately credited and we ask that you include the end user license and a DOI link to the formal publication on ScienceDirect.

If any part of the material to be used (for example, figures) has appeared in our publication with credit or acknowledgement to another source it is the responsibility of the user to ensure their reuse complies with the terms and conditions determined by the rights holder.

**Additional Terms & Conditions applicable to each Creative Commons user license:**

**CC BY:** The CC-BY license allows users to copy, to create extracts, abstracts and new works from the Article, to alter and revise the Article and to make commercial use of the Article (including reuse and/or resale of the Article by commercial entities), provided the user gives appropriate credit (with a link to the formal publication through the relevant DOI), provides a link to the license, indicates if changes were made and the licensor is not represented as endorsing the use made of the work. The full details of the license are available at <http://creativecommons.org/licenses/by/4.0>.

**CC BY NC SA:** The CC BY-NC-SA license allows users to copy, to create extracts, abstracts and new works from the Article, to alter and revise the Article, provided this is not done for commercial purposes, and that the user gives appropriate credit (with a link to the formal publication through the relevant DOI), provides a link to the license, indicates if changes were made and the licensor is not represented as endorsing the use made of the work. Further, any new works must be made available on the same conditions. The full details of the license are available at <http://creativecommons.org/licenses/by-nc-sa/4.0>.

**CC BY NC ND:** The CC BY-NC-ND license allows users to copy and distribute the Article, provided this is not done for commercial purposes and further does not permit distribution of the Article if it is changed or edited in any way, and provided the user gives appropriate credit (with a link to the formal publication through the relevant DOI), provides a link to the license, and that the licensor is not represented as endorsing the use made of the work. The full details of the license are available at <http://creativecommons.org/licenses/by-nc-nd/4.0>. Any commercial reuse of Open Access articles published with a CC BY NC SA or CC BY NC ND license requires permission from Elsevier and will be subject to a fee.

Commercial reuse includes:

- Associating advertising with the full text of the Article
- Charging fees for document delivery or access
- Article aggregation
- Systematic distribution via e-mail lists or share buttons

Posting or linking by commercial companies for use by customers of those companies.

## Reprint Permission for excerpt in chapter 5.4.2

RightsLink Printable License

4/1/18, 9:27 PM

### JOHN WILEY AND SONS LICENSE TERMS AND CONDITIONS

Apr 01, 2018

This Agreement between Hsiang ("You") and John Wiley and Sons ("John Wiley and Sons") consists of your license details and the terms and conditions provided by John Wiley and Sons and Copyright Clearance Center.

License Number	4320510124636
License date	Apr 01, 2018
Licensed Content Publisher	John Wiley and Sons
Licensed Content Publication	Progress in Photovoltaics
Licensed Content Title	Enhanced lateral current transport via the front N+ diffused layer of n-type high-efficiency back-junction back-contact silicon solar cells
Licensed Content Author	Filip Granek, Martin Hermle, Dominik M. Huljić, et al
Licensed Content Date	Oct 29, 2008
Licensed Content Volume	17
Licensed Content Issue	1
Licensed Content Pages	10
Type of use	Dissertation/Thesis
Requestor type	University/Academic
Format	Print and electronic
Portion	Text extract
Number of Pages	1
Will you be translating?	No
Title of your thesis / dissertation	Silicon Defect Passivation by H <sub>2</sub> S Reaction and Patterning Process of Interdigitated Back Contact Silicon Heterojunction (IBC-SHJ) Solar Cell
Expected completion date	May 2018
Expected size (number of pages)	1
Requestor Location	Hsiang-Yu Liu 451 Wyoming Rd  NEWARK, DE 19716 United States Attn: Hsiang-Yu Liu
Publisher Tax ID	EU826007151
Total	0.00 USD



[Terms and Conditions](#)**TERMS AND CONDITIONS**

This copyrighted material is owned by or exclusively licensed to John Wiley & Sons, Inc. or one of its group companies (each a "Wiley Company") or handled on behalf of a society with which a Wiley Company has exclusive publishing rights in relation to a particular work (collectively "WILEY"). By clicking "accept" in connection with completing this licensing transaction, you agree that the following terms and conditions apply to this transaction (along with the billing and payment terms and conditions established by the Copyright Clearance Center Inc., ("CCC's Billing and Payment terms and conditions"), at the time that you opened your RightsLink account (these are available at any time at <http://myaccount.copyright.com>).

**Terms and Conditions**

- The materials you have requested permission to reproduce or reuse (the "Wiley Materials") are protected by copyright.
- You are hereby granted a personal, non-exclusive, non-sub licensable (on a stand-alone basis), non-transferable, worldwide, limited license to reproduce the Wiley Materials for the purpose specified in the licensing process. This license, **and any CONTENT (PDF or image file) purchased as part of your order**, is for a one-time use only and limited to any maximum distribution number specified in the license. The first instance of republication or reuse granted by this license must be completed within two years of the date of the grant of this license (although copies prepared before the end date may be distributed thereafter). The Wiley Materials shall not be used in any other manner or for any other purpose, beyond what is granted in the license. Permission is granted subject to an appropriate acknowledgement given to the author, title of the material/book/journal and the publisher. You shall also duplicate the copyright notice that appears in the Wiley publication in your use of the Wiley Material. Permission is also granted on the understanding that nowhere in the text is a previously published source acknowledged for all or part of this Wiley Material. Any third party content is expressly excluded from this permission.
- With respect to the Wiley Materials, all rights are reserved. Except as expressly granted by the terms of the license, no part of the Wiley Materials may be copied, modified, adapted (except for minor reformatting required by the new Publication), translated, reproduced, transferred or distributed, in any form or by any means, and no derivative works may be made based on the Wiley Materials without the prior permission of the respective copyright owner. **For STM Signatory Publishers clearing permission under the terms of the [STM Permissions Guidelines](#) only, the terms of the license are extended to include subsequent editions and for editions in other languages, provided such editions are for the work as a whole in situ and does not involve the separate exploitation of the permitted figures or extracts**, You may not alter, remove or suppress in any manner any copyright, trademark or other notices displayed by the Wiley Materials. You may not license, rent, sell, loan, lease, pledge, offer as security, transfer or assign the Wiley Materials on a stand-alone basis, or any of the rights granted to you hereunder to any other person.

- The Wiley Materials and all of the intellectual property rights therein shall at all times remain the exclusive property of John Wiley & Sons Inc, the Wiley Companies, or their respective licensors, and your interest therein is only that of having possession of and the right to reproduce the Wiley Materials pursuant to Section 2 herein during the continuance of this Agreement. You agree that you own no right, title or interest in or to the Wiley Materials or any of the intellectual property rights therein. You shall have no rights hereunder other than the license as provided for above in Section 2. No right, license or interest to any trademark, trade name, service mark or other branding ("Marks") of WILEY or its licensors is granted hereunder, and you agree that you shall not assert any such right, license or interest with respect thereto
- NEITHER WILEY NOR ITS LICENSORS MAKES ANY WARRANTY OR REPRESENTATION OF ANY KIND TO YOU OR ANY THIRD PARTY, EXPRESS, IMPLIED OR STATUTORY, WITH RESPECT TO THE MATERIALS OR THE ACCURACY OF ANY INFORMATION CONTAINED IN THE MATERIALS, INCLUDING, WITHOUT LIMITATION, ANY IMPLIED WARRANTY OF MERCHANTABILITY, ACCURACY, SATISFACTORY QUALITY, FITNESS FOR A PARTICULAR PURPOSE, USABILITY, INTEGRATION OR NON-INFRINGEMENT AND ALL SUCH WARRANTIES ARE HEREBY EXCLUDED BY WILEY AND ITS LICENSORS AND WAIVED BY YOU.
- WILEY shall have the right to terminate this Agreement immediately upon breach of this Agreement by you.
- You shall indemnify, defend and hold harmless WILEY, its Licensors and their respective directors, officers, agents and employees, from and against any actual or threatened claims, demands, causes of action or proceedings arising from any breach of this Agreement by you.
- IN NO EVENT SHALL WILEY OR ITS LICENSORS BE LIABLE TO YOU OR ANY OTHER PARTY OR ANY OTHER PERSON OR ENTITY FOR ANY SPECIAL, CONSEQUENTIAL, INCIDENTAL, INDIRECT, EXEMPLARY OR PUNITIVE DAMAGES, HOWEVER CAUSED, ARISING OUT OF OR IN CONNECTION WITH THE DOWNLOADING, PROVISIONING, VIEWING OR USE OF THE MATERIALS REGARDLESS OF THE FORM OF ACTION, WHETHER FOR BREACH OF CONTRACT, BREACH OF WARRANTY, TORT, NEGLIGENCE, INFRINGEMENT OR OTHERWISE (INCLUDING, WITHOUT LIMITATION, DAMAGES BASED ON LOSS OF PROFITS, DATA, FILES, USE, BUSINESS OPPORTUNITY OR CLAIMS OF THIRD PARTIES), AND WHETHER OR NOT THE PARTY HAS BEEN ADVISED OF THE POSSIBILITY OF SUCH DAMAGES. THIS LIMITATION SHALL APPLY NOTWITHSTANDING ANY FAILURE OF ESSENTIAL PURPOSE OF ANY LIMITED REMEDY PROVIDED HEREIN.
- Should any provision of this Agreement be held by a court of competent jurisdiction

to be illegal, invalid, or unenforceable, that provision shall be deemed amended to achieve as nearly as possible the same economic effect as the original provision, and the legality, validity and enforceability of the remaining provisions of this Agreement shall not be affected or impaired thereby.

- The failure of either party to enforce any term or condition of this Agreement shall not constitute a waiver of either party's right to enforce each and every term and condition of this Agreement. No breach under this agreement shall be deemed waived or excused by either party unless such waiver or consent is in writing signed by the party granting such waiver or consent. The waiver by or consent of a party to a breach of any provision of this Agreement shall not operate or be construed as a waiver of or consent to any other or subsequent breach by such other party.
- This Agreement may not be assigned (including by operation of law or otherwise) by you without WILEY's prior written consent.
- Any fee required for this permission shall be non-refundable after thirty (30) days from receipt by the CCC.
- These terms and conditions together with CCC's Billing and Payment terms and conditions (which are incorporated herein) form the entire agreement between you and WILEY concerning this licensing transaction and (in the absence of fraud) supersedes all prior agreements and representations of the parties, oral or written. This Agreement may not be amended except in writing signed by both parties. This Agreement shall be binding upon and inure to the benefit of the parties' successors, legal representatives, and authorized assigns.
- In the event of any conflict between your obligations established by these terms and conditions and those established by CCC's Billing and Payment terms and conditions, these terms and conditions shall prevail.
- WILEY expressly reserves all rights not specifically granted in the combination of (i) the license details provided by you and accepted in the course of this licensing transaction, (ii) these terms and conditions and (iii) CCC's Billing and Payment terms and conditions.
- This Agreement will be void if the Type of Use, Format, Circulation, or Requestor Type was misrepresented during the licensing process.
- This Agreement shall be governed by and construed in accordance with the laws of the State of New York, USA, without regards to such state's conflict of law rules. Any legal action, suit or proceeding arising out of or relating to these Terms and Conditions or the breach thereof shall be instituted in a court of competent jurisdiction in New York County in the State of New York in the United States of America and each party hereby consents and submits to the personal jurisdiction of such court, waives any objection to venue in such court and consents to service of process by registered or certified mail, return receipt requested, at the last known address of such party.

**WILEY OPEN ACCESS TERMS AND CONDITIONS**

Wiley Publishes Open Access Articles in fully Open Access Journals and in Subscription journals offering Online Open. Although most of the fully Open Access journals publish open access articles under the terms of the Creative Commons Attribution (CC BY) License only, the subscription journals and a few of the Open Access Journals offer a choice of Creative Commons Licenses. The license type is clearly identified on the article.

**The Creative Commons Attribution License**

The [Creative Commons Attribution License \(CC-BY\)](#) allows users to copy, distribute and transmit an article, adapt the article and make commercial use of the article. The CC-BY license permits commercial and non-

**Creative Commons Attribution Non-Commercial License**

The [Creative Commons Attribution Non-Commercial \(CC-BY-NC\) License](#) permits use, distribution and reproduction in any medium, provided the original work is properly cited and is not used for commercial purposes.(see below)

**Creative Commons Attribution-Non-Commercial-NoDerivs License**

The [Creative Commons Attribution Non-Commercial-NoDerivs License](#) (CC-BY-NC-ND) permits use, distribution and reproduction in any medium, provided the original work is properly cited, is not used for commercial purposes and no modifications or adaptations are made. (see below)

**Use by commercial "for-profit" organizations**

Use of Wiley Open Access articles for commercial, promotional, or marketing purposes requires further explicit permission from Wiley and will be subject to a fee.

Further details can be found on Wiley Online Library

<http://olabout.wiley.com/WileyCDA/Section/id-410895.html>

Reprint Permission for chapter 4 (The IEEE does not require individuals working on a thesis to obtain a formal reuse license.)

Rightslink® by Copyright Clearance Center

4/1/18, 9:47 PM



RightsLink®

Home

Account  
Info

Help



**Title:** The role of back contact patterning on stability and performance of Si IBC heterojunction solar cells

**Conference Proceedings:** Photovoltaic Specialist Conference (PVSC), 2014 IEEE 40th

**Author:** Ujjwal K. Das

**Publisher:** IEEE

**Date:** June 2014

Logged in as:  
Hsiang-Yu Liu

LOGOUT

Copyright © 2014, IEEE

### Thesis / Dissertation Reuse

**The IEEE does not require individuals working on a thesis to obtain a formal reuse license, however, you may print out this statement to be used as a permission grant:**

*Requirements to be followed when using any portion (e.g., figure, graph, table, or textual material) of an IEEE copyrighted paper in a thesis:*

- 1) In the case of textual material (e.g., using short quotes or referring to the work within these papers) users must give full credit to the original source (author, paper, publication) followed by the IEEE copyright line © 2011 IEEE.
- 2) In the case of illustrations or tabular material, we require that the copyright line © [Year of original publication] IEEE appear prominently with each reprinted figure and/or table.
- 3) If a substantial portion of the original paper is to be used, and if you are not the senior author, also obtain the senior author's approval.

*Requirements to be followed when using an entire IEEE copyrighted paper in a thesis:*

- 1) The following IEEE copyright/ credit notice should be placed prominently in the references: © [year of original publication] IEEE. Reprinted, with permission, from [author names, paper title, IEEE publication title, and month/year of publication]
- 2) Only the accepted version of an IEEE copyrighted paper can be used when posting the paper or your thesis on-line.
- 3) In placing the thesis on the author's university website, please display the following message in a prominent place on the website: In reference to IEEE copyrighted material which is used with permission in this thesis, the IEEE does not endorse any of [university/educational entity's name goes here]'s products or services. Internal or personal use of this material is permitted. If interested in reprinting/republishing IEEE copyrighted material for advertising or promotional purposes or for creating new collective works for resale or redistribution, please go to [http://www.ieee.org/publications\\_standards/publications/rights/rights\\_link.html](http://www.ieee.org/publications_standards/publications/rights/rights_link.html) to learn how to obtain a License from RightsLink.

If applicable, University Microfilms and/or ProQuest Library, or the Archives of Canada may supply single copies of the dissertation.

BACK

CLOSE WINDOW

Copyright © 2018 Copyright Clearance Center, Inc. All Rights Reserved. [Privacy statement](#). [Terms and Conditions](#).

## Reprint Permission for chapter 6

Rightslink® by Copyright Clearance Center

4/1/18, 9:43 PM



RightsLink®

Home

Account  
Info

Help



ACS Publications  
Most Trusted. Most Cited. Most Read.

**Title:** Surface Defect Passivation and  
Reaction of c-Si in H<sub>2</sub>S

Logged in as:  
Hsiang-Yu Liu

**Author:** Hsiang-Yu Liu, Ujjwal K. Das,  
Robert W. Birkmire

LOGOUT

**Publication:** Langmuir

**Publisher:** American Chemical Society

**Date:** Dec 1, 2017

Copyright © 2017, American Chemical Society

### PERMISSION/LICENSE IS GRANTED FOR YOUR ORDER AT NO CHARGE

This type of permission/license, instead of the standard Terms & Conditions, is sent to you because no fee is being charged for your order. Please note the following:

- Permission is granted for your request in both print and electronic formats, and translations.
- If figures and/or tables were requested, they may be adapted or used in part.
- Please print this page for your records and send a copy of it to your publisher/graduate school.
- Appropriate credit for the requested material should be given as follows: "Reprinted (adapted) with permission from (COMPLETE REFERENCE CITATION). Copyright (YEAR) American Chemical Society." Insert appropriate information in place of the capitalized words.
- One-time permission is granted only for the use specified in your request. No additional uses are granted (such as derivative works or other editions). For any other uses, please submit a new request.

BACK

CLOSE WINDOW

Copyright © 2018 Copyright Clearance Center, Inc. All Rights Reserved. [Privacy statement](#). [Terms and Conditions](#).  
Comments? We would like to hear from you. E-mail us at [customer@copyright.com](mailto:customer@copyright.com)

## Reprint Permission for chapter 7

Regarding:

Title: A Novel Defect Passivation Method for Multicrystalline Si Wafer by H<sub>2</sub>S Reaction  
Authors: Hsiang-Yu Liu, Ujjwal K. Das, and Robert W. Birkmire  
Affiliation: Institute of Energy Conversion, University of Delaware, Newark, DE 19716, USA

Please retain this mail for your records and share with the appropriate people in your academic institution.

The IEEE does not require individuals working on a thesis to obtain a formal reuse license however, you must follow the requirements listed below:

### Textual Material

Using short quotes or referring to the work within these papers) users must give full credit to the original source (author, paper, publication followed by the IEEE copyright line © [Year of publication] IEEE.

In the case of illustrations or tabular material, we require that the copyright line © [Year of original publication] IEEE appear prominently with each reprinted figure and/or table.

If a substantial portion of the original paper is to be used, and if you are not the senior author, also obtain the senior author's approval.

### Full-Text Article

If you are using the entire IEEE copyright owned article, the following IEEE copyright/ credit notice should be placed prominently in the references: © [year of original publication] IEEE. Reprinted, with permission, from [author names, paper title, IEEE publication title, and month/year of publication]

Only the **accepted** version of an IEEE copyrighted paper can be used when posting the paper or your thesis on-line. You may not use the **final published** version

In placing the thesis on the author's university website, please display the following message in a prominent place on the website: In reference to IEEE copyrighted material which is used with permission in this thesis, the IEEE does not endorse any of [university/educational entity's name goes here]'s products or services. Internal or personal use of this material is permitted. If interested in reprinting/republishing IEEE copyrighted material for advertising or promotional purposes or for creating new collective works for resale or redistribution, please go to

[http://www.ieee.org/publications\\_standards/publications/rights/rights\\_link.html](http://www.ieee.org/publications_standards/publications/rights/rights_link.html)

to learn how to obtain a License from RightsLink.

If applicable, University Microfilms and/or ProQuest Library, or the Archives of Canada may supply single copies of the dissertation.

Kind regards,

M.E. Brennan

Ms M.E. Brennan  
IEEE  
Rights & Permissions  
[501 Hoes Lane](#)  
[Piscataway, NJ 08854](#)-4141 USA  
[me.brennan@ieee.org](mailto:me.brennan@ieee.org)

+1 (732) 562-2660